Modeling Radiation Damage in Nanostructured Ferritic Alloys: Helium Bubble Precipitation on Oxide Nanofeatures

Christopher Evan Nellis

Dissertation submitted to the faculty of Virginia Polytechnic Institute and State University in partial fulfillment of the requirements for the degree of

Doctorate of Philosophy
In
Nuclear Engineering

Celine Hin
Alireza Haghighat
Aditya Savara
Michael Von Spakovsky

11/10/2021
Blacksburg, Virginia

Keywords: Kinetic Monte Carlo, Nuclear Materials, Irradiation Damage

Modeling Radiation Damage in Nanostructured Ferritic Alloys: Helium Bubble Precipitation on Oxide Nanofeatures

Christopher Nellis

Abstract

The requirements for the next generation of nuclear reactors call for more radiation tolerant materials. One such material, nanostructured ferritic alloys (NFA) are a candidate material for use in cladding. The radiation tolerance of NFAs comes from the high number density of small oxide nanofeatures composed of Y, Ti, and O. These oxide nanofeatures or nano-oxides act as alternative nucleation sites for bubbles of transmutation He, thus preventing the accumulation of He atoms at the grain boundaries which would embrittle the metal.

To further study the material, a mean-field rate theory model (MF-RTM) was created to simulate the radiation-induced segregation (RIS) of the alloy components Y, Ti, and O to the grain boundaries. Later, a kinetic Monte Carlo model (KMC) was made that replicated the results from the rate theory for the radiation induced segregation. Then the KMC model was modified to study the nano-oxide behavior in a range of different behaviors; the nano-oxide precipitation kinetics during heat treatment, resistance to dissolution under irradiation regimes similar to reactor conditions, and ability to trap He bubbles on the nano-oxide surfaces rather than the grain boundary. This KMC model is more complex than others as it includes 5 different atomic species (Fe, Y, Ti, O, and He) which migrate through three different mechanisms. Findings from the precipitation heat treatments were able to replicate the size, number density, and composition of nano-oxides from experiments and determined vacancy trapping at oxide interfaces was a significant for the NFA's coarsening resistance as opposed to interference from dislocations. In

the irradiation simulations, the resistance of the nano-oxides to dissolution was confirmed and found the excess vacancy population plays an important role in healing the nano-oxides. He bubbles formed in the KMC simulations were found to preferentially form at the oxide interfaces, particularly the <111> interface, rather than the grain boundary and the characteristics of the He bubbles match expectations from literature. In the development of the KMC model, new insights into steady-state detection concepts were also found. A new type of steady-state detection (SSD) algorithm is described. Additionally, a method of forecasting the number of data points needed to make an accurate determination of steady-state, a 'predicting the pre-requisite to steady state detection' (ppSSD), is explored.

Modeling Radiation Damage in Nanostructured Ferritic Alloys: Helium Bubble Precipitation on Oxide Nanofeatures

Christopher Nellis

General Abstract

Nuclear reactors need more radiation tolerant materials in the future, such as nanostructured ferritic alloys (NFA), used for nuclear fuel rod cladding, whose large amount of nanometer sized oxide particles contribute substantially to the radiation resistance of the metal overall. A mean-field rate theory method (MF-RTM) and a Kinetic Monte Carlo (KMC) computer model were made to study radiation induced segregation in the material. A more complex 5 element (Fe, Y, Ti, O, and He) KMC code was later developed to study the influence of the oxides at high temperatures and dose rates to gain insight into the causes the oxides remarkable thermal stability and resistance to irradiation. At all stages, the KMC model was able to replicate material behavior under high temperature heat treatment and irradiation. The model was used to simulate the formation of these oxides under different temperatures during their initial processing to gain more knowledge on how the oxide characteristics (size and number density) are influenced by temperature so we can tailor the processing method to achieve an ideal distribution of oxides in the material. Additionally, a mechanism for the oxides resistance to high temperature coarsening unrelated to the expected one caused by dislocations. The irradiation resistance of oxides to dissolution from irradiation was also investigated. While experimental measurements give a before and after picture of a material that underwent irradiation, the KMC can show the time evolution of the oxide size with increasing irradiation damage so the mechanisms behind the radiation resistance can be understood. The oxides remained stable at all temperatures and dose rates. Excess

vacancies were found to play an important role in stabilizing the oxides against radiation damage. The KMC model also confirmed the ability of the oxides to trap transmutation He at the interfaces rather than the grain boundary and observed the process of He bubble nucleation. The He bubble form at the <111> oxide interface and they possess similar characteristics of He bubbles expected from literature. Additionally, a novel steady-state detection (SSD) algorithm was developed that can be used for long-term simulations and a method to determine how many data points the algorithm needs to accurately detect steady state is described here.

Acknowledgments

I would like to thank everyone who has helped me directly or indirectly for this dissertation would not have been possible without their support. First and foremost, my advisor Dr. Celine Hin whose guidance steered my research from rocky shores and provided opportunities for me to grow my skills. Her expertise in Monte Carlo simulations and rigorous validation techniques contributed greatly to this project. The many hours spent preparing for conference presentations and other functions has also been invaluable. Dr. Aditya (Ashi) Savara's statistical knowledge helped guide the development of the steady-state detection algorithm and whose professional example at ORNL continues to enrich my own habits. Dr. Joel Ribis provided invaluable discussions on the coarsening behavior of NFAs.

I thank all my committee members, Dr. Celine Hin, Dr. Alireza Haghighat, Dr. Aditya (Ashi) Savara, Dr. Michael Von Spakovsky, and Dr. David Clark for taking the time to serve and provide needed definition to the project.

To the other researchers I met along the way who may not have directly contributed to my research but influenced me through their example as scientists, I thank Dr. Maura Borrego and Dr. Remi Dingreville. The graduate students I met on Virginia Tech campus whose conversations and friendship supported me: Dr. Eric Tea, Dr. Jianqiu Huang, Dr. Thomas Danielson, Dr. Evan Margaretta, and Ryan Chan.

To my parents Donald and Donna Nellis who raised me to be who I am today and for their seemingly endless love and patience; especially when a temporary stay turned into 18 months. To my grandfather Donald Nellis Sr. whose decades of work in the nuclear field has come to inspire me.

Thank You.

Financial support for this research was provided by the Nuclear Regulatory Commission Fellowship Grant NRC-HQ-84-14-G-0035.

Table of Contents

Introduction

The modern energy landscape demands the usage of cleaner energy sources in the near future, as the usage of fossil fuels have fallen out of favor economically and socially. Nuclear energy offers an attractive option as a potential replacement for fossil fuel energy sources. However, the current reactor designs are insufficient to compete with other renewable sources. Therefore, new designs are being created that are both safer and more efficient so the designs can compete on the market. These new designs call for more intense operating conditions than previously created and require new materials to withstand the new reactor environment.

One particular area of focus is material used for the cladding whose function is to hold the nuclear fuel and separate it from the coolant. Previously used materials may not withstand the new environment, some due to cladding-coolant interaction at high temperatures and others due the embrittlement caused by the increased irradiation damage. Various processes are responsible for this embrittlement however we are focused on two major issues: radiation induced segregation (RIS) and helium bubble nucleation. RIS is the result of the large number of point defects created by the radiation causing an enrichment or depletion of solute atoms at the grain boundary which changes the mechanical properties and can even lead to nucleation of separate phases. Helium bubble nucleation occurs when the transmutation product helium atoms form bubbles at the grain boundaries which weakens the material.

A material currently being studied are the nanostructured ferritic alloys (NFAs). Their most notable attribute are a large number density of fine nm-sized oxide particles embedded in the grain bulk. These nanofeatures or nano-oxides provide two attractive advantages to the material. First by strengthening the material through impeding dislocation motion. The second advantage particularly relevant to radiation resistance is that the oxide particles act as alternative sink sites

for the point defects and the helium. This reduces the point defect lifetime (thus reduced RIS) and reduces the amount of He reaching the grain boundary [1].

As access to appropriate testing facilities is limited due to the large cost associated with subjecting specialty materials to neutron irradiation, there is an intense focus on computer modelling to simulate a material system under irradiation. Nordlund has compiled a review of the various models used for the radiation effects in materials over the last few decades [2]. We have developed two computer models to capture radiation effects in the nanostructured ferritic alloys. A mean-field rate theory model (MF-RTM) was made to simulate the extent of radiation induced segregation (RIS) and a Kinetic Monte Carlo (KMC) model was created to simulate the nucleation of the oxides, irradiation, and the formation of helium bubbles onto the oxide particles. To assist in the analysis of the KMC simulations, a steady-state detection algorithm was developed to find the point where the system achieves a statistical steady-state.

For the goal for this research project is to produce a computer model that can replicate the behavior of the behavior of the NFAs in their response to irradiation damage regimes similar to those seen in modern reactors, current and planned. The KMC model performed these simulations at different temperatures, irradiation types, and compositions so one can observe the influence of each factor on the overall response of the material system. The influence of the grain boundary was also observed. The types of simulations are cut into three broad classes:

1. Precipitation Simulations
2. Irradiation Simulations
3. Helium Bubble Nucleation Simulations

The Precipitation Simulations has the KMC model simulate the nucleation of oxide nanofeatures from solid solutions of Fe-Y-O and Fe-Ti-Y-O. This is to further affirm the validity

of the selected parameters. The final configuration (i.e. the distribution of nanofeatures) from the KMC nucleation experiments will be saved and used as the starting configuration for Irradiation and He Bubble Nucleation simulations.

The Irradiation Simulations has the configuration of nanofeatures embedded in bcc Fe subjected to an irradiation regime. It will incorporate the neutron irradiation method of introducing point defects in the material system. Though the inclusion of the He transmutation product were not yet incorporated. This type of simulation will give insight into the role of the oxide nanofeatures in reducing grain boundary segregation, as well as give indicators to the irradiation resistance of the nanofeatures themselves.

The Helium Bubble Nucleation Simulations mirror the Irradiation Simulations except now include of the insertion of transmutation He. The same distributions of oxide nanofeatures were subjected to irradiation regimes and He atoms were implanted at an appropriate He/dpa rate. The results of interest in these simulations will be the eventual nucleation sites of the He bubbles, the He interaction with the vacancies, and the overall size and distribution of the He bubbles. These results will be compared to those from experiment as applicable.

In the end, should the results of these simulations compare well to those from experiments then researchers can glean information from the path the system takes to nucleation, segregation, and He bubble formation. This information will helpful to understand the mechanisms behind each process as well give insight to what factors would be most helpful to control to increase the irradiation resistance of the NFAs.

Outline

The present work is divided into seven chapters:

Chapter 1: Background Information and Motivation: The details of irradiation damage are described here as well as the development track of the NFAs and the use of computer models to simulate the material behavior

Chapter 2: Material System and Computer Models: The material system of NFAs is described here and shows how the key parameters used to simulate in NFA systems are found. Where the MF-RTM and KMC models are described, including the solute migration methods and other factors that should be accounted for. The validation procedures of the models are demonstrated. The chapter contains exerts from a paper written about the rate theory model made to simulate grain boundary segregation [3].

Chapter 3: Steady-State Detection: This chapter describes the efforts taken in steady-state detection (SSD) for use in the KMC. It includes work done on a SSD algorithm (the F-t-Pj-RG method) with demonstrations of the algorithms versatility [4]. Additionally, previous work on a procedure to find the number of many data points need to collect before one can even test for steady-state (called 'predicting the pre-requisite to steady state detection' or the ppSSD method) is included [5].

Chapter 4: Oxide Precipitation: The KMC was set to subject a model system similar to NFAs to the heat treatments that spur the nucleation of the characteristic Y-Ti-O oxides. The precipitation

behavior of the oxides was investigated to find agreement against expectations from experiments. The oxide characteristics such as size, density, and composition are recorded for analysis and inferences about the effect of heat treatment temperature were made. From the results there will also be a commentary about the thermal stability of the oxides and their resistance to coarsening.

Chapter 5: Neutron Irradiation: The investigation of the response of oxides under neutron irradiation. The mechanism that creates the cascade of defects in the system was developed and validated. Changes in oxide characteristics from size, density, and composition was tracked and compared to experimental results. The influence of irradiation temperature and dose rate (dpa/s) was also investigated.

Chapter 6: Helium Implantation: For this chapter, the oxides are subjected to an irradiation regime with the added insertion of transmutation He with the defects. The multitude of He bubbles formed in this regime were investigated and compared to expectations for the size to the location of the He bubbles in the system. The influence of temperature and dose rate were also investigated.

Chapter 7: Discussion and Conclusions. The preceding chapters are summarized and the next possible steps with the KMC model are discussed.

Chapter 1: Background Information and Motivation

The material requirements for cladding material in the nuclear reactor are numerous and stringent. The cladding must have a low thermal expansion coefficient to reduce stress on the cladding during the fuel cycle. It must have a high thermal conductivity so the heat from fission can quickly transfer to the coolant without overheating the metal. It must be strong to withstand the high pressure environment and must be prevented from cracking during operation. Additionally, the material must maintain all of these properties while being subjected to intense irradiation conditions. The material is expected to withstand irradiation damage up to 200 displacements per atoms (dpa) [6]. Meaning statistically, the average atom in the material will be displaced by irradiation on average 200 times during its lifetime [7].

1.1 Damage From Irradiation

Nuclear fission reaction inside the nuclear fuel eject high energy particles from the fuel into other components of the reactor, including the metal cladding. The irradiation-induced degradation of material properties starts with the collisions of these high energy particles with the metal matrix. The energy of these neutron are in the 1 MeV range and a large amount is deposited on a primary knock-on atom (PKA). This PKA unleashes a cascade of displacements through the metal matrix. In the end of the cascade, several point defects will remain in the matrix that go on

to cause further events. These point defects include vacancies and dumbbells [8, 9]. Higher level defects like voids and dislocation loops are also created with continuing irradiation damage. The excess vacancies cause the formation of voids that expand the volume of the material. This void swelling phenomenon introduces stresses that serve to weaken the material [10]. How a material manages these defects forms the basis of the radiation resistance of the material [11].

1.1.1 Radiation Induced Segregation

The root cause of radiation induced segregation is the increased number of point defects in the material due to irradiation. In normal conditions, there is a thermal equilibrium of point defects in the material that occur through thermal processes. The irradiation processes create concentrations of point defects many orders of magnitude above their thermal equilibrium values. This greatly accelerates diffusion of solute atoms in the matrix. Since the grain boundaries act as defect sinks where the defects around it get annihilated on contact. This creates a gradient in the defect concentration profiles which in turn drives more diffusion of point defects towards the grain boundary.

When there is a flux of vacancies, there is a flux of atoms in the opposite direction. When there is a flux of interstitial dumbbells there is a flux of atoms in the same direction. The segregation comes as a result of preferential exchanges with certain atomic species. For example, the vacancy exchanges less frequently with the Y atom than with the Fe atom so more Fe leaves the grain boundary area thus leading to an enrichment of Y at the grain boundary. An opposite effect occurs when a solute migrates favorably via the interstitial dumbbell movement. The enrichment or depletion of a particular element at the grain boundary is dependent on the competing effects of these migration methods in a way referred to as the Inverse Kirkendall (IK)

effect. [12]. Like with corrosion, the grain boundary type can also have an effect of the degree of segregation even if it is radiation induced [13].

1.1.2 Damage from Helium

The presence of He has also been shown to degrade the tensile ductility and creep resistance of nuclear materials at the high temperatures in the reactor [14]. He producing transmutation reactions in the reactor are expected to insert He atoms into the cladding at a rate of 10 atomic parts per million per unit dpa (10 appm/dpa) [15]. Small clusters of He atoms and vacancies form the He bubbles, or cavities, at dislocation, grain boundaries, or in the matrix itself. These He bubbles grow slowly when first formed at a rate tied to He insertion and migration. Once a certain critical size is reached, the bubble converts into a void and proceeds to expand rapidly though vacancy accumulation [16]. A key aspect of radiation resistance for a material is the ability to keep the size of He bubbles small for as long as possible.

While voids and He bubbles appear to be interchangeable as they both impact the material properties by stressing the material, their relationship with each other is complex. In some instances, evidence suggests small He bubbles in the material can have a suppressing effect on void formation [17].

1.2 Nanostructured Ferritic Alloys

The NFAs are attractive to researchers since their key features are highly stable in the face of the intense irradiation environments. The main focus of research has been on NFAs with oxides composed of Y, Ti and O. The two NFA alloys, 12YWT and 14YWT,that were simulated were selected since these alloys have been extensively studied, including the processing conditions

required to achieve oxides of a certain size and number density [18-20]. There have been studies that incorporated other elements in the oxide like La/Ce [21], Al [22], and Zr [23], though these alloys have a smaller body of research attached to them. The size of the nanofeatures are typically in the range of 2-10nm for the NFA steels and have number densities in the $10^{23}/m^3$ range [1]. The nanofeatures nucleate throughout the metal but also nucleate around imperfections like grain boundaries and dislocations [24].

There is a confusion in terminology between NFAs and oxide dispersion strengthened (ODS) steels which have similar compositions and have the same tell-tale oxide particles as a defining feature. Typically, the ODS steels have larger oxides that are incoherent with the metal matrix [18] and NFAs have smaller grains coming in at less than 500 nm [25]. However, the exact distinction is not clearly defined and ODS is sometimes used as an umbrella term for a class of materials that includes NFAs.

1.2.1 Microstructure Characterizations

For radiation resistant steels, an advantageous structure of the steel is ferritic martensitic due to the general wisdom that austenitic steels are many times more vulnerable to swelling during irradiation [26, 27]. The common major constituent species other than Fe is Cr, for corrosion resistance, which in the various commercial NFA/ODS steels has atomic concentration between 9-14 wt%. Nickel is discouraged for use in a reactor due its susceptibility to produce transmutation He[28].

Furthermore, NFAs are designed to have a small grain size which is another factor helpful in reducing irradiation related swelling though the high grain boundary density since voids grow at a much reduced rate near grain boundaries [29]. This small grain size inherent in NFAs also

contributes to resistance to swelling from He bubbles as a small grain size has been shown to decrease He bubble density [30].

The crystal structure of the Y-Ti-O nanofeatures becomes hard to define due to their small size. However, the prevailing theory is that the Y_2O_3 have a bixbyite structure and the $Y_2Ti_2O_7$ has a pryoclore structure in the iron matrix though some studies have seen the Y_2TiO_5 in the mix. At small sizes, the oxide nanofeatures are more congruent with the bcc matrix, without the crystal structure of a second phase, and the composition does not follow the stoichiometry of the chemical formula [31]. In fact, with the small sizes of nano-oxides in NFAs like 14YWT, the structures are expected to be coherent with the bcc Fe matrix.

Miller investigates the various oxides in the metal and identified three types in descending order of size. 1) large (20-50 nm) Ti precipitates rich with non-metal N, O, and C. 2) Smaller (5-10nm) oxides with the structure $Y_2Ti_2O_7$ and Y_2TiO_5, though the compositions do not precisely follow this stoichiometry. 3) 1-4nm fine nanoclusters of Y, Ti, and O atoms that tend to be coherent with the bcc lattice. The first and second group of precipitates are found primarily at the grain boundaries while the third group is predominately located in the grain interior. The third group has a disordered structure coherent with the bcc matrix [32].

1.2.2 Processing

The NFAs are dispersion strengthened which is a different process from the more common precipitation strengthening. Both processes involve the precipitation of a secondary phase that are fairly small and numerous, so that dislocation movement can be impeded. Dispersion strengthening is for cases where the metal component has an operating temperatures close to its melting point where the main phase of the material stands to lose much of their strength due to

temperature. The secondary phase would have a melting temperature much higher than the base matrix so the material benefits afforded by the secondary phase remain present even if the main phase is weakened. However, this insolubility in the matrix phase and require a more rigorous processing path.

The NFAs undergo specific processing techniques in order to get the most desired size and distribution of oxide nanofeatures, microstructure, and grain size. Processing starts by collecting metal powders into a solid solution. The oxygen is introduced into the system as a Y_2O_3 powder. Since the Y-O bonds are so strong, the solid solution is mechanically alloyed through ball milling to break those Y-O bonds and a single solid solution. This process also adds a larger density of dislocations in the metal matrix which have their own advantages to radiation resistance [33]. The complete solid solution is then put through a heat treatment to produce a ferritic martensitic steel and nucleate the small oxide nanofeatures. Mostly commonly, this process is achieved with hot isostatic pressing (HIP). The advantage of this process is a higher number density of nanofeatures to more conventionally annealed NFAs [34]. Another processing technique being explored is to subject the metal powder to spark plasma sintering as a way to avoid contamination that could occur during the mechanical alloying [35].

The Cr in the solid solution should not have a great effect on the oxide structure or composition [36]. Studies show that the addition of Ti into the solution results in much finer oxides than the Y_2O_3 oxides. And the Ti containing oxides will be more favorable to form compared to Y_2O_3. Thus when Ti is present in the solid solution, it will inhibit the formation of Y_2O_3 nanofeatures and lead to most of the nanofeatures containing Ti [37].

1.2.3 Creep

Research finds that the higher the number density of these oxides, the stronger the material becomes [38]. The specific mechanism is related to the pinning effect the oxide nanofeatures have on dislocation movement [39]. For this same reason, the nanofeatures are credited for the high creep resistance in NFAs. The cladding material must be resistant to thermal creep due to the long operating times at high temperatures closer to the material melting temperature than with ordinary uses. Experiments where the NFA MA957 undergo high temperature creep testing show remarkable creep resistance [40].

1.2.4 Corrosion

Corrosion along the surfaces and grain boundary works to weaken the material and make it more susceptible to cracking in a process called intergranular stress corrosion cracking. Corrosion will also inhibit the heat transfer from fuel to coolant which affects the reactor conditions. Radiation can accelerate the corrosion due to chemical changes at the grain boundary. One could choose to combat corrosion encouraged by Cr depletion due to RIS through grain boundary engineering, where special boundary types can enhance corrosion protection [41].

1.2.5 Thermal Stability

The NFAs characteristic oxide nanofeatures have strong thermal stability, showing little coarsening when subjected to the high temperatures common in reactors [42]. The addition of Ti works to produce finer oxides in the NFA, resulting in an increased number density compared to NFAs with only Y-O oxides [43]. Additionally, the Y-Ti-O oxides are more thermally stable than the Y-O oxides, which largely alleviates concern about detrimental oxide coarsening. Very little coarsening is seen when the ratio of Ti:Y >1, even at temperatures greater than 1573K [44]. A

thermokinectic model by Barnard estimated that without irradiation damage the Y-Ti-O nano-oxides would survive in nonirradiated environments for over 80 years at temperatures as high as 1173K [45], which is well past the lifetime of the fuel rod cladding. This prediction of strong thermal stability has been backed up by long-term thermal aging experiments of NFAs containing Y-Ti-O oxides [20, 40, 42, 46]. Analysis of the kinetic evolution of precipitation [20] finds the coarsening of the nano-oxides does not follow the $\bar{R} \propto t^{1/3}$ power law typical according to Lifshitz-Slyozov-Wagner (LSW) theory when coarsening is diffusion-controlled [47], suggesting something is inhibiting atomic migration. Much of the deviation from the 1/3rd power law is attributed to the excess dislocations in NFAs influencing long range vacancy migration, though other causes should be investigated.

1.2.6 Irradiation Stability

The oxides also show a resistance to dissolution under irradiation conditions. In an example study, Liu tests the NFA MA957 and found that the larger nanoclusters undergoes a shrinkage until they reach an equilibrium radius, hinting that competing forces could be the cause of oxide survivability [48]. Another reason for this resistance to dissolution is thought to be the large grain boundary area as well as the oxides themselves acting as defect sinks. Liu compares the response of ODS and non-ODS steels and finds that the ODS steel is effective in reducing the defect population and thus is more resistant to radiation induced changes [49].

Simulations have shown that increasing the sink density decreases the degree of radiation induced segregation in a system [50]. Additional studies have found through experimental observations that the defect population in a material decreases with grain size (increasing the grain boundary area) [51].

To test for the irradiation resistance of the NFA, the alloy is subjected to an accelerated irradiation treatment with neutron irradiation or ion irradiation. There is some question to the applicability of using ions to replicate neutron damage, attempts have been made to emulate neutron damage using ions through careful accounting of the differences in the method [52]. Wharry did a fine review irradiation stability experiments done of the ODS (which includes NFAs) steels [53]. Given the multitude of different alloys tested on different irradiation conditions, it was difficult to see general trends beyond the nano-oxides becoming more spherical. The nano-oxide dispersion characteristics went everywhere with size increasing, decreasing and remaining the same. That is not say that the NFA steels that saw their nano-oxides dissolve were not resistant to dissolution.

1.2.7 Helium Bubbles in NFAs

A main factor for why NFAs are coveted are its resistance to swelling in the irradiation regime. This swelling is caused by the transmutation products from the nuclear reactions nucleating new phases or bubbles into the material which puts strain on the material and works to embrittle the material. Research suggests there is a critical size of He bubbles at grain boundaries which would lead to a sharp drop in desired mechanical properties [54]. While other transmutation gases like Ne and Ar are generated through nuclear reactions, the smaller He atoms are located on the interstitial sites which allows them to migrate much faster and nucleate at inconvenient locations [55]. The helium bubbles are seen as cavity in which He atoms reside. In the system, it is pictured as a cluster of vacancies filled with He atoms. Much of the reason for the formation of He bubbles are due to their interactions with the vacancies [56]. With the strong binding energy, between 4 and 6 He atoms can reside in one vacancy [57]

While homogenous nucleation of these He bubbles within the Fe matrix itself is possible, the He bubbles are far more likely to form heterogeneously at material imperfections like grain boundaries [58], dislocations [59], and the oxide nanofeatures. A thermodynamic study from Yang of the interface between the $Y_2Ti_2O_7$ oxides and the Fe matrix reveal that both the vacancies and He atoms will gather at the interface, thus affirming the oxides as preferential nucleation sites for He bubbles [60]. It may actually be relevant to account for He accumulation *inside* the oxide nanofeatures. Studies have shown that He can sit in the surface layers of oxides in Y_2O_3 [61] and $Y_2Ti_2O_7$ [62].

Helium implantation studies were conducted on the NFA MA957 and non-NFA F82H. For the same He implantation regime, the NFA MA957 saw a higher number density of He bubbles that were finer than those observed in the F82H [63]. Two companion papers by Kurtz [64] and Yamamoto [15] observe the He bubble characteristics in non-ODS steel and the NFA MA957 respectively which confirm the NFAs reduce the size of the bubbles and trap the bubbles at oxide sites. Affirming that the nanofeatures would reduce the size of He bubbles by providing more nucleation sites. Another He implantation study of an NFA by Edmondson reveals that roughly 50% of the He bubbles will nucleate at the nanofeatures and only 15% will nucleate at the grain boundaries [65]. When the existing He bubble containing steels are subjected to a heat treatment, the bubbles in the metal coarsen through the migration of vacancies [66].

1.3 Modeling

There are limited facilities that can produce the high energy neutrons to irradiate material samples for testing, so proton, electron, and ion irradiation is often used as a substitute for neutron irradiation. Ribis found that ion irradiation has a deep impact on the nano-oxide growth during

irradiation with radiation induced oxide growth occurring 17-40 times faster than the growth in samples that were neutron irradiated [67]. For physical evaluations of the helium bubble distributions, helium implantation techniques have been developed to mimic the irradiation regimes in reactors by having spallation neutrons induce a (n,α) reactions in a blanket material surrounding the sample, thus releasing He atoms into the sample material with great care made to get the correct He-to-dpa ratios [64]. Sometimes the neutrons are substituted with accelerated ions, though the applicability to neutron irradiation is debatable [68]. Swenson also saw differences in the stability of the nano-oxides when irradiated with protons and neutrons [69]. These experiments gained limited insight into the evolution of nano-oxide characteristics over total accumulated dose as most of the irradiation experiments only analyzed the oxides after two or three dosages.

One possible option to solve these problems is through the use of computer models to simulate the irradiation response [2]. The response of materials to irradiation can be simulated using computer models such as mean field rate-theory [3], molecular dynamics [70], cluster dynamics [71], and phase field [72] models. For the purposes of this project, two computer models were created to investigate the radiation induced segregation, nucleation of nanofeatures, and formation of He bubbles. They are the mean field rate theory model (MF-RTM) and the Kinetic Monte Carlo model (KMC).

1.3.1 Rate Theory Models

There is a rich work of literature on MF-RTM to predict the degree of segregation in various different types of alloys, most of which focus on the segregation of major elements like Cr in stainless steel cladding. The first models by Johnson and Lam [73] were used to predict segregation in austenitic (fcc) stainless steel and were continuously modified to fit with data from

reactor experiments [74]. Later, a study was conducted for the segregation in a ferritic martensitic (bcc) steel complete with its own reactor analysis [75] and a thorough investigation of factors such as solute drag and dislocations [76].

1.3.2 KMC Model

Atomistic Kinetic Monte Carlo (KMC) models have a history of being used to study phase transformations and thermal aging in metals. Additionally, kinetic Monte Carlo models have been used to study precipitation kinetics in the Fe-Cu system [77]. The advantages of KMC to rate theory and phase field models is the fact the KMC can better take into account the local environment by tying the migration energies to configuration around the point defect [78].

The KMC model is extended to look at precipitation of solute precipitates Fe-Nb-C[79], Fe-Y-O[80], Fe-Ti-O [81] systems. The heterogeneous nucleation at dislocations and grain boundaries has been identified as area of growth for more detailed observations from the model. There have been studies of using KMC in the Fe-Nb-C system to see NbC nucleation along dislocations [82] and grain boundaries [83] by adding a segregation energy term.

Soisson has developed a KMC model that could model RIS by introducing point defects via a Frenkel Pair mechanism at a common rate and compared the results against a mean-field rate theory model for simple ideal alloys [84]. There are many applications of this KMC model to simulate RIS in various material systems like Fe-Cu [85]. Becquart lays out a pathway to use the KMC to simulate more complex alloys under advanced irradiation by applying his KMC model to the multicomponent Fe-CuNiMnSi alloy [86], including a more detailed description of the dumbbell interactions. Becquart [86] and Vincent[87] incorporated neutron irradiation in their KMC models by inserting cascade debris from molecular dynamics (MD) simulations of

displacement cascades into the KMC simulation box [86, 87]. There have been some studies of the KMC with interstitial elements including helium in the pure bcc Fe [88-90], though there have not been KMC studies involving both He and NFAs.

One of the drawbacks of the MF-RTM and KMC is that so many events can happen and the modeler has to know the parameters needed beforehand. Many of the parameters needed in both models can be found through density functional theory (DFT) calculations, though a paper by Barnard cautioned for the need to tie some parameters to experimental values, owing to the sensitivity of the model [91].

Chapter 2: Material System and Computer Models

2.1 Material System

2.1.1 Atomic Locations

The Fe-Ti-Y-O material system is represented as a three-dimensional collection of points in the body-centered cubic (bcc) system with an octahedral sublattice for interstitial atoms. Figure 2.1 shows the basic bcc unit cell as reference. For computational efficiency, the models assume a rigid lattice system, meaning the distance between two points remains fixed regardless of the occupying atoms in those points. In reality, the atomic distances vary with the strain of nonuniform distributions of solute atoms. This rigid lattice approximation prevents the formation of phases of completely separate lattices like a hexagonal-closed pack (hcp) phase in bcc, however the models are still useful. The oxide particles are expected to be small enough that the nanofeature remains roughly coherent with the bcc crystal structure [19, 92]. Table 2.1 lists the matrix and solute elements studied and where they are expected to reside in a defect-free bcc Fe matrix from literature.

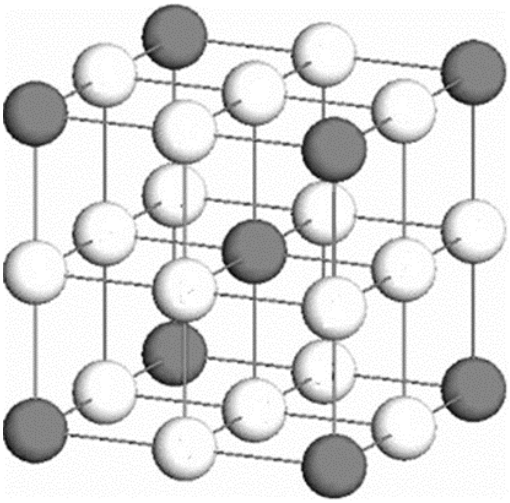

***Figure 2.1**: The lattice of the Fe-Ti-Y-O alloy. The dark circles represent bcc lattice sites and the white circles represent interstitial lattice sites. Image from Hin [80].*

***Table 2.1**: Preferred lattice positions of solutes and point defects in the bcc Fe lattice*

Atomic Species	**Preferred Lattice Site**
Y	Substitutional [93]
Ti	Substitutional [93]
O	Octahedral [93]
He	Octahedral [94]
Vacancy	Substitutional
Dumbbell	Substitutional

2.1.2 Defect Production

Numerous events can be represented in the presented models: Point defect generation, vacancy migration, interstitial migrations, and interstitialcy migration. There are two modes of point defect generation: Frenkel Pair generation and Cascade of Displacements. The MF-RTM only uses Frenkel Pair production while KMC uses Frenkel Pair and Cascade of Displacements.

For the Frenkel Pair mode, as its name suggests, a single Frenkel Pair of one vacancy and one dumbbell atom are placed into the system at least 10 atomic distances apart. This mode is modeled to emulate electron irradiation [84]. The second mode replicates the impact of a high

energy neutron on the lattice and will produce a large amount of point defects at one time in a localized area. The number of displacements $\overline{N_d}$ from the resulting cascade is estimated by the following equation:

$$\overline{N_d}=\frac{\Lambda E_n}{4*E_d} \quad (1)$$

$$\Lambda = \frac{4A}{(1+A)^2} \quad (2)$$

E_n is the initial energy of the neutron, A is the atomic mass number and E_d is the threshold displacement energy. For Fe, the E_d is set to 40 eV based on literature values [95]. Eq 1 is a general relation from Kinchin and Pease [96] that has been found to overestimate the number of displacements from neutron irradiation. Another way to calculate the number of displacements is from the primary knock-on atom through an estimation called Norgett-Robinson-Torrens [97]. These point defects recombine rather quickly, but some defects survive to cause changes in the material system.

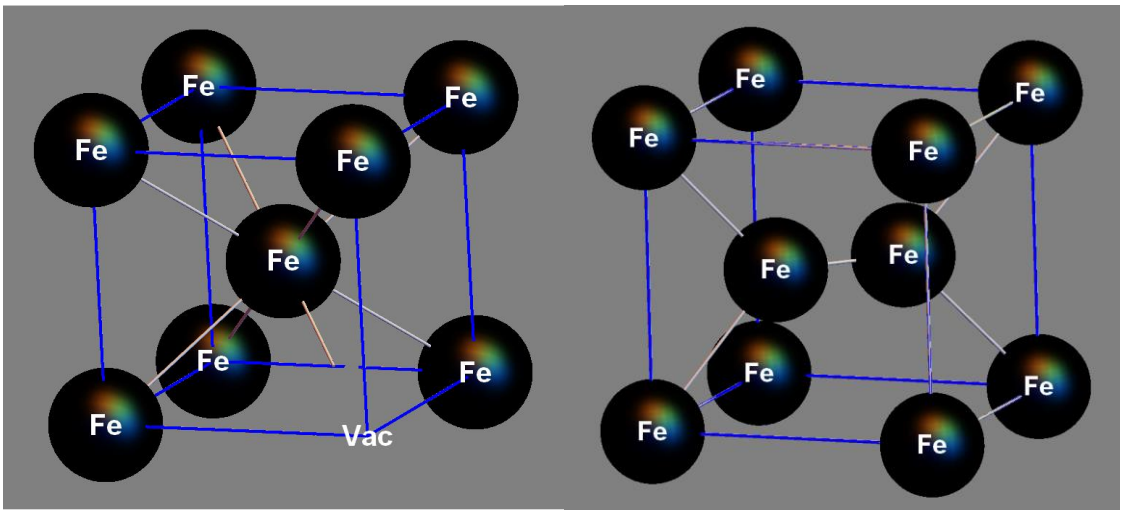

***Figure 2.2**: Depiction of the vacancy (a) and a <110> dumbbell (b) in a bcc iron lattice*

The atoms migrate through the system through the vacancy, interstitial and interstitialcy mechanisms. In the vacancy method, the vacancy pictured in Figure 2.2a exchanges positions with an atom in the adjacent substitutional lattice site. The vacancies can be introduced through thermal processes or irradiation. The vacancies can also leave the system through annihilation at defect sinks like grain boundaries or the nano-oxides. Or the vacancies can recombine with the dumbbells should they come within sufficient distance to each other.

The dumbbells, also called self-interstitial atoms (SIAs), pictured in Figure 2.2b are created from irradiation are expected to be in the form of dumbbells in the <110> configuration located on the substitutional sites. Research from Jiang [93] indicates this will be the most likely configuration for most interstitial dumbbells. For the purposes of the model, a dumbbell is considered to be two atoms occupying the same lattice site. These dumbbells will migrate through the translation or interstitialcy mechanism where one atom in the dumbbell will migrate to an adjacent lattice site and form a new dumbbell [87]. Which atom stays in place and which atom leaves is decided randomly regardless of the atoms that form the dumbbell. This is a simplified description as the actual dumbbell is a complex of the two substitutional atoms that has many different orientations and migration paths, including 2^{nd} nearest neighbor jumps. The dumbbells Fe-Ti and Fe-Y are also included in the model. The Ti-Ti, Y-Y, and Ti-Y dumbbells are not included since the amount of titanium and yttrium is expected to be small, making formation and long-distance migration unlikely. Though the literature commonly refers to dumbbells as SIAs, that term will be avoided in this manuscript as it can cause confusion when discussing interstitial species that primarily exist on interstitial lattices because of favorable thermodynamics.

The interstitial atoms that sit on the octahedral sites in the bcc Fe lattice migrate through the interstitial mechanism, where the interstitial atoms hop from octahedral site to octahedral site,

provided that they are not impeded. They will not jump onto a substitutional site even if that site is vacant. This element is also known as foreign interstitial atoms (FIA) to differentiate from the self-interstitial atoms (SIAs).

2.1.3 Diffusion

Ultimately, the severity and speed of the atom jumps in the models are determined by the number of point defects in the system and the diffusivities of the solutes by each mechanism. The following equations display how the diffusion coefficients and diffusivities are calculated:

$$D_{Fe} = d_{FeV}C_V + d_{FeI}C_I \quad (3)$$

$$D_V = d_{FeV}C_{Fe} + d_{YV}C_Y + d_{TiV}C_{Ti} \quad (4)$$

$$D_I = d_{FeI}C_{Fe} + d_{YI}C_Y + d_{TiI}C_{Ti} \quad (5)$$

$$d_{FeV} = a^2 \times v_{FeV} \times \exp(\frac{-E_{mig}}{k_b T}) \quad (6)$$

Concentrations C_V and C_I represent the vacancies and interstitial dumbbells that are created from irradiation. Using Fe as an example, Eq. 3 shows the calculation of the diffusion coefficient D_{Fe} from the individual contributions of the vacancy and interstitialcy mechanisms. Diffusion coefficients for vacancies and dumbbells are calculated in Eq 4 and 5 and are dependent on the alloy composition. The terms a and v_{Fe} are the lattice parameter and the attempt frequency. The Boltzmann constant and temperature are represented by k_b and T respectively. E_{mig} represents the migration energy of the element by a particular mechanism. A similar expression can be used for the diffusion of Ti and Y. Eq. 6 is the method used to calculate the diffusivity of each element by a particular mechanism. They are typically calculated as an exponential function representing the probability that a jump attempt succeeds multiplied by the frequency that jump is attempted.

2.1.4 Importance of the Point Defects

From the above equations, it should be noted that the concentration of point defects significantly impacts the diffusion coefficient. The more defects in a material, the higher the probability that an atom will encounter one and thus be able to migrate. Point defects are present in every metal as they can be created be thermal processes to minimize the free energy. There is a thermal equilibrium concentration of each point defect relies on the formation energy of that defect [98]. Estimates of the thermal equilibrium values are described in the following equations:

$$c_v^{eq} = \exp(\frac{-E_{Vac}^{For}(Fe)}{k_b T}) \quad (7)$$

$$c_{dumb}^{eq} = \exp(\frac{-E_{dumb}^{For}(Fe)}{k_b T}) \quad (8)$$

Ordinarily, the formation energies of the point defects are so large that there a very small number of point defects in the system. For instance, diffusion models do not typically account for diffusion by dumbbells because their contribution is negligible since their high formation energy $E_{dumb}^{For}(Fe)$ means very low thermal equilibrium concentration. Dumbbells are included in this work because irradiation creates dumbbells in similar numbers to vacancies in both Frenkel Pair production and displacement cascades.

At thermal equilibrium, the vacancies are the only point defects with a sufficient concentration to drive diffusion. So Eq 3 for the diffusion coefficient would become:

$$D_{Fe} = d_{FeV} C_V^{eq} \quad (9)$$

The expression can be expanded using Eq 6 and Eq 7 to show the factors for the diffusion coefficient for normal conditions.

$$D_x = v \times a^2 \times \exp\left(\frac{-E_{Mig}}{k_b T}\right) \times \exp\left(\frac{-E_V^{For}(Fe)}{k_b T}\right) \quad (10)$$

Which usually get reduced to a pre-exponential and an activation energy which is the summation of the migration and vacancy formation energy.

$$D_{Fe} = D_x^o \times \exp\left(\frac{-E_{act}}{k_b T}\right) \quad (11)$$

$$E_{act} = E_{Mig} + E_V^{For}(Fe) \quad (12)$$

Eq 11 the format typically used to describe the diffusion coefficient of solutes in a metal because most applications assume the point defects will remain at their thermal equilibrium values. Our models cannot assume that so the defect concentrations have to be tracked. It also means the system has to populated with the thermal equilibrium concentrations of point defects before starting the simulation to ensure the expected diffusion properties are present at the start.

2.2 Parameterization

2.2.1 Kinetic Parameters

For both the MF-RTM and KMC models, information about the diffusion properties and atomic interactions are required for the model to present results accurate to the chosen material system. This section describes how those parameters are found; from literature or our own calculations.

***Table 2.2**: Diffusion parameters for Fe-Ti-Y-O-He system*

Input Parameter	Value	Unit	Reference
lattice parameter	2.87 x 10^{-10}	m	
Vacancy Migration Energy, Fe	0.66	eV	[80]
Vacancy Migration Energy,Y	0.23	eV	[99]
Vacancy Migration Energy,Ti	0.81	eV	[81]
Interstitial Migration Energy, Fe	0.35	eV	[84]
Interstitial Migration Energy, Y	0.21	eV	calculated

Interstitial Migration Energy, Ti	0.24	eV	calculated
Vacancy Formation Energy	2.24	eV	[80]
Oxygen Migration Energy	0.48	eV	[100]
Helium Migration Energy	0.1	eV	[101]
Vacancy pre-exponential factor, Fe	$6.0x10^{-4}$	m^2/s	[80]
Vacancy pre-exponential factor, Y	$3.7x10^{-7}$	m^2/s	[99]
Vacancy pre-exponential factor, Ti	$2.1x10^{-1}$	m^2/s	[81]
Interstitial pre-exponential factor, Fe	$1.0x10^{-5}$	m^2/s	
Interstitial pre-exponential factor, Y	$1.0x10^{-5}$	m^2/s	
Interstitial pre-exponential factor, Ti	$1.0x10^{-5}$	m^2/s	
Interstitial attempt frequency	$1.0x10^{14}$	/s	

The system is set so that diffusion values of each solute in pure bcc metal reproduces with values from literature or experiments. Table 2.2 lists the diffusional values critical to the system. The diffusion of titanium in bcc Fe by vacancy method was found using a method called serial sectioning. A solution containing the radioactive ^{44}Ti isotope was spread on the surface of Fe samples that are heated over certain temperatures and time intervals. The sample is then cut into sections whose activities are measured to estimate the penetration of the ^{44}Ti. The data is then fit to an Arrhenius equation [102]. The yttrium vacancy diffusion values were found through a density functional theory (DFT) study [99]. The Fe vacancy diffusion values were found in a similar way to the titanium diffusion data. An internal oxidation method was used to determine the diffusion constants for oxygen in bcc iron [103]. These experiments give the pre-exponential factor and a migration energy.

The dumbbell migration energies are only approximations due to the many different mechanisms of dumbbell migration. The Fe-Fe dumbbells are predominantly in the <110> direction, so the model treats all dumbbells has having a <110> orientation. The interstitial migration energy for an Fe-Fe dumbbell has been settled through literature by using density functional theory calculations for a number of different jumps and finding an average. In this study

the Fe-Y dumbbell is assumed to jump to a second nearest neighbor and rotate 90 degrees to the <-110> orientation that is equivalent to the <110> orientation in a cubic system. Thus the migration energy can be calculated by subtracting the energy of yttrium in a tetrahedral position and the energy of when the yttrium is in <110> mixed dumbbell [104], using values from Jiang [93]. This method was likewise used for the titanium interstitial dumbbell migration. The pre-exponential factors for interstitial jumps were found by multiplying the square of the lattice parameter by a common attempt frequency [84].

2.2.2 Thermodynamic Parameters for Fe-Y-Ti-O

The energy of the system is calculated through Eq. 13:

$$E = \sum_{m.i,j} N_{ij}^{n} \varepsilon_{ij}^{n} \quad (13)$$

System energy *E* is the summation of the pair-interaction energies ε_{ij}^{n} between all atoms in the box at all recorded neighbor distances *n* in the system. Higher order interactions are not included in this model. As the system kinetically evolves, the energy of the system trends in a downward direction due to reduction of its energy through formation of the 2nd phase oxide particle. So, an accurate depiction of the thermodynamics of the system is required for the KMC model to accurately replicate the behavior of the Fe-Y-O and the Fe-Y-Ti-O systems.

Table 2.3: *Pair-interaction energies (eV) for the Fe-Y-Ti-O system taken to the 4th nearest neighbor in the simple cubic frame of reference*

Pair-Interaction Energies	**1 (eV)**	**2 (eV)**	**3 (eV)**	**4 (eV)**
Fe-Fe	-	-	-0.611	-0.611
Fe-Y	-	-	-0.59	-0.52

Y-Y	-	-	-0.57	-0.69
Fe-Ti	-	-	-0.65	-0.53
Ti-Y	-	-	-0.71	-0.68
Ti-Ti	-	-	-0.69	-0.70
Fe-V	-	-	-0.21	0.00
Y-V	-	-	-0.35	0.00
Ti-V	-	-	-0.35	0.00
Fe-I	-	-	-0.10	0.00
Y-I	-	-	0.25	0.00
Ti-I	-	-	-0.10	0.00
Fe-O	0.00	0.00	-	-
Y-O	-0.01	-0.11	-	-
Ti-O	-0.04	-0.04	-	-
O-O	0.10	-0.116	0.10	-0.116

Table 2.3 represents the pair-interaction energies ε_{ij}^{n} that each atom has with another atom located at a certain distance site. The *n* index ranges 1-4 based on the distance between the two interacting atoms according to the simple cubic model. The 1st and 2nd nearest neighbor interactions take place either on the octahedral lattice or between the octahedral and substitutional. Conventionally, the interactions labeled 3 and 4 can also be called the 1st and 2nd nearest neighbors between substitutional solutes in the body-centered cubic model.

The parameters listed above in Table 2.3 are calculated from the thermodynamics of the Fe-Y-Ti-O system. Many of these values can be found through DFT calculations. However, there have been cautions about using too many DFT-calculated values in the parameterization of computer models [91]. Therefore, rather than calculating the parameters using DFT, the KMC parameters were selected to replicate the experimental behavior of Y, Ti, O, Y_2O_3, and $Y_2Ti_2O_7$ in bcc Fe. Thermodynamic quantities utilized in the derivation of the pair-interactions include

cohesive energies, vacancy formation energies, solubility limits, and solubility products of Y_2O_3 and $Y_2Ti_2O_7$. Knowledge of the relationship of these properties with the pair-interaction energies allows for a system of equations to be developed to solve the necessary values. The relationship of the pair-interaction energies with each material property is shown below:

$$E_{coh}^{X} = -\frac{z_3}{2}\varepsilon_{XX}^{3} - \frac{z_4}{2}\varepsilon_{XX}^{4} \quad (14)$$

E_{coh}^{X} represents the cohesive energy of an atomic species, and z_3 and z_4 represent the number of 3rd and 4th nearest neighbor bonds in the simple cubic system. The ε_{FeFe}^{n}, ε_{YY}^{n}, and ε_{TiTi}^{n} interactions are fit the cohesive energy of their respective element.

The material parameters ε_{ij}^{n} are selected to satisfy multiple conditions to capture the behavior of each element. The approximate relationship between pair-interaction energies and the solubility limits/products at a given temperature T are shown below:

$$c_O^{sol} = \exp\left(\frac{4\varepsilon_{OO}^{2}+3\varepsilon_{OO}^{4}}{k_bT}\right) \quad (15)$$

$$c_Y^{sol} = \exp\left(\frac{3(\varepsilon_{FeFe}^{4}+\varepsilon_{YY}^{4}-2\times\varepsilon_{FeY}^{4})}{k_bT}\right) \quad (16)$$

A similar formulation to Eq. 16 to find c_{Ti}^{eq}. Pair-interactions $\varepsilon_{FeY}^{n}$and ε_{FeTi}^{n} interactions are selected to replicate the solubility limits of Y and Ti in bcc Fe in the KMC. The parameters ε_{oo}^{2} and ε_{oo}^{4} are set equal to each other and found using Eq. 15. The ε_{oo}^{1} and ε_{oo}^{3} are set to positive 0.1 eV to ensure the proper arrangement of O atoms in the second nearest neighbor positions on the octahedral sub lattice.

The relation of the solubility product of the Y-O oxides K_s^{Y-O} to the pair-interaction energies are based on derivations assuming a Y_2O_3 structure within the iron matrix.

$$K_s^{Y-O} = [c_Y^{Fe}]^{(2)}[c_O^{Fe}]^{(3)} = \exp\left(\frac{2\Omega_3^{FeY}+2\Omega_4^{FeY}+6(\varepsilon_{YO}^{1}-\varepsilon_{FeO}^{1})+12(\varepsilon_{YO}^{2}-\varepsilon_{FeO}^{2})+12\varepsilon_{Oo}^{2}+9\varepsilon_{Oo}^{4}}{kT}\right) \quad (17)$$

The order energies $\Omega_3^{FeY} = 4(\varepsilon_{FeFe}^3 + \varepsilon_{YY}^3 - 2\varepsilon_{FeY}^3)$ and $\Omega_4^{FeY} = 3(\varepsilon_{FeFe}^4 + \varepsilon_{YY}^4 - 2\varepsilon_{FeY}^4)$ represent the deviation of ideal interactions. c_Y^{Fe} and c_O^{Fe} represent the concentration of each solute in the bcc Fe matrix of an Fe-Y-O mixture at thermal equilibrium; note, these are not the same as solubility limits c_o^{sol} and c_o^{sol} due to the Y-O interaction. With the Fe-Y and Fe-Ti relationships known, the ε_{YO}^n and ε_{TiO}^n interactions are found through the solubility products of Y_2O_3 and Ti_2O_3.

For the Y-Ti-O oxides, the $Y_2Ti_2O_7$ structure cannot be represented on the bcc structure, so a formulation assuming a $YTiO_3$ structure is constructed to relate the pair-interaction energies to the solubility product K_s^{Y-Ti-O}.

$$K_s^{Y-Ti-O} = [c_Y^{Fe}][c_{Ti}^{Fe}][c_O^{Fe}]^{(3)} = \exp\left(\frac{2\Omega_3{}^{TiY} + \Omega_4^{FeY} + \Omega_4^{TiY} + 6(\varepsilon_{TiO}^1 - \varepsilon_{FeO}^1) + 12(\varepsilon_{YO}^2 - \varepsilon_{FeO}^2) + 12\varepsilon_{OO}^2 + 9\varepsilon_{OO}^4}{kT}\right) \quad (18)$$

The solubility product for $Y_2Ti_2O_7$ provides the information needed to extract ε_{TiY}^3. The solubility limits are found in the literature from the experimental measurements used for phase diagram construction for the Y [105], Ti [106] and O [107] solutes. The solubility product for the Y-O and Y-Ti-O are found using data in Barnard's precipitation model [78]. Relating these quantities to pair-interaction energies are detailed in works by Hin [80].

Certain structural assumptions are used to simplify the parameterization. The parameter ε_{FeY}^3 is set so that the order energy Ω_3^{FeY} >0, allowing the FeY phase to nucleate in Fe-Y. Likewise the ε_{TiY}^4 parameter is set for Y-Ti to have a repulsive interaction in the 4th nearest neighbor distance. Oxygen atoms have shown a preference for bonding with Ti in the first nearest neighbor position, and with Y in the second nearest neighbor position, so that $\varepsilon_{TiO}^1 < \varepsilon_{YO}^1$ and $\varepsilon_{TiO}^2 > \varepsilon_{YO}^2$, allowing them to align with observations.

$$E_V^{For}(X) = -\frac{z_3}{2}\varepsilon_{XX}^3 + z_3\varepsilon_{XV}^3 \quad (19)$$

$E_V^{For}(X)$ is the vacancy formation energy in an X matrix. Only the first nearest bcc neighbor (3rd nearest neighbor in the simple cubic setup) of vacancy with atomic species is used in this parameterization. The pair-interaction for the yttrium and titanium with a dumbbell was taken from the energies of formation of the <110> dumbbell when the solute atom is in one of its first-nearest neighbor positions [93]. The He pair-interactions are discussed in Chapter 6.

The complete derivation for the relations of K_s^{Y-O} to the pair-interactions is shown in below:

2.2.3 Derivation of the Solubility Product Equation

When an Fe-Y_2O_3 system is at equilibrium, the chemical potentials of the solutes in each phase are equal:

$$\mu_Y^{Prec} = \mu_Y^{Fe}$$

$$\mu_O^{Prec} = \mu_O^{Fe}$$

While μ_y generally is regarded as a derivative of the Gibbs free energy $\frac{\partial G}{\partial n_i} = \mu_i$ when the system has a constant temperature and pressure, when the system has a constant temperature and volume, the chemical potential can also be represented as a derivative of the Helmholtz free energy $\frac{\partial F}{\partial c_i} = \mu_i$. With the rigid lattice approximation disallowing volume changes, the Helmholtz free energy can be reduced to:

$$F = U - TS \tag{20}$$

Where S is the entropy term and the internal energy U can be approximated through this definition of the material system:

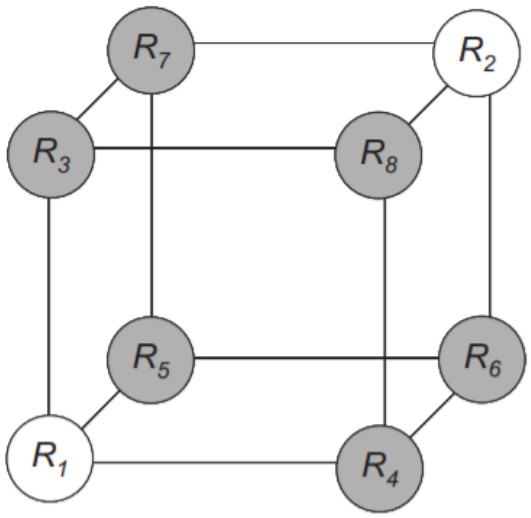

***Figure 2.3**: Simple cubic unit cell. White lattice sites are substitutional sites and grey sites are octahedral sites. Image from Hin [80].*

The unit cell of the BCC system can be reduced further down to simple cubic structure shown in Figure 2.3. Eight of these simple cubic cells make up one BCC unit cell. Where concentration values c_i refer to the atomic concentrations at site R_i in Figure 2.3. For the substitutional sites, the $c_{1,2} = 0$ means both sites are completely Fe and when $c_{1,2} = 1$ means the sites are completely Y. For $c_{[3,8]}$=0 means there is no oxygen on those lattice sites and $c_{[3,8]}$=1 means all the octahedral sites are full of oxygen. From this derivation, we can get an approximation for the internal energy U [80]:

$$U=2\Omega_3 c_1 c_2 + \Omega_4(c_1^2 + c_2^2) + 2W_1\big(c_1(c_3 + c_4 + c_5) + c_2(c_6 + c_7 + c_8)\big) + 4W_2\big(c_1(c_6 + c_7 + c_8) + c_2(c_3 + c_4 + c_5)\big) + 2\varepsilon_{oo}^1\big(c_3(c_7 + c_8) + c_4(c_6 + c_8) + c_5(c_6 + c_7)\big) + 4\varepsilon_{oo}^2(c_3c_4 + c_3c_5 + c_4c_5 + c_6c_7 + c_6c_8 + c_6c_8) + 8\varepsilon_{oo}^3(c_3c_6 + c_4c_7 + c_5c_8) + 3\varepsilon_{oo}^4(c_3^2 + c_4^2 + c_5^2 + c_6^2 + c_7^2 + c_8^2) \quad (21)$$

Where Ω_3 and Ω_4 are the order energies are related to the pair-interaction energies here:

$$\Omega_3 = 4(\varepsilon^3_{FeFe} + \varepsilon^3_{YY} - 2\varepsilon^3_{FeY}) \quad (22)$$

$$\Omega_4 = 3(\varepsilon^4_{FeFe} + \varepsilon^4_{YY} - 2\varepsilon^4_{FeY}) \quad (23)$$

$$W_1 = \varepsilon^1_{YO} - \varepsilon^1_{FeO} \quad (24)$$

$$W_2 = \varepsilon^2_{YO} - \varepsilon^2_{FeO} \quad (25)$$

And the configurational entropy term becomes:

$$TS = kT \sum_{i=1}^{8} c_i \ln(c_i) + (1 - c_i)\ln(1 - c_i) \quad (26)$$

To represent the Y_2O_3 system, only half of the octahedral sites will be occupied. In general, with the assumption that the oxygen will rest on one of the two sub lattices in the octahedral portion (c_3=c_4=c_5 or c_6=c_7=c_8), the chemical potential equations become:

$$\frac{\partial F}{\partial c1} = 2\Omega_3 c_2 + 2\Omega_4 c_1 + 6c_3 W_1 + 12c_7 W_2 - kTln(c_1) + kTln(1 - c_1) = \mu_y \quad (27)$$

$$\frac{\partial F}{\partial c2} = 2\Omega_3 c_1 + 2\Omega_4 c_2 + 6c_7 W_1 + 12c_4 W_2 - kTln(c_2) + kTln(1 - c_2) = \mu_y \quad (28)$$

$$\frac{\partial F}{\partial c3} = 2c_1 W_1 + 4c_2 W_2 - kTln(c_3) + kTln(1 - c_3) + 4\varepsilon^1_{oo} c_7 + 8\varepsilon^2_{oo} c_3 + 8\varepsilon^3_{oo} c_7 + 6\varepsilon^4_{oo} c_3 = \mu_o$$

(29)

Once equilibrium has been achieved, the equilibrium concentrations of Y and O in the bulk can be found by the relation of the grand potential of both phases. Equations for grand potential *A*:

$$A = F - \sum_{i=1}^{8} \mu_i c_i \quad (30)$$

It is assumed that the grand potentials for precipitate phase are equal to each other and the grand potential of the Fe phase is close to zero due to the low concentration of solutes:

$$A_{Prec} = A_{Fe} \tag{31}$$

$$A_{Fe} \sim 0$$

Therefore, the Helmholtz free energy is reduced to a summation of the chemical potentials:

$$A_{Prec} = F - \sum_{i=1}^{8} \mu_i c_i = 0$$

$$F = \sum_{i=1}^{8} \mu_i c_i \tag{32}$$

Assume the stoichiometry of the precipitate is expected to be 2Y:3O (c_1=$c_2 = 1$, c_3=c_4=c_5=1 and c_6=c_7=$c_8 = 0$). So the Helmholtz free energy becomes:

$$F = 2\mu_Y + 3\mu_o \tag{33}$$

Assume the concentrations of Y and O are so small in the Fe region that the chemical potential calculated through Eq. 27-29 corresponds to:

$$\mu_y = kTln(c_Y^{Fe}) \tag{34}$$

$$\mu_o = kTln(c_O^{Fe}) \tag{35}$$

Where c_Y^{Fe} and c_O^{Fe} correspond to the concentrations of Y and O in the bulk Fe. Follow previously shown procedure and using algebraic substitution of Eq. 34 and 35 into Eq. 33, the solubility product K_s^{Y-O} for Y_2O_3 in bulk Fe can be predicted by the following:

$$K_s^{Y-O} = [c_Y^{Fe}]^{(2)}[c_O^{Fe}]^{(3)} = \exp\left(\frac{F}{kT}\right) \quad (36)$$

The Helmholtz free energy F for the Y_2O_3 phase is found by entering the expected Y_2O_3 structure and the formula for the Y_2O_3 solubility product becomes:

$$K_s^{Y-O} = [c_Y^{Fe}]^{(2)}[c_O^{Fe}]^{(3)} = \exp\left(\frac{2\Omega_3+2\Omega_4+6W_1+12W_2+12\varepsilon_{OO}^2+9\varepsilon_{OO}^4}{kT}\right) \quad (37)$$

For the Y-Ti-O oxides, the $Y_2Ti_2O_7$ structure cannot be represented on the bcc structure, so a formulation assuming a $YTiO_3$ structure is constructed to relate the pair-interaction energies to the solubility product K_s^{Y-Ti-O}. The above derivation is repeated, this time with the Ti occupying lattice point c_1 and Y occupying c_2. A formula similar to Eq. 37 is the final result and shown below:

$$K_s^{Y-Ti-O} = [c_Y^{Fe}][c_{Ti}^{Fe}][c_O^{Fe}]^{(3)} = \exp\left(\frac{2\Omega_3{}^{TiY}+\Omega_4^{FeY}+\Omega_4^{TiY}+6(\varepsilon_{TiO}^1-\varepsilon_{FeO}^1)+12(\varepsilon_{YO}^2-\varepsilon_{FeO}^2)+12\varepsilon_{OO}^2+9\varepsilon_{OO}^4}{kT}\right)$$

(38)

The value predicted in Eqs 37 and 38 is used as a reference point to validate the KMC code in a procedure later in Chapter 2. The following section will explain the two computer models in detail.

2.3 Mean Field Rate Theory

For this project, the existing MF-RTM models for RIS were further extended to be representative of the NFAs. The set-up is for the quaternary alloy with a bcc crystal structure composed of Fe, Y, Ti, and O. The following model differs from the existing RIS models in literature in a number of ways:

- The model focuses on the segregation behavior of yttrium, titanium, and oxygen in bcc iron. They are minor constituents, as opposed to Cr or Ni.
- The investigation on the segregation behavior of oxygen, an element that exists on a separate sub-lattice (e.g., interstitial sublattices) than the other solutes. Investigations by Kano have shown that carbon, an element that likewise exists on the octahedral sites, has a suppressing effect on the segregation of substitutional elements [108]. The effect of oxygen on segregation would also be investigated.
- The implementation of the segregation energy of each element at the grain boundary into the RIS model. The influence of the segregation energy plays a dominant role in the segregation of the FIAs, which do not migrate via point defects. This would in turn influence the segregation of the substitutional impurities through their interactions with the interstitial solutes.

2.3.1 Formulation

For the mean-field rate theory, the material system is envisioned as a series of planes in the 1-D direction. The concentrations of solute atoms in each plane are recorded in the variable C_x. Where the concentration is a value between 0 and 1 and the summation of the substitutional atomic concentrations equals 1 ($C_{Fe} + C_Y + C_{Ti} = 1$). Thus, we only need to track the Y and Ti concentrations since we know the remainder will be Fe from that relationship. Oxygen is not a part of that relationship since it exists on a separate sub-lattice in bcc Fe. The rates of change for the concentration of solutes and point defects in each plane can be calculated from the following equations:

$$\frac{\partial C_V}{\partial t} = G - R \times C_V \times C_I + \nabla[-(d_{YV} - d_{FeV})C_V \nabla C_Y - (d_{TiV} - d_{FeV})C_V \nabla C_{Ti} + D_V \nabla C_V] \quad (39)$$

$$\frac{\partial C_I}{\partial t} = G - R \times C_V \times C_I + \nabla[-(d_{YI} - d_{FeI})C_I \nabla C_Y - (d_{TiI} - d_{FeI})C_I \nabla C_{Ti} + D_I \nabla C_I] \quad (40)$$

$$\frac{\partial C_Y}{\partial t} = \nabla[D_Y \nabla C_Y + C_Y(d_{YI} \nabla C_I - d_{YV} \nabla C_V)] \quad (41)$$

$$\frac{\partial C_{Ti}}{\partial t} = \nabla[D_{Ti} \nabla C_{Ti} + C_{Ti}(d_{TiI} \nabla C_I - d_{TiV} \nabla C_V)] \quad (42)$$

$$\frac{\partial C_O}{\partial t} = \nabla[D_o \nabla C_o] \quad (43)$$

The production term G is the same for both defects since the collisions of high energy particles create a Frenkel Pair, one vacancy and one dumbbell, every time an atom is knocked off of its lattice site. Since the MF-RTM simulates electron irradiation it can be assumed that the production of point defects will be homogenous throughout the material. The recombination constant R is the same for both defects since both are eliminated when a dumbbell atom returns to a vacant site. In this model, only substitutional elements can be knocked off to form interstitial dumbbells. The displacements of atoms on the octahedral sub-lattice are not tracked, since the majority of these sites are already vacant. Additionally, any oxygen atom that is knocked onto a substitutional site would almost immediately fall back to an octahedral site by virtue of the more favorable energetics. The numerous vacant sites on the octahedral lattice ensures the substitutional oxygen will have an opportunity to jump back.

For constituent atoms, any concentration change is the result of an imbalance of that species's atoms flowing in and out of the plane. This imbalance is normally the result of a concentration gradient of the solute in the system, with its atoms travelling to fill in areas of low concentrations to make a uniform distribution of alloying elements in the system. In the case of irradiation, an imbalance will arise from a gradient in the point defects from high to low towards the defect sinks since the sinks maintain an area of low point defect concentration around itself.

Again, in this study, the equations differ from previous models by the inclusion of an element that exists on a separate sub-lattice.

2.3.2 Migration Energies

The migration energies are very important inputs values for an RIS model, as shown in a sensitivity analysis by Wharry [76]. They represent an energy barrier that must be overcome for the migration to take place. These migration energies are composition-dependent, which is reflected in the incorporation of pair interactions in the calculation of migration energies. The difference between a composition-independent saddle point energy and the sum of the interactions with the migrating solute and point defect with their neighbors provides the migration energy.

$$E_{mig} = e^{SP} - I_3 - I_4 - I_o - I_{PD} \tag{44}$$

$$E_{mig} = e^{SP} - \overbrace{(z_3 - 1)\sum_j \varepsilon_{Fej}^3 \times C_j}^{I_3} - \overbrace{z_4 \sum_j \varepsilon_{Fej}^4 \times C_j}^{I_4} - \overbrace{\sum_{n=1,2} z_n \varepsilon_{FeO}^n \times C_O}^{I_o} - \overbrace{z_3 \sum_j \varepsilon_{jV}^3 \times C_j}^{I_{PD}} \tag{45}$$

$$E_{mig} = e_O^{SP} - 2\sum_j \varepsilon_{jO}^1 \times C_j - 4\sum_j \varepsilon_{jO}^2 \times C_j - \sum_{j=1,2} z_n \varepsilon_{oO}^n \times C_O \tag{46}$$

Eq. 45 represents the different interactions that may play a role in the calculation of the migration energy. The term e^{SP} stands for the saddle-point energy and it is constant regardless of any changes in composition. The other models only use the first nearest neighbors of the solute atom and point defect when calculating the migration energy, denoted as I_3 and I_{PD}. However, in hopes of greater accuracy, our model includes the 2nd nearest neighbor, denoted as I_4. Another addition to previous models is the inclusion of interactions of atoms on different sublattices as the atom that is migrating, denoted as I_O. The terms z_1 and z_2 are the number of 1st and 2nd nearest

octahedral neighbors while z_3 and z_4 are 1st and 2nd *substitutional* neighbors. Eq. 46 represents the calculation of the oxygen migration energy with its own interaction with substitutional and octahedral atoms. The interaction of point defects and foreign interstitial atoms were not included in this model.

The set of equations 39-43 are numerically integrated using a finite difference method where the grain boundary is in the middle of the simulation box. At the beginning of the MF-RTM, the concentrations of solutes are uniform throughout the grain and the point defect concentrations are set to their thermal equilibrium values c_v^{eq} and c_{dumb}^{eq}. Throughout the simulation, the point defect concentration at the grain boundary remains at the thermal equilibrium level while the adjacent planes increase in concentration. Over time, a ∇C_V and ∇C_I gradient is formed which in turn drives segregation. At the grain center, the concentration gradients for all solutes and defects are set to zero.

2.3.3 Thermal Segregation

This model also differs from previous work studying RIS using rate-theory by the implementation of the segregation energy at the grain boundary. The nature of the grain boundary changes the energetics around the grain boundary and can drive segregation without a point defect gradient. This effect could not be simulated with existing models as the system remains at a state of equilibrium when it is not under irradiation due to the lack of a concentration gradient of solutes or point defects around the grain boundary. The equations do not reflect that the atoms are always moving throughout a given material despite there being no concentration gradient of point defects.

$$\frac{\partial C}{\partial t} = -\nabla \mathrm{J} = -(J_{in} - \cancel{J_{out}}) = -\frac{D}{a^2}\left(C_{i+1} \times \exp\left(\frac{\Delta G_{seg}}{k_b T}\right) - C_i\right) \quad (47)$$

Eq. 47 calculates the flux at the grain boundary using work by Hofmann to allow segregation without a point defect gradient [109]. ΔG_{seg} represents the standard segregation energy. J_{in} and J_{out} represent the flux of atoms that flows into the grain boundary from each plane adjacent to the selected plane. J_{out} is set to zero since the solutes cannot cross the grain boundary in this simulation. The term *a* is the lattice parameter of bcc iron.

The MF-RTM can be tested for validity against segregation due to thermal forces. The degree of attraction can be represented by the Gibbs free energy of segregation, the standard entropy and enthalpy of which can be calculated from experimental data. The extent of the segregation can be predicted thermodynamically using mean-field Langmuir-Mclean isotherms with given segregation energy, temperature, and bulk solute concentrations:[110]

$$\frac{X_I^{GB}}{1-\sum_{J\neq M} X_J^{GB}} = \frac{X_I^{B}}{1-\sum_{J\neq M} X_J^{B}} \times \exp\left(\frac{-\Delta G_{seg}}{k_b T}\right) \quad (48)$$

X^{GB} is the grain boundary concentration of the solute and X^{B} is the bulk concentration. The system in this case is assumed to be so large that any change in bulk concentration due to segregation is considered negligible. One isotherm is created for each solute element and are solved as a system of equations to find the grain boundary concentration of each solute.

Though when using Eq. 48, there are cases where the size of the grain plays an impact on the segregation of the constituent atoms. A small grain may not contain the required amount of atoms to fulfill a complete segregation or enough atoms are depleted from the bulk to have an effect on the degree of segregation as a whole. The following equation reflects the grain size influence on segregation:[111]

$$\frac{X_I^{GB}}{1-\sum_{J\neq M} X_J^{GB}} = \frac{X_I^B - f\times X_I^{GB}}{1-\sum_{J\neq M} X_J^B} \times \exp\left(\frac{-\Delta G_{seg}}{k_b T}\right) \quad (49)$$

The term *f* is the volume factor, or the ratio of the area of the grain boundary to the size of the grain. In this model, the area of the grain boundary is assumed to be the width of one lattice parameter of the bcc iron, while the size of the grain is taken to be the average grain size of the given material.

The calculation gets more complex when the interactions of solute with other atoms in its environment are included in estimating the segregation energy, using a method described by Guttman [112]. The interactions are extended to incorporate the second nearest neighbor effects.

$$\Delta G = \Delta G_o - 2\alpha_{IM}(X_I^{GB} - X_I^B) + \sum_{J\neq I,M} \alpha'_{IJ}\left(X_J^{GB} - X_J^B\right) \quad (50)$$

$$\alpha_{IJ} = \sum_n Z^n \left(\varepsilon_{IJ}^n - \frac{\varepsilon_{II}^n + \varepsilon_{JJ}^n}{2}\right) \quad (51)$$

$$\alpha'_{IJ} = \alpha_{IJ} - \alpha_{IM} - \alpha_{JM} \quad (52)$$

In Eq. 50, ΔG_o is the standard free energy of segregation and α are interaction coefficients calculated using pair interaction energies in Eqs. 51 and 52. Now to find the grain boundary concentrations, the Langmuir-Mclean isotherms and segregation energy equations must be solved simultaneously. The enthalpy and entropy of segregation of an element in a particular matrix can be predicted by the solubility of the element in Eqs. 53 and 54. In turn, these values are used to find the standard free energy of segregation in the matrix.

$$\Delta H_I(GB, X_I^*) = \Delta H_I(GB, X_I^* = 1) + vR[T \times lnX_I^*(T)] \quad (53)$$

$$\Delta S_I^O = \frac{\Delta H_I^O}{T_c} + \sigma_I \quad (54)$$

$$\Delta G_o = \Delta H - T \times \Delta S \quad (55)$$

X^* is the solubility of a selected element within a given matrix, in this case bcc iron. $\Delta H^*(GB,X^*=1)$ is the enthalpy of segregation if the element were completely soluble in the matrix. It is a given constant that depends on the boundary type, with different types having different segregation behavior. For example, Fields found that in ferritic martensitic steel, there was a larger enrichment of Cr at high-angle grain boundaries than there were at low-angle or special grain boundaries [13]. For simplicity, the boundary is assumed to be a general type. R is the gas constant. The term $vR[TxlnX^*(T)]$ reflects the departure from ideal behavior in the binary systems of that particular matrix element. *v* is a material parameter unique to the given matrix. So the enthalpy of segregation can be found knowing the bulk solubility of an element in a matrix at a given temperature. In addition, the segregation entropy has a relationship with the enthalpy, as shown in Eq. 54. σ is the configuration entropy of the element at the boundary. It differs depending if the element is on the substitutional site or interstitial site. T_c is the temperature at which the segregation energy is the same regardless of the boundary type.

To test the MF-RTM, a simulation is run with the standard energy of segregation plugged in to Eq. 47. The solute interaction is already included in the calculation of migration energies in Eqs. 45-46. No excess point defects are created in this simulation (G=0) such that any segregation is due to the segregation energy. Once the segregation has reached equilibrium, the final grain boundary concentration values are compared to those predicted thermodynamically by Eq. 48.

***Table 2.4**: Segregation enthalpy and entropy of selected solutes in bcc Fe*

	ΔH	**ΔS**
O	0.9984 eV	$4.784x10^{-4}$ eV/K
Ti	0.3328 eV	$3.016x10^{-4}$ eV/K
Y	0.6448 eV	$6.552x10^{-4}$ eV/K

Standard entropy and enthalpy values predicted by Lejcek for elements in bcc iron were used for the titanium and oxygen segregation [113]. The bulk solubility of a solute in bcc iron is used to estimate the enthalpy of segregation. Then the entropy was found using the relationship between segregation enthalpy and the knowledge of the lattice sites a solute atom occupies. Though there is some question to the reliability of the oxygen segregation values due to its low solubility limit in Fe [114]. The segregation values for yttrium were found using Eqs. 53-55 with the bulk solubility of yttrium in alpha iron from other data [115]. The grain boundary in this case is assumed to be a general grain boundary type.

2.3.4 Validation of MF-RTM

In this section, the MF-RTM is run to simulate the thermal segregation of the solute elements. This helps test for the validity of the MF-RTM before adding complexities like irradiation. So should the MF-RTM rate-theory with irradiation fail, some processes can be ruled out as culprits. Then the MF-RTM is run with irradiation to show the overall behavior of the point defects as a function of temperature and dose rate. These relations help us understand their effect on the defect population and overall the radiation damage.

First the MF-RTM was run without irradiation (G=0) to test the model for validity in predicting thermal segregation. The simulation box is filled with the thermal equilibrium concentrations of point defects and segregation energies are attached to the grain boundary to drive thermal segregation. Both the Fe-Y-O and the Fe-Ti-Y-O were run at a temperature of 1000 K, chosen in part for a faster time to reach steady-state behavior. In turn, the thermodynamic Eqs. 48-49 were solved to provide an estimate of the grain boundary segregation of these alloys.

***Table 2.5**: Starting concentrations of each solute for each simulation*

	Ti	Y	O
Concentrations	.5 at%	.5 at%	.75 at%

The compositions of the sample alloys listed in Table 2.5 were selected to mirror those found in commercial alloys.

***Table 2.6**: Thermodynamics vs Kinetics of Segregation of Fe-Y-O*

	Y	O
Segregation Isotherm	0.885 at %	41.2 at%
MF-RTM	0.894 at %	39.2 at%

***Table 2.7**: Thermodynamics vs Kinetics of Segregation of Fe-Ti-Y-O*

	Ti	Y	O
Segregation Isotherm	1.26 at%	0.833 at%	41.2at%
MF-RTM	1.37 at%	0.847 at %	38.7 at%

***Table 2.8**: Thermodynamics vs Kinetics of Segregation of binary Fe-X*

	Ti	Y	O
Segregation Isotherm	0.717 at%	0.423 at %	41.2 at%
MF-RTM	0.707 at%	0.452 at %	40.4 at%

In Tables 2.6 to 2.8, the thermal segregation has been shown to compare nicely to values that predicted from the Langmuir-Mclean isotherms. Tables 2.6and 2.7 compare the steady-state grain boundary concentration found in the irradiation-free mean-field model versus the value predicted from these thermodynamic equations. This is assuming the distance between sinks to be 40 nm. The oxygen is shown to be highly segregating, increasing its grain boundary concentration nearly 100 times the original value. The titanium and yttrium are more subdued in comparison.

Table 2.8 looks at the thermal segregation in a binary Fe-X alloy to see segregation without the interference of the other solute atoms. When either the yttrium or the titanium is alone in a binary Fe-X alloy, the substitutional solutes tend to deplete due to thermal forces. Though when the titanium and yttrium are in a system containing oxygen, as shown in Tables 2.6and 2.7, the titanium and yttrium will enrich with grain boundary concentrations being 2-3 times higher than if the solutes did not interact with oxygen. This speaks to the high amount of attractive force that the oxygen has on the substitutional solutes. The oxygen does not appear to be affected by the presence of other solute atoms.

2.3.5 Point Defect Population with Irradiation

Next, the simulations were run with radiation(G>0) to see the behavior of the defect populations. The simulation box is again filled with the thermal equilibrium concentrations of vacancies and dumbbells. Then the system is irradiated to a specific temperature and dose rate regime. Over time the evolution in concentration of these point defects reaches a steady-state region where they are being removed at the same rate they are being added. The final point defect concentrations are collected and compared below to see the influence of radiation and temperature.

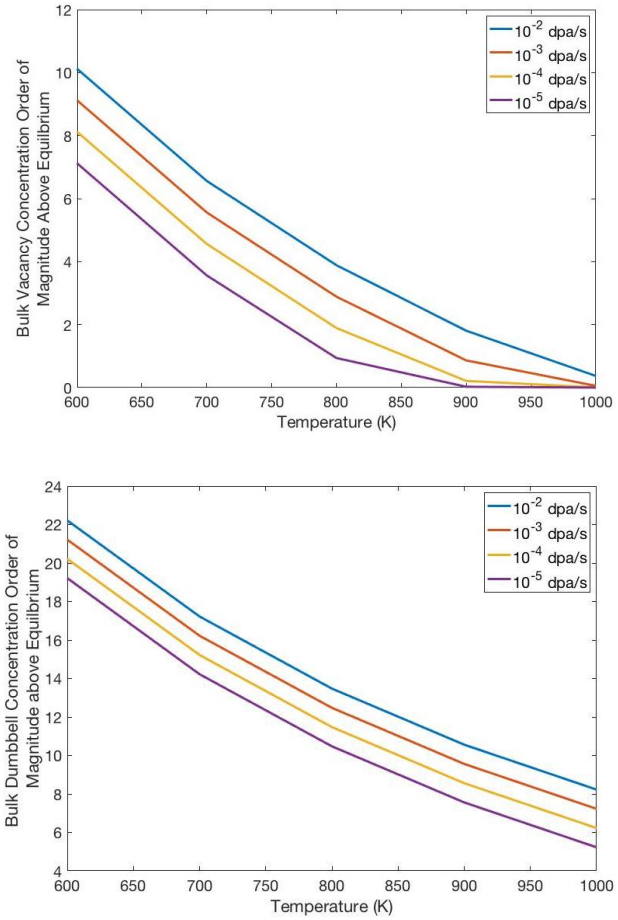

Figure 2.4*: The orders of magnitude above thermal equilibrium for a). Bulk vacancy concentration. B) Bulk interstitial dumbbell concentration.*

To get a sense of the degree of disorder caused by irradiation, the bulk defect concentrations are expressed in orders of magnitude above the thermal equilibrium value (Orders of Magnitude = $\log_{10} C_V^{Irr} - \log_{10} C_V^{eq}$). Figures 2.4a, and 2.4b display the bulk concentrations at steady-state of the vacancies and interstitial dumbbells respectively. The bulk concentration values are useful to understand the segregation trends. These concentration values are taken from the plane furthest away from the grain boundary. It can be noted that as the dose rate increases, the steady-state point defect concentrations increase as well. This general behavior of the bulk point defect concentrations is expected. At the higher dose rates, more point defects are being created than can be taken away due to recombination or annihilation at sinks. Thus the bulk point defect

concentrations will continue to increase as it takes longer to reach a steady-state equilibrium. The removal processes of recombination and migration to sinks have an Arrhenius relationship with temperature, occurring at faster rates at higher temperatures. Thus, a general decrease in the excess bulk point defect concentrations are seen when temperature is increased.

In Figure 2.4a shows that at higher temperature the vacancy concentration becomes closer to the thermal equilibrium value and eventually the difference becomes close to zero. The result indicates temperature makes the vacancy diffuse fast enough so they recombine or annihilate at sinks before any accumulation of excess defects occurs. It is expected that it would not be possible to have a vacancy concentration lower than the thermal equilibrium. Otherwise the disorder caused by the irradiation would make the system *less* disordered when the system started. The dumbbell concentration does not act this way because the thermal equilibrium concentration of dumbbells is very small due to their high formation energy (Example: $c_{dumbbell}^{eq} = 6.4 \times 10^{-25}$at% at 800 K).

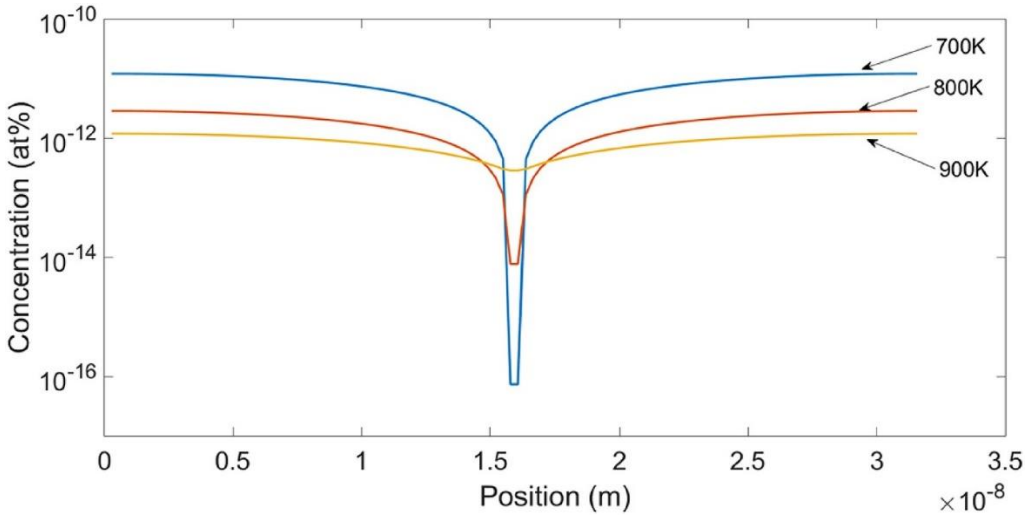

***Figure 2.5**: Vacancy concentration profile in Fe-Ti-Y-O at 10^{-2} dpa/s at various temperatures.*

When the bulk vacancy concentrations trend closer to the thermal equilibrium value, it means the vacancies produced by irradiation are extremely short-lived and are annihilated almost immediately. As a result any vacancy gradient ∇C_V would be very low. This can be seen in the

concentration profile of vacancies in Figure 2.5, with the center being the grain boundary. At 900K and 1000K, there is hardly a perceptible gradient in comparison to the lower temperatures. It can be inferred that at these temperatures, any segregation from irradiation would have to be result of migration of the interstitial dumbbells.

Presently, the model assumes the point defects are generated from electron irradiation. A feature of this type of irradiation is the homogenous production of vacancies and interstitials in the material. Irradiation from different particles, such neutrons or protons, has produced discrepancies in the amount of vacancies versus interstitials that escape from initial cascades. This discrepancy is called a production bias and should be considered when looking at materials under cascade conditions [12]. In typical observations, there are more freely migrating vacancies than interstitials. Due to the focus on the IK effect, the bias is not included in this model.

The MF-RTM model only works for a single-phase material and is unable to account for any precipitation that may take place in the material. The primary goal was to see the degree of segregation due to the coupling of solute and point defect fluxes. When the simulating the irradiation response of NFAs involving the 2nd phase oxides, a different model should be used.

2.4 The Kinetic Monte Carlo Model

The Kinetic Monte Carlo model differs greatly from MF-RTM, the former being a stochastic method with the latter being deterministic. The description of the material in the model also differs. In the MF-RTM, the system is 1-D array of cells inside which the atomic concentrations are assumed to be homogenous within each cell in the 1-dimensional system. For the KMC, the system is described by a 3D lattice built much like what is seen in Figure 2.1, where an atom sits on each lattice site corresponding to the elements preference. The position of each

atom being tracked by the model. Given this stipulation, the size of the simulation can be limited. With sizes going at a maximum of 10^7 atoms leaving the maximum simulation box size for the NFAs <50 nm. Through simulating atomic events that take place in the material, the atoms migrate around the simulation box until a sufficient stopping point is achieved.

2.4.1 Monte Carlo Algorithm

Numerous events can be represented in the Monte Carlo model: point defect generation, vacancy migration, interstitial migrations, and interstitialcy migration. The frequency of these events are quantified and given an event frequency Γ_x defined as the number of times per second the event is expected to occur. The model tabulates all the possible events and finds a total frequency.

$$\Gamma_{Tot} = \sum \Gamma_x \tag{56}$$

For each Monte Carlo step, a single event is chosen by multiplying the total frequency Γ_{Tot} by a random number (0<r<1) and going through the event list until the following is true:

$$\sum_n \Gamma_x < r \times \Gamma_{Tot} < \sum_{n+1} \Gamma_x \tag{57}$$

Then the event corresponding to event frequency Γ_n is chosen and acted upon. Then the possible events are tabulated again and the next Monte Carlo step is enacted. The amount of time that passes is the inverse of the total event frequency:

$$t_{mcs} = \frac{1}{\Gamma_{Tot}} \tag{58}$$

2.4.2 Calculation of Jump Frequencies

There are 8 different directions (corresponding to the 8 nearest neighbors) that vacancy can jump and exchange places with an atom. The probability of each jump occurring is dependent on the neighboring atoms of the moving atom through the calculation of the migration energy for that particular jump. These jump frequencies Γ_x for the migration event can be calculated through the following relation:

$$\Gamma_x = v_{Fe} \times \exp(\frac{-E_{mig}}{k_b T}) \tag{59}$$

Where, like in Eq. 6 of the diffusivity calculation, v_{Fe} is the attempt frequency and E_{mig} is the migration energy. The calculation of the migration energy in the KMC differs slightly than how it was calculated in the rate theory code.

$$E_{mig} = e^{SP} - I_3 - I_4 - I_o - I_{PD} \tag{60}$$

$$E_{mig} = e^{SP} - \sum_j \varepsilon_{Fej}^3 N_j^3 - \sum_j \varepsilon_{Fej}^4 N_j^4 - \sum_{n=1,2} \varepsilon_{FeO}^n N_O^n - \sum_j \varepsilon_{jV}^3 N_j^3 \tag{61}$$

Where $N_j^n$is the number of n nearest neighbors of species j the migrating atom has. For example, N_Y^3 is the number of Y atoms in the third nearest neighbor position that the Fe atom has. Unlike the MF-RTM, where the interaction with the local environment is averaged, the specific atomic configurations can be visualized. Therefore, we can see more effects like binding more easily. It also allows for the formation of clusters to occur that lead into precipitation.

The effect of the segregation energy is incorporated into the model when the point defect is directly adjacent to the grain boundary. All jumps that have the point defect move to the grain boundary will include the segregation energy in the E_{mig} calculation.

$$E_{mig} = E_{mig}^{o} + E_{seg} \tag{62}$$

Where E_{mig}^{o} would be the migration energy in bulk and E_{seg} is the segregation energy. The segregation values in Table 2.4 used for the MF-RTM are the same values put into the KMC model.

Certain events in the Monte Carlo occur instantaneously when certain conditions are met. When a vacancy and an interstitial dumbbell come within 3 atomic distances from each other, both point defects are destroyed. A randomly selected atom from the dumbbell fills the vacant lattice site and the other atom remains at the original site of the dumbbell. The 3 atomic distances approximation for recombination is a common assumption in the KMC for iron [84] based on experimental studies [116]. When a point defect encounters a defect sink like a grain boundary, it is considered annihilated. When a dumbbell is destroyed by the defect sink, one its two atoms is placed in a "reservoir" and the other remains on the substitutional lattice site. This reservoir is used in KMC to maintain conservation of atoms. For when a vacancy is annihilated at the grain boundary, its vacant lattice site is filled in by an atom chosen from the reservoir.

The KMC simulation box is chosen to have periodic boundary conditions by having a mobile species emerge at the other side of the matrix when it jumps out of bounds. The grain boundaries are represented as perfectly planer sinks a single atomic layer wide.

2.5 KMC Validation Procedure

In order to validate the parameters used by the KMC model written for this project, the model needs to replicate the behavior of the phases being observed. A testing procedure was developed for these validation exercises consisting of two tests. The solubility product test and the precipitate shape test.

2.5.1 Solubility Product Test

Current procedure:

1. Build a new set of parameters to test
2. Make a prediction of the solubility product using the following analytical equation, that was developed using the assumption that the %Fe in the oxide precipitate would be very small.

$$K_{Predicted}^{Y-O} = c_y^2 c_o^3 = \exp\left(\frac{2\Omega_3 + 2\Omega_4 + 6W_1 + 12W_2 + 12\varepsilon_{oo}^2 + 9\varepsilon_{oo}^4}{kT}\right)$$

3. Create a box of with two sides. Y_2O_3 on one side with Fe on the other. Run the KMC simulation until the concentration of Y and O in the Fe side is at an equilibrium. Collect concentration of Y and O in Fe (c_y and c_o) and make an estimation of the solubility product, $K_{sim}^{Y-O} = c_y^2 c_o^3$
4. Compare the collected and predicted solubility product. If $K_{Predicted}^{Y-O} \approx K_{sim}^{Y-O}$ then the solubility product test is passed.

Start of simulation:

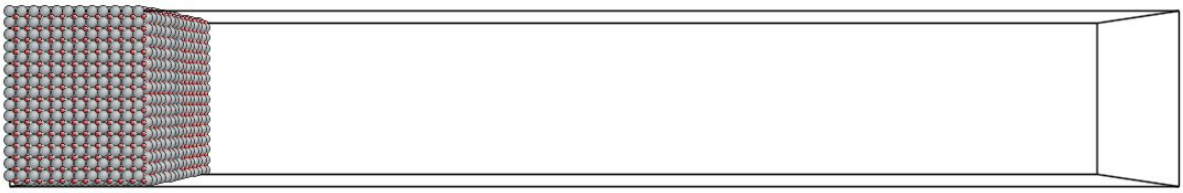

***Figure 2.6**: Y_2O_3-Fe system. The Y_2O_3 crystal is located on the left side (grey spheres are Y atoms and red spheres are oxygen atoms). The Fe atoms are invisible in these exercises in order to visualize the solute in the Fe side. Grey spheres: Y atoms, Red spheres: O atoms.*

***Table 2.9**: Stoichiometry of the Y-O and Fe phases in the simulation box at the start of the solubility product test.*

	. Y_2O_3 Phase	Fe Phase
Structure	$c_1 = 1.0$ $c_2 = 1.0$ $c_3 = 1.0$ $c_4 = 1.0$ $c_5 = 1.0$ $c_6 = 0.0$ $c_7 = 0.0$ $c_8 = 0.0$	$c_1 = 0.0$ $c_2 = 0.0$ $c_3 = 0.0$ $c_4 = 0.0$ $c_5 = 0.0$ $c_6 = 0.0$ $c_7 = 0.0$ $c_8 = 0.0$

Initially, the two sides are not in equilibrium due to the unbalanced chemical potentials.

$$\mu_Y^{Prec} \neq \mu_Y^{Fe}$$

$$\mu_O^{Prec} \neq \mu_O^{Fe}$$

The unequal chemical potentials create a driving force where Y and O atoms are leeched out of the Y_2O_3. The system drives towards equilibrium as Fe region gains more Y and O. When equilibrium is reached, both sides will have an equilibrium concentration of all solutes. The KMC code tracks the solubility product in the Fe region over the course of the simulation. The steady-

state detection algorithm discussed in Chapter 3 is used to find when the system reaches an equilibrium and the simulation ends.

End of Simulation:

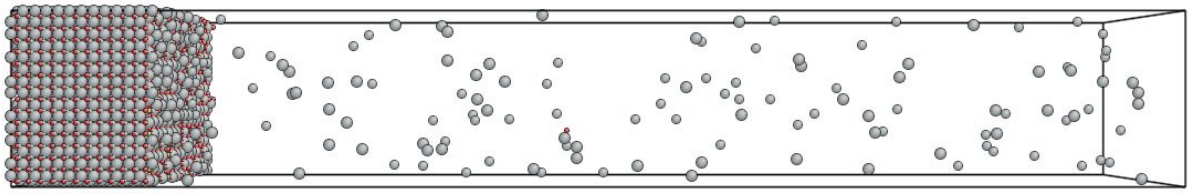

***Figure 2.7**: Y_2O_3-Fe at steady-state. There is now an equilibrium amount of Y and O in the Fe region. Grey spheres: Y atoms, Red spheres: O atoms.*

***Table 2.10**: Stoichiometry of the Y-O and Fe phases in the simulation box at the end of the solubility product test.*

	. Y_2O_3 Phase	Fe Phase
Structure	$c_1 = 1.0 - x$ $c_2 = 1.0 - y$ $c_3 = 1.0 - z$ $c_4 = 1.0 - z$ $c_5 = 1.0 - z$ $c_6 = 0.0$ $c_7 = 0.0$ $c_8 = 0.0$	$c_1 = c_Y^{Fe}$ $c_2 = c_Y^{Fe}$ $c_3 = c_O^{Fe}$ $c_4 = c_O^{Fe}$ $c_5 = c_O^{Fe}$ $c_6 = c_O^{Fe}$ $c_7 = c_O^{Fe}$ $c_8 = c_O^{Fe}$

$$\mu_Y^{Prec} = \mu_Y^{Fe}$$

$$\mu_O^{Prec} = \mu_O^{Fe}$$

When the system has reached an equilibrium where the chemical potentials in both phases have equalized. This mean that the concentrations of Fe, Y, and O in both phases will stay roughly constant no matter how much long the simulation runs for. We can calculate the solubility product

from the concentrations Y and O in the Fe-phase. Should the solubility product match that from the thermodynamic predictions, then it adds a degree of confidence to the validity of the KMC model.

The solubility product test is run for both Y-O and Y-Ti-O at two temperatures to ensure confidence in the model. The test for Y-Ti-O follows the same procedure. Like with the derivation of the Y-Ti-O solubility product, the Ti occupies lattice point c_1 and Y occupies c_2.

***Table 2.11**: Solubility Products from thermodynamic prediction compared to results from the KMC solubility product test at two temperatures 1300K and 1573K.*

	Y-O (1573K)	Y-O (1300K)	Y-Ti-O (1573K)	Y-Ti-O (1300K)
From Thermodynamics	5.4×10^{-18}	2.52×10^{-22}	5.35×10^{-13}	1.04×10^{-15}
From KMC	7.2×10^{-18}	4.28×10^{-22}	4.6×10^{-13}	2.89×10^{-15}

Table 2.11 shows the results of the solubility product validation results. The KMC model is able to replicate the solubility product of both the Y-O and Y-Ti-O systems. The agreement holds even at different temperatures.

2.5.2 Equilibrium Shape Test Simulations

Just like in the solubility product test simulations, this test observes a system reach a stable state. Though this time, the critical observation is how the precipitate reshapes itself over the course of the test. The expectation is that the oxide precipitates will shape themselves to achieve the lowest energy. From experimental observations from Ribis, it is expected that the Y_2O_3 and

$Y_2Ti_2O_7$ precipitate will retain a cubic shape [92]. To test this, the current procedure was developed:

Current procedure:

1. Create a box of bulk Fe with a large cubic Y_2O_3 precipitate in the center.
2. Run the KMC simulation and observe the shape of the precipitate
3. Compare the shape to predictions

Start of Simulation.

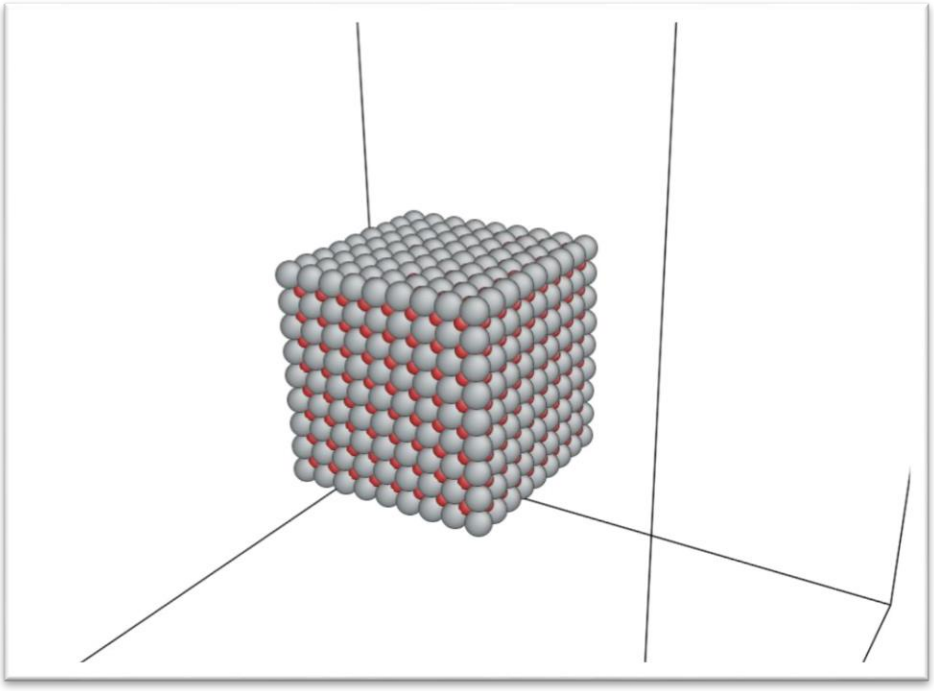

Figure 2.8*: A cubic Y_2O_3 crystal is placed in the center of the bcc Fe matrix. Here is the shape before any interaction with the vacancy. Grey spheres: Y atoms, Red spheres: O atoms.*

***Table 2.12**: Stoichiometry of the Y-O and Fe phases in the simulation box at the start of the equilibrium shape simulation*

	. Y_2O_3 Phase	Fe Phase
Structure	$c_1 = 1.0$ $c_2 = 1.0$ $c_3 = 1.0$ $c_4 = 1.0$ $c_5 = 1.0$ $c_6 = 0.0$ $c_7 = 0.0$ $c_8 = 0.0$	$c_1 = 0.0$ $c_2 = 0.0$ $c_3 = 0.0$ $c_4 = 0.0$ $c_5 = 0.0$ $c_6 = 0.0$ $c_7 = 0.0$ $c_8 = 0.0$

Just like the solubility product simulations, the system does not start in a stable state and that instability drives changes to the precipitate.

$$\mu_Y^{Prec} \neq \mu_Y^{Fe}$$

$$\mu_O^{Prec} \neq \mu_O^{Fe}$$

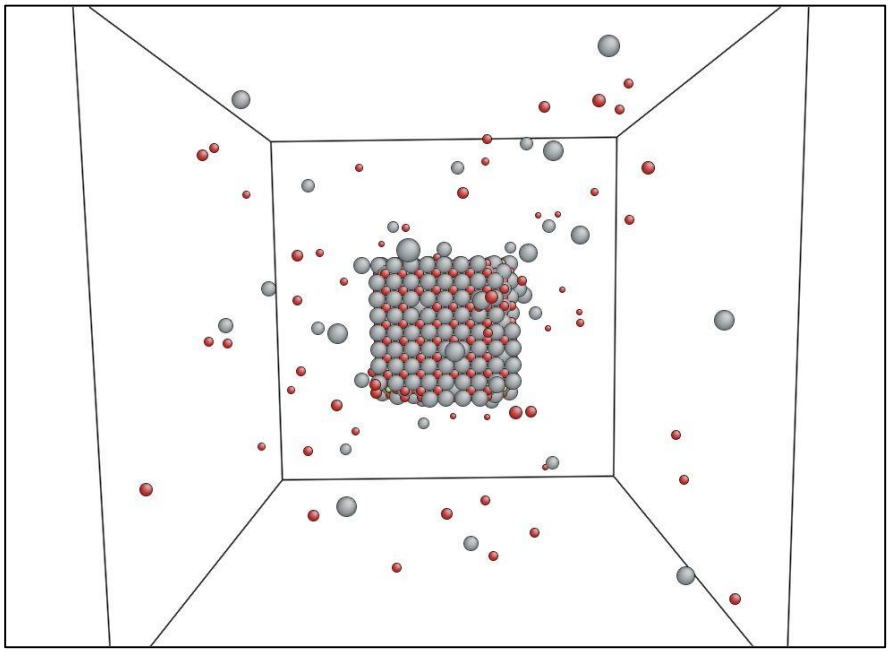

***Figure 2.9**: The equilibrium state of a Y_2O_3 oxide and the bcc Fe matrix at 1573K. Grey spheres: Y atoms, Red spheres: O atoms.*

In Figure 2.9, we see that numerous Y and O atoms remove themselves from the central precipitate into the bulk, responding to an imbalance in chemical potential. This continues until the imbalance is corrected, what follows is an equilibrium state between the precipitate and the bcc Fe matrix. Despite the partial depletion of constituent atoms, the central precipitate is able to adjust to the loss in atoms and is still able to retain its cubic shape as observed in experiments thus giving greater confidence in the validity of the model. It was also found that the precipitate maintained its 2Y:3O stoichiometry.

***Table 2.13**: Stoichiometry of the Y-O and Fe phases in the simulation box at the end of the equilibrium shape simulation.*

	Y_2O_3 Phase	Fe Phase
Structure	$c_1 = 1.0 - x$ $c_2 = 1.0 - y$ $c_3 = 1.0 - z$ $c_4 = 1.0 - z$ $c_5 = 1.0 - z$ $c_6 = 0.0$ $c_7 = 0.0$ $c_8 = 0.0$	$c_1 = c_Y^{Fe}$ $c_2 = c_Y^{Fe}$ $c_3 = c_O^{Fe}$ $c_4 = c_O^{Fe}$ $c_5 = c_O^{Fe}$ $c_6 = c_O^{Fe}$ $c_7 = c_O^{Fe}$ $c_8 = c_O^{Fe}$

$$\mu_Y^{Prec} = \mu_Y^{Fe}$$

$$\mu_O^{Prec} = \mu_O^{Fe}$$

Validation of the Y-Ti-O

Equilibrium shape simulations were completed for the Fe-Y-Ti-O system at all precipitation temperatures in Chapter 4. The original Y-Ti-O cubic precipitates were each reshaped by thermal vacancies into their equilibrium shape. The final atomic positions of the Y, Ti, and O

atoms were recorded and visualized using the ATOMEYE software [117]. The matrix Fe atoms were made transparent for the purpose of visualization.

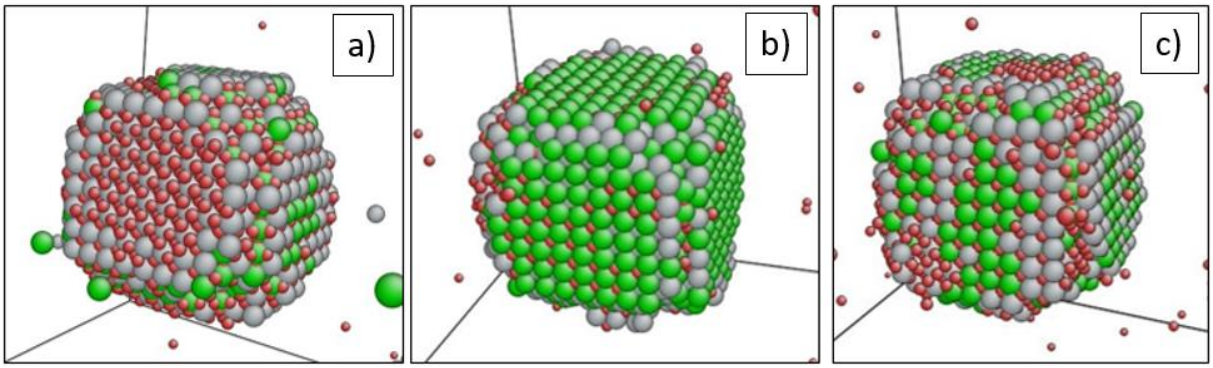

Figure. 2.10: Equilibrium shape of the Y-Ti-O oxide at a) 1023K, b) 1123K, and c) 1223K. Green spheres: Ti atoms, Grey spheres: Y atoms, Red spheres: O atoms

Fig. 2.10 a-c displays the precipitate equilibrium shape of the Y-Ti-O oxides in Fe after being reshaped by the thermally generated vacancies at the three heat treatment temperatures. Over all tested temperatures, the shape of the precipitate remains cubic, as observed by Ribis [92]. The <100> interface is most prominent with a small area of the <110> and <111> interfaces being present. Oxides of this shape have also been seen in TEM observations of 14YWT [118]. As the temperature increases, the <110> and <111> interfaces become more pronounced.

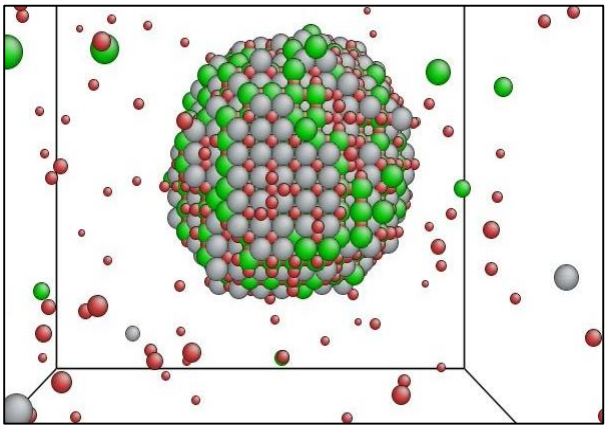

Figure. 2.11: a) Equilibrium shape of the Y-Ti-O oxide at 1673K from KMC model. Green spheres: Ti atoms, Grey spheres: Y atoms, Red spheres: O atoms

Fig. 2.11 shows the equilibrium precipitate shape for a Y-Ti-O oxide at 1673K. The oxide precipitate starts to lose constituent atoms due to the increased solubility limits of the system at high temperatures. To reduce system energy, the oxide's initial cubic shape is reshaped into a more spherical shape. This is consistent with experimental observations from Ribis after thermal aging at 1673K [119].

The shape of the precipitate follows expectations from the calculated interface energies at various orientations. The interface energies of each oxide can be extracted using a broken bond model by counting the number of broken bonds over a representative interface area [120].

Table 2.14: Interface energy of the Y-O and Y-Ti-O interfaces in various orientations

Interface Energy	**Y-O**	**Y-O Ribis**	**Y-Ti-O**	**Y-Ti-O Ribis**
$\boldsymbol{E_{100}^{\gamma}}$	0.31	0.35	0.41	0.26
$\boldsymbol{E_{110}^{\gamma}}$	0.61	N/A	0.52	N/A
$\boldsymbol{E_{111}^{\gamma}}$	0.77	N/A	0.63	N/A

Table 2.14 lists the interface energy in the <100> direction calculated from the pair-interaction energies, using the findings from an experiment [92] for comparison. The <100> interface is most prominently featured due to its low interface energy, compared to <110> and <111> interfaces. Likewise, the <110> is the second most featured since $\boldsymbol{E_{110}^{\gamma} < E_{111}^{\gamma}}$.

The interface energies of the Y-O and Y-Ti-O oxides also add a measure of validity to the parameters when checking against experimental findings. The Y-O interfaces have a closer agreement with the literature value than the Y-Ti-O interfaces, although both should be sufficient for the purposes of the simulation. Other researchers have found that the Y-Ti-O interface energy is in the 0.4-0.6 range [121].

2.5.3 Validation with the Mean-field Model

Fe-Y-O

Another method to gain confidence for the MF-RTM and KMC models is to compare the results to each. If the same pair interaction energies and kinetic parameters are inputted into both models, they should return similar results provided there are no nucleation events in the KMC simulations.

Multiple simulations were done to model radiation induced segregation in two material systems: the Fe-Y-O and the Fe-Ti-Y-O systems. For the testing procedure, the same parameters and starting conditions are fed into both the MF-RTM and KMC models. The point defects are produced through Frenkel Pair insertion (emulating electron irradiation) and the solutes are all dispersed in the matrix. The irradiation environments and starting conditions listed in Tables 2.15 and 2.16 are modeled after observations from Ribis [67].

***Table 2.15**: Starting concentrations of each solute in the MF-RTM for each RIS simulation*

	Ti	Y	O
Concentrations	.5 at%	.5 at%	.75 at%

***Table 2.16**: Irradiation conditions for rate-theory and KMC RIS testing.*

System Size	G	T	dpa
200 cells (MF-RTM) 200X100X100 (KMC)	0.01 dpa/s	600K, 700K	1 dpa

The simulations in both the mean-field and KMC are run until the irradiation reaches about 1 dpa then the results are compared. At 500 different points in time, the KMC model records the

solute atom concentration at the grain boundary. Profiles of the atomic concentrations of each solute at the grain boundary over system dpa are graphed and compared.

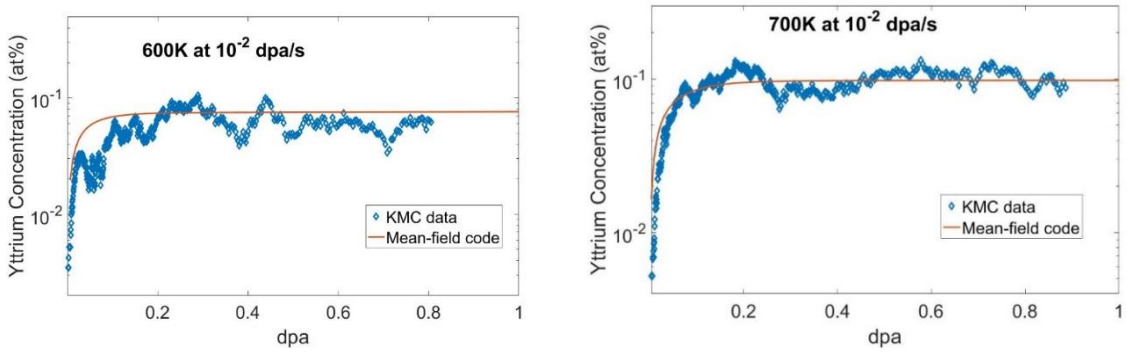

***Figure 2.12**: The Yttrium concentration at the grain boundary in the MF-RTM (mean field) and the KMC simulation over dpa at 0.01 dpa/s at a)600K and b)700K*

Figures 2.12a and 2.12b show the Y concentration at the grain boundary for the Fe-Y-O system at 600 K and 700 K respectively. They show that the mean-field model and the KMC model have close agreement with each other. Displaying a large enrichment of Y at the grain boundary.

Fe-Ti-Y-O

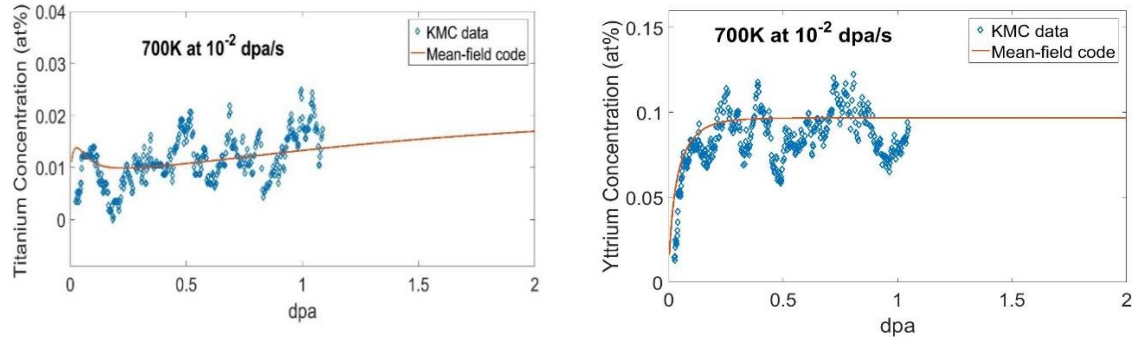

***Figure 2.13**: The a) Yttrium and b) Titanium concentration at the grain boundary in the MF-RTM (mean field) and the KMC simulation over dpa at 0.01 dpa/s*

Figures 2.13a and 2.13b show the grain boundary concentration over dpa of Ti and Y respectively at 700K respectively. Again there is good agreement between the MF-RTM and the KMC model. It should be noted that given the relative size of the simulation box, the addition or

removal of a single atoms from the grain boundary will make a significant impact on the concentration read. And the nature of the KMC has the atoms in constant motion. Even the atoms that are reluctant to move from a site. This is the cause of the fluctuations in the grain boundary concentration from the KMC. Thus it is more useful to see the data as it oscillates around the results from the mean-field model. It is this phenomenon which in part lead to the development of the steady-state detection algorithm.

2.6 Conclusions

This chapter first discussed how the Fe-Y-O and Fe-Y-Ti-O material systems are described in the computer models. Which lattice the solutes sit on the lattice and how the atoms diffuse through the Fe matrix via point defects or through interstitial jumps. Then details of the kinetic and thermodynamic parameterization of the system was discussed; including the literature values the models are meant to emulate. A series of validation procedures were conducted to ensure the models were able to replicate basic material behavior. With the KMC model able to reproduce the solubility products, have a thermal equilibrium shape within expectations from literature, and produce similar segregation results to the MF_RTM, there is a degree of confidence in the KMC to simulate the Fe-Y-Ti-O system under high temperature thermal heat treatment and irradiation which will be discussed in Chapters 4-6.

The process of these simulations revealed a need for proper stopping criteria for the KMC model. The stopping criteria of a certain dpa was sufficient for the validation exercise but for the future simulations where the stopping point is less clear (i.e. when the system reaches an equilibrium). A steady-state detection algorithm was developed and used to assist in the solubility product validation exercises. Details about this algorithm are provided in the next chapter.

Chapter 3: Steady State Detection

3.1 Introduction of F-t-Pj-RG Method

The ending condition for these KMC simulations is when the system reaches a steady-state region where certain values remain relatively constant. It is relatively straightforward to set a condition where the change in some material value falls below a certain threshold over a period of time. However, setting these conditions often requires specific knowledge of the system being studied. In cases where computational expense is important, a nebulous stopping criteria can lead to the simulation stopping too soon or going on far longer than need be. Thereby wasting computational resources. There is an idea to develop a statistical test that can more confidently find a statistical steady-state. With the goal of finding a reliable steady-state detection method, the F-t-Pj-RG method was developed. It is a window based method that performs an f-test, t-test, and projection test in sequence.

One of the most direct methods to detect steady-state is to calculate the slope of the monitored data using linear regression, [122-124] and to simply assume that when the slope of the data is close to zero, the system is unchanging and at steady-state. In practice, real data generally has noise, and does not have a slope that is truly zero at finite timescales. Again, in this work, the terms steady-state (SS) and steady-state detection (SSD) refer to statistical steady-states, where the changes in the system (i.e., slopes) are sufficiently close to zero for a statistical threshold, and not truly zero. Slope based methods require defining the tolerance of how close to zero is acceptable, and also require performing regression upon either the full data set or making a choice of the size of a data window to perform regression upon and rolling/shifting that window [125]. In this work,

rolling a data window means shifting the data window position along the x-axis while holding either the number of data points or the x-axis span constant (i.e., after rolling a data window, the new data window has the same size as the previous data window). A problem with simply performing regression on the full data set is that many types of simulations, including KMC simulations, go through a significant warm-up period: the warm-up period is defined for our purposes as period of transient behavior that starts at the system initialization and spans until the system achieves steady-state. From a physical sciences point of view, this transient warm up period is a period during which the system is relaxing towards the steady-state. The final state of the system, if a steady-state is reached, may either be an equilibrium steady-state or a non-equilibrium steady-state; depending in part on whether the system is a closed system or an open system. Completely automated algorithms for steady-state detection using these types of methods must thus be able to exclude the warm up period, and must have a mechanism for determining an appropriate window size with as little user input as possible, and these requirements were considered in the design of the F-t-Pj-RG method.

Early research into SSD revolved around the problem of initialization bias [126]. That is, the issue of removing the transient region of a dataset so the researchers can focus on analyzing the steady-state region without being tainted by the transient [127]. However, for some applications, steady-state detection is used for determining the point in which an action is required, such as terminating the experiment or beginning another step in the process [128], and in this case the computing time does become a consideration. Additionally, many diagnostic programs require the machine to be operating in a steady-state regime to ensure correct interpretation of operating conditions [129]. Determining the exact point at which the process reaches steady-state is not essential. A tutorial by Rhinehart discusses issues with SSD in a noisy process [130].

Many methods listed in Rhinehart's tutorial use moving windows as a basis for the analysis. The general method is to use linear regression to find the slope of a data window. If the slope is below a certain threshold, the system is assumed at steady state [131]. However, noisy processes decrease the accuracy of the linear regression and subsequently the detection. Another window based method declares steady-state if the standard deviation of the window falls under a set threshold. This has been used in the assessment of helicopters engine flight data [132] but requires the standard deviation expected from normal operating conditions to be known beforehand. Another method is to use two rolling adjacent windows and compare the statistics in each window. The statistical tests can be a t-test [133] or an f-test. Jiang uses a wavelet method to reduce noise in the data before analyzing a window [134]. Cao proposed an R-statistic test that calculates a ratio of variances to determine steady-state [135] and has been shown to be useful in process optimization [136]. The tuning of this method using three filter factors has been extensively studied [137, 138].

In the next section, the F-t-Pj-RG method is described and shown to be suitable for detecting steady-state on the functional forms required for KMC data

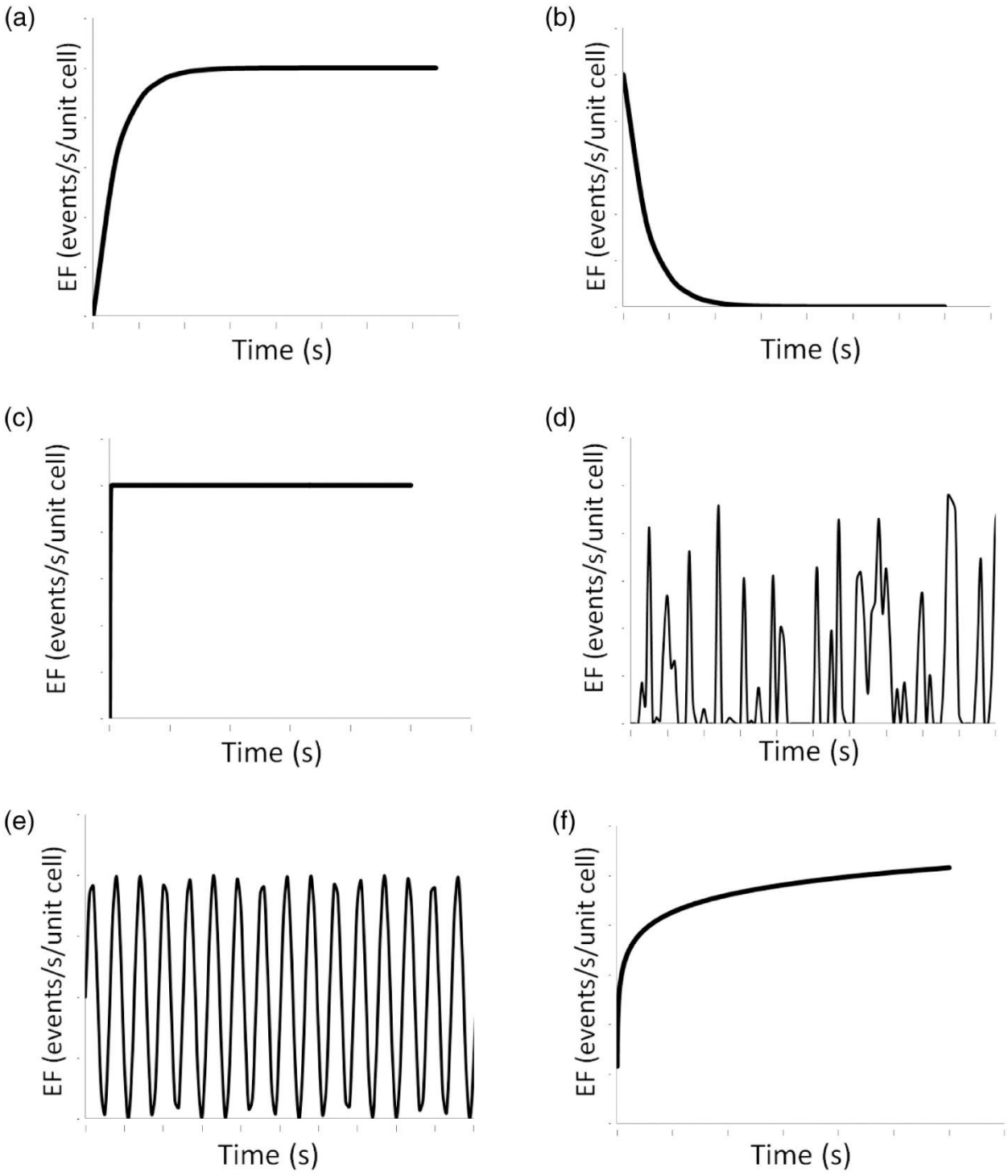

Figure 3.1: *There are 6 trends that the steady-state algorithm must be able to handle: 1) Raising exponential 2) Falling exponential 3) immediate steady state 4) Spikey data 5) undulating steady-state and 6) infinitely raising.*

The types of trends that can been anticipated from KMC data are shown in Figure 3.1. Each of the example trends in Figure 3.1 require a finite time before steady-state can be detected, with the exception of Figure 3.1 f (which never reaches steady-state due to being infinitely rising). There can be an initial warm-up period, as seen in Figures 3.1 a-c. Thus, SSD methods for these types of systems must be able to exclude or get past the warm up period, preferably while preserving computational effort by not performing the full SSD test during the computational time. To exclude the warm up period, the common practice of using finite data windows (subsets of the data) is used in the F-t-Pj-RG method. The F-t-Pj-RG method includes three statistical tests: a F-test, a t-test, and a projection test on j sequential windows with an oscillating-slope restriction when $j \geq 2$. During the F-test and the t-test, adjacent data windows are statistically compared to see if the variance of the system has statistically converged (F-test), and then to see if the mean of the variable of interest has statistically converged (t-test). Information on the F-test for equality between two variances and t-test for equal means can be found in standard statistics textbooks[139, 140]. The F-test serves as the primary convergence test (to detect exiting of warm-up), while the t-test also serves to confirm the convergence of the system while also confirming that the prerequisites for a converged mean SSD are met. As the F-test is the primary convergence test, anytime it fails there is a large shifting of the windows to later data (here, the shift is by the size of one full window width), which reduces the number of times that statistical tests are run on the data prior to exiting the warm-up period, and thus reducing computational time. The t-test and the oscillating-slope projection test are also not run when the F-test fails. Each time the F-test fails, the windows are not only shifted, but also grown by one point. Thus, both shifting and growing occur for each failure of the F-test. After the F-test has been passed one time, the system is assumed to be sufficiently converged to likely be past the warm-up. Next, the t-test is performed on these

data windows and if it passes the oscillating-slope, projection test (Pj) is then performed. The oscillating-slope projection test consists of checking that the slopes of j adjacent windows are within tolerance (see below), and also that there is at least one slope oscillation when $j \geq 2$ (see below). This projection test ensures that a user-defined tolerance of steady-state is met (i.e., maximum rate of change allowed for steady-state to be declared). If either the t-test or oscillating-slope projection test are failed, the first of the pair of adjacent windows are rolled and grown by one point: the rolling corresponds to a horizontal shift with no change in the number of points, while the growing by one point indicates an increase in the number of points per window, N. The ordering of the tests (F-t-Pj) is not only an appropriate ordering for efficiency, but also for having meaningful confidence intervals. This confidence interval of the t-test is only meaningful if the variance is converged. The confidence interval of the projection test is also only meaningful if the residuals are appropriately distributed (and this sequence of the tests thus avoids cases that do not match those prerequisites). It is worth recognizing that the strategy of starting with a small window and growing it upon test failure should eventually achieve SSD: there is no upper limit for a window size that is suitable for SSD, though larger windows do have added computational expense (require more data). Thus, the strategy is to start with a small window and grow it slowly once the warm-up period has been exited. No noise filtering or removal of underlying trends occurs in this method, and none were used in this work, though in principle such data manipulations could be applied prior to or concurrently with the F-t-Pj-RG method. The three tests and their purposes are as follows:

3.1.1 Stages of the tests

1. F-test to check that the weighted standard deviations of the two windows are statistically equal (i.e. the null hypothesis is that $\sigma_{W1} = \sigma_{W2}$)
2. Two sample t-test that checks that the weighted means of each window are statistically equal (i.e. the null hypothesis is that $\mu_{W1} = \mu_{W2}$)
3. A projection test that checks that a projected value in the future will fall within a set tolerance that indicates the rate of change in the system is so small the system could be at steady-state. The null hypothesis is that $|\hat{y} - \mu| \leq \Delta Y_{pass}$.

95% confidence intervals are used for the F-test and the two-sample t-test to ensure that the data statistics have converged prior to attempting the projection test. A distinction is drawn here between the "F-t-Pj test" and the "F-t-Pj-RG method": the F-t-Pj test refers to the requirement that each of the 3 tests are passed by the final data window, while the F-t-Pj-RG method refers to the method (algorithm) which involves rolling and growing the windows as described above until a steady-state is reached that can pass the F-t-Pj test (i.e., when all three portions of the F-t-Pj test are passed at the same time).

While the F-t-Pj-RG method does not require empirical choices, it does require a user defined definition of steady-state, as the tolerances for steady-state must be system specific and application-specific (e.g., changing by less than 0.1 moles in 1 hour might be acceptable for one application but changing by less than 0.1 moles in 1 year might be needed for another application). The projection test requires two user inputs, the length of the projection and the passing threshold. The length of the projection is user-defined either by explicitly defining x* as a given or by the multiple of window lengths, ζ, between $x^*$and the center of the data window, such that:

$$x^* = \zeta * (x_n - x_o) + \bar{x}, \quad (1)$$

where x_o and x_n are the starting and ending index of the data window. The passing threshold for each projection test, ΔY_{pass}, is the maximum change (y-deviation) allowed for the projected value of the dependent variable at x*, $\hat{y}$, in relation to the sample mean. Such that passing a single projection test requires:

$$\left|\widehat{\beta_1}(x^* - \bar{x})\right| + \varsigma_\alpha \leq \Delta Y_{pass} \quad (2)$$

Where $\left|\widehat{\beta_1}(x^* - \bar{x})\right|$ is the change in the dependent variable from the projection and ς_α is the confidence interval given by $\varsigma_\alpha = t_{(1-\alpha),N} SE_{\hat{\mu}}$, where α is the level of confidence (e.g. 0.95 for the 95% confidence interval). The confidence of the test is controlled by the *t* value that follows the t-distribution. For this paper, the projection test is set to have 95% confidence intervals. The passing threshold ΔY_{pass} can be set as either an absolute threshold (i.e., a scalar), or a relative threshold. Using a threshold relative to the standard deviation can be used to set a confidence interval, and is convenient for the present work because SSD will be achieved with similar numbers of points between different noise levels, once steady-state is reached. A relative threshold is used and set the threshold to $\Delta Y_{pass} = 4s_y$. The choice of a multiple of 4 in this work was based on convenience as it corresponded to a tolerance level that resulted in window sizes sufficiently small for the data sets used. In practice, the tolerance must be set based on the user's application. When an absolute tolerance is used, the absolute tolerance must still be converted to a relative tolerance to calculate confidence intervals for the projection test (though the relative tolerance conversion could be done on-the-fly). A practical implication of Eq. 2 is that steady-state detection for future times that are much larger than the size of the window requires very small noise to signal ratios.

Note the projection test does not check if the calculated slope equals zero, but rather that the slope falls below a user defined threshold, within a certain confidence interval: the threshold

should be set to the rate of change that would be small enough to be considered steady-state for that application.

3.2 Testing of F-t-Pj-RG Method

The F-t-Pj-RG method was applied to the sample data sets with the functional forms (shown in Figure 3.1). The data sets were generated with the base functions plus noise, and with either "even spacing" or "random spacing" along the *x*-axis. In our testing, different levels of noise were applied to each of the data trends (noise levels of 0.01, 0.2, and 0.6, as will be explained below). The (*x*,*y*) data were generated as follow:

- The x-spacing between adjacent points for "even spacing" was always 1.0
- The x-spacing between adjacent points for "random spacing" was set by r_s: where $0 < \boldsymbol{r_s} < 1$, with the values of r_s picked with uniform probability within that range, and a fresh picking of $\boldsymbol{r_s}$ for each space between data points.
- The noise levels (*n*) were applied additively to each of the continuous base functions – all cases except for spikey data and KMC data as: $y = f(x) + wr_n\,, where\ 0 < \boldsymbol{r_n} < 1$. The distributions of the noise levels were either normal or uniform. Knowing the distribution and noise level, the constant *w* is calculated such that the standard deviation of added noise corresponds to the noise level *n*. That is, for a noise level of *n* =0.6, the function wr_n has a standard deviation of 0.6.
- The y data for "spikey" data has been obtained by first setting a range between 0 and the maximum bound (y_m). The output value is calculated using the form: $y = y_m r_n\,, where\ 0 < \boldsymbol{r_n} < 1$. The random number generation being strictly uninform.

Importantly, this generation method would not produce data with a standard deviation equal to the maximum bound y_m.

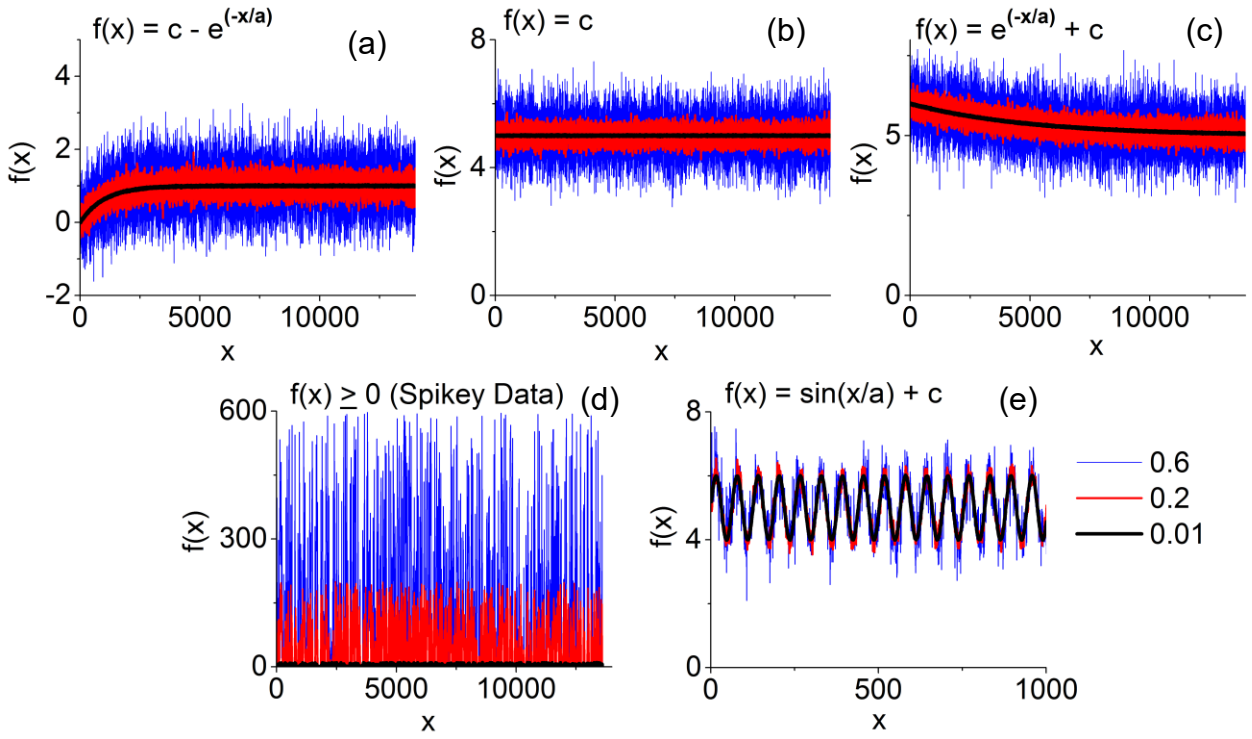

***Figure 3.2**: Comparison of the noise levels applied to the functional forms that reach steady-state. The legend indicates the colors associated with different values of rn.*

The algorithm was tested on the five functional forms shown in Figure 3.2, as well as an infinitely rising function and KMC data. Figure 3.2 shows the magnitude of the three noise levels tested relative to the base functions. An appropriate SSD algorithm would be able to perform well for each of the noise levels and functions. A logarithmic function that never reaches steady-state was also considered, to test the case that the algorithm *should not* detect steady-state. The different

base functional forms tested are as follows, with noise or fluctuations added upon each base functional form prior to testing, where in each case “a” and “c” are constants:

1. ln(x*a) + c
2. c-exp(-x/a)
3. c
4. c_+ exp(-x/a)
5. x +r_1*a > 0 (see text for details)
6. sin(x/a) + c

In the following subsections, the F-t-Pj-RG method has been applied to each of the noted functional forms. The base testing for the following subsections requires the projection test (Pj) (i.e. the final test to trigger steady-state) to pass j consecutive times (j=1, 2, or 3 in the current work) with oscillating-slope (no oscillation is required if j=0 or j=1). In all cases, the predicted value of the dependent variable during projection tests are calculated with $\zeta = 10$ so that comparisons can be made even between different functional forms. The images shown in the below sections contain results for 0.6 Gaussian noise levels (the results for the lower levels of noise were qualitatively similar). For each of the functional data sets, the average window size and the average number of steps before SSD was detected are reported based on 10 SSD runs. The error bars are reported as the standard error of the average values, based on the sample size of 10. Given that the errors of the SSD are not normally distributed, the standard error can be regarded as an order of magnitude estimate of the error. We first start with the infinitely rising case where steady-state should not be detected, followed by the cases where steady-state should be detected.

3.2.1 Application of the F-t-Pj-RG method to Different Functional Forms

a) Infinitely Increasing, f(x) = ln(x*a) + c

The purpose for testing the function *ln(x*a) + c* is to ensure that the algorithm will not erroneously report steady-state in an infinitely rising data set. This increases the confidence in the accurate detection of steady-state in the following sections. In the tests being run here, the SSD attempt is allowed to run until steady-state is detected or the data set reaches a pre-determined cut-off position along the x-axis. If this cutoff position is reached, it is assumed that the initial conditions are not capable of producing a steady-state in the time scale (or x-axis measurement) of interest.

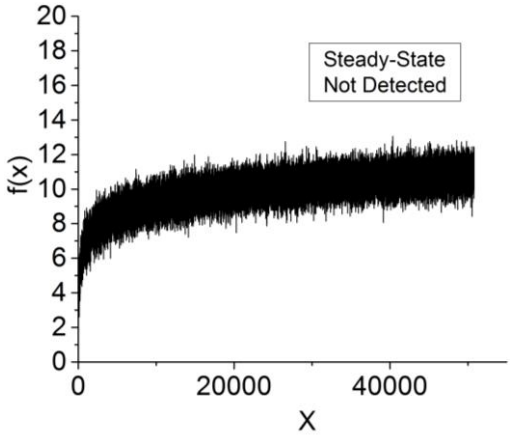

***Figure 3.3**: Applying the F-t-Pj-RG steady-state detection algorithm to infinitely rising data generated by ln(*a) + c + noise (0.6 noise level) did not detect steady-state.*

Ln(x) approaches infinity as *x* goes to infinity, though the approach to infinity becomes increasingly gradual as *x* increases. As such, this is not a true steady-state and thus, a steady-state detection algorithm should be capable of differentiating such a trend from steady-state. As seen in Figure 3.3, the currently implemented algorithm did not detect steady-state in data generated with a ln(x*a) + c with a=1 and c=0 for any of the noise levels, or spacing tested, within 50,000 data points. In fact, the t-test rarely passes for this data set, so the projection test rarely occurs. This

suggests that the window sizing methods used here (similar to that of other previous works) aid in avoiding false SSD detection.

In general, the level of noise can overwhelm even an infinitely rising function (for a given window size) such that steady-state could be falsely detected. The tolerances required are application specific, so it is necessary that the user appropriately defines the value of ΔY_{pass} for a given projection distance, such that the projection test is effective at excluding such false steady-states.

***Table 3.1**: The average number of data points in each window and the average number of steps to steady-state from 10 separate runs of the F-t-Pj-RG method, for ln(1*x) + 0. Data sets with Gaussian and uniform noise (level 0.6), random and uniform spacing along the x-axis, and j values of 1, 2, and 3 were tested.:*

Type of Noise	Type of Spacing	j value	N_F	Detected After
Gaussian	Random	1.0	Not Detected	Not Detected
		2.0	Not Detected	Not Detected
		3.0	Not Detected	Not Detected
Gaussian	Even	1.0	Not Detected	Not Detected
		2.0	Not Detected	Not Detected
		3.0	Not Detected	Not Detected
Uniform	Even	1.0	Not Detected	Not Detected
		2.0	Not Detected	Not Detected
		3.0	Not Detected	Not Detected

b) Rising Exponential, f(x) = c - exp(-x/a)

A rising exponential trend is a common trend for chemical kinetics, and an example is shown in Figure 3.4. In our tests, SSD occurred successfully in the asymptotic region of the functional trend. This functional form tests the capability of the F-t-Pj-RG method to successfully exit a warm-up period that may exist within KMC data. The point at which steady-state has been detected (for one particular trial) is shown in Figure 3.4. It is clearly seen that the data windows have surpassed the warm-up period and reached the asymptotic region. The average number of data points in the data windows, and the average number of steps to steady-state across 10 runs are shown in Table 3.2for the largest noise level tested.

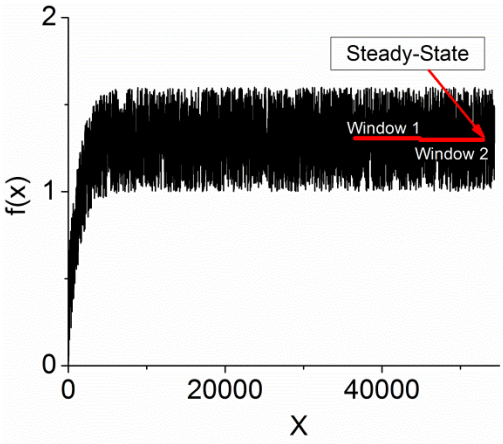

***Figure 3.4**: Applying the F-t-Pj-RG steady-state detection algorithm to data generated by a rising exponential (0.6 noise level) detected steady-state after the transient period. An illustrative example is shown with the windows at which steady-state is detected in red.*

***Table 3.2**: The average number of data points in each window and the average number of steps to steady-state from 10 separate runs of the F-t-Pj-RG method for 1 - exp(-x/1000). Data sets with Gaussian and uniform noise (level 0.6), random and uniform spacing along the x-axis, and j values of 1, 2, and 3 are shown.*

Type of Noise	Type of Spacing	j value	N_F	Detected After
Gaussian	Random	1.0	538 +/- 166	2050 +/- 665
		2.0	892+/- 145	7083 +/- 968
		3.0	901 +/- 145	8323 +/- 1102
Gaussian	Even	1.0	554 +/- 197	2118 +/- 789
		2.0	845+/- 1871	6627 +/- 1178
		3.0	969 +/- 236	9089 +/- 1983
Uniform	Even	1.0	497 +/- 163	1888 +/- 651
		2.0	624 +/- 166	4661 +/- 978
		3.0	678 +/- 159	7340+/- 948

c) Straight Line, f(x) = c

The functional form for a straight line with noise is representative of a KMC data trend that would correspond to a nearly immediate steady-state. The detection of steady-state and the associated data windows for one particular trial are plotted in Figure 3.5. The average number of data points in the data windows and the average number of steps to steady-state across 10 runs are shown in Table 3.3 for the largest noise level tested.

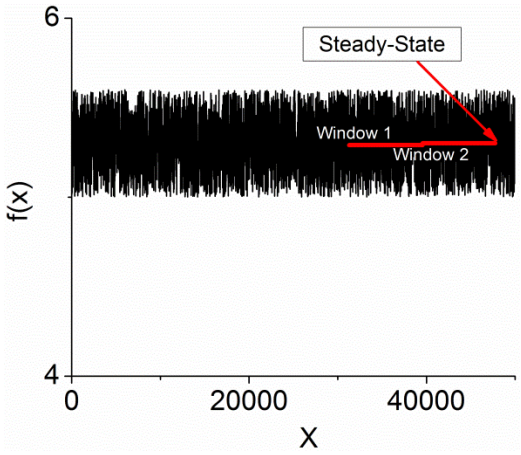

***Figure 3.5**: Applying the F-t-Pj-RG steady-state detection algorithm to data generated by a flat line (0.6 noise level) detected steady-state. An illustrative example is shown with the windows at which steady-state is detected indicated in red.*

***Table 3.3**: The average number of data points in each window and the average number of steps to steady-state from 10 separate runs of the SSD algorithm, for f(x) = 5. Data sets with Gaussian and uniform noise (level 0.6), random and uniform spacing along the axis, and j values of 1, 2, and 3 are shown.*

Type of Noise	Type of Spacing	j value	N_F	Detected After
Gaussian	Random	1.0	347 +/- 22	1286 +/- 86
		2.0	622 +/- 36	6655 +/- 784
		3.0	746 +/- 74	8688 +/- 1191
Gaussian	Even	1.0	337 +/- 11	1246 +/- 45
		2.0	561 +/- 40	5632 +/- 915
		3.0	633 +/- 45	6938 +/- 845
Uniform	Even	1.0	341 +/- 22	1265 +/- 87
		2.0	684 +/- 57	5520 +/- 572
		3.0	728 +/- 46	6855+/- 610

d) Falling Exponential, f(x) = c + exp(-x/a)

The falling exponential functional form is another case where there exists a distinctive warm-up period at the initial stages of the data in the manner expected for chemical kinetics, and thus, it is an important test case for the effectiveness of the SSD algorithm applicability to KMC generated data. As with the rising exponential, the algorithm successfully exited the warm-up period and detects steady-state in the asymptotic region of the generated data for all noise levels, spacing, and j values. The data windows and the point at which steady-state was detected (for one particular example) are shown in Figure 3.6. The average number of data points in the data windows and the average number of steps to steady-state across 10 runs are shown in Table 3.4 for the largest noise level tested.

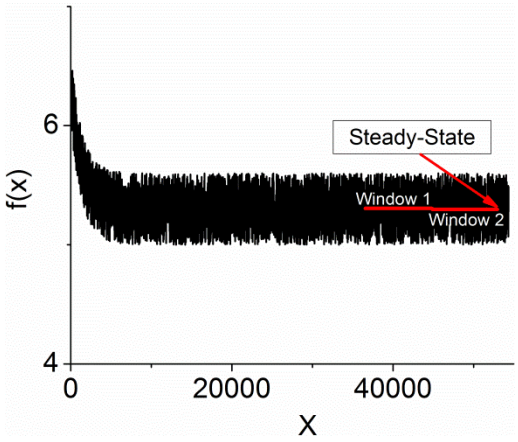

Figure 3.6*: Applying the F-t-Pj-RG steady-state detection algorithm to data generated by a falling exponential (0.6 noise level) detected steady-state after the transient period. An illustrative example is shown with the windows at which steady-state is detected in red.*

Table 3.4*: The average number of data points in each window and the average number of steps to steady-state from 10 separate runs of the F-t-Pj-RG method for f(x) = 5+exp(-x/5000). Data sets with Gaussian and uniform noise (level 0.6), random and uniform spacing along the x-axis, and j values of 1, 2, and 3 are shown.*

Type of Noise	Type of Spacing	j value	N_F	Detected After

Gaussian	Random	1.0	349+/- 18	1289 +/- 69
		2.0	3916 +/- 2262	24831 +/- 13510
		3.0	4141 +/- 2233	28864 +/- 13577
Gaussian	Even	1.0	377 +/- 19	1406 +/- 74
		2.0	2111 +/- 1596	12075 +/- 7962
		3.0	3751+/- 2119	24879 +/- 12584
Uniform	Even	1.0	1638 +/- 1302	6452 +/- 5209
		2.0	3094 +/- 1704	17338 +/- 8310
		3.0	3196 +/- 1687	22662 +/- 9672

e) Undulating, $f(x) = \mathrm{Sin}(x/a) + c$

The functional form for undulating data (wavelike) is another possible trend that could result from KMC generated data, and has autocorrelation. When such cases undulate around a mean value, the data would still be considered to be at steady-state. The data windows and the point at which steady-state was detected are plotted in Figure 3.7 (for one particular example, different from the function coefficients used in this work).

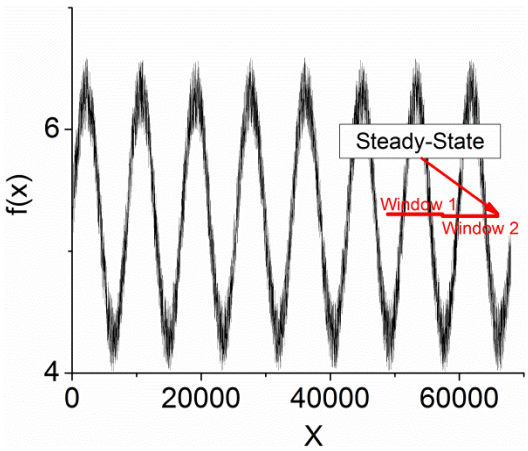

***Figure 3.7**: Applying the F-t-Pj-RG steady-state detection algorithm to data generated by a sinusoidal function (0.6 noise level) detected steady-state. An illustrative example is shown. For most cases, steady-state detection for sinusoidal data will encompass many periods.*

In the sinusoidal case, if a small data window is largely comprised of points that are near the maxima or minima of the curve, the slope would be close to zero. However, an appropriate rolling and growing window method, in conjunction with an oscillating-slope projection test, is unlikely to falsely detect steady-state in such a scenario. The windows will proceed to roll and grow across the data set until the window size will sample across one full period, and then further than one period. This behavior demonstrates the importance of the requirement to have the projection test pass at least twice, with oscillating-slope. The average number of data points in the data windows and the average number of steps to steady-state across 10 runs are shown in Table 3.5 for the largest noise level tested.

***Table 3.5**: The average number of data points in each window and the average number of steps to steady-state from 10 separate runs of the F-t-Pj-RG method for f(x) = sin(x/10) + 5. Data sets with Gaussian and uniform noise (level 0.6), random and uniform spacing along the x-axis, and j values of 1, 2, and 3 are shown.*

Type of Noise	Type of Spacing	j value	N_F	Detected After
Gaussian	Random	1.0	330 +/- 8	1220 +/- 34
		2.0	424 +/- 8	4437 +/- 270

		3.0	528 +/- 31	10974 +/- 1630
Gaussian	Even	1.0	317 +/- 5	1168 +/- 18
		2.0	431 +/- 19	6149 +/- 987
		3.0	480 +/- 23	10257 +/- 1844
Uniform	Even	1.0	320 +/- 6	1220 +/- 34
		2.0	451 +/- 19	6836 +/- 824
		3.0	519 +/- 24	11559 +/- 1165

f) Spikey Data, $f(x) \geq 0$

The spikey datasets are representative of rare or slow events in KMC simulations. In this scenario, it is possible that no events of a particular type occur in a single snapshot. Since all reactions in a network have to be unchanging for the system to be declared at steady-state, the SSD algorithm must be able to handle spikey data. Especially since these processes are likely to be interpreted as a departure from steady-state by many algorithms. The data windows and point of detection for one example are plotted in Figure 3.8.

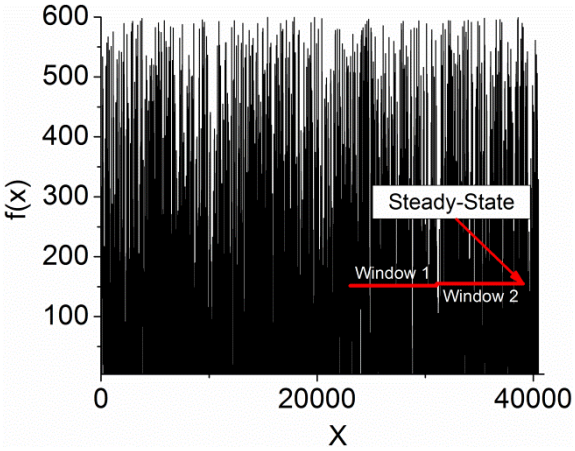

***Figure 3.8**: Applying the F-t-Pj-RG steady-state detection algorithm to data generated by a rising exponential (maximum amplitude of 600) detected steady-state. An illustrative example is shown with the windows at which steady-state is detected indicated in red.*

The average data window lengths and average points of steady-state detection are listed in Table 3.6. The behavior for spikey data is qualitatively similar to that of the straight-line case.

***Table 3.6**: The average number of data points in each window and the average number of steps to steady-state from 10 separate runs of the F-t-Pj-RG method for Spikey Data that had a maximum amplitude of 600.*

Type of Noise	Type of Spacing	j value	N_F	Detected After
None	Random	1.0	339 +/- 9	1283 +/- 36
		2.0	614+/- 52	5850 +/- 803
		3.0	791 +/- 80	8998 +/- 1135
None	Even	1.0	346+/- 12	1286 +/- 48
		2.0	506 +/- 34	4222 +/- 476
		3.0	590 +/ 54	6019 +/- 639

3.2.2 Discussion

Functional forms representative of the behavior of KMC data were tested. The F-t-Pj-RG steady-state detection method detected steady-state in each case (with the exception of the infinitely rising function), and successfully excluded warm-up (transient) periods at the beginning of data sets. Importantly, the algorithm was able to handle the following features of data: a) both evenly and unevenly spaced data, b) data with transient periods, c) discontinuous "spikey" data, d) data with fluctuations. The strategy used to exclude the warm-up period and eventually detect steady-state was to start with an initial window of N=100 (sufficient for initial statistical analysis) that is then subjected to rolling and growing until the F-t-Pj test is passed. This is similar to the strategy used by Núñez et al.[141]. Thus, there is no analytical estimate of what window size will be needed: the algorithm simply rolls and grows the windows until steady-state is detected. The asymptotic limit of the windows being infinitely far in time and infinitely large in size will ultimately satisfy any user-defined tolerance of steady-state. The algorithm simply proceeds until the tolerance is met.

It is not surprising that the algorithm can handle unevenly spaced data, as the spacing along the *x*-axis is accounted for in weighted standard deviations (for the F-test), weighted means (for the t-test), and weighted linear regression (projection test). Many existing algorithms assume a uniform spacing between the points as they are designed for looking at time series measurements taken at constant intervals. The ability to handle variable spacing is a strength of this algorithm because it can be used on data generated by KMC simulations with variable time-spacing.

The oscillating-slope test is one of the unusual features of the method. As shown for each data trend, higher values for j in the oscillating-slope projection test are harder to pass. The importance of performing the oscillating-slope projection test on more than one consecutive

window can be understood by considering a slowly rising monotonic function or the oscillating data trend. For these cases, the oscillating-slope and consecutive window tests prevent false-positives from cases where the slope is approximately zero (such as a crest or trough of the sin wave, or simply from a low slope or a fluctuation). Thus, cases with j=0 and j=1 should not be trusted (indeed, in the tests here, j=1 and j=0 sometimes passed during the transient period). However, increasing the number of consecutive attempts also increases the number of data points required. As such, a compromise between certainty and computational efficiency exists.

If one considers the possibility of extending the F-t-Pj-RG method to data with multiple dependent variables, you should recognize that for sufficiently large numbers of variables the F-t-Pj test will not return 'passing' for all variables at the same time (even when the system is at steady-state). While it is beyond the scope of this work to extend the F-t-Pj-RG method to multiple variables, a feasible approach is described for systems where the variances are not correlated for the different variables. The F-t-Pj-RG method could be applied to each variable independently, and run until the F-t-Pj test has been passed at least once for each variable. From that point, a number of data windows on the order of 10 adjacent data windows could be analyzed, and the observed percent chance of passing the F-t-Pj test could be calculated for each of the variables across those ~10 adjacent data windows to ensure that it is sufficient for the confidence level desired: passing for each of the ~10 adjacent windows, or 100% passing rates, are not needed -- only sufficient passing rates for the confidence level are desired. Alternatively, a method based on Šidák corrections or similar [125] could be used to soften the multi-variable test once each variable has passed individually. It should be noted that in practice, with the method presented here, the windows continue to grow when the F-t-Pj test is failed. This means that if an asymptotic steady-state exists, then eventually the passing rate will exceed that required for a particular confidence

interval (the passing rate does approach 100% in the limit of infinite window size, and thus the passing rate will eventually be sufficient).

3.2.3 Conclusion of F-t-Pj-RG Method

The F-t-Pj-RG method, a window based steady-state detection method, was developed and tested on a variety of potential data trends (functional forms) that could be produced by kinetic Monte Carlo simulations. The method relies upon applying the F-test, then t-test, and finally an oscillating-slope projection test (Pj) to successive data windows. The sampled data windows roll and grow until the standard deviation and mean of the data are converged (F-test and t-test). Importantly, the method works on spikey data, data with warm-up periods, data with fluctuations (sinusoidal), and data that is not evenly spaced. When all 3 tests are passed, the system can be said to have passed the F-t-Pj test, and is considered to be at steady-state.

3.3 Introduction of ppSSD

A steady-state (SS) is a state in which measurable variables of a system are 'constant' over time, which means their rate of change across time has a slope of zero. The term is meant to be more general than 'equilibrium' which can have more a specific definition depending on the field. Steady states are important in a wide range of applications, including the field of materials science [142], biology [143], queuing management [144], fault detection[145], etc. Steady state detection (SSD) has high importance in these fields, and is also an often required subtask in the field of simulations. Often, a goal of simulations is to reach a steady-state and then terminate the simulation to analyze the data associated with the steady-state. In general, real systems do not have slopes that are truly zero, instead real systems have finite nonzero slopes due to two sources: (a) noise and fluctuations (b) gradual but very small changes that can still be approximated as constant. Thus, identifying a true SS (with slope zero) in a real system is not possible with 100% certainty, and instead the goal when analyzing real data is actually to seek a statistical steady-state (sSS). A sSS is defined as the system having no change according to a *specified level of change tolerance* for a *specified duration of time*. Thus, sSS is defined only in the context of chosen values for these two variables.

In some cases, when there is no noise or oscillation, finding a steady-state is as trivial as detecting when the slope is sufficiently near zero, but it can become more difficult to identify the steady state with noisy processes. Crucially, when there are noisy processes, SSD can be inconclusive -- purely due to the need to collect more data points to obtain sufficient statistics for SSD. Experimentalists and computationalists then face a dilemma: how many more points must be collected? This question is important to answer to determine whether it is even feasible to collect

the number of points required for SSD. This work provides a method to answer the question of how many points are required. Since having the number of points required is a pre-requisite for steady state detection, we will refer to the concept in the present work as “ppSSD” for ‘predicting the pre-requisite to steady state detection’. This is a central concept which most readers are not familiar with and so it must be emphasized: until a sufficient number of points have been acquired (i.e., until the data length is sufficiently long), SSD is not possible. The objective of ppSSD is to determine how many points are required before even considering SSD.

One scenario in which ppSSD would be used is if the user is running thousands of simulations of a process with each simulation being under unique and slightly different conditions. These conditions can change the noise behavior of the process such that the length of data required for SSD is different for each simulation. In this scenario, ppSSD could be accomplished with our method by reading an initial set of data from early in a simulation (for a specific set of conditions) and return the minimum number of points needed to attempt SSD (for that specific set of conditions). The required number of points for SSD would be unique for each set of conditions, but by using ppSSD the user can ascertain whether they have a sufficient number of points for SSD to be feasible. More importantly, if a simulation has an insufficient number of points, ppSSD provides the information of how many more points are needed.

The typical scenario would be that during data collection (either from simulation or experiment), the user would use ppSSD to predict how much data they must collect for SSD. Two outcomes are imagined from using ppSSD: If the required data length for SSD is feasible, the user would continue collecting data. Alternatively, if applying ppSSD predicts a required amount of data collection that the user considers unfeasible (i.e., would require too long of an experiment or too many simulation hours), the user can terminate data collection and save resources (whether

computational or experimental).

Presented here is a ppSSD method that can predict the window size required for SSD to be possible (the method returns the number of points required). The method requires a user specified change tolerance (for how much the mean can vary within a specified amount of time) and a specified amount of time to remain within that tolerance. The method works for arbitrary confidence intervals: the user defines the required probability for being within the change tolerance after he specified amount of time. The method is based upon derivations that begin with a φ-relation that was found, which relates the slopes of steady-state data to their inherent statistics. The method only requires reading a small initial window to gather the system's inherent statistics, and then ppSSD can be performed using our relations and algebra. We present the method, then show with a simple SSD test that our initial window ppSSD method correctly predicts the number of points that will be required for SSD, for a variety of noise distributions.

3.3.1 Statistical Steady State Derivation

The starting point in the derivation is recognizing that at a statistical steady state, the rate of change (or slope) is approximately zero, based on a specified level of change tolerance for a specified time (and a change over time is a slope). The data is assumed to consist of a series of data points (x,y), with noise. In statistical steady state, the deviations from the mean that come from noise must be considered when analyzing the change tolerance. In our formalism, we first describe the case where the noise is normally distributed according to a Gaussian distribution. For the normal distribution, it is accepted that 68% of the values will fall within one standard deviation σ of an unchanging mean μ , $(\mu - \sigma, \mu + \sigma)$. However, we show that even though the equations

being used are derived for a normal distribution, this method still works well for other noise distributions without further corrections.

a) Linear Regression and φ-relation for Steady-States

The ability to predict the output of linear projection is essential to steady state detection. The null hypothesis is that the process is at steady-state unless there is sufficient evidence to the contrary. In this case, when the calculated slope of a data window, defined as b_1, is outside the range expected from a steady-state process. Linear regression provides an estimate of the slope, though the noise in the process causes regression to "see" trends that are not there. So even if the true slope is zero, regression will still return a non-zero value. However, we find that the distribution of possible non-zero slopes is predictable, and that this distribution can be compared to the slopes from real datasets. The distribution is depicted in Figure 3.9.

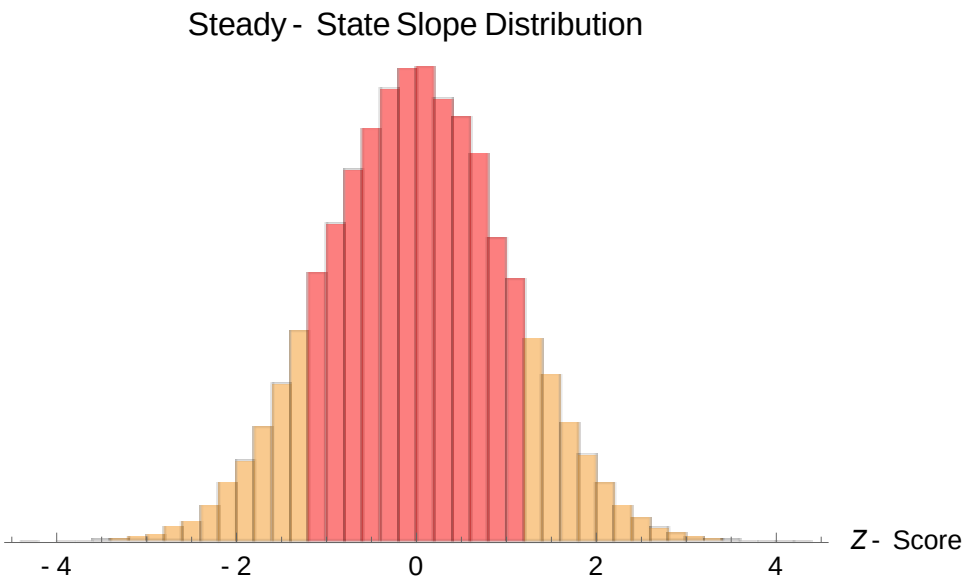

***Figure 3.9**: Distribution of slope of a steady-state data window. The x-axis is the number of S_{b1} away from the mean. It follows a normal distribution. The red region notes the region where 68% of the slopes are expected to fall, bounded by the 68% confidence interval.*

We can find the standard deviation of the distribution of slopes S_{b1} , which are centered around a mean slope of zero when in a steady-state. Thus we determine the probability *P* that the slope of a steady-state data window will be within certain confidence intervals. The threshold desired for a certain probability *P* is computed by the following equation:

$$b_{1,th} = Z_P S_{b1} \tag{3}$$

Where $b_{1,th}$ is the slope value associated with a threshold that is Z_P standard deviations away from zero. The term Z_P is related to the probability P that linear regression will not return a value above $b_{1,th}$ if the data represents a steady-state process. A two-tailed Z-table provides the value of Z_P for a given value of *P*. Conventional two-tailed Z-tables are typically constructed for a normal distribution, though conventional two-tailed Z-tables should be sufficient for other distributions as well, as will be shown.

For a SS detection free from outliers, the best fit slope can be intuitively related to the aspect ratio of the data, which can be defined by the ranges of the x and y data such that $b_1 \propto {\Delta Y_w}/{\Delta X_w}$. The range of x is simply the data window length Δx_w (the difference between the first x value in the window and the last x value in the window). Due to outliers and noise, ΔY_w can significantly distort the aspect ratio, and the sample standard deviation s_y is thus used instead to define an effective aspect ratio. The slope is expected to become closer to zero as the aspect ratio is increased by adding additional data points, N, in the data window. The results of linear regression outputs are thus expected to have a relation with the values s_y, Δx_w, and N associated with a data window. Based on this intuition of what affects a linear regression, the three terms were combined into a single term φ, which could be a good statistical indicator of the regression

output at steady-state and our derivation and tests show this to be the case. The formula for φ is shown below:

$$\varphi = \frac{s_y}{\Delta x_w \sqrt{N}} \tag{4}$$

The standard deviation S_{b1} of the slopes returned by regression on a steady-state data window was found to have a linear relationship with the term φ:

$$S_{b1} = \varepsilon\varphi \tag{5}$$

We will refer to Eq. 5 as the **φ-relation**, where the variable ε is a constant, and its value was determined to be $\varepsilon_N = 3.4633$ in this study, as shown in the next section. Based on our conjecture and our derivations, Eq. 5 should hold true regardless of the step size, noise level, or average value in the datasets: φ depends only on the three variables s_y, Δx_w, and N. As will be shown, this means that ppSSD based on the φ-relation relies only on the number of points and on inherent statistics of the system (i.e., the standard deviation s_y and average x-distance between points $<\Delta x_i>$). Given these three characteristics from an initial data window, we can predict the maximum magnitude of the slope found from linear regression, using the φ-relation and the null hypothesis that the series is at a steady-state. This in turn enables us to perform ppSSD, by answering the question of how many points will be needed for SSD. As will be seen, this method is very accessible. Using the equations derived using the φ-relation as a base, users are able to apply our method using solely algebra, and it is applicable to many types of scenarios.

To obtain the value of ε and show that Eq. 5 is valid, several series of (x,y) values emulating steady-state behavior were generated. The goal being the ability to sample steady-state

data windows with different φ values. The y-value is the output of a function of x with added random noise in the form:

$$y = f(x) + noise \quad (6)$$

In this case the function is a perfectly flat line $f(x) = constant$. The noise level is set to give a certain standard deviation s_y to each data series. The random number generator used is a function from Python. The spacing between each point Δx_i, where $\Delta x_w = \Delta x_i N$, is a constant that is varied to ensure that not every data series will have the same ratio of Δx_w and N. In the end, the S_{b1} for 120 different φ values were found. The combination of characteristics, s_y, Δx_w, and N to get each φ are listed in Table 3.7.

Table 3.7*: Range of each characteristics that is inputted into window generator and total number of unique combinations of s_y, Δx_w, and N.*

Characteristics	N	Δx_w	Sy or 0.5δ **
Possibilities	[100,200,300,400,500, 600,700,800,900, 1000]	[10 x N, 100 x N]	[0.33,0.66,1.0,1.5,2.0,4.0]
# of Possibilities	10	2	6
Total # Combinations: 120			

**For data series with normally distributed noise, the noise distribution has a width related to s_y with an infinite tail on the distribution. For uniformly distributed noise, the maximum y-offset from the mean is given the symbol δ (thus a data series where 0.5δ = 2.0 has a uniform noise distribution with 4.0 as the maximum y-offset from the mean.

During analysis of the set of generated series, a number of (φ, S_{b1}) points were gathered. First, the slopes of 1000 windows of the same φ were collected and the mean slope $\langle b_1 \rangle$ was calculated. Since these windows had a base function of a flat line with noise on it, the aggregate set of windows had a value of $\langle b_1 \rangle \sim 0$. Then, using the same 1000 data windows, the standard deviation of the slope S_{b1} is calculated to make a (φ, S_{b1}) point. Some of the points had the same value of φ but are created from analyzing a set of windows with different s_y, Δx_w, and N characteristics. Linear regression was performed on the large set of (φ, S_{b1}) points to obtain the value of ε reported. This regression is shown in Figure 3.10.

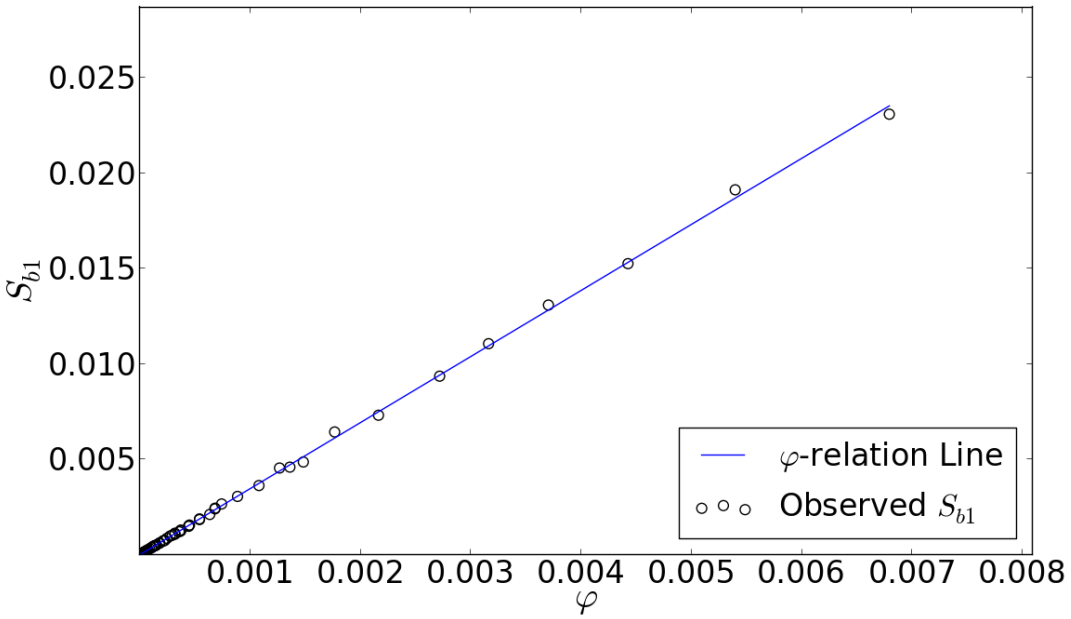

***Figure 3.10**: The S_{b1} returned by linear regression performed on a data window with a given φ*

The linear relationship from the φ-relation , Eq. 5, relates S_{b1} to φ. The linearity of this relationship is shown in Figure 3.10. 120 different φ values were investigated over a wide range of s_y, Δx_w, and N values for datasets with normal noise distributions (see Table 3.7 for details). Each point in Figure 3.10 represents a unique combination of s_y, Δx_w, and N from Table 3.7, and

each point was obtained from averaging 1000 data windows for that unique combination. It is worth noting that while many of the points have similar φ values, their respective window characteristics s_y, Δx_w, and N vary widely (neighboring points in the line may have values of s_y, Δx_w, and N that vary by one order of magnitude or more) – this shows the strength of using φ as a statistical indicator of S_{b1}. From this data with normally distributed noise, the constant ε was obtained from a linear fit, yielding a value $\varepsilon_N = 3.4633$. The same procedure was then applied to data sets with uniformly distributed noise and an equivalently broad range of s_y, Δx_w, and N (see Table 3.7), yielding a value of $\varepsilon_U = 3.4648$ -- which does not differ significantly from the value obtained from the data with normally distributed noise. This shows that not only is the φ-relation more general than just for data with normal noise distributions: this further shows that the same value of $\varepsilon = 3.46$ is sufficient to describe the relationship between S_{b1} and φ for both normal and non-normal (at minimum for uniform) noise distributions.

3.3.2 ppSSD Tests Based on the φ-relation and ppSSD Equations

Projection Test

As described in the introduction, the concept of a sSS requires a system response to remain within a y-scale tolerance for a specified length of time (i.e., distance along the x-axis). Our ppSSD will thus be measured against a projection test which matches this restriction: that y-values for a projected future-time would remain within a specified tolerance. There are more sophisticated methods for SSD, but the projection test directly tests the definition of sSS, and is compatible with conventional statistical confidence limits, so it is sufficient for our purposes. The projection test starts with calculating the slope of a window of (x,y) points that are scattered around an average x-position $\bar{X}$ and mean y-value μ. In order to pass, the projected change in y over distance $(X^* - \bar{X})$

must be less than a set threshold ΔY_{pass}. The projected y-value, $\hat{y}$, at a specified future position, X*, is given by:

$$\hat{y} = b_1(X^* - \bar{X}) + \mu \tag{7}$$

Here, b_1 is the slope found by performing linear regression on a data window. If the predicted value $\hat{y}$ falls consistently within the specified y-tolerance of $\mu - \Delta Y_{pass} \leq \hat{y} \leq \mu + \Delta Y_{pass}$, then the data windows are considered to be at steady-state. This test can also be described with the following inequality:

$$|b_1|(X^* - \bar{X}) \leq \Delta Y_{pass} \tag{8}$$

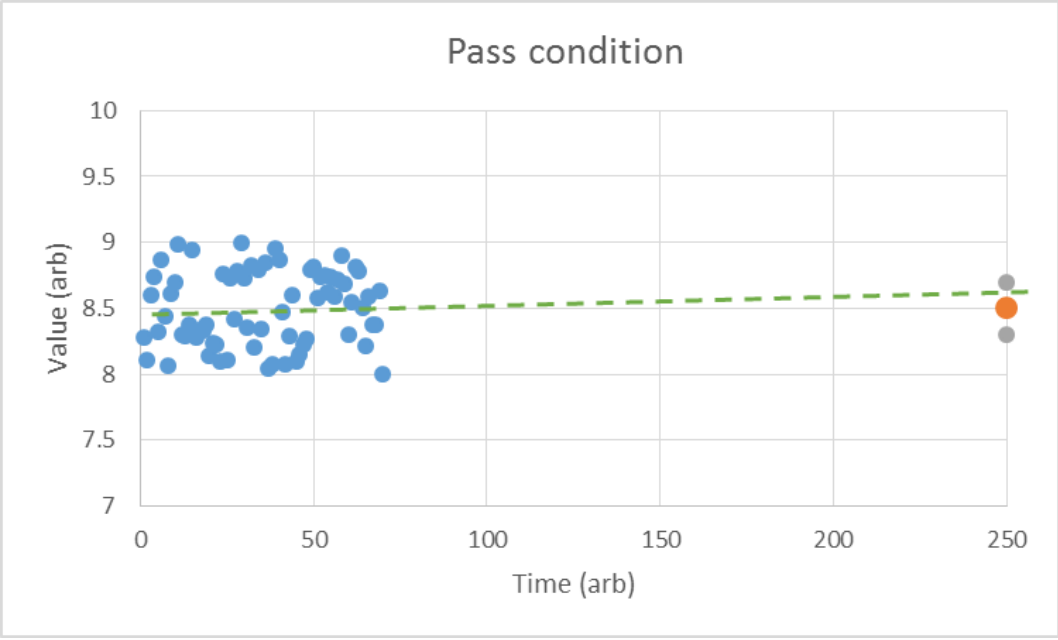

Figure 3.11: Visualization of the pass condition. The blue points represent the data window analyzed. The dotted green line is the regression slope. The orange dot is the sample mean of the data window. The regression line must pass between the orange dot and the gray dots. The distance between the orange and gray dots are ΔY_{pass}. The length of the projection is X^*.

A derivation of Eq. 8 is provided in the Appendix A.1. A reader is encouraged to remember at this point that in real data there can only be a *statistical* stationary-state that is detectable, and therefore statistical tolerances are a *required* parameter (typically user defined). An important aspect to consider is that, due to noise, a system that is (or is not) at steady-state will still have a finite probability of passing/failing an SSD test. In essence, this is due to error in estimating the underlying rate of change in the system. This error manifests itself within the regression slope calculation, and can be reduced by collecting additional data points, which has the effect of reducing the magnitude of the average slope returned from regression if the system is truly at a stationary-state. The ppSSD method estimates the necessary window size for a truly stationary-state to pass an SSD test within a specified probability (e.g., what window size would be required for the system to have a 95% chance of passing SSD if the system were truly at SS). With the φ-relation derived here, ppSSD can be performed to determine the required window size to achieve SSD in various situations.

In general, the projection distance can be described either by a fixed position, X^* or by a fixed multiple of the initial data window length, ζ. The threshold ΔY_{pass} can either be set at a scalar value (Fixed / Absolute) or set to being a multiple of s_y (Relative). Table 3.8 lists the four cases under which the projection test can be used, based on how the projection length and threshold are expressed. We will show that Case 4 is a special case where the inherent statistics of the system do not need to be known to preform ppSSD. Below the relevant ppSSD equations are presented, and examples for these four cases will each be presented in the body of this work.

***Table 3.8**: Cases of Possible Constraints for Projection Test*

Cases	ΔY_{pass}	Projection To:
Case 1	Fixed / Absolute	X^*

Case 2	Relative to s_y	X^*
Case 3	Fixed / Absolute	ζ
Case 4	Relative to s_y	ζ

a) Specified X^* (Cases 1 and 2)

Its anticipated that a user will typically set the criteria for sSS based on requirements relevant to the specific process. In some cases, there will be a maximum desired time period (e.g., 500 hours) in which case the user might specify that the system response should not change by more than ΔY_{pass} when projected to time X^*. The fixed X* cases are further divided into whether ΔY_{pass} is a fixed value or a relative value. In Case 1, ΔY_{pass} is a fixed tolerance threshold (as opposed to being defined as a multiple of s_y). In Case 1, the projection-length can be expressed as a function of the average distance between the points, $\langle \Delta x_i \rangle$ and X^*, as shown in the derivation in Appendix A.2. This makes of the equation for N_f a function of the distance projected X^*, the threshold ΔY_{pass}, and the inherent statistics of the system determined from an initial window of data:

$$N_f \sim \left(\frac{(X^* - \bar{X})}{\langle \Delta x_i \rangle}\right)^{2/3} \left(\frac{Z_p \varepsilon}{(\Delta Y_{pass}/s_y)}\right)^{2/3} \tag{9}$$

This equation returns a prediction for the data window size required for sSS detection, N_f, after obtaining the inherent statistics of the data from an initial window. The inputs needed include the inherent statistical characteristics s_y and $\langle \Delta x_i \rangle$, and the desired probability, P of a truly stationary-state window passing the projection test up to point $X^*$with the threshold set to ΔY_{pass}.

P serves a purpose analogous to a confidence interval. Strictly speaking, a confidence interval cannot be defined for complex systems because there is no way to discriminate between a true steady-state and a metastable steady-state, which is one of the reasons that one should only use the term *statistical* steady-state.

Case 2 occurs when the term ΔY_{pass} is set to a multiple of s_y, such that $\Delta Y_{pass} = M_S\, s_y$, and the ppSSD expression for N_f becomes:

$$N_f \sim \left(\frac{(X^* - \bar{X})}{\langle \Delta x_i \rangle}\right)^{2/3} \left(Z_p \varepsilon / M_S\right)^{2/3} \tag{10}$$

b) Specified ζ (Cases 3 and 4)

There may be applications where a user desires to detect sSS by projecting to a fixed multiple of windows away (e.g., to project to 10 times out), after collecting an initial data window. The inequality in Eq. 8 can also be rewritten as:

$$|b_1| \zeta \Delta x_w \leq \Delta Y_{pass} \tag{11}$$

Where the term ζ is defined as $\zeta = (X^* - \bar{X})/\Delta x_w$, such that ζ is a dimension-less number that indicates the length of the projection in terms of a multiple of the initial data window length, Δx_w. ζ can then be used for how far out the projection will be. Using the equation for $b_{1,th}$ (Eq. 3) and the inequality in Eq. 2, an equation was derived that determines the minimum window size N_f needed for a truly steady-state data window to achieve a probability P of passing the test for a given projection length ζ and a fixed threshold ΔY_{pass} (Case 3). The derivation yields the following equation for ppSSD.

$$N_f = \zeta^2 \left(\frac{Z_p \varepsilon}{(\Delta Y_{pass}/s_y)} \right)^2 \quad (12)$$

In Case 4, like for Case 2 , the term ΔY_{pass} is set to a multiple of s_y, by $\Delta Y_{pass} = M_S \, s_y$ and the ppSSD expression for N_f becomes:

$$N_f = \zeta^2 \left(Z_p \varepsilon / M_S \right)^2 \quad (13a)$$

for the sub-case of setting $M_S = 1$, then ΔY_{pass} = s_y and the ppSSD expression simplifies to:

$$N_f = \zeta^2 \left(Z_p \varepsilon \right)^2 \quad (13b)$$

Note that all of the terms on the right side of Eqs. 13a and 13b are free from the inherent statistics of the data set. Thus, when the threshold ΔY_{pass} is defined as a specific multiple of S_y, then the ppSSD window size required for a particular value of ζ (in number of points, N_f) is independent of the inherent statistics of the system.

3.3.3 Results

Using the ***φ*-relation,** Eqs. 9-13b will be used for ppSSD to predict the proper window size N_f for SSD, and then the predictions will be compared to the outputs from the projection test. For testing purposes, several datasets emulating SS behavior were created. The functional form $f(x)$ in Eq. 6 was represented by either a perfectly flat line or a sine wave. Each data series generated has a unique combination of functional form $f(x)$, noise distribution, and noise level, which are listed in Table 3.9. Additionally, we also apply the ppSSD method introduced here to some data generated from kinetic Monte Carlo simulations (KMC).

***Table 3.9**: Range of characteristics used to generate the data series and total number of unique data series for ppSSD*

Characteristic Type	Function Form	Distribution	x-Spacing	Sy or 0.5δ
Possibilities	Flat/Sine	Uniform/Normal	1.0	[1.0, 2.0, and 3.0]
# of Possibilities	2	2	1	3
Total # of data series: 12				

**For data series with normally distributed noise, the noise distribution has a width related to S_y with an infinite tail on the distribution. For uniformly distributed noise, the maximum y-offset from the mean is given the symbol δ (thus a data series where 0.5δ = 2.0 has a uniform noise distribution with 4.0 as the maximum y-offset from the mean.

The goal is to use ppSSD to predict the window size required for the projection test to pass at a desired rate. Then the actual passing rates from using the predicted window sizes are recorded and compared to the desired rate. Both the desired and actual rate of passing should be in agreement. Below examples are presented to show that the ppSSD method works for normal noise distributions.

a) Specified X^* Example (Case 1 and 2)

Finding N_f for a Fixed ΔY_{pass} (Case 1)

The first example of ppSSD uses the specified X^* prediction equation with fixed value for the tolerance ΔY_{pass}(Case 1). A dataset is used where a data window with converged statistics has the following characteristics:

***Table 3.10**: Characteristics of the data window*

$\langle \Delta x_i \rangle$	s_y	μ
1.0	2.0	100,000.0

The user wants to project out to $X^* = 1 \times 10^6$ and does not want there to be a deviation larger than $\Delta Y_{pass} = 4$. First, a small data window size $N_c = 100$ is analyzed to find the characteristics s_y and $\langle \Delta x_i \rangle$. From there, Eq. 9 was used to find a prediction line to find the size N_f where a particular percentage of the projected points will fall below the set ΔY_{pass}. The desired passing rate is inputted in Eq. 9 in the form of a Z_P value from the two-tailed probability table. Then SSD tests are performed on 5000 N_f sized data windows randomly taken from the dataset. The rate at which these windows pass is recorded and compared to the rate expected for that window size from ppSSD.

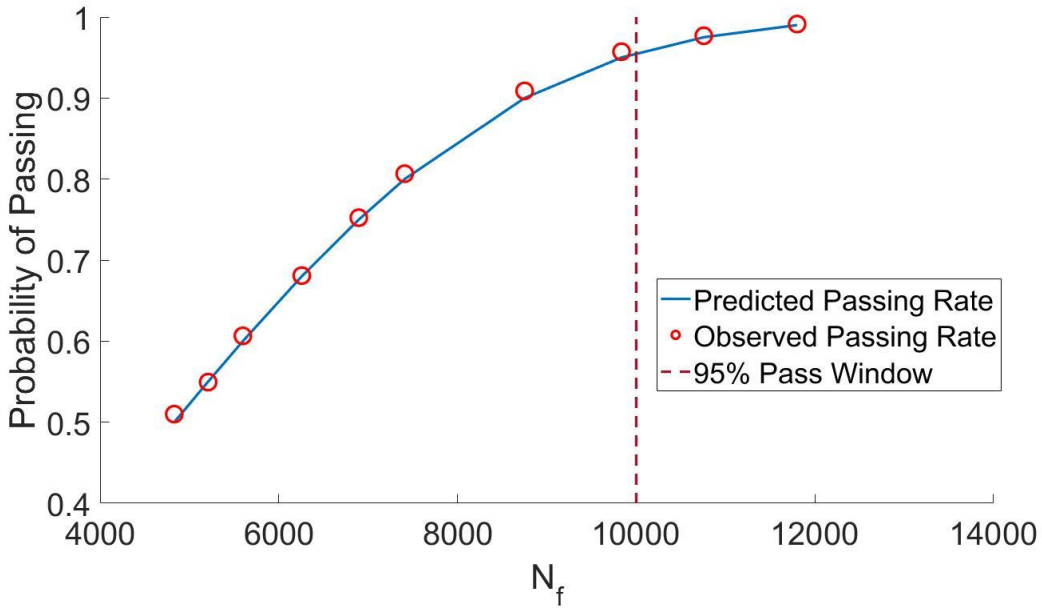

***Figure 3.12**: Required window size for the probability the projection from a data window with Table 3.10 characteristics projected to X^*=10^6 will fall below threshold ΔY_pass=4*

Figure 3.12 shows the confidence that the projection will not deviate from the mean by more than ΔY_{pass} for a given window size in the case described previously. There is good agreement with the prediction line which shows that a window size of $N_f \sim 10000$ would be a good choice if the user wants 95% confidence.

Finding N_f for a Relative ΔY_{pass} (Case 2)

An example of Case 2 is prepared using the same data as in Case 1. Except in this case the ΔY_{pass} is a multiple of the window's s_y. An initial data window is read to create the prediction line for the window size needed for SSD with the criteria of $X^* = 1 \times 10^6$ and $\Delta Y_{pass} = 1.0 \times s_y$.

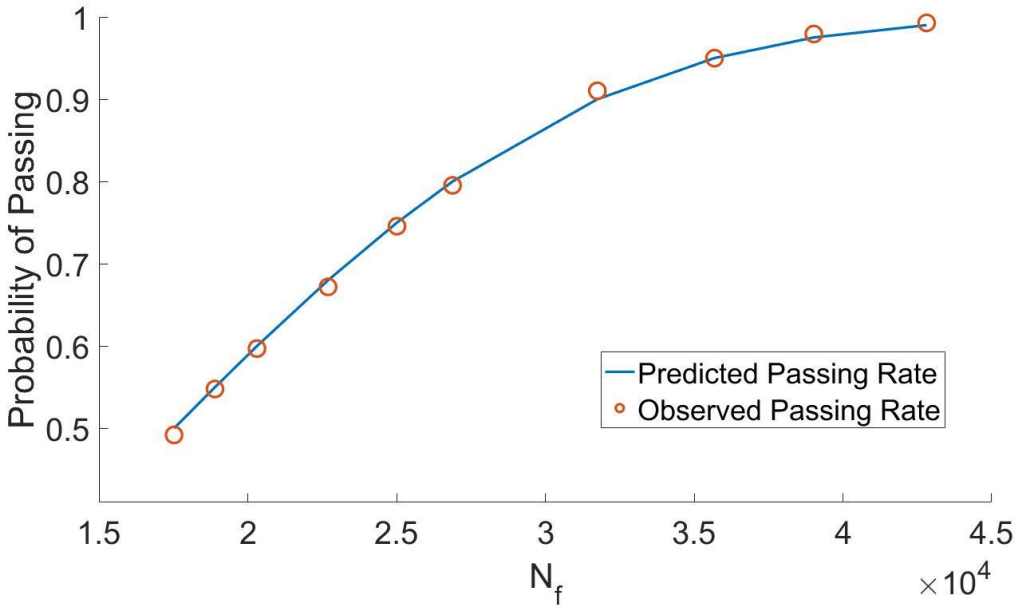

***Figure 3.13**: Required window size for the probability the projection from a data window with Table 3.10 characteristics projected to X^*=10^6 will fall below threshold ΔY_pass=1.0×s_y*

As seen in Figure 3.13, the trend of predicted passing rate to window size from Case 2 ppSSD closely aligns with the trend of the observed passing rate with increasing window size.

Performing a projection test with the additional restriction that the slope must stochastically oscillate above and below zero is a more stringent criteria for steady state. Our relations can also

be applied to these types of criteria. In this example, we will require three adjacent data windows pass the projection test with the additional constraint that there be at least one positive and one negative slope recorded among the three windows. The relation of the single projection passing probability and the aforementioned triple projection passing probability is as follows:

$$P_{triple} = \left(P_{single}\right)^3 \times \left(\frac{6}{8}\right) \tag{14}$$

Where the (6/8) term comes from the eight possible combinations of positive and negative slopes for the three windows, two of which are either all positive or all negative. In those two cases, the triple pass test will fail regardless of the flatness of the data. Subsequently, there will only be a maximum passing probability of 75%. These concepts can be carried forward to require larger numbers of windows to pass, and more complex requirements.

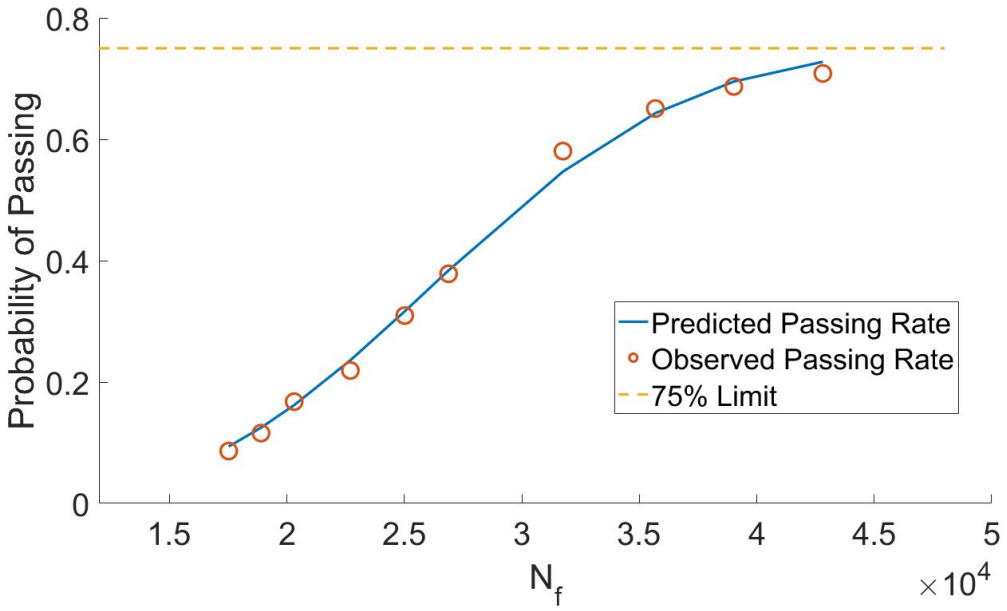

***Figure 3.14**: Actual passing of triple passing of the Case 2 projection test (X^*=10^6 and ΔY_pass=1.0s_y compared to the predicted rate (blue line) for different levels of normally distributed noise. The dark yellow line corresponds to the 75% probability,*

As in the case of a single projection test, the ppSSD based on our relations enable prediction of the passing rate as a function of the number of points in data window, N_f. For example, if a user has a confidence interval that corresponds to passing this test ~ 70% of the time, the user can see in Figure 3.14 that a window size ~ 40000 is needed. With three windows, that means that~120000 data points will need to be collected to achieve that passing rate for steady state data.

Specified ζ Examples (Case 3 and Case 4)

b) Finding N_f for a Fixed ΔY_{pass} (Case 3)

Case 3 occurs when the user would project out to a set ζ to test if the projection exceeds a fixed ΔY_{pass}. The data set used here is that the flat line with normally distributed noise giving an approximate s_y~1.0, noted in Table 3.10. ppSSD was performed with Eq. 12 for ζ=100 and $\Delta Y_{pass} = 5.0$. The results of the ppSSD prediction is compared to the actual passing rate of the projection test in Figure 3.15, and good agreement is observed.

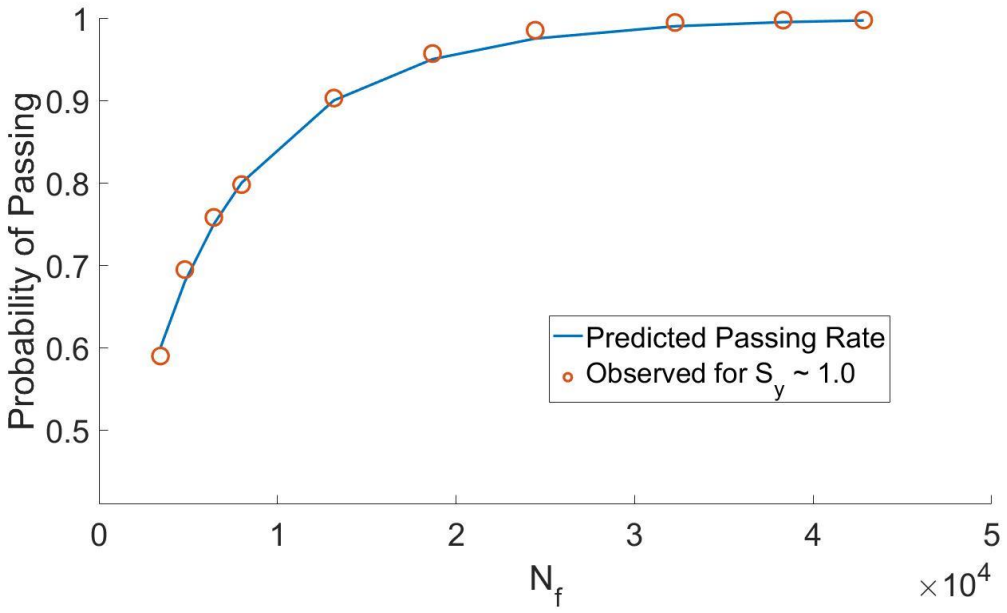

***Figure 3.15**: Actual passing rates of a single instance of the projection test (ζ=100 and ΔY_pass=5.0) compared to the predicted rate (blue line) for different levels of normally distributed noise. The blue line corresponds to the window size desired to have a 95% probability of passing.*

c) Finding N_f for a Relative ΔY_{pass} (Case 4)

As mentioned previously, Case 4 is a special case because the ppSSD prediction is independent of the statistics of the data, provided that the threshold can be expressed as a multiple of S_y. To test this property, the Case 4 projection test was performed using window sizes given by Eq. 13b for a particular ζ on several of the datasets listed in Table 3.10, all with different values for s_y.

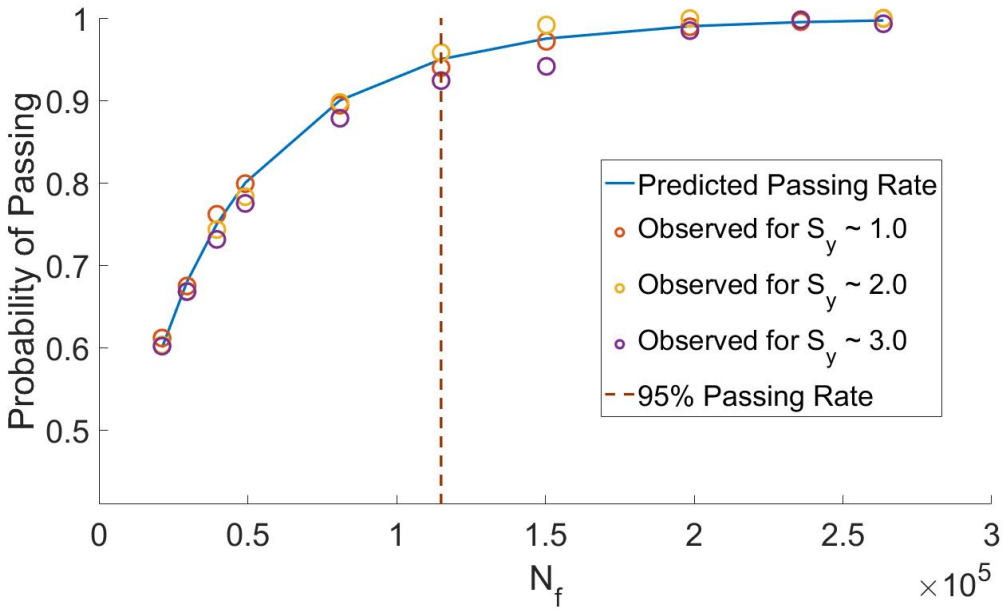

***Figure 3.16**: Actual passing rates of a single instance of the projection test (ζ=50) compared to the predicted rate (green line) for different levels of normally distributed noise. The brown line corresponds to the window size desired to have a 95% probability of passing*

Figure 3.16 displays the probability of passing as a function of the number of points, N_f, given a single projection passing test when ζ=50 with the threshold of ΔY_{pass} = s_y for steady-state data with normally distributed noise. The predicted curve is based on our ppSSD method, and it can be seen that this curve aligns closely with the observed probabilities of passing. If a user desired a confidence interval that corresponded to a 95% probability of passing with ζ=50, the user would predict that a system actually at steady-state would require a little over 1000 points to pass the test (indicated by the dashed vertical line in Figure 3.14). Thus, the user is able to predict, *before measuring* the data, the approximate number of data points required before steady state would be detected.

As in Case 2, it shows that the oscillating triple passing tests can also be applied to Case 4. Figure 3.17 displays the passing rate for a system at steady-state with normally distributed noise, along with the ppSSD prediction line for Case 4 using the same ζ and ΔY_{pass} choices as Figure

3.16. Figure 3.17 shows (like Figure 3.16) that Case 4 is special in that the window size returned by ppSSD is independent of the noise level since it is independent of the system's internal statistics.

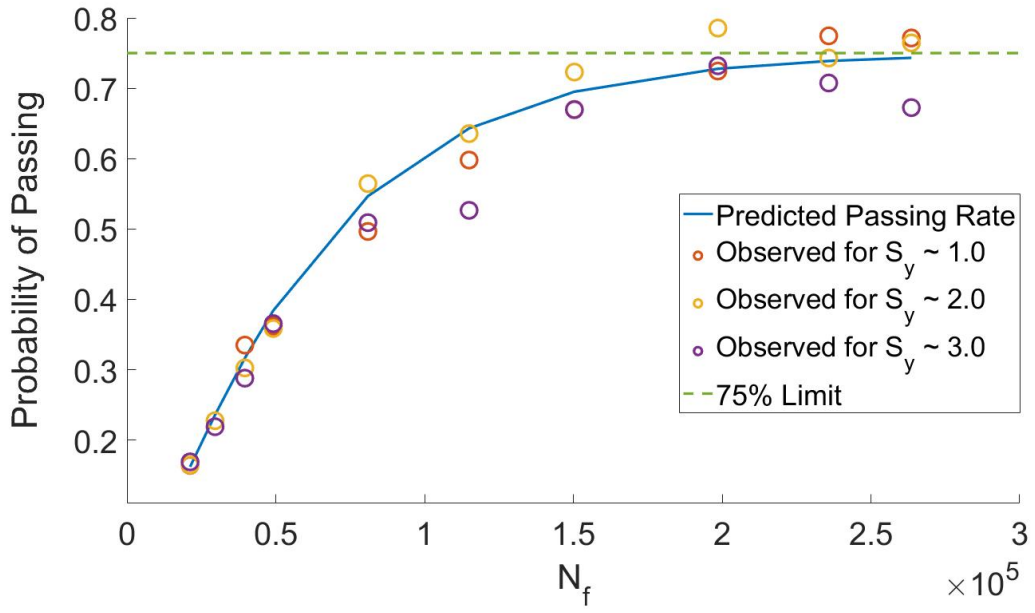

***Figure 3.17**: Actual passing of triple passing of the projection test (ζ=50) compared to the predicted rate (green line) for different levels of normally distributed noise. The dark yellow line corresponds to the 75% probability, which appears to be an asymptote.*

d) Application to Monte Carlo

One of the applications where ppSSD has significant value is in kinetic Monte Carlo simulations, in these simulations it is common to desire terminating simulations at sSS. In this context, knowing how long it might take to gather enough data for SSD is extremely important for resource conservation (since for some simulations SSD may not feasible, and in those cases the computational resources may be squandered). In kinetic Monte Carlo simulations, the event frequencies of first order processes follow a poisson distribution [146]. This poisson distribution is asymmetric because there is no probability of a rate less than zero. When the average number of events per unit time is on the order of 10 or more, the poisson distribution becomes similar to a normal distribution. These types of distributions are very important for real applications. In this

example, we use kinetic Monte Carlo data generated for interconversion of species in a network of 8 possible species[147]. As the concentrations of each species are not constant, the event frequencies associated with each type of event do not follow a poisson distribution, but instead follow a modulated poisson distribution due to the modulation of the concentrations of each of the species. Thus, this example has neither normally distributed noise nor uniformly distributed noise, and uses data taken from a real study using real simulation software.

Here, Case 1 and Case 2 ppSSD was performed on two data sets generated from KMC simulations described above. With the inputs for ppSSD being appropriate for the data evaluated. Case 1 was performed on a data set from CH_2O reaction rates corresponding to Figure 8 in Ref[147]. An initial window was read and the prediction line formed from Eq. 9. Then, SSD tests were performed on the data set with a X^*=36000 s and a ΔY_{pass}=1, with 1000 trials per N_f value. The actual passing rates differ from the ppSSD lines displayed in Figure 3.18. However, the observed rates run parallel to the prediction line and are in the same order of magnitude as the prediction (which was the target of this work).

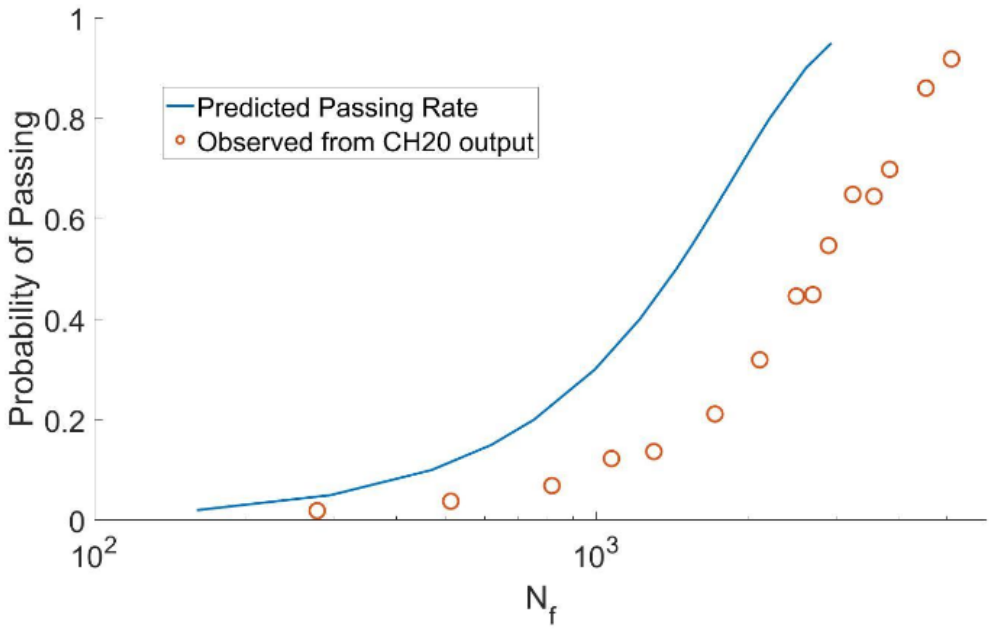

***Figure 3.18**: Predicted and actual rates of passing* of a Case 1 SSD test (X^*=36000 s and ΔY_{pass}=1) on *the CH2O reaction rates dataset*

In a second example, Case 2 was performed on another KMC dataset, this time corresponding to the event frequencies from the forward reaction of 5.0 in the system provided in the supporting information of Ref [147]. Again, an initial window was read in a non-transient region and a prediction line was formed using Eq. 10. Case 2 SSD tests were then performed on the KMC dataset with the criteria that X^*=300 s and a $\Delta Y_{pass} = 1.0 \times s_y$, with 1000 trials per N_f value.

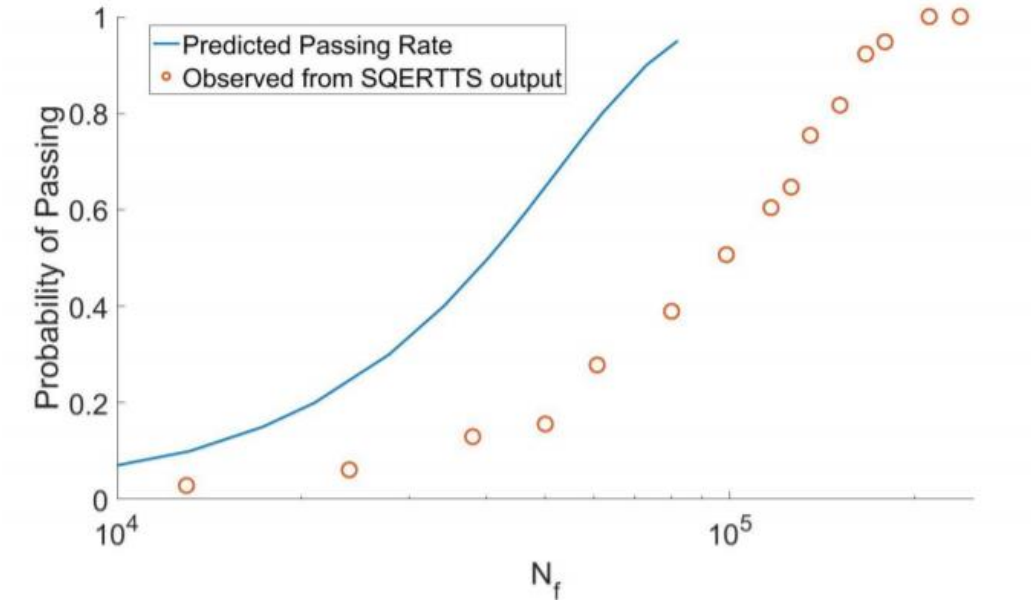

***Figure 3.19**: Predicted and actual rates of passing of a Case 2 SSD test (X^*=300 s and ΔY_{pass}=1.0 × s_y) on the CH2O reaction rates dataset*

Figure 3.19 displays the passing rate predicted from applying ppSSD Case 2 on KMC dataset 2, along with observed passing rates. The predicted line is the same shape and parallel to the observed line for the KMC dataset, and that the predicted values of Nf for SSD are the same order of magnitude as for the observed vales of Nf for SSD (within a factor of 2-5). Thus, the goal of order of magnitude ppSSD is still achieved (which was the target of this work) even for KMC dataset 2. A more accurate estimate can be formed when a system specific value is used for ε.

3.3.4 Discussion

The φ-relation, a postulated linear relationship of the S_{b1} of steady-state data series with φ (a statistical indicator introduced in this work, defined as $\varphi = \frac{s_y}{\Delta x_w \sqrt{N}}$) was confirmed to exist, $S_{b1} = \varepsilon\varphi$. It is significant that the results also showed that the same value for the constant, $\varepsilon = 3.46$, works well with both normally distributed and uniformly distributed data, and even with

sine-wave distributed data and KMC data (which has a modulated Poisson distribution). It demonstrates the applicability of the empirical constant to different types of noise. This relationship enabled us to use an initial window of current data points, N_c, to predict the minimum number of points of a future window, N_f, which would be needed to pass various types of sSS projected-mean tests. This method is applicable when a system is known to have converged statistics. It should be noted that the empirical constant ε has been calculated when the x-spacing between each point is constant, or where the data is collected at constant set intervals. However, the prediction equations would still work for data with uneven x-spacing provided that the number of points is sufficiently large that $N_c\langle\Delta x_i\rangle \sim \Delta x_w$ (i.e., the initial window should be sufficiently large that an *average* spacing between points is proportional to the *total* spacing for that number of points). In principle, users can find a more accurate value of ε for noise distributions that are neither normal nor uniform. However, the difference in the value of ε between the normally and uniformly distributed is very small and would not change the window size prediction significantly. Most realistic noise distributions are unlikely to deviate significantly from those found for the two mentioned distributions (even rare event processes approach a normal distribution with sufficient sampling), and thus the value of $\varepsilon = 3.46$ can be considered generally applicable.

The types of applications can be divided into two categories, specified X* (Cases 1 and 2) and specified ζ (Cases 3 and 4). For both categories, ppSSD with our method was shown to be accurate for both types of noise distributions using the same value of ε, whether using a fixed threshold (absolute value of ΔY_{pass}) or relative threshold ($\Delta Y_{pass} = M_S\, s_y$). For Cases 1 to 3, one first analyzes a small initial data window with size N_c. We found that 100 data points was typically sufficient: the number of data points must simply be large enough to gather reliable statistics such as standard deviation s_y and average step size Δx_i. This information is plugged into ppSSD

equations in order to get the number of points N_f required to make an accurate determination of sSS. The data must have converged statistics. The agreement found in Figure 3.12-3.15 show the accuracy of the window size predictions. It should be noted that Figures 3.12-3.15 produced good agreement because the initial data window was already at a sSS. Were that not the case, the equation would give a window size larger than what would be needed. So when a user inputs a particular confidence, the equation will give a window size that ensures a passing rate of *at least* that confidence.

It was found that Case 4, which has a relative threshold ($\Delta Y_{pass} = M_S\, s_y$) and a specified projection length ζ, that the value for N_f is independent of the statistics of the data. Figure 3.16 shows that passing rate of projection test using a window size found by Eq 13b matched the confidence that was input into the equation. As expected, the noise amplitude *did not* affect the passing rate. Thus, Case 4 can even be used in cases where the user cannot obtain the inherent statistics of the data.

For Cases 1-4, our φ-relation ppSSD method was also shown to be effective for sine wave distributed data. This indicates that the method is also suitable for cases with cyclic fluctuations, provided that the initial window is large enough to have a converged s_y. The method was also shown to be effective for the KMC data. The KMC data came from simulations, which have an interplay between various Poisson distribution events, and thus have a modulated Poisson distribution (fluctuations are also visible in the KMC data due to system dynamics that greatly deviate from a normal distribution). Additionally, the KMC data is not an evenly spaced time series. Despite these differences, ppSSD using the same value of ε returned window sizes within the correct order of magnitude for the KMC data sets. Thus, our tests show that the ppSSD method presented here is quite, general even without adjusting the value of ε for different noise

distributions. The ppSSD method was shown to work for both single-window projection tests, as well as for multi-window oscillating slope constraint projection tests.

3.3.5 Conclusion of ppSSD

We have found a method that can predict the minimum number of points, N_f, required to detect a statistical steady-state, based on statistical analysis of an initial set of data points from the current data window, N_c. This ppSSD method is very simple and widely applicable. The method relies upon a realization that the ratio $\varphi = \frac{s_y}{\Delta x_w \sqrt{N}}$ can be used as a descriptor of the system's state, which is then found to be related to the distribution of the slopes of the data through the unitless constant, ε= 3.46. When given the statistics of an initial data window, this method can determine the number of points required to run a reliable projection test for both specified X^* and ζ projections. This method is applicable to arbitrary confidence intervals: Z_P is obtained from two-tailed probability tables. Case 4, which has a specified ζ and relative threshold ($\Delta Y_{pass} = M_S\, s_y$) is a special case where the statistics of the initial window are not needed to perform ppSSD to predict N_f. The method was found to work for both normally distributed and uniformly distributed noise with $\varepsilon = 3.46$, as well as with KMC data which had a modulated poisson distribution. Having tested these three types of noise distributions, and even tested data with a sine-wave distribution, one can believe that this method will work sufficiently well with the same value of $\varepsilon = 3.46$ for other realistic noise distributions.

Chapter 4: Bulk Precipitation in Simulated Fe-Y-Ti-O Alloys

As stated earlier, much of the strength of the NFAs are due to the high number density of the nanoparticle oxides containing solutes like Y, Ti, and O. Finding the right processing characteristics to get the most advantageous material properties is an obvious goal of manufacturers of NFAs. The KMC model outlined in Chapter 2 was used to simulate heat treatments of the NFAs 12YWT and 14YWT to observe the precipitation of these nano-oxides so the relationship of resulting oxide size and number density in the bulk with heat treatment was determined. Additional insights into the growth and coarsening stages of precipitation are also expected with this study investigating the adherence of nano-oxide precipitation to classical nucleation, growth, and coarsening.

4.1 Thermodynamics of Precipitation

A metal alloy system can only accommodate a certain threshold of solute atoms before thermodynamics require action to reduce the system energy. A multicomponent alloy system that is supersaturated with solutes atoms that is may seek to reduce its overall energy by separating into two distinct phases.

$$\Delta f \cong -\frac{R_g T}{V_\beta} \times \ln(\frac{c_o}{c_s}) \quad (1)$$

Eq 1 describes the general equation for the chemical driving force for homogenous nucleation in binary alloys where the 2nd phase is primarily solute. R is the gas constant, T is temperature, c_s is the solubility limit for B in A, and $c_o$is the current concentration of solute in the matrix. When the c_o is greater than c_s (supersaturation), there will be a relevant driving force for nucleation. The c_o will continually decline in the matrix as nucleation and growth proceeds in a material until the condition $c_o \leq c_s$ is met and the driving force disappears.

$$\Delta F(R) = \frac{4\pi}{3} R^3 \Delta f + 4\pi R^2 \sigma_{\alpha\beta} \quad (2)$$

$\Delta F(R)$ is the Helmholtz free energy of homogenous nucleation which is described in the general form by Eq 2 where $\sigma_{\alpha\beta}$ is the interface energy between the two phases and Δf is the chemical driving force for homogenous nucleation. The critical size of precipitate (where the nucleate becomes stable) would be where the 1st derivate of $\Delta F(R)$ with respect to R equals zero (i.e. When the volume term overcomes the surface area term). It can be seen the size of the precipitate is influenced by two competing forces, the driving force and interface energy.

4.2 Kinetics of Precipitation

Assuming that the precipitates will be small and coherent with the matrix (a given in the KMC model), then the diffusion of solutes will be the limiting factor in the kinetic growth of the precipitate. A general relationship of radius of a particle with time during the growth regime can then be described as:

$$R = k(Dt)^{1/2} \quad (3)$$

Classical theory predicts that the evolution of the average precipitate size will have a power (scaling) law-dependence with time, i.e., average radius will have an $R \sim t^{1/2}$ [148] relationship

in the growth stage. Where R is the average radius of the particle (assuming a spherical precipitate) and t representing time. The variable D is the diffusion coefficient of the slowest moving (limiting) atomic species belonging to the precipitate. The variable k is a constant relating to the degree of supersaturation of solutes in the matrix.

The next stage is the coarsening stage though there is not a clear distinction between end of the growth stage and the beginning of the coarsening stage. Generally, the coarsening stage occurs when the solute concentration in the matrix becomes so low (where $c_s \approx c_o$) that there will be little driving force to form any new precipitates. Thus the source of new solute atoms for the precipitate comes not from the matrix but from other precipitates. In this stage, the smaller precipitates will appear to dissolve and their contents consumed by the large more stable precipitates. Coarsening, or Ostwald ripening, is an effort by the system to reduce its total energy by removing excess interfacial energy. Small precipitates inherently have a higher ratio of surface area to volume and thus are more prone to dissolution under coarsening. Thermodynamically, the logical end stage of coarsening is the consolidation into a single large precipitate; though the slow kinetics and low driving force makes that outcome unlikely to be seen in most practical applications. The average radius of the precipitates is then expected to grow with a different relationship with time. Something more akin to

$$R \propto t^{1/3} \tag{4}$$

LSW theory anticipates a $R \sim t^{1/3}$ [47] relationship in the coarsening stage when the coarsening is dominated by long-range diffusion. However, there are exceptions to these power laws, for e.g., NFAs have been reported to have coarsening kinetics deviating from the $t^{1/3}$ time dependence [34]. The KMC model will be used to evaluate the coarsening phase of precipitation to identify a cause for this deviation.

Additional goals for the KMC model will be to replicate the shape of the precipitates at equilibrium as observed in experiments, and evaluate the change in composition of the oxides during all stages of precipitation. With this data, there will be a better understanding of the stages of NFA precipitation. Success in replicating the oxide characteristics of the NFAs will give researchers confidence in the KMC model to extend it to simulate the irradiation environment in a nuclear reactor.

4.3 Method

4.3.1 Kinetic Monte Carlo Model

The material system is represented in the KMC simulation box as a lattice of points in the unstressed bcc structure. The metal atoms (Fe, Y, and Ti) exist on the substitutional lattice, while the O atoms exist on a separate octahedral sub-lattice that is more energetically favorable [93]. The KMC model assumes a rigid lattice where the distance between each lattice site remains constant regardless of the atoms occupying the lattice sites. The full description is available in Chapter 2.

4.3.2 Parameterization

Table 4.1: *Pair-interaction energies (eV) for the Fe-Y-Ti-O system taken to the 4th nearest neighbor in the simple cubic frame of reference*

Pair-interactions	**1 (eV)**	**2 (eV)**	**3 (eV)**	**4 (eV)**
Fe-Fe	-	-	-0.611	-0.611
Fe-Y	-	-	-0.59	-0.52
Y-Y	-	-	-0.57	-0.69
Fe-Ti	-	-	-0.65	-0.53

Ti-Y	-	-	-0.71	-0.68
Ti-Ti	-	-	-0.69	-0.70
Fe-V	-	-	-0.21	0.0
Y-V	-	-	-0.35	0.0
Ti-V	-	-	-0.35	0.0
Fe-O	0.0	0.0	-	-
Y-O	-0.01	-0.11	-	-
Ti-O	-0.04	-0.04	-	-
O-O	0.1	-0.116	0.1	-0.116

Table 4.2: *Diffusion parameters of Fe, Y, Ti, and O in bcc Fe*

Input Parameter	**Value**	**Unit**	**Reference**
Lattice parameter	2.87×10^{-10}	m	
Vacancy Migration Energy, Fe	0.66	eV	[80]
Vacancy Migration Energy, Y	0.23	eV	[99]
Vacancy Migration Energy, Ti	0.81	eV	[81]
Vacancy Formation Energy	2.24	eV	[80]
Oxygen Migration Energy	0.48	eV	[100]
Vacancy pre-exponential factor, Fe	6.0×10^{-4}	$m^2 s^{-1}$	[80]
Vacancy pre-exponential factor, Y	3.7×10^{-7}	$m^2 s^{-1}$	[99]
Vacancy pre-exponential factor, Ti	2.1×10^{-1}	$m^2 s^{-1}$	[81]
Oxygen Interstitial attempt frequency	1.0×10^{14}	/s	

The thermodynamics described in Chapter 2 are used for these simulations and repeated for reference in Table 4.1. The KMC needs to replicate the kinetics of the system as well as the thermodynamics. Thus, the mobilities of each solute via vacancy migration are tied to the measured values from literature. The attempt frequency v_x and saddle point energy e_x^{SP} in atom

species *x* are fitted so that the diffusion values in Table 4.2 are replicated in the KMC. The vacancy formation energy E_{for} is also needed to find the equilibrium vacancy concentration in the KMC, following the general equations $C_v = \exp(\frac{-E_{for}}{k_b T})$. With the small size of the KMC simulation box, the presence of a single vacancy would be a gross supersaturation of vacancies in the system. The KMC model's method of thermal vacancy generation and annihilation for recreating the thermal vacancy concentration followed Hin's method [80].

Once the parameterization of the Fe-Y-Ti-O material system is complete, the precipitation simulations can begin. Then a heat treatment simulation plan is developed for three simulated alloy systems; one that precipitates Y-O oxides and two that precipitate Y-Ti-O oxides.

4.3 Simulation Procedure

The oxide consolidation behavior of both Y-O and Y-Ti-O oxides were simulated by the KMC model in the next section. The two NFA alloys, 12YWT and 14YWT, that were simulated were selected since these alloys have been extensively studied, including the processing conditions required to achieve oxides of a certain size and number density [18-20]. The atomic compositions of the solutes in the bcc Fe matrix are listed below in Table 4.3. The first two compositions used for the KMC simulations are the same compositions used by Boulnat in their attempt to make a model of oxide precipitation [121], while the third composition is a separate Y-Ti-O oxide-bearing alloy. The Ti-containing alloys have Y-Ti-O concentrations, similar to the 12YWT and 14YWT alloys, to demonstrate the robustness of the parameterization and to accurately replicate the precipitation behavior of two different Y-Ti-O oxide containing NFAs.

Table 4.3: *Atomic compositions for the Y-O and Y-Ti-O model alloys*

Model Alloys	**Y**	**Ti**	**O**
Y-O Alloy	0.15 at%	0.0 at%	0.22 at%

Y-Ti-O Alloy (12YWT)	0.13 at%	0.4 at%	0.18 at%
Y-Ti-O Alloy (14YWT)	0.08 at%	0.27 at%	0.30 at%

The simulation box starts as pure bcc Fe with the solute atoms randomly placed throughout the matrix in proportion to their set atomic composition. The KMC simulation box contains no other features, such as grain boundaries or dislocations, and no other solutes commonly found in NFAs, such as Cr or tungsten (W), are included with the Y, Ti, and O in the Fe matrix. The heat treatment temperatures tested and the size of the simulation box are listed below in Table 4.4. The 1123K temperature was selected as there are experimental results for precipitation behavior at this temperature, so that the KMC can be compared for both Y-O and Y-Ti-O oxides. The temperatures 1023K and 1223K were also chosen so that the simulations can show the influence of temperature on the oxide characteristics.

Table 4.4: *Simulated heat treatments for both the Y-O and Y-Ti-O alloys*

Alloy Treatments	**Size of KMC Box**	**Temperature**	**# Simulations**
Y-O alloy Heat Treatments	400X100X100 lattice points	1023K, 1123K, 1223K	3
Y-Ti-O alloy Heat Treatments (12YWT)	400X100X100 lattice points	1023K, 1123K, 1223K	3
Y-Ti-O alloy Heat Treatments (14YWT)	400X100X100 lattice points	1123K	3

During the heat treatments, the average radius, number density, and composition of the oxides were tracked over time. Adherence to the expected nucleation growth and coarsening laws were also analyzed. So, the growth and coarsening stages were identified, and the power relationship of the evolution of size with time were examined and checked against the theory. Once the simulations were completed, the average size and number density of the oxides were compared

to the experimental results where there is data. The composition of the oxides for all temperatures were also compared to the literature.

In addition to collecting these characteristics, the shape of the precipitates was analyzed. After the end of the simulation run, the final configuration of the atoms were visualized so that the shape of the Y-O and Y-Ti-O precipitates could be compared to expectations from experimental observations. It is another test of the validity of the KMC model.

4.4 Results

4.4.1 Fe-Y-O Materials

A solid solution of randomly dispersed Y and O atoms in the bcc Fe matrix was placed into a heat treatment where vacancies drive the nucleation growth and coarsening of Y-O precipitates. The time evolution of the oxide characteristics is recorded and shown below:

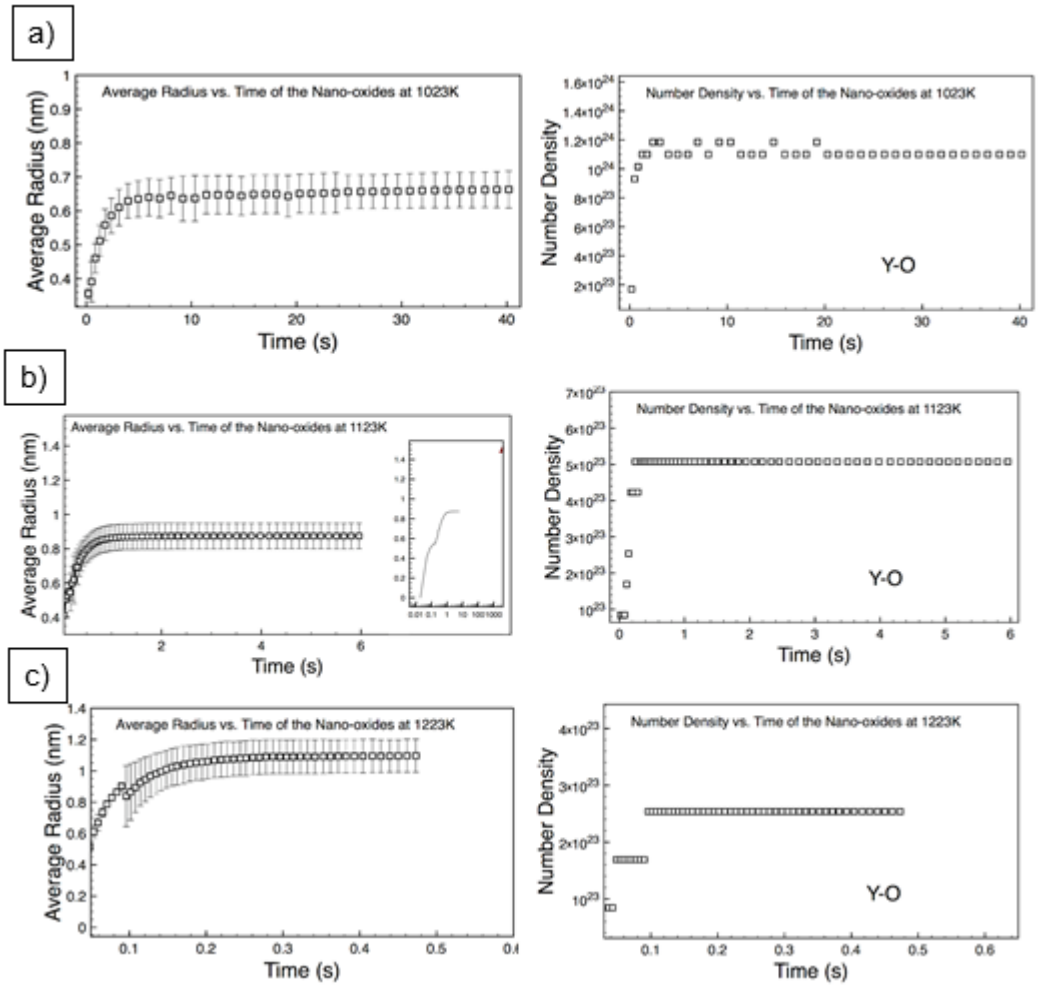

Figure 4.1: *The time evolution of the Y-O oxides at the three prescribed temperatures a) 1023K, b) 1123K, and c) 1223K. The red triangle in the 1123K case represents data from Ratti [43]*

Figure 4.1 shows the time evolution of the average size and number density of the Y-O precipitates for all three tested temperatures. At all conditions, there is a rapid nucleation of small oxides at the onset, and the number density quickly reaches a maximum. At this point, there is no more nucleation of new oxides, but the existing oxides continue to grow in size until the evolution of average size reaches a similar plateau. This is presumed to be the start of the coarsening stage of the oxide evolution.

Table 4.5: *Characteristics of the Y-O oxides after heat treatment at a given temperature*

Material System	**Average Radius**	**Number Density**

Y-O -1023K from KMC	0.66 nm	$1.1 \times 10^{24}\ m^{-3}$
Y-O -1123K from KMC	0.87 nm	$5.08 \times 10^{23}\ m^{-3}$
Y-O -1123K from Ratti [43]	1.5 nm	$9.1 \times 10^{23}\ m^{-3}$
Y-O -1223K from KMC	1.09 nm	$2.53 \times 10^{23} m^{-3}$

Table 4.5 shows the final oxide characteristics at the cessation of the heat treatment for each temperature. There is increasing average oxide size with increasing temperature. In turn, there is a decreasing number density with increasing temperature. The experimental observations from Ratti [43] are both roughly twice the size and twice the number density as the results from the KMC. Since all the Y and O solutes left in the Fe matrix would not make up the difference, discrepancies between the experiment and simulation could be due to measurement differences or the presence of other solute material, such as Cr.

The growth stage is judged to end when new precipitates are no longer being formed, and where the number density stops increasing and reaches a plateau. The relationship of the growth of the precipitates with time can be described by a power law relationship $\bar{R} \propto t^a$ where $\bar{R}$ is the average radius and *a* is the time exponent [149]. This relationship is only expected in the growth regime of precipitation and is typically 0.5. To extract this relationship from the data, the points that are at the center in between the start and end of the growth stage were evaluated and placed in a power law regression to find the power-law relationship of the average radius with time.

Table 4.6: *Exponent of time in the relation $\bar{R} \propto t^a$ in the growth regime of the nucleation simulations*

Material System	**Power Law (growth) a**
Y-O-1023K	0.27
Y-O-1123K	0.51
Y-O-1223K	0.54

Table 4.6 displays the results of this power law analysis. The precipitation of Y_2O_3 oxides in the Fe-Y-O alloy follows the a=0.5 time-dependence at 1123K and 1223K, while the 1023K heat treatment has a lower power relationship of a=0.27. The rapid consolidation of the Y-O oxides at 1023K into numerous nuclei (removal of excess solutes in the Fe matrix) probably causes an early exit from the growth stage before the system can meet the conditions for achieving a power law relationship of 0.5.

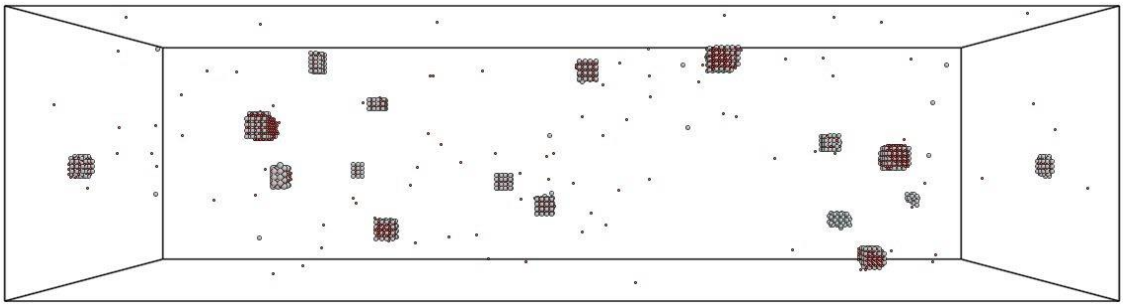

Figure 4.2: *Visualization of Y-O nano-oxides after the 1223K heat treatment. Yttrium=Grey spheres, Oxygen=red spheres*

Figure 4.2 shows the oxide distribution in a Y-O NFA sample after the 1223K heat treatment. The oxides are reasonably well-spaced, with the vast majority of the Y and O atoms associated with an oxide. The shape of the oxide is the same cubic shape expected from experimental observations. These characteristics are consistent in the 1023K and 1123K heat treatments.

4.4.2 Fe-Y-Ti-O Materials

After completion of the precipitation heat treatments for the Y-O NFAs, the KMC simulations for the precipitation of the Y-Ti-O oxides proceeded. New solid solution samples with new atomic concentrations of Y, Ti, and O atoms, as seen in Table 4.3, were generated with the solutes randomly dispersed in the Fe matrix. The KMC then began the consolidation heat treatments from these starting configurations at the temperatures specified in Table 4. The

simulations were run until an apparent plateau appeared in the time evolution of the oxide characteristics.

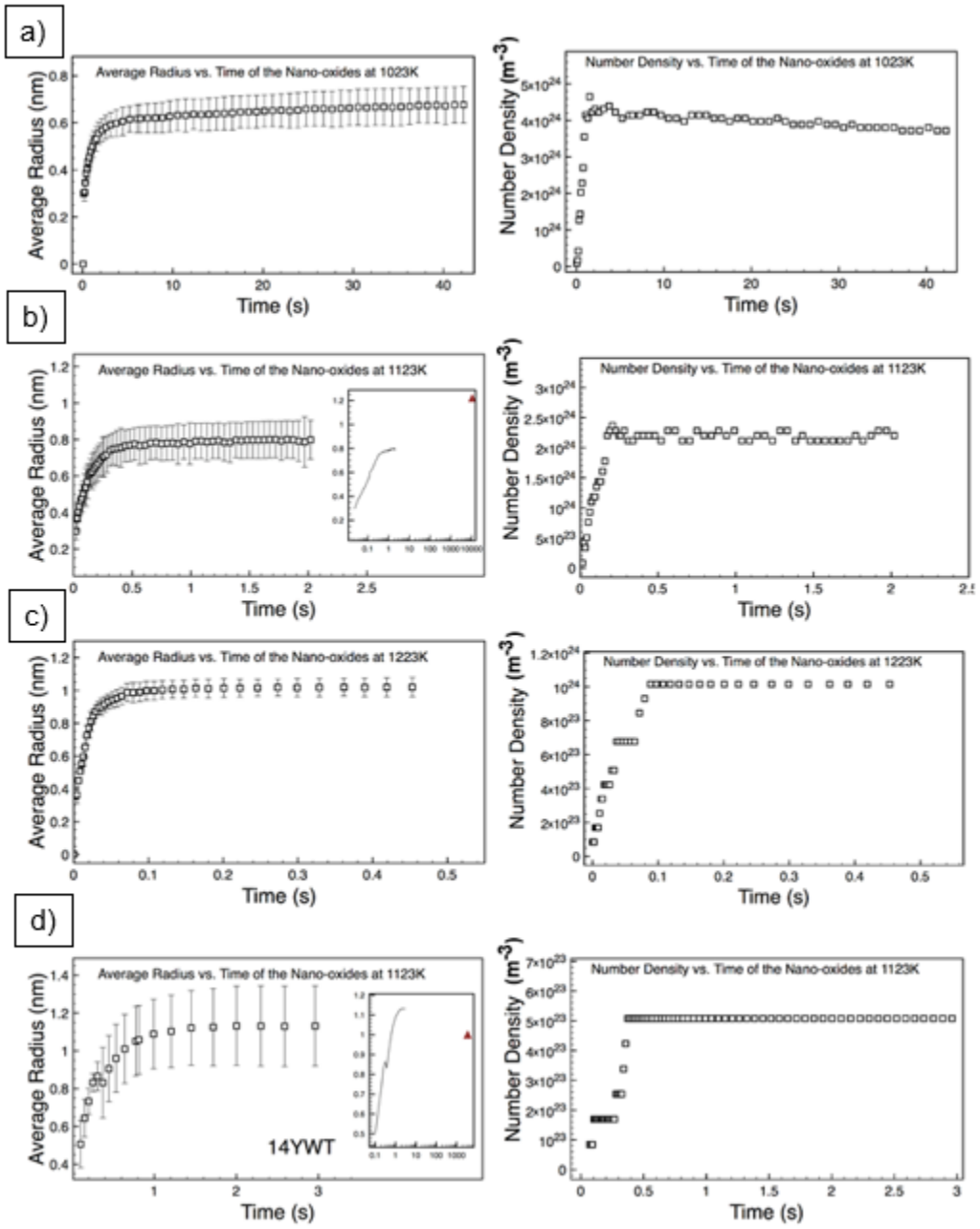

Figure. 4.3 *Average radius (nm) and number density (m^{-3}) growth of the Y-Ti-O nano-oxides of the 12YWT composition at heat treatment a) 1023K, b) 1123K, and c) 12223K, and of the 14YWT composition at d) 1123K. Red triangles correspond to data from Alinger [20] and Miller [19] from heat treatments for 12YWT and 14YWT respectively*

Figure 4.3 shows the nucleation, growth, and coarsening curves for all three heat treatments for the 12YWT composition and the 14YWT composition at 1123K. There is a period of strong growth that gave way to a seemingly level plateau where there was very slow precipitate growth and no new oxide nucleation. It is at this point that the oxide characteristics were extracted.

Table 4.7: *Nano-oxide characteristics after heat treatment at a given temperature*

Material System	**Average Radius**	**Number Density**
12YWT-1023K from KMC	0.6 nm	$5 \times 10^{24}\ m^{-3}$
12YWT-1123K from KMC	0.8 nm	$2.1 \times 10^{24}\ m^{-3}$
12YWT-1123K from Alinger [20]	1.25 nm	$2.5 \times 10^{24}\ m^{-3}$
12YWT-1223K from KMC	1.1 nm	$8 \times 10^{23} m^{-3}$
14YWT-1123K from KMC	1.04 nm	$4.7 \times 10^{23}\ m^{-3}$
14YWT-1123K from Miller [19]	1.0 nm	$4.3 \times 10^{23}\ m^{-3}$

Table 4.7 displays that, with increasing temperature, the average radius of the oxide precipitates increases while the number density decreases. This was expected, as increased temperature reduces the rate of formation of stable nuclei so that more solutes will join existing oxides rather than form a new oxide. This results in a small number of larger oxides than at lower temperatures. There appears to be agreement in the number density and average radius readings when the 12YWT-1123K nucleation run results were compared to the results from Alinger. There was also agreement with the 14YWT-1123K nucleation runs with the Miller experiments [19].

The power law relationships of the growth stage for all three heat treatment temperatures were also analyzed. Table 4.8 shows the results.

Table 4.8: *Exponent of time in the relation* $\bar{R} \propto t^a$ *in the growth regime of the nucleation simulations*

Material System	**Power Law (growth)** a

12YWT-1023K	0.2
12YWT-1123K	0.54
12YWT-1223K	0.45

The 1123K and 1223K heat treatments show a power law relationship similar to the expected 0.5 from theory [149], while the 1023K heat treatment does not do this, showing a small power law relationship of 0.2. This is caused by the rapid consolidation of the solutes into the oxide precipitates, due to the very low solubility product. The Supporting Information visualizes the time dependence of each heat treatment in the growth stage, so that the adherence or departure from the a=0.5 expectation for each temperature can be shown. Additionally, once the matrix is depleted of Y and Ti atoms, there is very little coarsening that occurs thereafter. The cause of this lack of coarsening is explored in later sections.

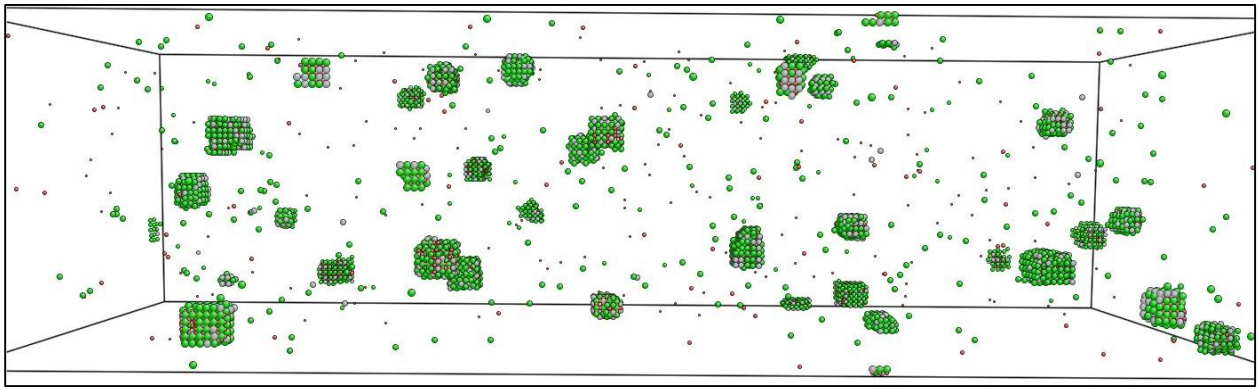

Figure 4.4: *Visualization of Y-Ti-O nano-oxides after the 1123K heat treatment. Green spheres: Ti atoms, Grey spheres: Y atoms, Red spheres: O atoms*

Figure 4.4 shows the oxide system after heat treatment at 1123K. The Y-Ti-O oxides are formed into cubic shapes, in line with expectations from Ribis [92] where the oxides have large <100> interfaces and smaller <110> and <111> interfaces. The same oxide shapes also are found at 1023K and 1223K.

4.4.3 Oxide Composition

The composition of the oxides was tracked through every phase of precipitation. To further validate the KMC, the composition of the oxide precipitates was compared to experimental values.

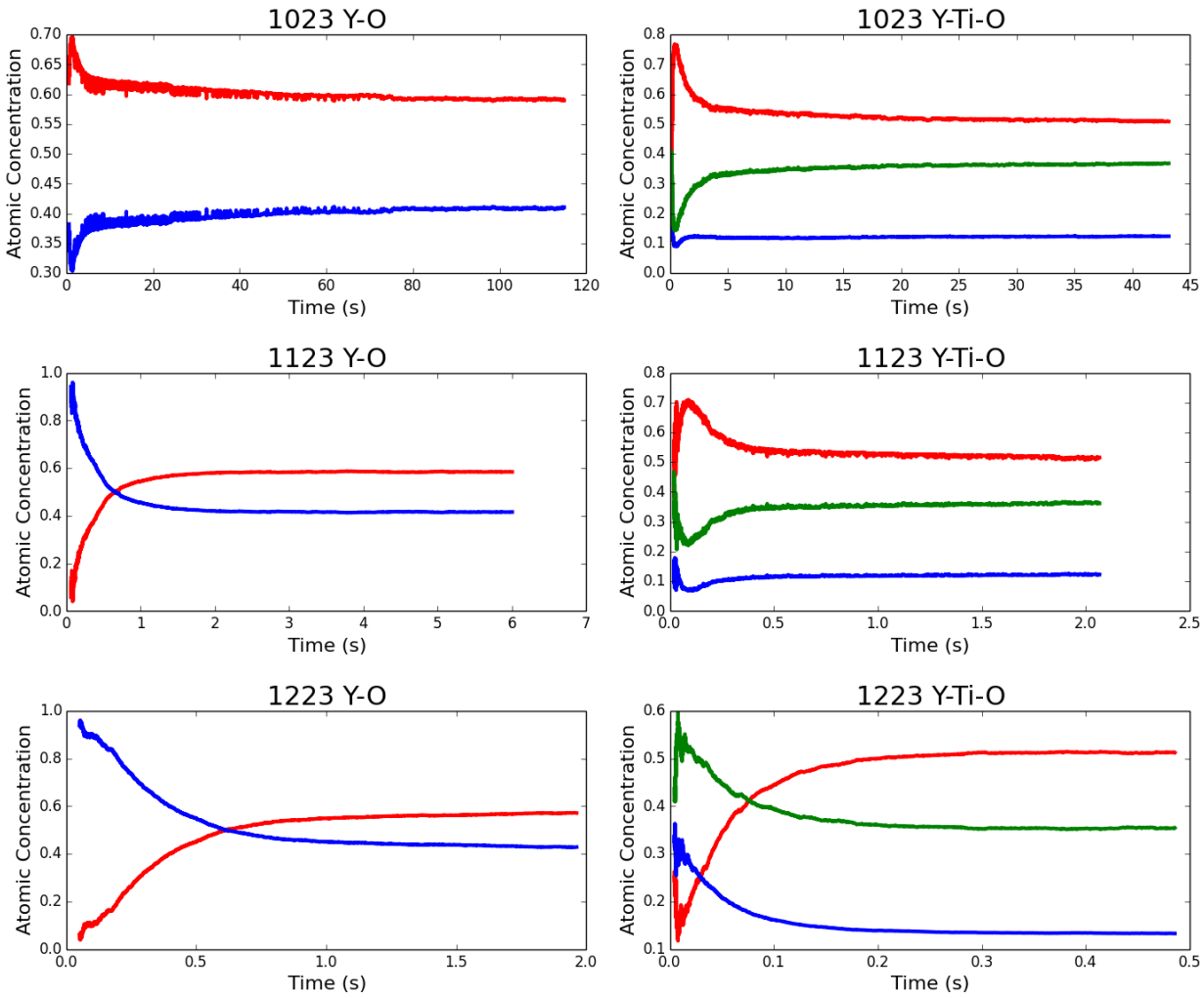

Figure. 4.5: *The evolution of oxide composition over time for the Y-O oxides and Y-Ti-O oxides at all temperatures for 12YWT. Red line = Oxygen, Green Line= Titanium, Blue Line= Yttrium*

Figure 4.5 shows the evolution of the oxide composition in all 12YWT cases. In all cases, the evolution reached a plateau at the end of the simulations. Each of the compositions from KMC were gathered at the very end of the simulation for analysis.

Table 4.9: *Atomic compositions of the Y-Ti-O oxides of the 12YWT -1123K heat treatment and an experimental comparison*

Material System	**at% Y**	**at% Ti**	**at% O**
12-YWT from KMC	13.4%	38.7%	47.2%
12-YWT from Alinger [20]	14.8%	33.6%	39.4%

Table 4.10: *Atomic compositions of the Y-Ti-O oxides of the 12YWT -1123K heat treatment and an experimental comparison*

Material System	**at% Y**	**at% Ti**	**at% O**
14YWT from KMC	12.0%	36%	51%
14YWT from Miller [19]	7.5 ± 4.3	42.2 ± 5.6	43.3 ± 5.3

Tables 4.9 and 4.10 reveal the composition of Y, Ti, and O in the oxides precipitated in the nucleation heat treatments, as well as their expected results. The M:O ratio is roughly 1:1 and the proportion of Ti atoms in the oxide is greater than the Y atom proportion. This is in relatively close agreement with the experimental findings of the oxide composition. The oxides do not follow the stoichiometry of the chemical formulas due to the uneven additions of Y, Ti, and O atoms to the system where there is nearly 3x more Ti than Y. This is reflected in the stoichiometry, since nearly all the solutes were in the oxides.

4.4.4 On Coarsening

The tail end of the KMC simulations showed temporal evolution of the average radius of the oxides decelerating from its initial rapid growth. The growth stage has clearly ended with the plateauing of the evolution of both the average radius and number density of the oxides. At this point, the concentration of solutes in the Fe matrix hovered at the value of the solubility product. The system further decreased the system energy by minimizing the total interface area through coarsening the nano-oxides. Knowing the NFAs inherent resistance to thermal coarsening, the

coarsening stage was analyzed for its behavior according to expectations from classical theory. The temporal evolution of coarsening was expected to follow this law:

$$\bar{R} \sim k \times t^{a}$$

Where *k* is a material constant and *a* is the time exponent. The value of *a* for coarsening is generally 1/3, although there are exceptions. The general theory assumes that the volume diffusion of solutes will be the dominant contributor to coarsening. Research has found that, when coarsening is facilitated by diffusion along grain boundaries and dislocations, the value of *a* will be 1/4 and 1/5, respectively [150]. A combination of the different mechanisms can also lead to *a* values in the same ranges from 0.2 to 0.33. Additionally, the LSW theory assumes a very dilute phase and does not account for the influence of the spatial distribution of the adjacent precipitates [151]. During early coarsening, the time exponent may not align well with the predicted value, but it is agreed that the coarsening exponent will eventually converge to a=1/3 with infinite time.

Table 4.11: *Value of the time exponent a at the tail end of the precipitation simulations*

Material System	**1023K**	**1123K**	**1223K**
Y-O	0.02	0.01	0.02
Y-Ti-O (12YWT)	0.05	0.03	0.012

Table 4.11 shows the value of the power law exponents at the tail end of the precipitation curve. The oxides coarsen through emission and absorption of solutes from their respective precipitates. During the coarsening phase, the nano-oxides were not mobile and there was no coalescence of the oxides. For all compositions and temperatures tested, the power law exponent fell well below the asymptotic growth law $t^{1/3}$. This suggests that the systems are in a pre-ripening stage before they can follow more expected coarsening behavior, especially given that the number densities in each case did not decline from their respective peaks at the end of the growth stage.

This deviation was not unexpected in KMC simulations. Liang saw a time exponent as low as 0.07 in the early stages of coarsening in their Monte Carlo simulations [152].

4.4.5 Additional Investigation

Further investigations of the role of thermodynamics and vacancy movement in coarsening were conducted to identify possible sources for the inhibition of coarsening. The KMC model recorded the energy difference before and after the system underwent thermally induced coarsening in a small simulation box. Information on the location of the vacancy during the coarsening section of precipitation was also gathered.

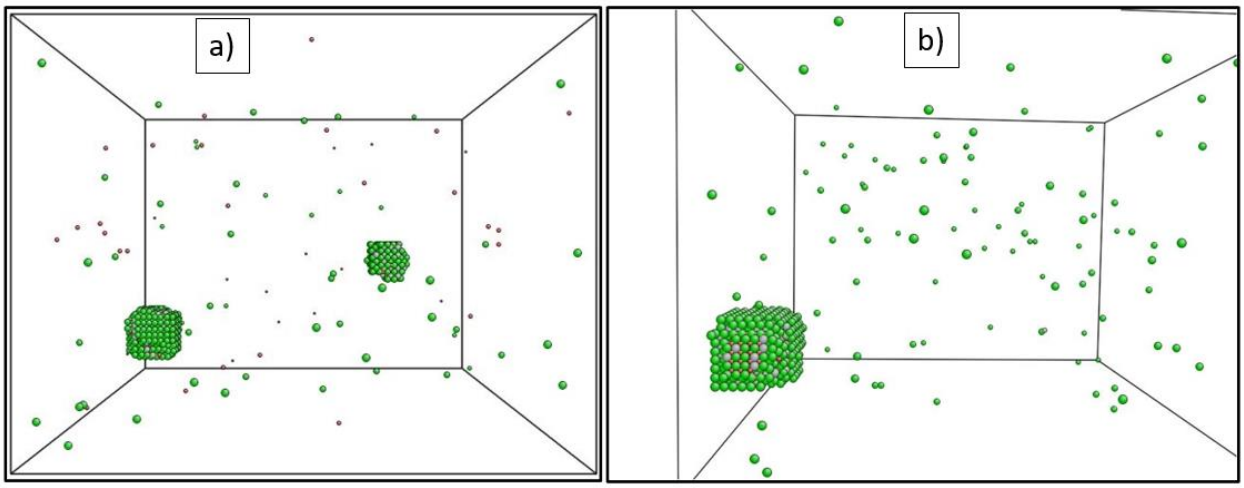

Figure 4.6: *Before and After images of two oxides coarsening into a single oxide at 1673K. Green spheres: Ti atoms, Grey spheres: Y atoms, Red spheres: O atoms*

For ease of investigation, two oxides of different sizes were extracted from the 12YWT composition and placed into a new cell. These oxides were subjected to a much higher temperature at 1673K until the smaller oxide completely dissolved and its constituent atoms joined the larger oxide. The difference in total energy between these two states shown in Figure 4.6 is only -27 eV, making a 0.003% change in the total system energy. This suggests there is a low thermodynamic imperative for the oxides to coarsen.

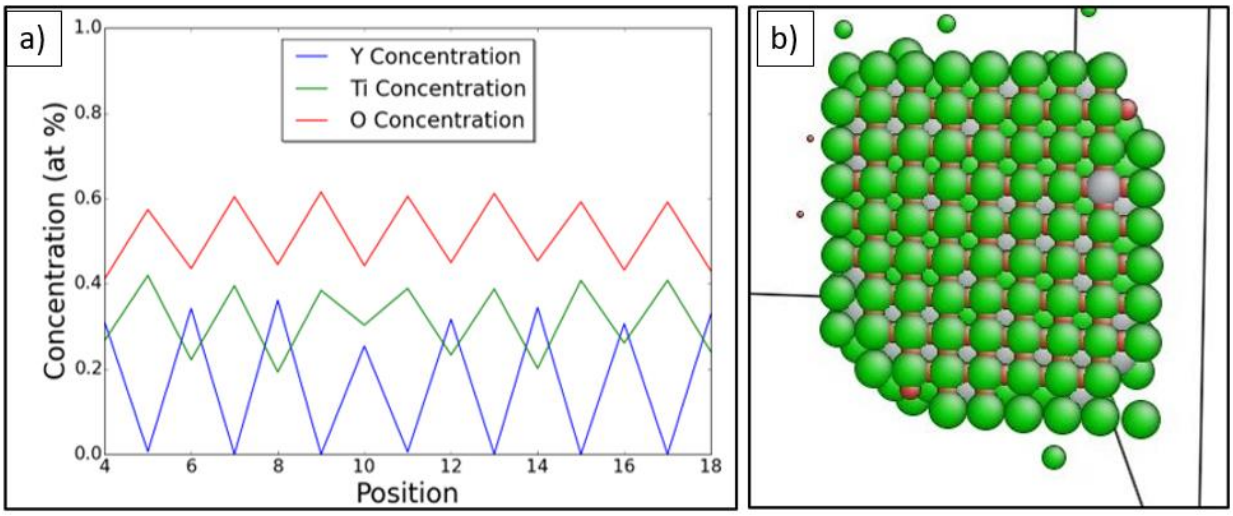

Figure 4.7: *a) Composition profile of a typical oxide in the proportions of 12YWT. b) A cross-section of the oxide precipitate. Green spheres: Ti atoms, Grey spheres: Y atoms, Red spheres: O atoms*

Figure 4.7a displays the composition profile of the single oxide in Figure 4.6b, which is representative of the typical profile in the simulated oxides. Figure 4.7b shows the cross-section of the center of the precipitate. The composition throughout the oxide remains consistent with the absence of a core/shell structure, although there are plane by plane variations in composition that gives information about the structure of the oxide phase. The composition of Y atoms varies the most, oscillating plane by plane between 0 and 30 at%. This structure reflects the thermodynamic preference for the Y atoms to have Ti as their nearest neighbors.

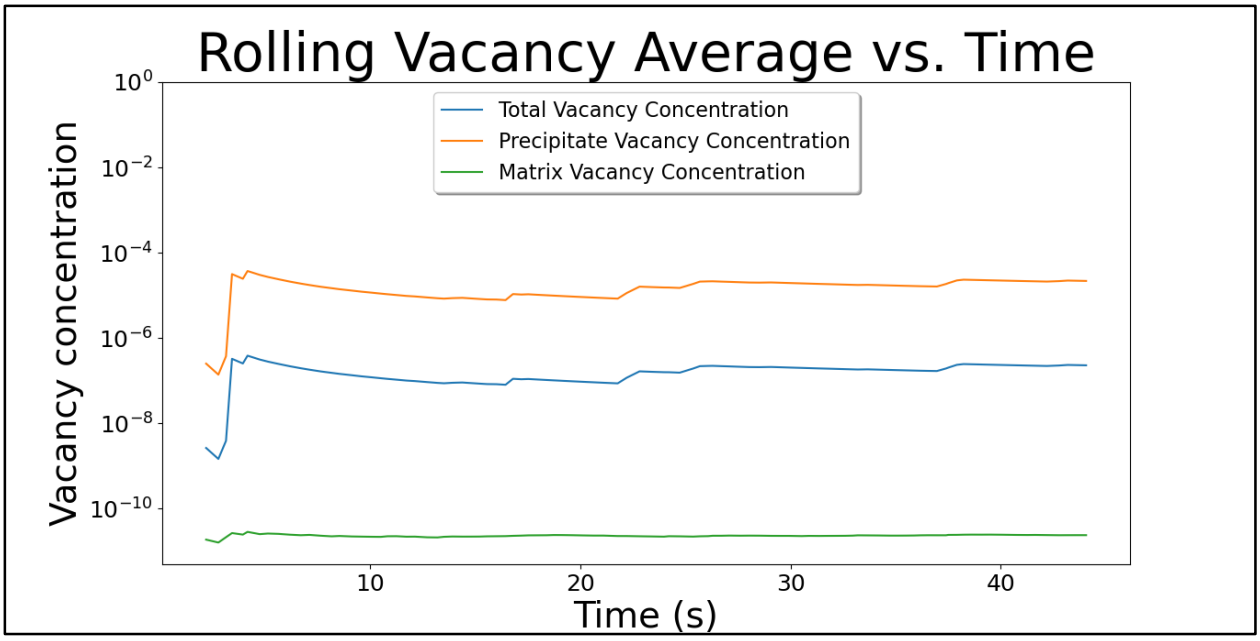

Figure 4.8: *Vacancy Concentration over time at various locations in the simulation box at 1123K*

Figure 4.8 shows the vacancy concentrations in the matrix and at oxide interfaces in the single precipitate simulation box over the course of time at 1123K. While the vacancy concentration in the Fe matrix remains in line with expectations of the thermal equilibrium concentration, the average vacancy concentration at the oxide interfaces is much higher. This means that the vacancy spent a disproportionate amount of time at the interface rather than in the matrix. The attraction is likely due to the high binding energy of the vacancy with Y, Ti, and O.

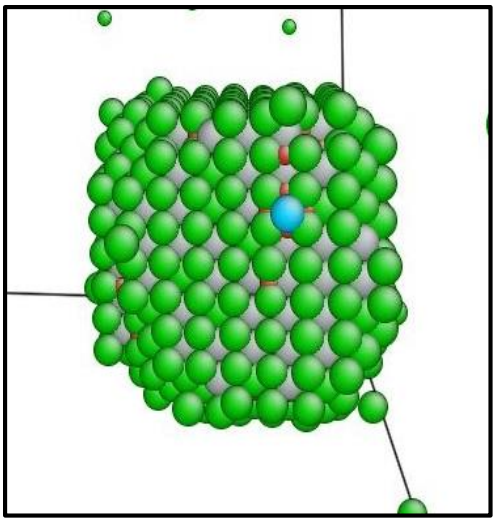

Figure 4.9: *Snapshot of a vacancy at the <100> interface of the YTO oxide. Blue sphere: Vacancy, Grey spheres: Y atoms, Red spheres: O atoms*

Figure 4.9 shows a vacancy at the interface. Following the formulation for binding energy, the energy states of the system (with oxide+vacancy, just vacancy, just oxide, and with neither oxide or vacancy) were collected and it was determined that a vacancy has a binding energy of -1.1 eV at the regular <100> interface.

4.5 Discussion

The KMC precipitation simulations confirmed the oxide precipitation behavior expected from the literature. Given the extremely low solubility product at all temperatures, the majority of the available solutes consolidated into the second-phase oxides with only a small amount of solute remaining, corresponding to the solubility product in the matrix Fe. Increasing the heat treatment temperature resulted in the formation of larger oxides but at a lower number density in both the Y-O and Y-Ti-O cases. The elevated temperature required a larger critical mass of stable nuclei; thus, slowing the rate of nucleation so that more free solutes migrated to existing oxides rather than formed a new stable nucleus.

The Y-O oxides were undersized in the KMC compared to the experimental observations of Ratti [43]. In the current KMC set-up, 8 times the solute material would be required to develop oxides of that size and number density inside the simulation. There could be unseen influences present in the actual material that could enlarge Ratti's average [43], namely the presence of other solutes. Shells of Cr have been observed to form around oxides in ODS steels [153] and larger oxides have been found to contain larger amounts of other impurities [32].

The oxide characteristics of both Ti-containing alloy compositions heat treated at 1123K were compared to experimental results. There was found to be close agreement in the size and number density of the oxides in both the 12YWT and 14YWT cases. The compositions were consistent throughout the precipitate and followed a predictable structure, with Y atoms preferring to be adjacent to Ti atoms. The composition of the Y-Ti-O oxides were also compared to the measured values with similar agreement. The Fe-Ti-Y-O systems were expected to induce the formation of finer oxide precipitates than the Fe-Y-O systems. This behavior was shown when the 12YWT alloys samples produced a higher number density of oxides of similar size to the Y-O results, despite having 3x as much solute material. The cause of these differences occurred during the nucleation stage, as Ti makes it easier for oxides to form. The addition of Ti did not appear to influence the behavior of the alloys in the growth stage, with both Y-O and Y-Ti-O alloys displaying similar growth behavior at all temperatures.

While the Y-Ti-O precipitates from Alinger's nucleation experiments were, on average, larger than the precipitates formed in the model, there were a few differences that could account for it; namely that the material in Alinger's experiments contained many other solutes, such as Cr and W, that could be additional impure components of the oxides. Additionally, the KMC simulations here were limited by the size of the simulation box. With the starting compositions

used, it would take all the solute atoms in the current box to make a single oxide with a radius of 1.5 nm, which is the upper limit expected from the NFAs.

The power law relationship of the precipitate growth with time was investigated for all temperatures studied for the Y-O and Y-Ti-O oxide precipitation. For both alloy compositions, the growth stage of the 1123K and 1223K simulations followed the a=0.5 relationship, while the 1023K simulation did not. The 1023K possibly could be a case of the growth regime ending early due to the lower solubility limits increasing the nucleation rate, so that the relatively large number density of oxides exhausts the matrix of all its solute atoms before the growth rate can achieve the ideal 0.5 time-dependence.

It does not appear that any of the precipitation simulations reached a coarsening stage that showed significant changes in oxide size after the end of the growth stage. Although some research does suggest that the coarsening stage is not expected to be significant during the proscribed heat treatment [42]. However, since the thermal stability of the oxides are a defining feature of the NFAs, coarsening resistance is an expected behavior of the nano-oxides. The inclusion of Ti as a major component in the NFA is a significant reason for the resistance [43]. Once the oxides are formed, atomic material rarely separates from smaller oxides to enrich the larger ones. Miller did an annealing study on three NFAs (12YWT, 14YWT, MA957) at 1573K for 24 hours and found minimal coarsening in the 12WT and 14YWT [154]. Cunningham thermally aged MA957 at more relevant temperatures and found that coarsening would not be significant in the lifetime of the reactor at temperatures below 1173K [42]. Barnard's model also found that, at temperatures below 1175K, the oxides would be thermally stable well past nuclear relevant timeframes [45]. When coarsening did occur in NFAs, it was primarily enabled by a pipe diffusion mechanism involving dislocations which the KMC model did not incorporate [155]. The coherency inherent in the KMC

model's rigid lattice could also influence the coarsening behavior, since coherency reduces the interfacial energy, which weakens the Gibbs-Thomson effect that drives coarsening [156].

Values of the coarsening exponent *a* found in the KMC are very low, in the 0.01-0.05 range. It could be that the KMC model is limited in its timescale, given that the low thermodynamic push for oxide coarsening ensures very slow rates of change in oxide size in this stage. So, the coarsening stage may not have been reached or been detectable upon cessation of the simulations. Huse found that lower *a* values are probably the result of insufficiently long simulation times [157]. Coarsening requires solutes to be removed from existing oxides; an event that occurs much less frequently than the vacancy jump of an isolated solute in the matrix. The low solubility of Y in the Fe matrix is credited more for coarsening resistance in the NFA than the slow Y diffusion [45]. Therefore, the timescale to observe the coarsening stage could be many orders of magnitude greater than the timescale to observe the nucleation and growth stages. Indeed, the limitations of the KMC in fully reaching the coarsening stage due to computational expense is a common issue even for other systems [158], although the models can be carefully modified [159].

The effect of the local environment on the early stages of coarsening should also be considered. The LSW theory of coarsening is based on assumptions of a dilute system and of coarsening controlled through long range diffusion of solutes in the bulk. When the transport of solutes occurs via vacancies, there is potential for deviations from the $t^{1/3}$ law. Huse predicted that early departures occur when there is a large amount of diffusion activity at the interfaces between the two phases [157]. This is relevant, given that the small size and high number density of the nano-oxides result in a high oxide interface area in NFAs. The high vacancy binding energies of the solutes, combined with the oxides' thermodynamic desire to reshape themselves, as seen in Section 4.4.5, suggests that the vacancy in this KMC model will spend disproportionate time at

the oxide interfaces. Follow-up investigations confirm that the thermal vacancies spend much more time at the interfaces than transporting solutes from oxide to oxide, due to vacancy binding with the solutes. As the total interface area declines and the oxides coarsen into larger precipitates, the time exponent should grow to a value more in line with the asymptotic law, as evidenced by Prévot [160].

Now that there is reliability of the KMC model to replicate the precipitation behavior of the NFAs and reproduce the equilibrium shape, there is confidence to extend the KMC model to replicate other relevant behavior. The stability of the oxides under neutron irradiation bombardment is the obvious next step in the research of NFA material. Additionally, a 5^{th} element, the He produced from transmutation, can be added to the KMC model so that formation of He bubbles can be analyzed.

4.6 Conclusions

A Kinetic Monte Carlo was created to simulate the homogeneous precipitation of Y-O and Y-Ti-O nano-oxides in idealized NFAs. The KMC model was able to replicate the expected size, number density, and shape of the Y-Ti-O oxides. The role of Ti in producing finer oxides was confirmed in the comparison between Y-O and Y-Ti-O results. The coarsening behavior was also investigated and showed that, despite not having dislocations in the simulated material, the nano-oxides still were very resistant to coarsening in the timeframe of the KMC because of the vacancy trapping at the oxide interfaces.

Chapter 5: Grain Boundary Precipitation and Neutron Irradiation in Fe-Y-Ti-O Alloys

A critical aspect to the material strength of the NFAs are the behavior around defect sinks like the grain boundary during precipitation and irradiation. The precipitation simulations from Chapter 4 were repeated with the KMC model adjusted to include a grain boundary in the simulation box. After analysis, the oxide distributions generated were subjected to irradiation conditions similar to a reactor environment. The results were analyzed for insight into the mechanisms controlling the growth and decay of nano-oxides under irradiation.

5.1 Nano-oxide Dissolution Mechanisms

Another attractive property of nano-oxides are their resistance to dissolution under intense irradiation, which helps ensure that the material remains in good condition throughout its lifespan. A literature review from Wharry on experimental studies testing the survivability of nano-oxides under intense irradiation found mixed and sometimes contradictory results across the studies [53]. Some studies found that the oxides were stable when irradiated above 873K, while other studies showed that the oxides became less stable at that same temperature. Many of these discrepancies are attributed to differences in material processing, testing environment, and characterization techniques; thus, more study is required.

The changes in size and composition of the nano-oxides under irradiation have been attributed to a number of proposed mechanisms. The most prominent being: Ostwald ripening, ballistic dissolution, and irradiation enhanced diffusion, and homogeneous nucleation.

Ostwald ripening of the precipitates, where the smaller oxides dissolve and have their constituent atoms join larger precipitates in an effort to lower the system energy by reducing the surface area of the oxides. This a thermal process that would be brought on by the elevated temperatures in the reactor rather than the irradiation. Though, it has been suggested the Ostwald ripening would only occur for incoherent nano-oxides. As a study by Chen showed that changes in size were much more pronounced in incoherent particles than coherent particles, likely owing to the much larger interface energy of incoherent oxides [161]. Since the current KMC model can only simulate coherent precipitates, it is unlikely we will observe such an effect.

Ballistic Dissolution: In this relatively self-explanatory mechanism, the high-energy particles blast atoms out of the oxide precipitates. These solute atoms will either diffuse back into the precipitate, join another precipitate, attach itself to a defect sink, or form a new precipitate.

Irradiation enhanced diffusion: The premise being that the increased amount of point defects in the system is primarily responsible for any dissolution and coarsening of the oxide particle. Since diffusion in the metal matrix hinges on the point defects to act as diffusion carriers for the atoms, the increased amount of point defects due to irradiation will speed the kinetic processes inside the material, including dissolution of unstable particles to occur at relevant time scales. Also, the introduction of the interstitial dumbbells as diffusion carriers changes how the solutes diffuse through the metal. It can lead to segregation of solute elements at the defect sinks or coarsening of oxides in ways not seen under just vacancy mediated diffusion. A previous review by Wharry highlights the role of interstitials in the grain boundary segregation of Cr [76].

This study used a newly developed KMC method to model the NFA system under neutron irradiation. The project builds off the KMC model that simulates the precipitation of Y-Ti-O oxides in the bulk region of an NFA in Chapter 4. First the presence of a grain boundary was incorporated into the model to provide a sink for the point defects. Then, a method for simulating neutron irradiation was developed for the model.

The end goal of this study is to construct a KMC computer model that can both simulate the precipitation kinetics of the oxides in an Fe-Ti-Y-O system and the response of the oxides to neutron irradiation events inside a reactor. The KMC model was able to simulate neutron irradiation and the resulting cascade of displacements efficiently enough to reach relevant dpas (i.e., those seen in irradiation experiments). The relationship of oxide survivability under conditions such as temperature and dose rate were investigated. Additionally, this study aimed to compare findings regarding precipitation behavior of $Y_2Ti_2O_7$ in the bulk and near a grain boundary, the shape of the oxides produced, and the irradiation response of the system to other irradiation experiments and to the literature.

5.2 Methods

5.2.1 The KMC Model

The material system is represented in the KMC model similarly to the model constructed by Hin [80, 81]. The point defects required for atomic migration - the vacancies and interstitial dumbbells - both exist on the substitutional lattice: the vacancy as a vacant site and the dumbbell as two atoms occupying the same lattice site. For thermodynamic considerations, all interstitial dumbbells are assumed to be oriented in the <110> position since it is the most energetically favored position of the Fe-Fe dumbbell [93].

***Table 5.1**: Diffusion parameters for Fe-Ti-Y-O-He system*

Input Parameter	Value	Unit	Reference
lattice parameter	2.87×10^{-10}	m	
Vacancy Migration Energy, Fe	0.66	eV	[80]
Vacancy Migration Energy,Y	0.23	eV	[99]
Vacancy Migration Energy,Ti	0.81	eV	[81]
Interstitial Migration Energy, Fe	0.35	eV	[84]
Interstitial Migration Energy, Y	0.21	eV	calculated
Interstitial Migration Energy, Ti	0.24	eV	calculated
Vacancy Formation Energy	2.24	eV	[80]
Oxygen Migration Energy	0.48	eV	[100]
Vacancy pre-exponential factor, Fe	6.0×10^{-4}	m^2/s	[80]
Vacancy pre-exponential factor, Y	3.7×10^{-7}	m^2/s	[99]
Vacancy pre-exponential factor, Ti	2.1×10^{-1}	m^2/s	[81]
Interstitial pre-exponential factor, Fe	1.0×10^{-5}	m^2/s	
Interstitial pre-exponential factor, Y	1.0×10^{-5}	m^2/s	
Interstitial pre-exponential factor, Ti	1.0×10^{-5}	m^2/s	
Interstitial attempt frequency	1.0×10^{14}	/s	

***Table 5.2:** Pair-interaction energies (eV) for the Fe-Y-Ti-O system taken to the 4^{th} nearest neighbor in the simple cubic frame of reference*

Pair-Interaction Energies	1 (eV)	2 (eV)	3 (eV)	4 (eV)
Fe-Fe	-	-	-0.611	-0.611
Fe-Y	-	-	-0.59	-0.52
Y-Y	-	-	-0.57	-0.69
Fe-Ti	-	-	-0.65	-0.53
Ti-Y	-	-	-0.71	-0.68
Ti-Ti	-	-	-0.69	-0.70
Fe-V	-	-	-0.21	0.00
Y-V	-	-	-0.35	0.00
Ti-V	-	-	-0.35	0.00
Fe-I	-	-	-0.10	0.00
Y-I	-	-	0.25	0.00

Ti-I	-	-	-0.10	0.00
Fe-O	0.00	0.00	-	-
Y-O	-0.01	-0.11	-	-
Ti-O	-0.04	-0.04	-	-
O-O	0.10	-0.116	0.10	-0.116

Tables 5.1 and 5.2 list the kinetic and thermodynamic parameters for the Fe-Ti-Y-O system. The rationale behind each parameter is detailed in Chapter 2.

Migration of the interstitial dumbbells, recombination of point defects, and the treatment of grain boundary point defect annihilation for the KMC model follows the method laid out by Soisson [84]. This KMC model has periodic boundary conditions where mobile defects that migrate out of the simulation box emerge at the opposite side. To study the influence of a defect sink on precipitation, a grain boundary is placed inside the simulation box, where the grain boundary is represented as a perfect planer sink that is a single atomic layer wide. During irradiation simulations, defect sinks (like the grain boundaries) and recombination of the vacancy and interstitial dumbbells are primarily responsible for the removal of point defects from the simulation box.

5.2.2 Treatment of the Grain Boundary

At the grain boundary (simulated here as a perfectly planar sink), energy exists from the imperfections at the boundary. This energy makes it more or less preferable for particular solutes to congregate at the grain boundary. Each solute species has a certain segregation energy that is added to the calculation of the migration energy while the solute is in the plane of the grain boundary. There is a slight temperature dependence of the segregation energies given by the entropy.

Table 5.3: *Segregation enthalpy and entropy of selected solutes in bcc Fe*

Atomic Species	**ΔH**	**ΔS**
O	0.9984 eV	4.784×10^{-4} eV/K
Ti	0.3328 eV	3.016×10^{-4} eV/K
Y	0.6448 eV	6.552×10^{-4} eV/K

The O and Ti segregation values are from values calculated by Lejcek and the Y segregation values were found for this study from the solubility limit of Y in bcc Fe using Lejcek's method [113]. Each of the solutes are assumed to be encountering a general type grain boundary. The KMC model treats the segregation as such: when solute atoms are present on the same plane as the grain boundary, the segregation energies are added to the migration energies calculations. This either repulses the solute or inhibits the solute's departure from the grain boundary and on the large scale potentially results in the enrichment or depletion of that solute's atomic species at the grain boundary.

5.2.3 Neutron Irradiation

The primary source of damage during irradiation is from the impact of high energy neutrons with metal atoms in the material. The collision creates a cascade of displacements, which introduces defects into the material such as vacancies and interstitial dumbbells. Neutrons emitted from the nuclear reactions in the fuel are expected to have energies in the 0.1 MeV to 10 MeV range [162].

To simulate the neutron impact, we start with the assumption that the neutron has an energy of 1 MeV. The neutron strikes a random substitutional site in the matrix and is assumed, due to the small box size, to proceed out of the matrix without depositing more energy. The atom struck is

referred to as the primary knock-on atom (PKA) and all subsequently displaced atoms are called secondary knock-on atoms (SKAs). These SKAs, imparted with an energy E_{SKA}, will then move through the metal matrix and lose energy as they collide with other atoms and energy will be exchanged. The exchange of energy in the collisions is assumed to be elastic.

$$\begin{cases} E_{SKA} \geq E_d & Dislodge\ new\ atom\ and\ make\ new\ SKA \\ E_{SKA} < E_d & Form\ interstitial\ dumbbell \end{cases}$$

If the E_{SKA} of the resting atom rises above the threshold displacement energy E_d, then the resting atom will be energized to vacate its lattice site on its own path and become another SKA in the cascade. When the energy of the SKA falls below the threshold energy and collides with a sitting atom, an interstitial dumbbell forms on that lattice site. Once formed, this dumbbell is open to recombination with the vacant sites left behind in the cascade. At the end of a cascade, a small amount of vacancies and dumbbells that have not recombined are left in the simulation box.

Displacement cascades have been simulated using molecular dynamics (MD) [70], although it is cost prohibitive to computationally use for long term irradiation studies. Atoms do not stay on a rigid lattice in molecular dynamics simulations and the atoms are allowed to relax to more energetically favorable positions. This requires constant tracking of atomic locations and recalculation of the atomic interactions so that the timescale of MD simulations is in the nanosecond range. Relaxation of atoms is not accounted for in the KMC model with the atom strikes taking place instantaneously in a rigid lattice point. This sacrifice in precision allows the KMC model to achieve timescales that can reach irradiation doses up to 70 dpa and beyond. The irradiation mechanism also does not account for bonds between atoms with the E_d of the atom only being dependent on the atomic species. A method validating the neutron irradiation mechanism by tracking the number of displacements generated is provided below as well as a description of the ‘dpa’ unit that measures irradiation damage.

Neutron Irradiation Mechanism

With the adoption of the 'dpa' unit in the literature, neutron absorption cross-sections and neutron fluxes are not required. It has become common for the rate of accumulated damage from irradiation to be expressed as the simple dpa/s. While the damage rate in any material will vary by depth, for small targets like the simulation box, the dpa/s remain practically constant across the entire volume. The probability of a neutron strike $\Gamma_{neutStrike}$ is set to the user-inputed dose rate G_{dpa} in dpa/s and adjusted using the ratio of number lattice points in the box N_{box} and the average number of displacements in a cascade $\overline{N_d}$. This ensures that the correct number of neutron strikes occurs to give the right dpa over the right time period.

$$\Gamma_{neutStrike} = G_{dpa} \times \frac{N_{box}}{\overline{N_d}} \quad (1)$$

The $\overline{N_d}$ from the resulting cascade is estimated by the following equation:

$$\overline{N_d} = \frac{\Lambda E_n}{4 * E_d} \quad (2)$$

$$\Lambda = \frac{4A}{(1+A)^2} \quad (3)$$

E_n is the initial energy of the neutron, A is the atomic mass number, and E_d is the threshold displacement energy. For Fe, the E_d is set to 40 eV based on literature values. Inside the oxides, the threshold displacement energy for the atoms is set to 57 eV, which is tied to other irradiation studies [163]. Note that these formulas represent an average rather than a set constant [95]. This is a general relationship from Kinchin and Pease [96] that has been found to overestimate the number of displacements from neutron irradiation. Thus, the neutron irradiation is validated by tracking the number of displacements generated by a single displacement cascade and averaging over several trials. For a single 1 MeV neutron striking an all Fe matrix, the resulting displacement

cascade should be around 430 displacements if Eq. 2 and Eq. 3 are followed. A validation procedure was developed and utilized below.

Validation Procedure:

1. Construct a simulation box 100X100X100 of pure Fe with no defects.
2. Track 3000 separate displacement cascades caused by 1MeV neutrons in the box.
3. Find the average $\overline{N_d}$ of displacements per cascade in the KMC and compare against prediction.

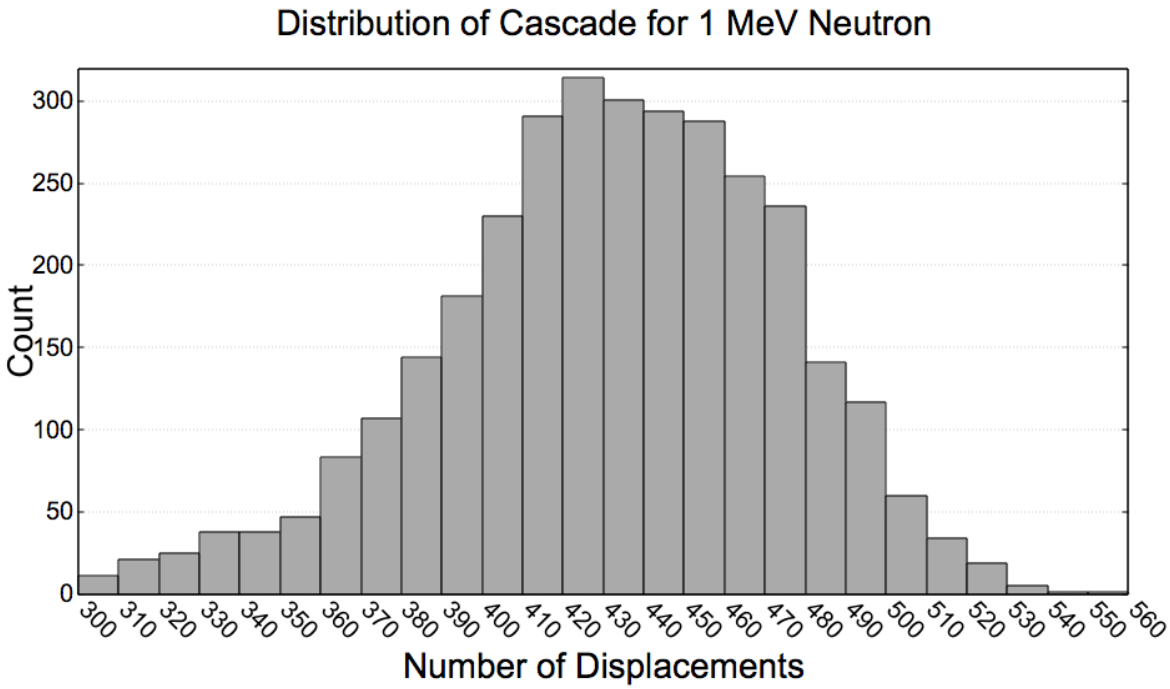

Figure 5.1: *Histogram of the number of displacements produced by each 1MeV neutron strike*

Figure 5.1 is a histogram of the collected number of displacements in each of the 3000 neutron strikes. The average $\overline{N_d}$ was found to be 430.9 displacements per neutron strike in the

pure Fe, which aligns with the prediction from the formulas. From this accounting of $\overline{N_d}$, the displacement cascade mechanism is proven to be usable for the KMC.

5.3 Simulation Procedure

5.3.1 Precipitation

To observe the precipitation behavior of $Y_2Ti_2O_7$ in a ferritic matrix, the bulk processing simulations for 12YWT and 14YWT-like alloys performed in Chapter 4 were used as a reference against KMC simulations that performed the same procedures here except in the presence of a defect sink. The alloy of choice to observe the influence of temperature on precipitation was similar to the commercial alloy 12YWT. Samples of another alloy, 14YWT, were heat treated in simulation alongside the 12YWT for later use in the irradiation simulations.

Table 5.4: *Model alloy compositions for the 12YWT and 14YWT cases*

Material System	**Y at%**	**Ti at%**	**O at%**
12YWT Atomic Concentration	0.13 %	0.4 %	0.18 %
14YWT Atomic Concentration	0.08 %	0.27 %	0.3 %

Table 5.4 lists the atomic concentrations for both alloys of the key solutes Y, Ti, and O in the bcc Fe matrix with the remainder being Fe. Other elements, such as Cr and W, were not included. Note that the atomic concentrations of the constituent solutes are not an exact reflection of the expected stoichiometry of the oxide nanoparticles. There are various reasons for this—

research has shown that keeping the Ti:Y ratio above 1 and limiting excess oxygen in the metal matrix is important for the thermal stability of the oxides at high temperatures [44]. These factors also limit the degree of coarsening in the system.

A simulation box of the same size as the prior bulk precipitation simulations was constructed with a simulated grain boundary in the center. The grain boundary was represented by a perfect planar sink where vacancies were annihilated once they migrated onto the boundary plane. Once the Fe-Ti-Y-O system was populated with the appropriate number of atoms and makes a supersaturated solution, the thermal precipitation simulation began. The simulations were run at 3 temperatures (1023K, 1123K, and 1223K) for the 12YWT and at 1123K for the 14YWT composition. The 1123K simulation was compared to experimental results obtained by Alinger for the 12YWT [20] and Miller for the 14YWT [19]. Table 5.5 lists the conditions of the simulation including the size of the simulation box.

Table 5.5: *Test conditions for the precipitation heat treatment simulations with a grain boundary*

	Size of KMC Box	**Temperature**	**# Simulations**
12YWT Conditions	400X100X100 lattice points	1023K, 1123K, 1223K	3
14YWT Conditions	400X100X100 lattice points	1123K	3

The precipitation simulations ceased when there was little change in the oxide characteristics after the nucleation and growth stages. Then, the average radius and number density of the oxides were recorded for comparison to the results found for homogeneous precipitation in

bulk from a prior study. The shape of the precipitated oxides was also qualitatively compared against the expectations from Ribis[92] for the general shape of Y-Ti-O oxides.

5.3.2 Neutron Irradiation

To study survivability of the oxides, oxide distributions created during the precipitation simulations were subjected to a simulated irradiation environment. For the sake of controlling possible factors, the atomic configuration from a single heat treatment simulation was used. For this study, we used the end configuration from the 1123K precipitation heat treatment. The oxide characteristics for the 12YWT-1123K simulation has a number density of 2.0×10^{24} m^{-3} with an average radius of 0.8 nm. The simulations were set up to mimic reactor environments in the same ranges as Wharry collected for their review[53].

These irradiation simulations explored the influence of temperature and dose rate on oxide characteristics by varying the irradiating conditions for each set of samples. The dose rate, based on average displacements per neutron strike, had a range of three possible values: 10^{-3} dpa/s to determine resistance of the oxides to dissolution under very heavy irradiation, 10^{-5} dpa/s to determine the results at a dose rate closer to experimental rates, and 10^{-4} dpa/s to observe any patterns from the direction of dose rate. In the simulation box, the dose rates 10^{-3}, 10^{-4}, and 10^{-5} dpa/s would correspond to total neutron fluxes of 1 MeV neutrons of roughly 1.7×10^{17}, 1.7×10^{16}, and 1.7×10^{15} $\frac{neutrons}{cm^2\ s}$ respectively. Three irradiation temperatures were evaluated to observe the temperature dependence of oxide survivability. The temperatures were 673K, 773K, and 873K so as to capture the widest range of reactor conditions. Table 5.6 lists these conditions along with simulation box size.

Table 5.6: *Irradiation conditions for the neutron irradiation simulation on 12YWT*

	Size of KMC Box	**Temperature**	**Dose Rate**	**# Simulations**
12YWT Conditions	400X100X100 lattice points	673K, 773K, 873K	$10^{-5}, 10^{-4}, 10^{-3}$ dpa/s	3

Additionally, the KMC model attempted to replicate the findings from a neutron irradiation simulation. The composition of the alloy in question was the 14YWT rather than the 12YWT alloy. The exact irradiation conditions and oxide characteristics are listed in Table 5.7.

Table 5.7: *Irradiation conditions described in the neutron irradiation experiments on 14YWT from Aydogan [164]*

	Size of KMC Box	**Temperature**	**Dose Rate**	**# Simulations**
14YWT Conditions	400X100X100 lattice points	633 K	6.5×10^{-7}, dpa/s	6

For all cases, the size and number density of the nano-oxides were recorded over the course of the simulation run at regular intervals. From this information, a curve was constructed to show the change in oxide characteristics over irradiation damage in units of dpa. The distribution of the oxide sizes before and after the irradiation were also recorded and compared. The composition of the oxides was tracked over the accumulated dose as well.

This KMC model can only be used for cases where a grain boundary exists in the simulation box because the presence of a point defect sink for the vacancies and interstitials was required. Otherwise the only mechanism for point defect removal would be through recombination, which would keep the concentration of vacancies and interstitials equivalent to each other at all points in

time. That would not be an accurate depiction of the point defect population in an NFA under irradiation. Therefore, there are no irradiation simulations in bulk Fe in this study.

5.3.3 Long-term Irradiation

Since the NFAs are expected to receive a lifetime dose in the 100 dpa range, an investigation of the stability of the nano-oxides under longer term irradiation was merited. It is presently impractical to extend the simulated irradiation regimes past 8 dpa for all conditions. The single regime selected for long-term irradiation was chosen primarily for the real-time speed of completion as opposed to the other regimes. In this case, the irradiation regime at 873K and 10^{-3} dpa/s was used to take three 12YWT samples to a total dose of 66 dpa. The evolution of the oxide characteristics as a function of dose was also recorded for analysis.

5.4 Results

5.4.1 Precipitation Results

A. Precipitation in the Presence of a Defect Sink

To study the influence of the grain boundary, results for precipitation in the presence of a defect sink from the KMC were compared to results from a prior study that simulated precipitation in the bulk region of NFAs. The only distinction between the two cases was the presence of the grain boundary. Any differences in the oxide characteristics between the two simulation conditions were noted.

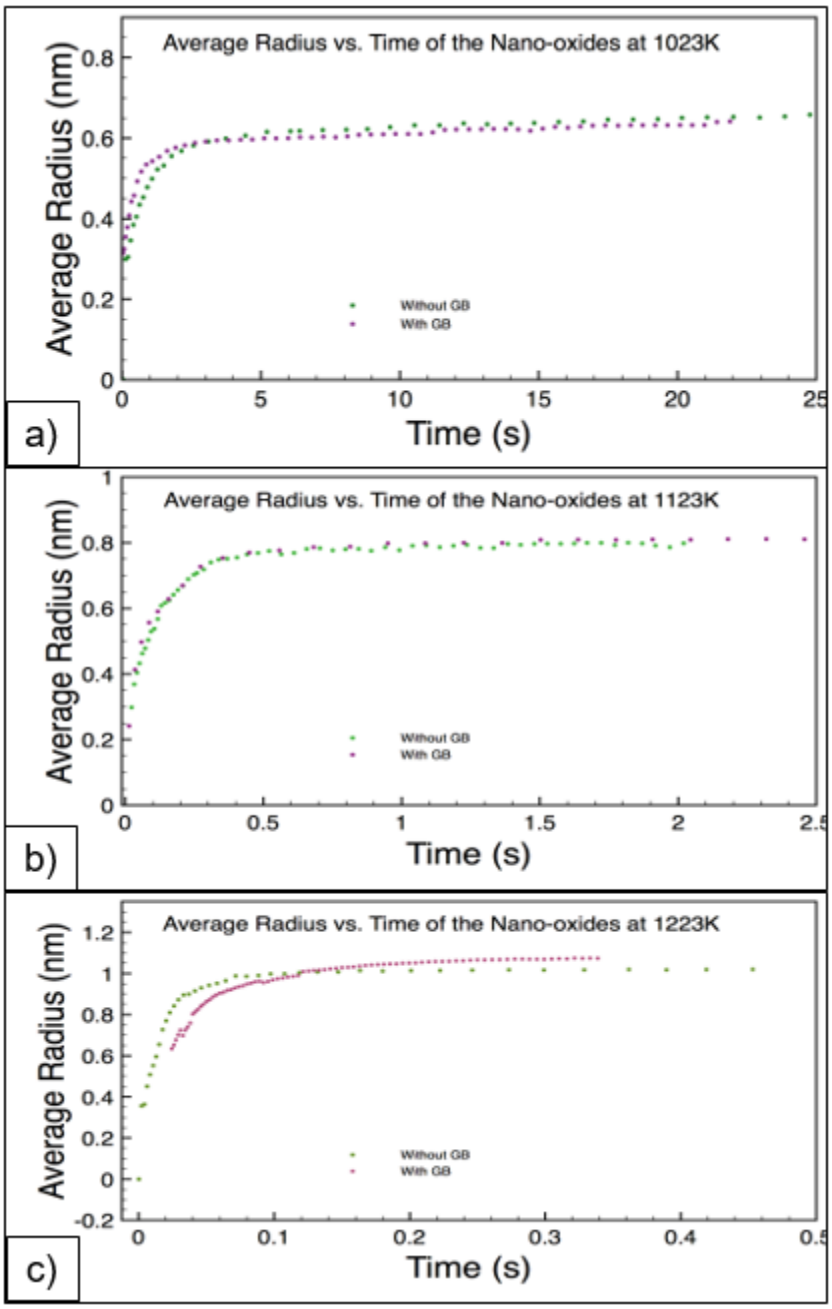

Figure 5.2: *The evolution of oxide size with time with and without a grain boundary for the 12YWT composition at a) 1023K b) 1123K and c) 1223K*

Figure 5.2 compares the kinetic evolution at three temperatures for the 12YWT with and without a grain boundary in the box. There was little difference in the average size of the oxides between the two conditions. There was, however, a qualitative difference in the location of the

oxides. While the oxides were evenly distributed in the bulk precipitation simulations, the area around the planar sink in the grain boundary simulations was depleted of oxide precipitates. However, this precipitate free zone only extended 1-2 nm away from the planar sink.

B. Oxide Composition

The KMC model was further validated by comparing the composition of the oxides formed during the simulation against experimental findings. The oxide compositions in the KMC model were gathered at the end of the precipitation simulations.

Table 5.8: *The atomic compositions of the Y-Ti-O oxides of the 12YWT -1123K heat treatment with and without a grain boundary in the simulation box and an experimental comparison*

Material System	**Y at%**	**Ti at%**	**O at%**
12-YWT KMC Without GB	12.9%	37.6%	47.9%
12-YWT KMC With GB	12.7%	36.1%	50.9%
12-YWT Alinger[20]	14.8%	33.6%	39.4%

Table 5.9: *The atomic compositions of the Y-Ti-O oxides of the 14YWT -1123K heat treatment with and without a grain boundary in the simulation box and an experimental comparison*

Material System	**Y at%**	**Ti at%**	**O at%**
14YWT KMC Without GB	12.1%	36.9%	50.8%
14YWT KMC With GB	12.0%	36.4%	51.6%
14YWT Miller[19]	7.5 ± 4.3	42.2 ± 5.6	43.3 ± 5.3

Tables 5.8 and 5.9 show the composition of the oxides formed in the precipitation heat treatments in systems with and without the grain boundary as well as their expected results from

the literature. For both sets of simulations, the compositions of the oxides were very similar, suggesting that the defect sink had little influence on the composition of oxides outside its immediate vicinity. There was roughly a 1:1 ratio of metal to oxygen atoms (M:O) and there were more Ti atoms in the oxide than Y atoms. This is in relatively good agreement to the experimental findings of the oxide composition, although the minor constituent Cr was absent from the oxide compositions since the element was excluded from the KMC model. The oxides deviated from the stoichiometry of the oxide chemical formula due to the unbalanced starting concentrations of solutes.

C. Precipitate Shape

After thermal aging, the vast majority of the Y, Ti, and O atoms were associated with an oxide precipitate and the concentration of solutes in the Fe matrix corresponded to the solubility product in iron. The shape of the oxides at this new equilibrium was investigated visually for compliance with expectations from experiments. The final recorded atomic positions of the Y, Ti, and O atoms were visualized using ATOMEYE software [117]. The matrix Fe atoms were made transparent for the purpose of visualization.

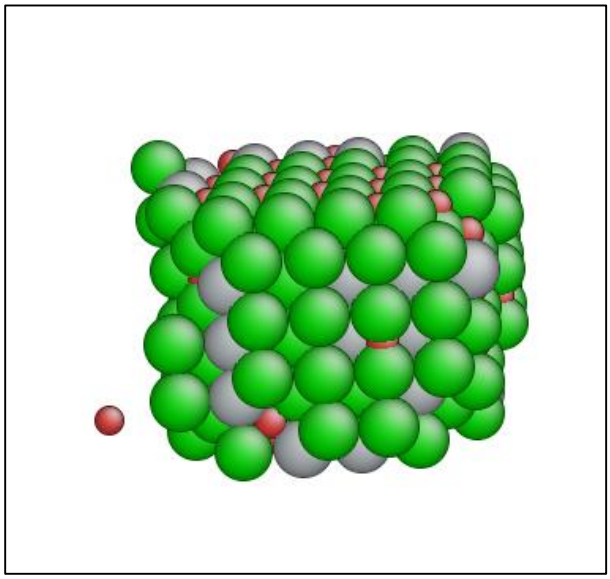

Figure 5.3: *Oxides in 12YWT-1123K after heat treatment. Green spheres: Ti atoms, Grey spheres: Y atoms, Red spheres: O atoms*

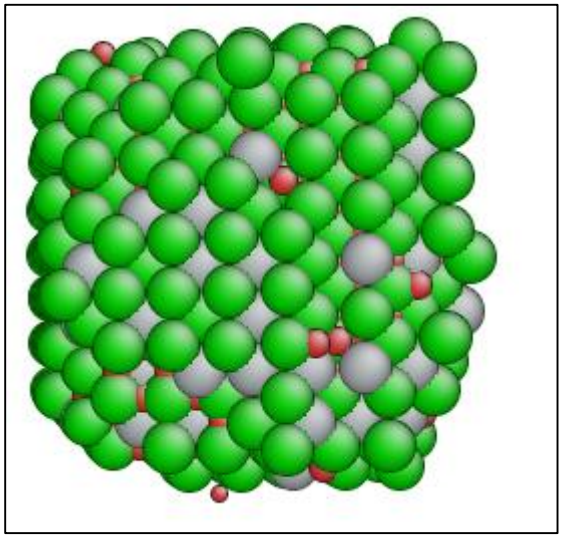

Figure 5.4: *Oxides formed in the 14YWT-1123K section. Green spheres: Ti atoms, Grey spheres: Y atoms, Red spheres: O atoms*

Figure 5.3 is a representation of the simulation box at the end of precipitation for the 12YWT-1123K concentrations. Figure 5.4 is a representation of the simulation box for the 14YWT-1123K concentrations. In all heat treatments, the Y, Ti, and O atoms clustered together

and formed cubic oxides. The interfaces were sharp with <100> faces and fairly small <110> and <111> faces. The cubical shape that the oxide precipitates tended to nucleate into was expected from Ribis [92].

5.4.2 Irradiation Results

Using the oxide distributions created during the thermal aging simulations with a grain boundary, the set of neutron irradiation simulations commenced. The 12YWT-1123K distribution was subjected to nine total irradiation regimes at three temperatures and three dose rates. 14YWT-1123K was subjected to irradiation conditions similar to an experiment for comparison purposes. The observed trends are recorded below in Figures 5.5 and 5.6.

A. 12YWT Irradiation Simulations

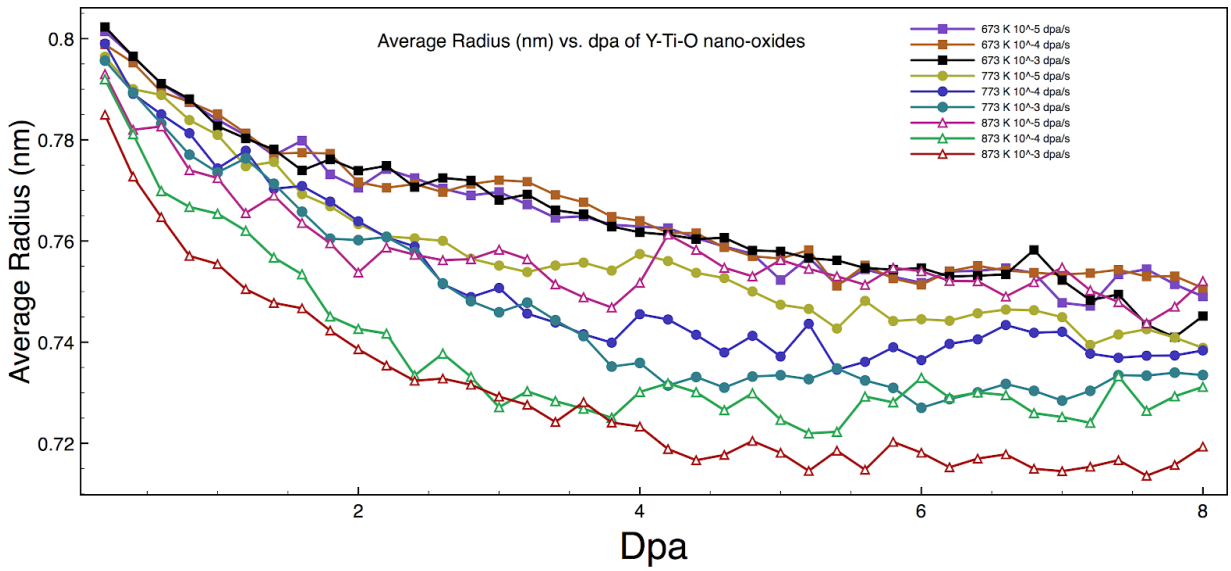

Figure 5.5: *Evolution of the average oxide size in 12YWT over total accumulated dose at a variety of irradiation regimes*

Figure 5.5 shows the average radius of the oxides over accumulated damage dpa for all tested temperature and dose rate combinations. Across all irradiation regimes, a small decline was seen in the size of the oxides that sharply began at the 1-4 dpa region before appearing to reach a

plateau in the 4-8 dpa range. The oxides experienced less atom loss with decreasing temperature. At the lowest dose rate ($10^{-5}\ dpa/s$), there was more loss of oxide size compared to the oxides irradiated at the same temperature but at higher dose rates, although the differences in the precipitate size per dose rate declined with decreasing temperature with the 673K batch showing little variability between dose rate results.

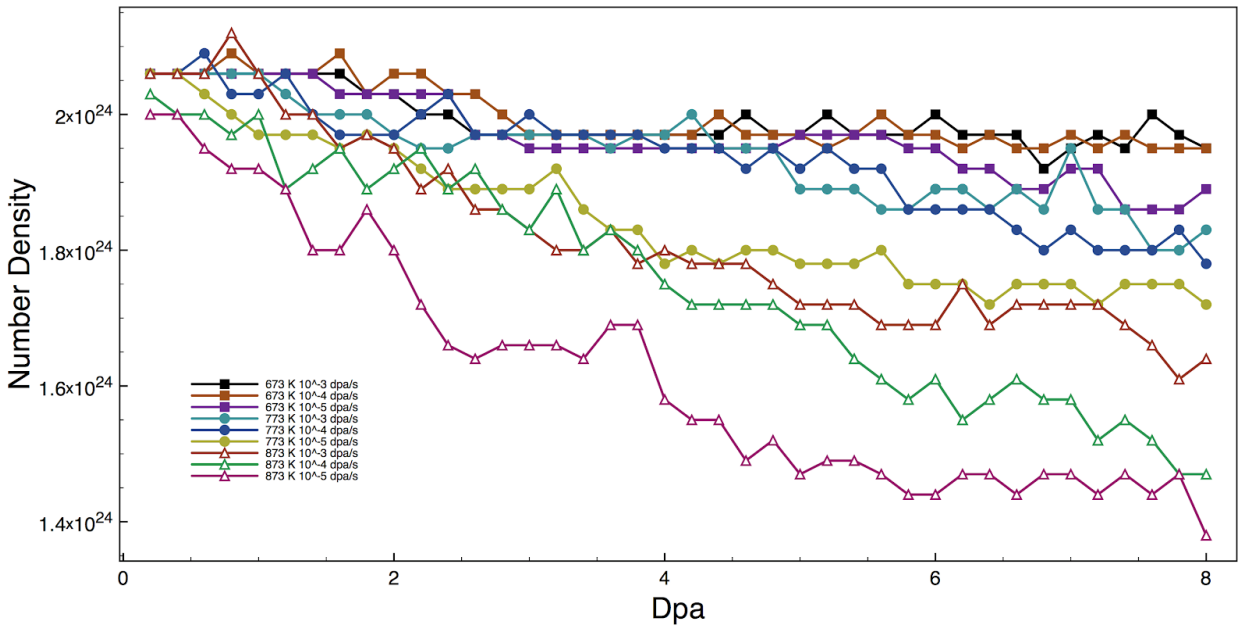

Figure 5.6: *Evolution of the number density of oxides in 12YWT over total accumulated dose at a variety of irradiation regimes*

Figure 5.6 shows the change in the number density of oxides in 12YWT over accumulated dose dpa for all tested temperature and dose rate combinations. Like the average size findings, there was a sharp initial drop in the number density before reaching an apparent plateau in the 4-8 dpa range. More oxides were dissolved at higher temperatures. This was most pronounced at the 873K temperature while there was only at most a 10% decline in the number density at the 673K and 773K temperatures. There was more oxide dissolution at low dose rates than at higher dose rates across all temperatures tested, with the 873K $10^{-5}\ dpa/s$ case experiencing the largest decline with nearly a 30% loss in number density.

B. Interfaces:

Similar to the thermal aging simulations, after the neutron irradiation simulations were completed, the shape of the precipitates were visually inspected. The images were compared to shapes seen from thermal aging and the oxide equilibrium shape at the irradiation temperatures. Any deviation from the expected cubic shape with sharp interfaces was noted.

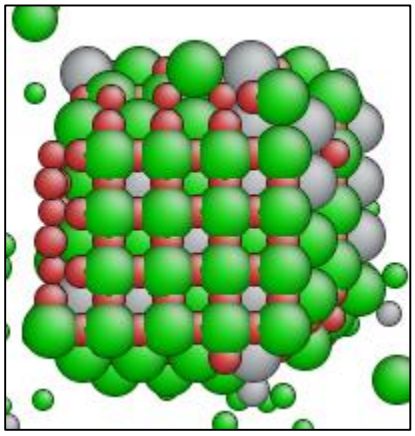

Figure 5.7: *12YWT-1123K after irradiation at 773K at a dose rate of* 10^{-3} *dpa/s to a total dose of 8 dpa*

Figure 5.7 is an image of an oxide in 12YWT-1123K after irradiation and was representative of the changes in oxide shape seen in all the simulations. With increasing irradiation, these faces became more diffuse and irregular while maintaining a cubic/rectangular shape, which was also in line with expectations [119].

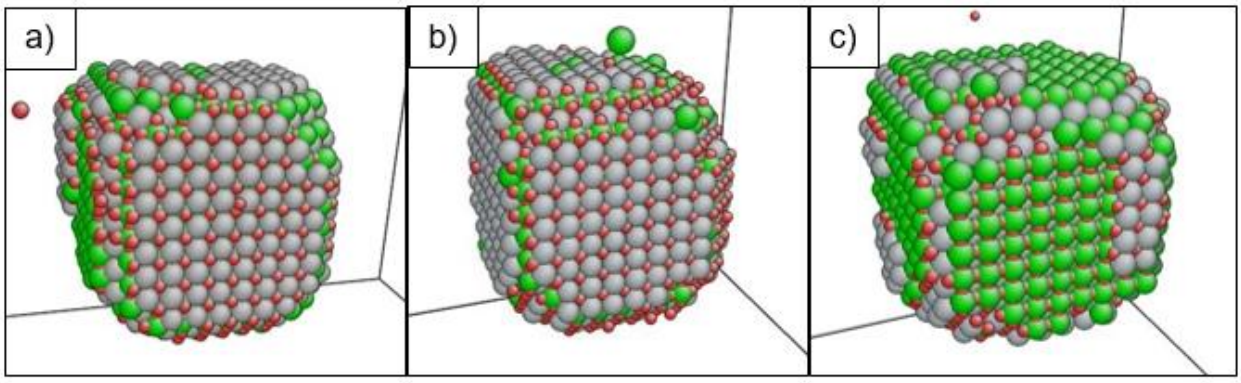

Figure 5.8: *Equilibrium shape of the Y-Ti-O oxide at a) 673K b) 773K c) 873K*

The equilibrium shape simulations performed in a prior study were repeated at the same temperatures in the irradiation simulations (673K, 773K, 873K). The resulting equilibrium shapes are displayed in Figure 5.8. As with the higher temperature, the oxide precipitates were dominated by the <100> interface with smaller areas of the <110> and <111> interfaces. The oxides in the irradiation simulations continued to maintain this shape as shown in Figure 5.7.

C. 14YWT Irradiation Replication Simulations

After completion of the irradiation simulations of the 12YWT-1123K samples at the three test temperatures and three dose rates, the general response of the oxides to irradiation was understood and found to align with expectations. We then compared the 14YWT irradiation simulations to experimental results.

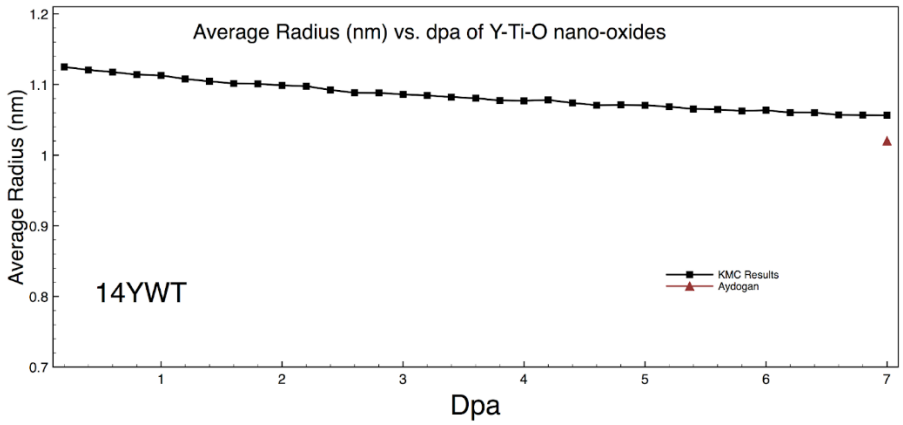

Figure 5.9: *Average radius over dpa for the 14YWT-1123K irradiation at 633K*

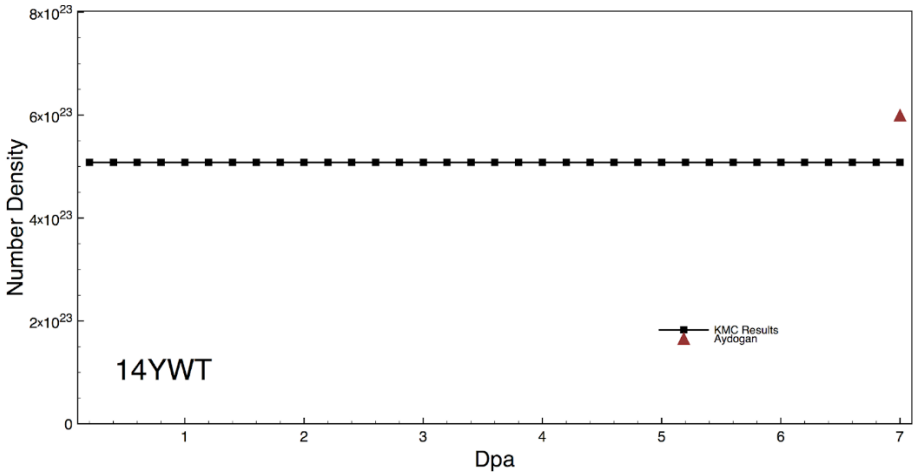

Figure 5.10: *Change in the number density over dpa for the 14YWT-1123K irradiation at 633K*

Figures 5.9 and 5.10 show the average radius and number density change with accumulated damage in 6 simulations of 14YWT at the conditions described in Aydogan[164]. There was a decrease in the average radius that appeared linear with the accumulated dpa damage. A plateau did not appear to have been reached like the 12YWT irradiation simulations. The number density of the oxides remained constant over the irradiation treatment across all samples.

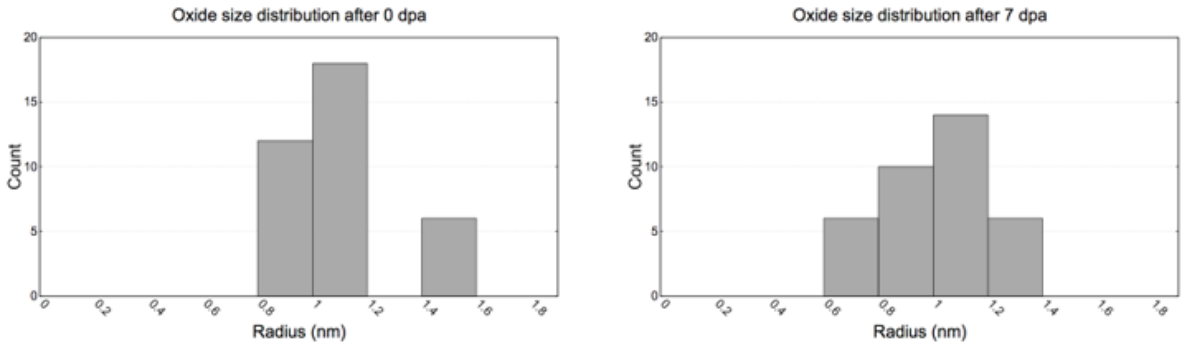

Figure 5.11: *Oxide size distributions of 14YWT before and after irradiation*

Figure 5.11 shows the size distribution of the oxides across all 6 simulations before and after irradiation to 7 dpa. None of the oxides were shown to have fully dissolved, which is in line with expectations from the number density results. However, all of the oxides experienced a decrease in their size with no irradiation induced growth shown. This concurs with the average size and number density trends seen in Figures 5.9 and 5.10.

D. Composition Change after Irradiation

The nature of neutron irradiation leads to shifts in the composition of the oxides in the NFA, which could affect their performance and stability. The composition change in the oxide precipitates at the end of the irradiation treatment were compared against the values at the beginning of the simulation for the 12YWT and 14YWT compositions.

Table 5.10: *Composition of oxides after irradiation to 7 dpa at* 6.5×10^{-7} *dpa/s*

	O at%	**Y at%**	**Ti at%**	**Fe at%**
14YWT from KMC at 0 dpa	51%	12.0%	36%	-
14YWT KMC After Irradiation	54.1%	9.8%	28.85%	7.14%
14YWT Miller	43.3 ± 5.3	7.5 ± 4.3	42.2 ± 5.6	-

Table 5.11: *Composition of oxides in 12YWT after irradiation to 8 dpa per irradiation regime*

	Dose Rate (dpa/s)	**O at%**	**Y at%**	**Ti at%**	**Fe at%**
12YWT Before	N/A	50.94	12.76	36.17	0.17
673 K	10^{-3}	56.10	10.23	28.18	5.48
673 K	10^{-4}	55.57	10.45	28.48	5.49
673 K	10^{-5}	55.58	10.14	27.77	6.27
773 K	10^{-3}	58.61	9.71	26.08	5.59
773 K	10^{-4}	58.6	9.51	26.34	5.51
773 K	10^{-5}	58.789	9.53	25.63	6.04
873 K	10^{-3}	61.58	9.14	22.45	6.81
873 K	10^{-4}	62.44	8.88	22.27	6.39
873 K	10^{-5}	62.35	9.00	22.38	6.25

Tables 5.10 and 5.11 show the composition of the oxides after irradiation and their respective compositions prior to irradiation. In both cases, the proportion of oxygen in the oxide goes up as well as the amount of Fe in the oxide. In turn, the proportion of Y and Ti in the oxides decreases. There is no consistent variation in oxide composition with dose rate, with the

composition being more strongly dependent on temperature. The proportion of Ti in the oxide declined the most over the course of the irradiation, particularly as the irradiation temperature increased. Nearly a third of Ti atoms in the oxide were expelled at 873K.

E. Composition Evolution

The composition of solute atoms in the oxides was tracked over received dose. The evolution of the oxide composition was plotted and analyzed for notable trends.

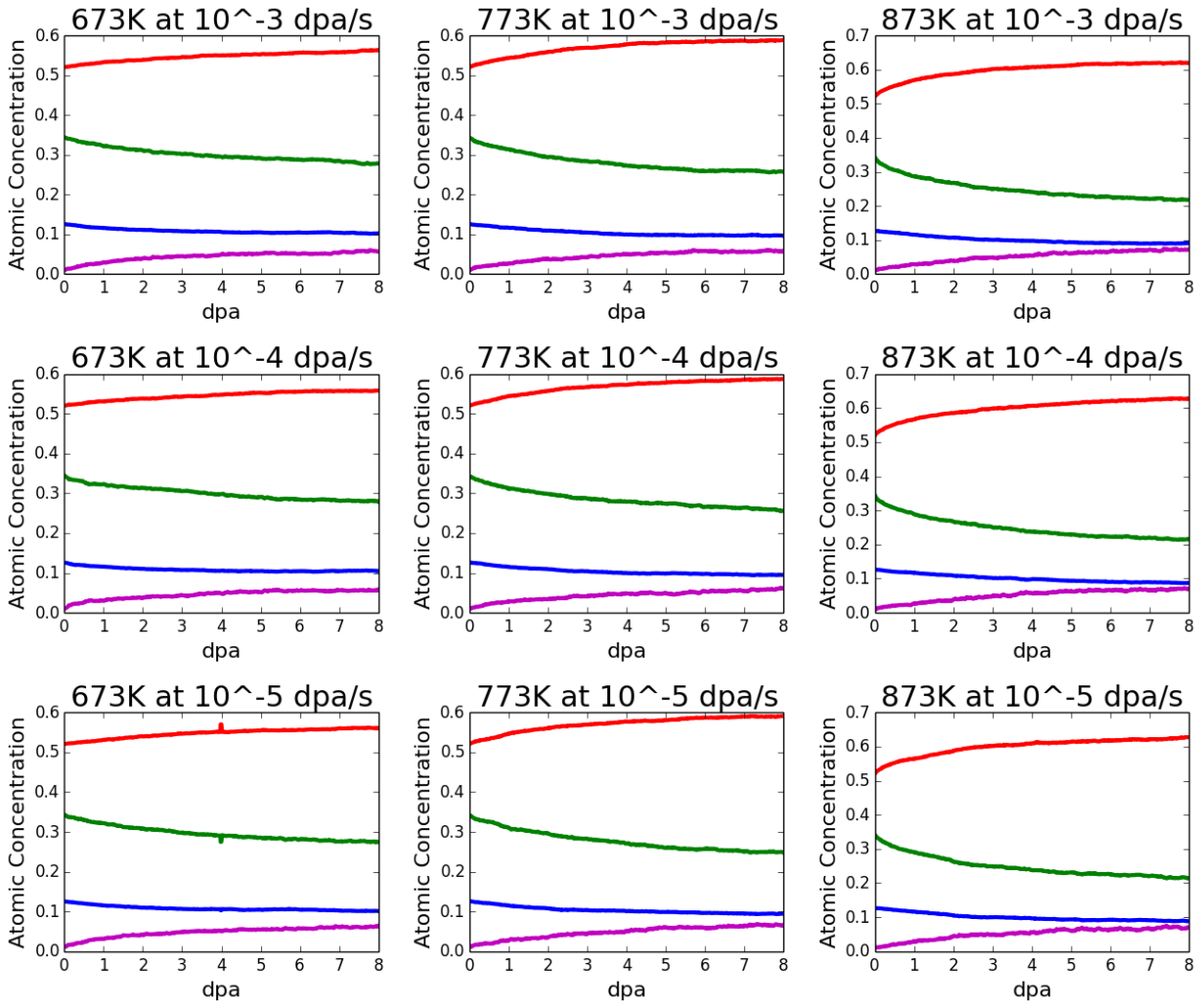

Figure 5.12: *Evolution of oxide composition in 12YWT over accumulated dose at various temperatures and dose rates. Red=Oxygen, Green=Titanium, Blue=Yttrium and Purple = Iron*

Figure 5.12 shows the composition evolution during the irradiation simulations. As the total accumulated dose increased, more of the Y and Ti solutes were ejected from the oxides into the bulk. Fe was gradually introduced as a replacement component in the oxide, going from near non-existent to up to 7 at%. All cases appeared to be heading towards a plateau near the end of the simulation, suggesting that the oxide composition would reach an equilibrium value where solutes are replaced as quickly as they are ejected from the precipitates. Again, through this visualization, the composition was more strongly influenced by the irradiation temperature than the dose rate.

5.4.3 Further Investigation

After observing an apparent plateau in the decline of the size and number of oxides in the system across all irradiation regimes, an additional limited investigation was conducted to see if that plateau represented the emergence of a steady-state or only a temporary metastable stage. Three samples from a single irradiation regime (873K at 10^{-3} dpa/s) were taken further to 66 dpa and the evolution of oxide characteristics over dpa was recorded.

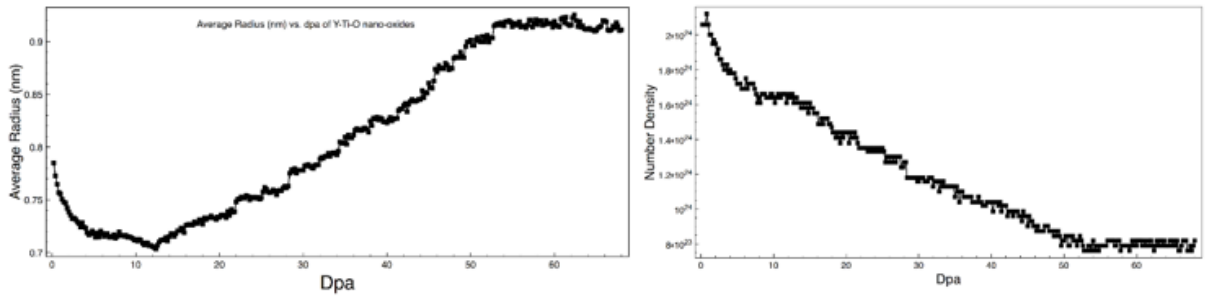

Figure 5.13: *The evolution of 12YWT oxide characteristics in long-term irradiation simulation at a single irradiation regime (873K at* 10^{-3} *dpa/s)*

Figure 5.13 shows the evolution in oxide size and number density as they were irradiated to a total dose of 66 dpa at 873K at 10^{-3} dpa/s. After 8 dpa, the plateau in oxide size started to decline again before reversing and increasing in size after 12 dpa. The change in the number density of oxides continued to hold its initial downward trend through the whole simulation and no longer mirrored the change in oxide size. The evolution reached an apparent steady-state after 54 dpa.

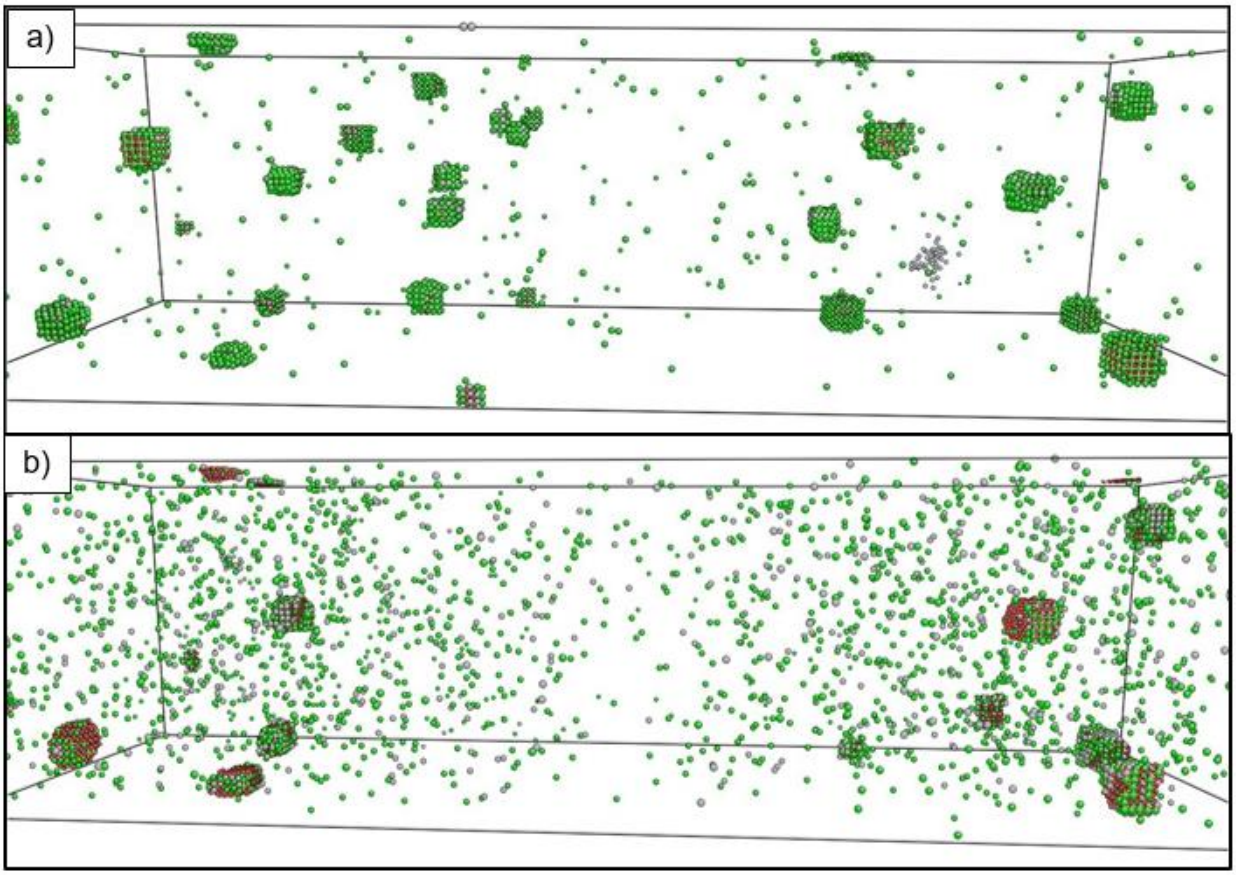

Figure 5.14: *Oxide distributions of the 12YWT-1123K a) before neutron irradiation, b) after neutron irradiation with a total dose of 66 dpa at 873K at a dose rate of* 10^{-3} *dpa/s*

Figure 5.14 shows pictures of the 12YWT simulation box before and after neutron irradiation to 66 dpa. In the irradiated sample, there was a higher density of free solutes Ti and Y

in the Fe matrix, separated from their original oxides from irradiation. Many of the original oxides dissolved under irradiation, with oxides around the grain boundary suffering the most losses. The grain boundary itself was largely devoid of free solutes and no new oxide precipitates were found at the grain boundary.

The tendency of a solute species to enrich or deplete at defect sinks is attributed to the inverse Kirkendall effect where preferential transport of the solute via the vacancy or dumbbell migration compared to matrix atomic species leads to segregation around defect sinks. There is a formulation [12] that predicts whether a solute enriches or depletes at defect sinks using the diffusivities of the solute and matrix atoms.

$$\left(\frac{d_{AV}}{d_{BV}} - \frac{d_{AI}}{d_{BI}}\right) \rightarrow \begin{cases} < 0 & Enrichs \\ > 0 & Depletes \end{cases} \quad (6)$$

The diffusivities d_{XV} and d_{XI} of atomic species X are via vacancy and dumbbell migration respectively. To check the direction of segregation using Eq. 6, atomic species A is the solute (Y or Ti) and atomic species B is the matrix atom (Fe).

Table 5.12: *The Ratio of Diffusivity of Y and Ti with Fe*

$\left(\frac{d_{AV}}{d_{BV}} - \frac{d_{AI}}{d_{BI}}\right)$	A=Y B=Fe	A=Ti B=Fe
673K	-10.32	19.68
773K	-7.84	31.60
873K	-6.23	43.33

Table 5.12 shows the diffusivity ratios for the Y and Ti solutes in bcc Fe at three irradiation temperatures. There was a slight preference for enrichment for the Y atoms at defect sinks while the Ti atom was more strongly led to depletion. The presence of oxides and the supersaturation of

the Y and Ti solutes in the Fe matrix was the likely cause of the differences in predicted behavior for the Y solute, as Was's formulation assumes these conditions are not present.

The nano-oxides are suspected to suppress the point defect population and therefore slow down the diffusion processes that drive segregation. To investigate this, the KMC simulations were run at three temperatures (673K, 773K, and 873K) at a single does rate 10^{-3} dpa/s for two starting configurations. The first being a simulation box of pure Fe with no other solutes and the second being the 14YWT configuration. The average concentration of point defects in the bulk matrix (not bounded to the oxides) is recorded and compared between the two cases.

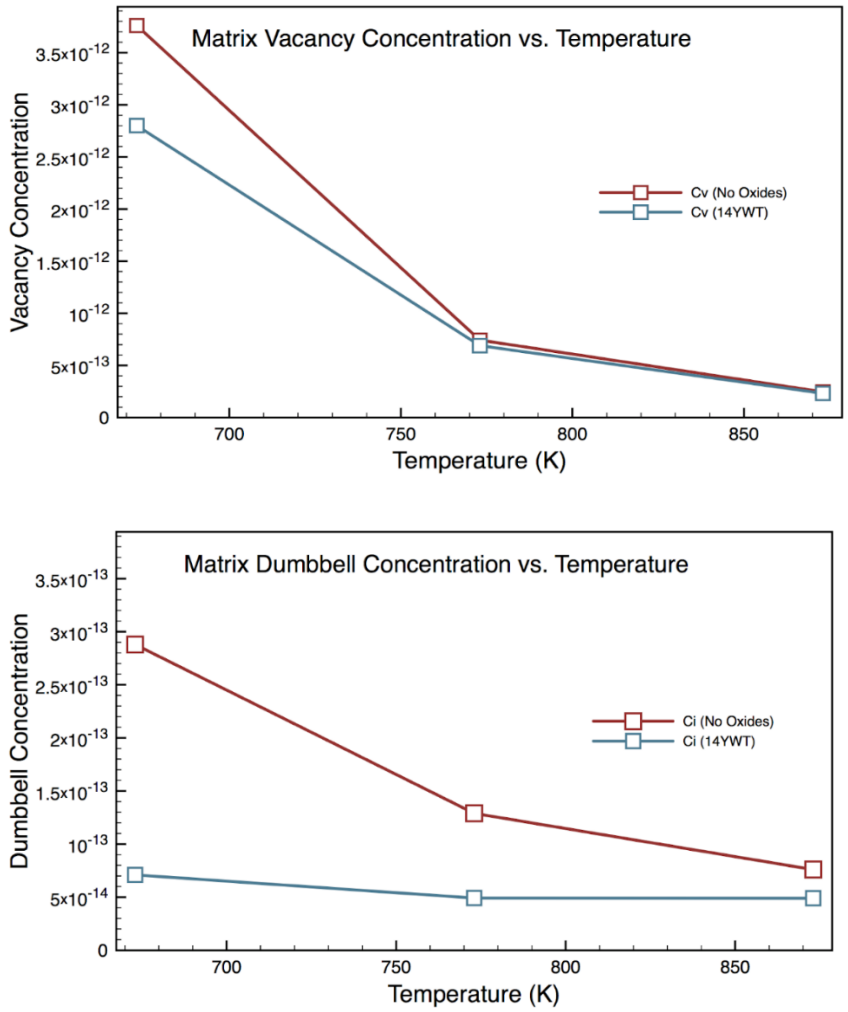

Figure 5.15: *The concentration of point defects in pure Fe and 14YWT vs temperature. a) Vacancy Concentration. b) Dumbbell Concentration.*

Figure 5.15a and 5.15b shows the average concentration of vacancies and dumbbells respectively in the simulation box during irradiation at 10^{-3} dpa/s over temperature for two cases: in pure Fe (without nano-oxides present) and in the 14YWT composition. The plots show the nano-oxides in 14YWT do have a suppressing effect on the average population of point defects. This suppression effect weakens with increasing temperature. At 873K, there is almost no difference in the concentration of vacancies. This is likely due to the high temperature speeding recombination and diffusion to the grain boundary so much the vacancy concentration does not rise much above the thermal equilibrium value as described in Figure 2.4.

5.5 Discussion

5.5.1 Precipitation

The precipitation simulations showed a pattern of increasing oxide size with increasing temperature, which was anticipated due to the thermodynamics of precipitation. As the temperature rose, the solubility product of the oxide also increased, making the critical radius of a stable nuclei larger and less frequently achieved. The free solutes mass of the fewer stable nuclei resulted in a lower number density of oxides that were larger in size. The size, number density, and composition of the oxides in both 12YWT and 14YWT compared favorably to experimental results. The absence of solutes such as Cr in the KMC could be a factor in any discrepancies. The shape of the precipitates was also observed with the oxides in the precipitation heat treatments taking a cubic shape, with broad <100> interfaces and small areas of <110> and <111> interfaces at higher temperatures, which was expected from our observations. Equilibrium shape simulations that were later performed affirmed that the cubic shape represented the equilibrium shape when the KMC forced a preexisting oxide to reshape into the equilibrium shape seen in experiments.

The influence of the grain boundary on precipitation was studied at the same temperatures as bulk simulations in Chapter 4. The results found little difference in the average radius and number density of the oxides between the bulk and grain boundary simulations. There were differences in oxide distribution between the two cases as no oxide precipitates formed in the immediate vicinity of the planar sink, leaving a noticeable gap.

There is literature that observed the formation of oxides at the grain boundary. These grain boundary nano-oxides were typically larger than the oxides in the intergranular region. It has been theorized that the presence of interstitial elements such as C and N play a role in facilitating the formation of nano-oxides at the grain boundary, so the absence of these elements could explain the absence of grain boundary nano-oxides.

Another factor to consider is the opportunity for vacancy movement at the grain boundary. Since the sink annihilated the point defects on contact, this region had a much lower average concentration of vacancies than regions away from the boundary. Thus, there was less opportunity for atomic diffusion around the grain boundary, which inhibited the nucleation of the Y-Ti-O precipitates. Given NFA's known inclination towards rapid oxide nucleation, the matrix would likely be depleted of free solute material before any nucleation near the grain boundary could occur. Additionally, segregation of intergranular Ti, Y, and O atoms to the grain boundary during thermal heat treatments was not found by Alinger [18], leaving less available material to form grain boundary nano-oxides.

5.5.2 Irradiation

A. Overall Survivability

The neutron irradiation simulations found that the oxides behaved in an expected manner in response to irradiation. They appeared resistant to dissolution even at the relatively high dpa rate of 10^{-3} dpa/s with the high dose rate appearing less effective at dissolving oxides. The presence of vacancies worked to heal the oxide structures even when the displacement cascade ejected solutes from the oxides. Nevertheless, there was still a decrease in the overall size of the oxides over the irradiation regime. Through observations of the size distributions before and after the irradiation, it was seen that the smallest oxides quickly dissolved while the larger oxides were more stable. There were no oxides larger than 1 nm in radius for the 12YWT cases at accumulated damage >4 dpa. The oxide stability could also be a product of the inherent KMC set-up. Chen found that oxides coherent with the Fe matrix were more stable than incoherent oxides [161], meaning that the oxides in the rigid lattice KMC set-up may have too much stability.

Inherent stability is likely explained by Nelson-Hudson-Mazey's theory of stability, which is dependent on two competing forces, both caused by irradiation [165] where irradiation that expels debris from oxides is the cause of oxide loss and radiation enhanced diffusion drives the regrowth of the oxides. Since vacancies drive nucleation and growth during the heat treatment phases, the increased vacancy concentration due to irradiation has a 'healing' effect on the damaged oxides and drives restoration of the oxides. Smaller oxides proportionally lost more material in the irradiation cascade and were, therefore, more susceptible to dissolution.

The long-term irradiation simulations at 873K and 10^{-3} dpa/s saw the decline in oxide size reverse itself and had the surviving oxides grow larger than the original average. Atomic material for this growth comes from oxides dissolved during irradiation, resulting in a decrease in the oxide number density. This radiation induced coarsening of the oxides is seen in similar NFAs [67].

A compositional analysis of the oxides after irradiation for both 12YWT and 14YWT found an overall decrease in the proportion of Ti atoms in the oxide with a corresponding increase in the Fe atoms in the oxide. The Ti atoms accounted for most of the solute atoms in the matrix. Since the Y atoms bound more strongly to oxygen than Ti, the Y atoms were less likely to separate from the oxide and were more likely to rejoin the oxide after being ejected. Overall, across the temperatures sampled, the oxide compositions generally approached a stable plateau after irradiation to 8 dpa.

B. Precipitate Shape

During the heat treatments, the oxides precipitated into cubical shapes that were in line with expectations, giving another measure of validity to the KMC model. The shape of a precipitate was determined by the differences in energies at the oxide/matrix interfaces at various orientations. If the energetics of the system are set up properly, then the oxides formed will match experimental observations, which was found to be the case across all simulations. The shape was orderly with sharp interfaces that became more diffuse upon irradiation, owing to the constant dislodging of atoms by irradiation. These interfaces would likely become orderly again when the irradiation ceased and the oxides interacted with the thermally produced vacancies again.

C. Effect of the Dose Rate

When examining the relationship of dose rate with survivability of the oxides, the following relationship was revealed: with the higher dose rate leading to larger loss of size among the oxides and at the lowest dose rate, there was less of a decrease in oxide size, although at both of the lowest dose rates, $10^{-4}$and 10^{-5} dpa/s, the difference in oxide size was very small. The lower dose rates equated to a smaller supersaturation of point defects, which slowed the diffusion that heals the oxides and causes them to experience more atomic loss by the 8 dpa range. All of

the irradiation simulations with the 12YWT reached a certain plateau where the average size, number density, and composition did not change as quickly as before. This is where enough solutes have been ejected into the matrix to provide a sufficient source of solutes for vacancy diffusion to start to stymy oxide material loss.

The limited long-term irradiation investigation, conducted to further explore the extent of oxide stability, found that this period of stability after 8 dpa was temporary and oxide loss continued. Eventually, a period was reached where the oxide loss stabilized after 54 dpa. The average size and number density of the oxides remained roughly constant until the end of the simulation at 66 dpa. This was where the smallest oxides dissolved completely and the more stable larger oxides remained and where the loss and gain of atomic material in the oxides cancel each other out.

D. Segregation

In the irradiation simulations, there was a lack of segregation to the grain boundaries of the solute Y, Ti, and O atoms. There even appeared to be an inverse Kirkendall effect where the solutes were depleted in the region around the grain boundary. The lack of segregation of Y-Ti-O elements has been observed in experimental observations of irradiated NFAs with an apparent preference for the solutes to return to the oxides[166]. Other studies have seen both segregation of Ti[167] and no segregation[168] to the grain boundary reported in some cases; however, these experiments involved heavy ion irradiations. The simplistic description of the grain boundary in the KMC could have influenced the resulting segregation profiles. Field[13] showed that Cr segregation could be highly dependent on grain boundary structure.

E. Fate of atoms

Using the diffusivities of the solutes, Eq 6 predicted that Ti depletes and Y enriches at defect sinks from Was's formulation. While the tendency of Y to deplete is in contrast to the predicted Y behavior at defect sinks, factors unaccounted for in the formulation, such as the influence of oxides, should also be considered. During irradiation, atoms are ejected from the oxides into the Fe matrix. Once in the matrix, there are several destinations for the atoms: 1) return to the original oxide, 2) join a preexisting oxide, 3) form a new nucleate with other ejected solutes, and 4) congregate at the grain boundary and possibly precipitate a new phase. The oxides acted as competing sites for Y segregation, which dampened the level of enrichment that could be achieved at the grain boundary. The Y atoms expelled from the oxides, having only been knocked a short distance, were inclined to rejoin the oxide by both the supersaturation of Y in Fe and the preferential transport of Y to the oxides. The disproportionate amount of Ti atom loss in the oxides compared to Y atoms lends further evidence of a Kirkendall effect where Y atoms enrich at the oxides while Ti is driven to deplete into the oxide region. Point defects still transported the Ti atoms to the oxides but at slower rates than Fe and Y, resulting in composition loss in the oxide.

In visual observations of the oxide, there was no oxide precipitation in the region around the grain boundary and few stable precipitates elsewhere. Instead, the free solutes rejoined the pre-existing oxides to heal the damage from irradiation. While there was a greater concentration of free solutes in the Fe matrix, there was little increased concentration of solutes in the region around the simulated grain boundary. The oxides closer to the grain boundary were even more susceptible to the dissolution. This behavior is in agreement with the theory that the defect populations help stabilize oxides since the region around the defect sink has a lower average point defect concentration than the rest of the system. So, the oxides in the grain boundary region are not healed as quickly and, therefore, suffer dissolution under irradiation. Binding of the vacancies to the oxide

interfaces can also play a role in segregation behavior as it has been noted that similar vacancy binding[169] limits the migration of point defects and makes them more susceptible to recombination instead of journeying to the sink (and taking solutes with them) for annihilation. There would, therefore, be less segregation at the grain boundaries.

F. Replication of the 14YWT neutron experiment.

The oxide response to irradiation in the 14YWT replication simulations showed good agreement with the results from Aydogan[164]. There was a marginal decrease in the average size of the oxides and none of the oxides dissolved in the face of irradiation damage, although there were occasional short-lived oxides formed from the irradiation debris that quickly dissolved under irradiation. These results display the inherent survivability of oxides in the environments required in nuclear reactors.

With the KMC model showing agreement with experimental observations during heat treatment and irradiation, the model can be further extended to observe more phenomena that take place under irradiation. The next steps for this model are to include insertion of transmutation He into the system. Then observations can be made of the nucleation of He bubbles into the NFAs and the degree to which the nano-oxides inhibit the formation of bubbles at the grain boundaries.

5.6 Conclusion

A Kinetic Monte Carlo model was created and parameterized for the Fe-Ti-Y-O system. Several simulations of the nucleation and growth stages of nano-oxide $Y_2Ti_2O_7$ formation along the grain boundary were observed for temperatures of 1023K, 1123K, and 1223K for the 12YWT alloy. The characteristics of the oxides formed were in good agreement with experimental results in size, number density, and shape for the bulk precipitation. The influence of the grain boundary

on oxide characteristics were found to be limited in this system. Later, the model subjected the same oxides to neutron irradiation and the changes in oxide size were recorded. Unlike reactor experiments, the short-term time evolution of the system under irradiation was able to be visualized in the KMC. The results found that the oxides were stable against irradiation but suffered a gradual decline in size as the material became more damaged. This was true at all temperatures and dose rates studied. An attempt was made to replicate findings for a neutron irradiation experiment of 14YWT and found good agreement with the findings showing little change in oxide characteristics.

Chapter 6: Helium Bubble Nucleation on 14YWT Nano-oxides under Irradiation

6.1 Helium Bubbles on NFAs

Research into the NFA's ability to trap He atoms at the oxides is ongoing. There is some difficulty replicating the insertion of transmutation helium into metals in experimental settings outside an actual nuclear reactor. When the bubbles do nucleate in an NFA like the 14YWT alloy, the helium bubbles are smaller in size and volume than a conventional steel [170]. Other experiments observe that the helium bubbles tend to nucleate at the <111> interface of the oxides owing to the <111> interface's high interface energy [118]. This also notes that it is difficult to get imaging down to the 2nm scale so modelling of the shape of the oxide and location of the He bubbles using a computer model would be useful.

The precipitation and irradiation investigations completed in Chapters 4 and 5 gave satisfactory insight into the stability of the nano-oxides. The KMC model for neutron irradiation of NFAs in an Fe-Y-Ti-O system from Chapter 5 was extended to incorporate the insertion of interstitial helium into a model NFA during the neutron bombardment. The size, location, and He/Vac ratio of the He bubbles in the model NFA were noted and compared to experimental results. A preliminary investigation was conducted to observe the effect of temperature on the characteristics of the He bubbles. Investigations into the effect of the He bubbles on oxide stability and the segregation of solutes were also conducted.

6.2 Material/Methodology

6.2.1 KMC Model

The KMC model was extended from the work in Chapter 5 used to study neutron irradiation in NFAs to incorporate the addition of He atoms. A fixed lattice in the bcc system is constructed to represent the bcc cell. The simulation box is populated with atoms at the substitutional sites (Fe, Ti, Y) and at the octahedral sites (O and He) in the bcc system. The substitutional atoms (Fe, Ti, Y) migrate through exchange mechanisms with the vacancy and interstitial dumbbell point defects. The He and O atoms migrate through an interstitial mechanism to hop between empty interstitial sites.

Several events are not given a frequency and instead occur as soon as a condition is met. Free vacancies and interstitial dumbbells both recombine and annihilate at grain boundaries instantaneously in the manner described in Soisson [84]. When a vacancy has a He atom as a first-nearest neighbor, that vacancy is not subject to the automatic recombination when the interstitial dumbbell is in the immediate vicinity.

6.2.2 He Insertion

Unlike the in-situ helium implantation techniques, the He atom is inserted into the simulation box without an energy that could displace atoms. All displacements are due to displacement cascades caused by neutron impacts. The information of the mechanism for the displacement cascades are described in Chapter 5. The He implantation rate is tied to the expected He appm/dpa ratio expected from the reactors. Once an appropriate dpa is reached in the simulation, a single He atom is added to a random location in the simulation box. This is a process that occurs automatically and thus is not an event frequency does not need to be established.

Literature found the expected He appm/dpa ratio is around 10 He appm/dpa [15], though in this model the He/dpa rate is set to a higher 50 He appm/dpa to see timely formation of He bubbles and to emulate rates from some experimental studies.

The He-Vacancy interactions in the KMC model are expected to be the most influential parameters in the He simulations, since He "bubbles" are really very large He-Vac complexes where the helium atoms take the voided space left by the vacancy clusters. The diffusion properties of the He-Vac complexes are described in a paper by Ortiz[171], although this model treats the migration of He and Vac in clusters as separate entities but are expected to behave the same way. Unlike other KMC models, the clusters are not treated as separate entities with their own migration properties. The association and dissociation events of the individual He atoms with clusters are not given a separate event frequency with a specifically calculated dissociation energy. Rather the local environment is reflected through the calculation of the migration energy of the vacancy using pair-interaction energies.

6.2.3 Parameterization

A. Pair-interaction energies

Table 6.1: *Pair-interaction energies (eV) for Fe-Ti-Y-O-He system as a function of nearest neighbors*

Pair-Interaction Energies	**1 (eV)**	**2 (eV)**	**3 (eV)**	**4 (eV)**
Fe-Fe	-	-	-0.611	-0.611
Fe-Y	-	-	-0.59	-0.52
Y-Y	-	-	-0.57	-0.69
Fe-Ti	-	-	-0.65	-0.53
Ti-Y	-	-	-0.71	-0.68
Ti-Ti	-	-	-0.69	-0.70
Fe-Vac	-	-	-0.21	0.00
Y-Vac	-	-	-0.35	0.00
Ti-Vac	-	-	-0.35	0.00
Fe-I	-	-	-0.10	0.00

Y-I	-	-	0.25	0.00
Ti-I	-	-	-0.10	0.00
Fe-O	-0.00	0.00	-	-
Y-O	0.01	-0.11	-	-
Ti-O	-0.04	-0.04	-	-
O-O	0.10	-0.116	0.10	-0.116
He-O	-0.34			
He-Vac	-2.10			
Fe-He	0.00			
Y-He	-0.46			
Ti-He	-0.14			
He-He	-0.35	-0.42		

Table 6.1 displays the pair-interaction energies used for the KMC model. The rationale for the non-He interactions are discussed in Chapter 2. There is not a good estimation of the He solubility in bcc Fe so the He-He pair-interaction energies are found using the binding energies found in the binding energies of two He atoms in the octahedral sites of pure bcc Fe [172]. The binding energies of the He interstitial with the Ti and Y solutes are described in a paper by Vallinayagam [173] as -0.14 and -0.46 eV respectively. The binding energy for O with He is -0.34 eV. These are used to construct the ε^3_{YHe}, ε^3_{TiHe}, and ε^1_{OHe} pair-interaction energy with the inherent assumption that all the He interactions can be described by first nearest neighbor interactions. The He-Vacancy interaction energy comes from the binding energy between a single He atom and the vacancy taken from literature [174]. The interaction between the He atom and the interstitial was not included in this model.

A grain boundary was placed in the center and a segregation energy is applied to the migration energy calculation whenever the He atom is seated on the grain boundary. This segregation energy was set to 1.3 eV based on literature data from [175, 176]. Note that unlike the

Ti and Y segregation energy, the entropy and enthalpy contributions are not evaluated and the segregation energy is assumed to be constant.

6.2.4 Helium Diffusion Properties

For the purposes of the KMC, the helium atoms reside on the octahedral sites like the oxygen atoms. The diffusion of the He atoms are expected to be very quick owing to a very low barrier of migration 0.06 eV. The full characteristics are described in Table 6.2.

Table 6.2: *Helium Diffusion characteristics*

	Pre-exponential	Migration Energy	Source
He interstitial	$2.8 \times 10^{-8}\ m^2/_s$	0.064 eV	[177]

Irradiation simulations from a prior irradiation study are repeated now with the He injection mechanism adding He atoms into the system at regular total dose intervals. The final location and total number of He bubbles are observed and recorded. In addition, the influence of the He bubbles on the stability of the oxides and of segregation of solutes to the grain boundary was studied.

6.3 Simulation Procedure

6.3.1 Interface Study

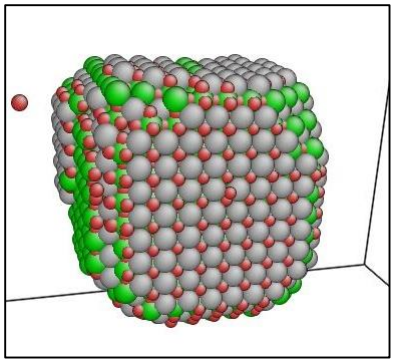

Figure 6.1: *The equilibrium shape of the Y-Ti-O precipitate at 700K. Green =Ti, Gray=Y, and Red=Oxygen*

In an effort to understand all aspects of He bubble behavior, a focused simulation treatment was designed to study the preferential locations of He bubble nucleation in the KMC model and verify that the behavior matches expectations. Previously conducted simulations in the KMC crafted a large oxide in its thermal equilibrium shape with clearly defined interfaces as seen in Figure 6.1. The oxides take a cubic shape like observations from Ribis at 1573K [92] with large <100> interfaces and smaller <110> and <111> interfaces. For the interface study, this single large precipitate was placed in a simulation box of pure Fe plus a grain boundary and subject to irradiation conditions listed in Table 6.3. Since this test part was only interested in the nucleation site, the He appm/dpa rate was set higher than usual to facilitate the timely growth of large He bubbles. After the irradiation, the locations of the bubbles are noted for reference.

Table 6.3: *Irradiation conditions for the Interface Study.*

	Size of KMC Box	Temperature	Appm/dpa	Dose Rate	# Simulations
Interface Study Conditions	400X100X100 lattice points	773K	100	$10^{-3}\ dpa/s$	1

6.3.2 14YWT temperature investigation

Another behavior characteristic studied was the influence of irradiation temperature on the size and number density of the He bubbles in the model NFA. For this investigation, the material studied was the 14YWT-1123K using the simulated oxides atomic configuration that was collected in a previous study.

Table 6.4: *The composition of the 14YWT tested*

	Y	Ti	O
14YWT Atomic Concentration	0.08 at%	0.27 at%	0.3 at%

Table 6.4 lists the amount of primary components of the nano-oxides (Y, Ti, and O) in the iron matrix of the model NFA to mimic the 14YWT. It's important to note this model representation of the 14YWT does not include elements such as Cr and W. Table 6.5 lists the characteristics of the oxides after an isothermal heat treatment in the KMC at 1123K.

Table 6.5: *Oxide characteristics of the 14YWT alloy*

	Average Radius	Number Density
14YWT-1123 K	1.12 nm	4.7x10^23 m^{-3}

Table 6.6 describes the irradiation conditions simulated in this investigation. The temperatures chosen were 673K, 773K, and 873K. The dose rate chosen was the relatively high 10^{-3} dpa/s to due to limitations in the timescale of the simulations. The average size and number density of the bubbles were recorded as well as the locations of the bubbles (on oxides, in the bulk, at grain boundaries). Since the He bubble characteristics between systems would only be

comparable with similar amounts of He in the systems, the stopping condition for these simulations has all the simulations achieving the estimated appm He in the simulation box as the reference experiment. In this case, the KMC simulations will stop at 8 dpa when total He concentration will be 400 atomic parts per million (appm).

Table 6.6: *Irradiation Conditions to observe the formation of He bubbles.*

	Size of KMC Box	Temperature	Appm/dpa	Dose Rate	# Simulations
14YWT	400X100X100 lattice points	673K, 773K, 873K	50	$10^{-3}\ dpa/s$	3
14YWT	400X100X100 lattice points	773K	50	$10^{-5}\ dpa/s$	3
Pure Fe (No Oxides)	400X100X100 lattice points	773	50	$10^{-3}\ dpa/s$	3

To observe the influence of dose rate on He bubble nucleation, the 14YWT simulations at 773K were repeated at the lower dose rate 10^{-5} dpa/s. Additionally, a simulation box of pure Fe is subjected to the 773K 10^{-3} dpa/s irradiation environment to observe whether the oxides reduce the size of the He bubbles. Computational expense prevented the investigation of dose rate at all tested temperatures.

Another aspect of the study was to see the characteristics of the He bubbles. Stable bubbles will maintain a particular ratio of helium atoms and vacancies. While this ratio was not found through physical experiments, there were energetic studies of the He bubbles that estimate the ideal He/Vac ratio [56, 174]. Having the KMC replicate the ideal ratio for the nucleated He bubbles would be another assurance of the model's validity.

6.3.3 Microstructure Evolution

The He bubbles could also have an impact on the long-term survivability of the oxides under this irradiation. Therefore, this study also looked the change in oxide size over the course of the neutron irradiation with and without He insertion. For comparison, a 14YWT oxide configuration was subjected the same irradiation environment at 773K but without the He insertion. Any differences in the oxide characteristics will be noted and investigated. Table 6.7 lists the irradiation conditions. The segregation of the solutes to the grain boundary and the influence of the He bubbles on the segregation was investigated since an area of concern for the embrittlement of NFAs is the degree of radiation-induced solute segregation at the grain boundaries.

Table 6.7: *Irradiation Conditions to observe without the formation of He bubbles.*

	Size of KMC Box	Temperature	Appm/dpa	Dose Rate	# Simulations
14YWT Conditions	400X100X100 lattice points	773K	0.0	$10^{-3}\ dpa/s$	3

6.4 Results

6.4.1 Interface Study

The Y-Ti-O precipitate was placed in a simulation box and subjected to neutron irradiation with the He insertion mechanism activated in the KMC. The simulations continue until several He bubbles were observed on the surface of the oxide. A visual snapshot of the precipitate with He bubbles was created using the software ATOMEYE [117] and inspected for insights into He bubble nucleation behavior.

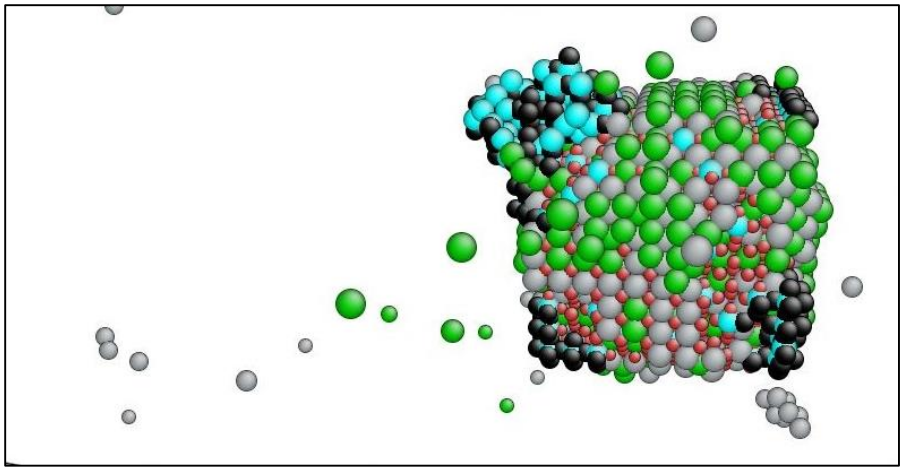

Figure 6.2: *Helium Bubbles nucleated at the interfaces at the oxide. Green spheres: Ti atoms, Grey spheres: Y atoms, Red spheres: O atoms, Blue spheres: Vacancies, and Black spheres: He atoms*

Figure 6.2 shows several He bubbles nucleated at the interfaces of the oxide. Most of the He-Vac complexes coated the edges of the oxide with only the largest collection of He and vacancies forming a spherical shape. It appears that the He bubbles prefer to nucleate at the corners of the oxide precipitates at the <111> interface. This result is in line with experimental observations from Stan for He bubbles in 14YWT [118].

6.4.2 14YWT Temperature Investigation

After the study of He bubble nucleation behavior on a lone Y-Ti-O oxide, the 14YWT oxide distributions were subjected to neutron irradiation with insertion of transmutation He. The KMC runs simulations at the three temperatures at the same 10^{-3} dpa/s dose rate until the system reaches a total irradiation dose of 8 dpa and 400 appm He. The characteristics of the He bubbles were collected and analyzed for any noticeable trends.

A. Characteristics of He Bubbles

Table 6.8: *Average size and number density of the He bubbles in the 14YWT after irradiation to 8 dpa*

	Average Diameter (nm)	**Number Density**
673 K 10^{-3} dpa/s	0.68	1.8×10^{24}
773 K 10^{-3} dpa/s	0.81	5.4×10^{23}
773 K 10^{-5} dpa/s	0.81	5.4×10^{23}
873 K 10^{-3} dpa/s	1.46	1.42×10^{23}

Table 6.8 lists the average size and number density of the He bubbles in the 14YWT-like alloy irradiated to 8 dpa. There were roughly 400 appm He atoms in the simulation box of each sample. There was a clear trend in relation to the effect of temperature with the average He bubbles diameter increasing with temperature while the number density declines. At 673K and 773K, the He bubbles nucleate mostly at the interfaces of the nano-oxides and prevent nucleation towards the grain boundary. There is very little difference between dose rates at 773K. Both the 10^{-5} and 10^{-3} dpa/s case nucleated the same total number of He bubbles across the three simulation runs that averaged to the same size.

Table 6.9: *Average size and number density of the He bubbles in the 14YWT and pure Fe after irradiation to 8 dpa at 773K* 10^{-3} *dpa/s.*

	Average Diameter (nm)	**Number Density**
14YWT	0.81	5.4×10^{23}
Pure Fe (No Oxides)	1.19	1.42×10^{23}

Table 6.9 shows the difference in He bubble size and density between a simulation box that contains no oxides and one that contains the 14YWT composition. As expected, the 14YWT is shown to precipitate more He bubbles that are smaller in size than those encountered in a system without nano-oxides.

B. 14YWT Experimental Replication

In addition to the simulations attempting to understand the general temperature trends in the 14YWT NFA, we were also interested in the KMC's ability to replicate findings from experimental observations. The findings from the irradiation simulations at 773K were compared against findings from Yamamoto[15].

Table 6.10: *Comparison of the He bubble characteristics between the KMC and experiment*

	Average Diameter (nm)	**Number Density (m^{-3})**
From KMC	0.81	5.41×10^{23}
From Yamamoto [15]	0.9 ± 0.3	3×10^{23}

The distribution of He bubbles in an NFA has been observed experimentally by Yamamoto at 773K in conditions similar to what was conducted. The comparison of these observations and the KMC results are seen in Table 6.10. There was a close agreement in the bubble size while the KMC has nearly double the number density of He bubbles.

C. Distribution of He Bubbles

To gain a better understanding of the above results, the complete distribution of He bubbles across all the simulations at each temperature were collected and displayed in the following histograms:

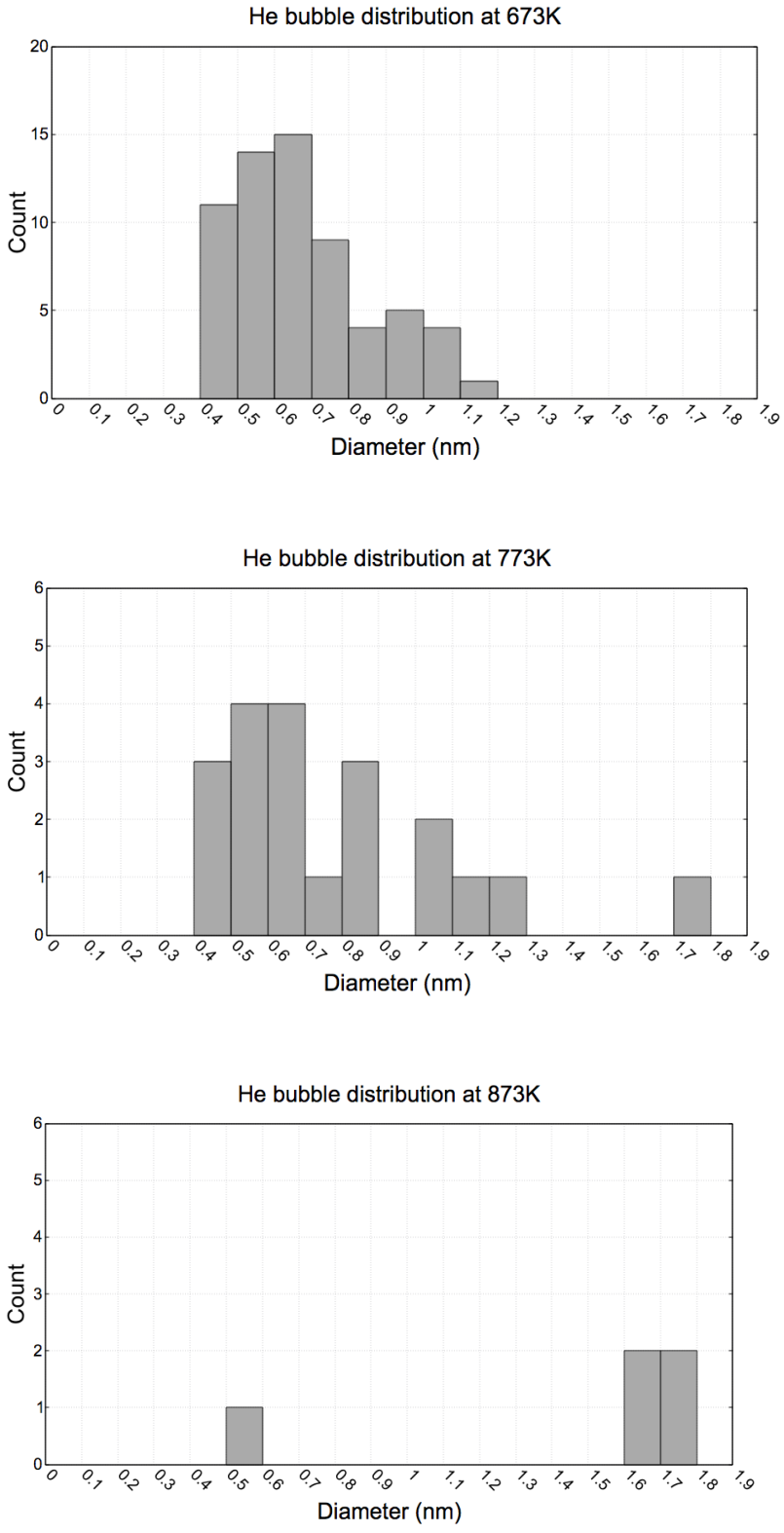

Figure 6.3: *Helium bubble size distributions after irradiation to 8 dpa at a) 673K b) 773K c) 873K*

Figure 6.3 shows the size distribution of He bubbles in the simulation box after 8 dpa for the three test temperatures. For the 673K and 773K cases, the highest frequency of bubbles were small bubbles < 1 nm with large >1nm diameter bubbles occurring less frequently. The bubbles in the 673K case were smallest in size with nearly half less than 6 Angstroms in diameter. The bubble size got progressively larger as the simulation temperature was increased with 30% smaller than 0.6 nm for the 773K temperature and only a single bubble under 1 nm for the 873K. The maximum bubble size across all temperatures was 1.8 nm diameter.

D. He/Vac ratio

Another characteristic of the He bubbles observed was the ratio of He atoms to vacancies in the He bubbles for comparison to the ratios expected from literature. The ratio of each bubble was collected and graphed according to their size in order to observe any trends in He/Vac ratio and bubble size.

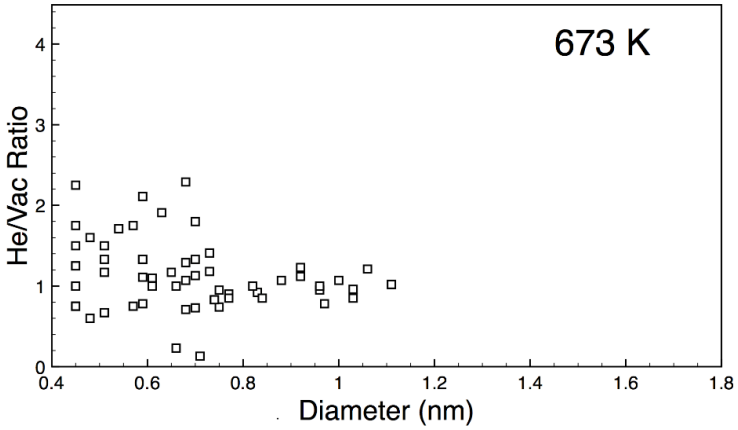

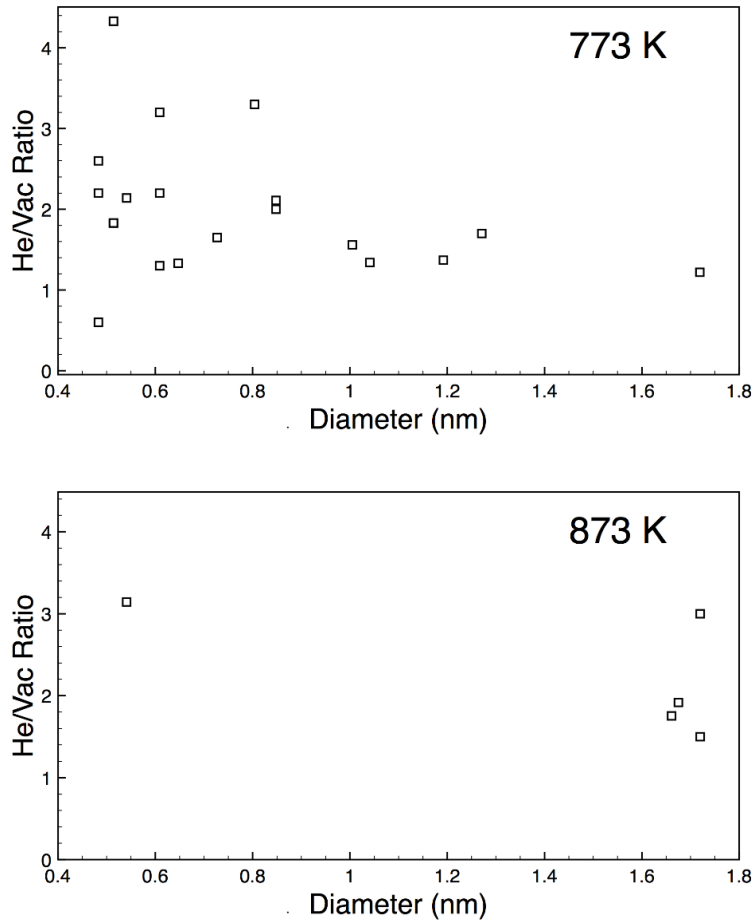

Figure 6.4: *He/Vac ratio of the He bubbles in the KMC 14YWT at 8 dpa/400 appm He in irradiation temperatures a) 673K b) 773K c) 873K*

Figure 6.4 displays the average He/Vac ratio in the He bubbles for each simulation temperature. The majority of the bubbles across all temperatures have a He/Vac ratio that ranges between 1.3 and 1.8. Any bubbles that have ratios outside this range were so different as to be outliers. Many were rather small in comparison to the average bubble size where a change of a single defect/atom will cause a large deviation in the ratio and where the small size could be a factor in the stability. As a He bubble gets larger, the variability decreases with He/Vac ratio appearing to settle into a stable range.

6.4.3 Evolution of the He Bubble

Insights were gained into the nucleation and growth of the He bubbles. For the first step, the vacancy becomes trapped at the oxide interface with the bcc Fe. Then the He atoms migrating through the matrix binds with this single vacancy. This first initial He bubble is He-rich but as the bubble grows, the ratio of He/Vac reaches a more stable range. There is no formulation of voids during the irradiation simulations.

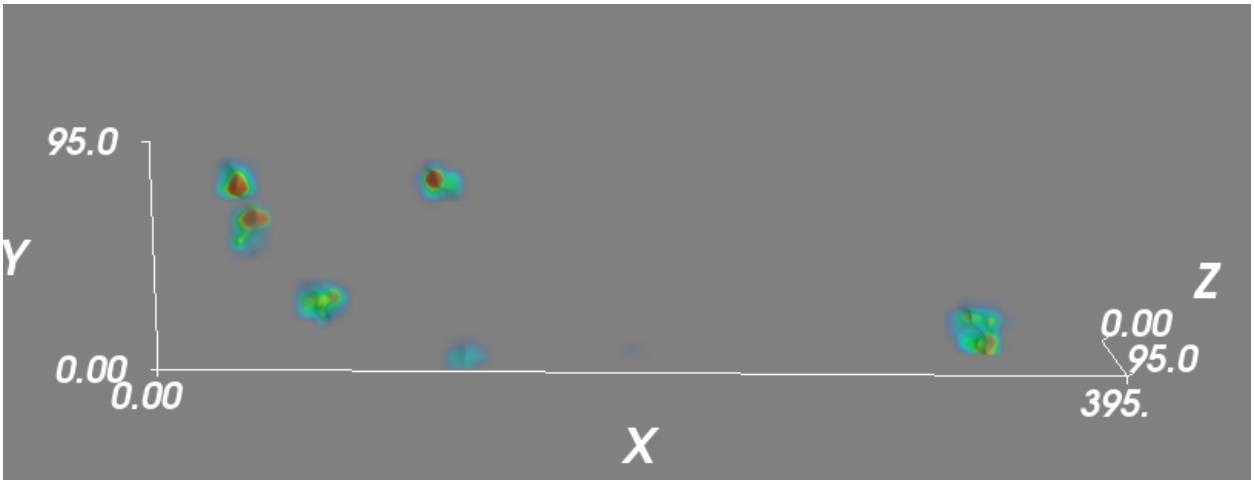

Figure 6.5: *Heat map of vacancy concentration in 14YWT at 773K irradiation simulations.*

Figure 6.5 is a heat map of vacancy movement in the simulation box during the irradiation simulations. The areas with the highest average vacancy concentration correspond to the locations of the oxides. With the vacancy spending significantly more time of the interfaces, it is inherently more likely for the He bubbles to form there than in the Fe matrix.

6.4.4 Effect of He Bubbles on Segregation and Oxide Stability

A separate irradiation simulation was run alongside the He simulations at 773K with the same irradiation conditions as the 773K case except that no transmutation He was inserted. The concentration profile of the solute atoms in the box was collected and the segregation of the solutes

in the grain boundary region of both irradiation cases is noted and compared. The evolution of the oxide size over dpa under the irradiation treatments were also studied in both cases.

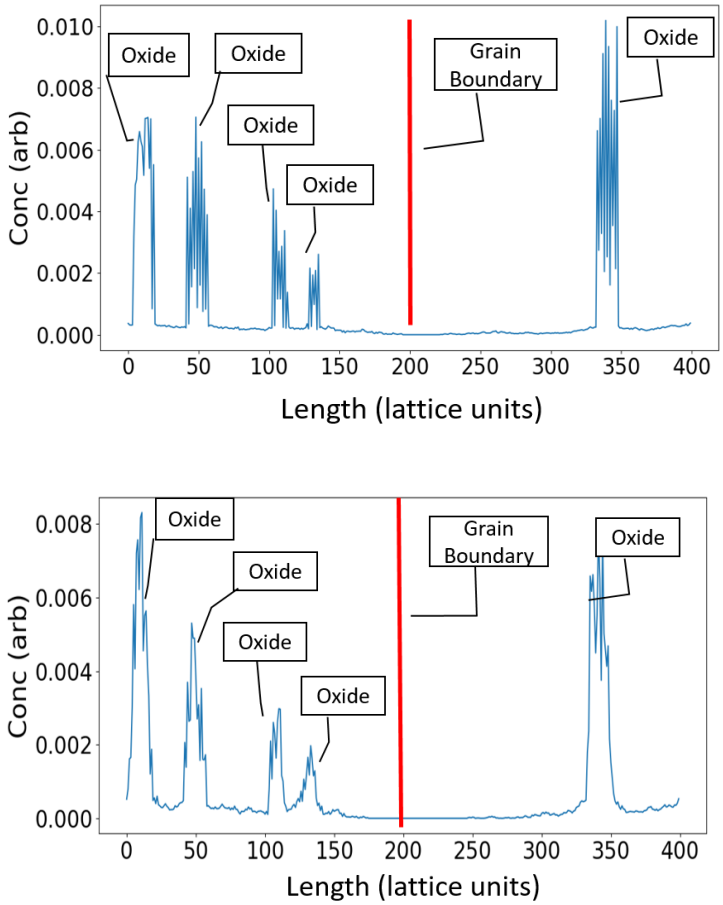

Figure 6.6: *Yttrium concentration profile of the 14YWT system after irradiation to 8 dpa a) without He insertion b) with He insertion to 400 appm He. The red line represents the grain boundary.*

Figure 6.6 shows the profile of the Y concentration profiles after irradiation. There does not appear to be any enrichment at the grain boundary sites of the solute atoms of Y and Ti with or without He insertion. Rather there was a depletion of both elements around the grain boundary. Most of the free solutes not associated with an oxide are located in the area immediately around the oxides.

6.4.5 Microstructure evolution

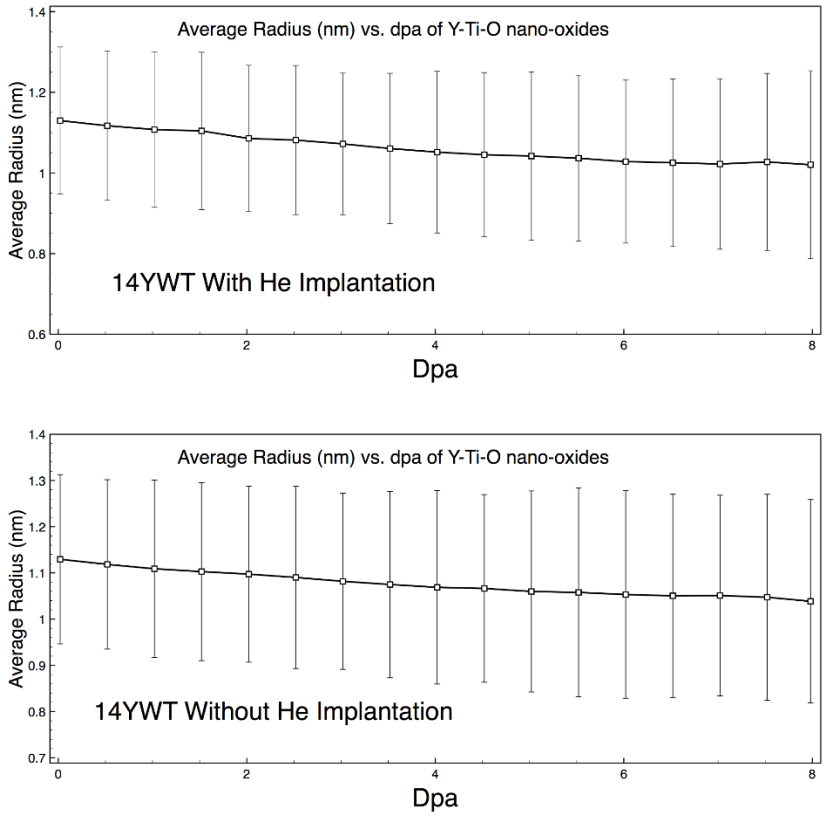

Figure 6.7: *The microstructure evolution of the 14YWT at 773K and* 10^{-3} *dpa/s a) without He insertion and b) with He insertion.*

Figure 6.7 shows the microstructure evolution of the 14YWT oxides during the irradiation regime up to 8 dpa with and without He insertion. Both cases show a slight decline in the average radius of the oxides during irradiation while there was no decline in the number density and no new precipitates were formed from the ejected solutes in either case. There was no meaningful difference in average radius between the He and non-He cases.

6.5 Discussion

6.5.1 He Bubble Nucleation Behavior

The oxide particles were shown to act as alternative nucleation sites for He bubbles. First, the interfaces trapped vacancies which served as the first building block of the He bubble. The resulting high concentrations of the vacancies around the oxides led to the nucleation and growth He bubbles at the interfaces as it is easier to join an existing bubble than nucleate a new one. There is a lower barrier to nucleation through this path so the He bubble distribution in 14YWT are smaller and more frequent when compared to a pure Fe sample. The interface study in Section 6.4.1 conducted in the beginning sections found the He bubbles preferentially nucleated at the <111> interfaces of the Y-Ti-O oxide. Even the corners without a qualitatively spherical He bubble were found covered in He-Vac complexes. Similar findings were found in experimental results from Stan in an He implantation study, who used larger oxides of the same composition for better imaging[118]. The behavior was also in line with expectations from thermodynamics. The He bubble tends to nucleate at the interface with the highest interface energy and the <111> interface has the largest interface energies for the three primary faces of the Y-Ti-O oxides. The high interface energy of the <111> interface was shown by the small surface area of the <111> interface in the shape of the oxide precipitates, since the oxides reduce their energy by minimizing the surface area of their high energy interfaces.

6.5.2 Influence of Temperature

The He bubbles observed at 773K were only ~30% the number observed in the 673K simulations while being twice the diameter. A similar difference was seen when comparing the 873K and 773K simulations with the 873K having half the bubble density with 50% larger size by diameter. The observed relation of high number of small He bubbles at low temperatures and small number of larger He bubbles at high temperatures given the same dpa and appm He in the material

was backed by literature. In investigations of He bubble characteristics of the non-NFA non-ODS steel Eurofer 97 find substantial differences in average diameter and number density between 673K and 773K [64]. The effectiveness of the nano-oxides in trapping He has not experimentally observed at temperatures beyond 773K [14]. The clear trend of larger bubbles at high temperatures would push the limits of the KMC at those conditions.

When comparing the He bubble characteristics to those found by Yamamoto, the KMC found good agreement with the bubble size though there was a discrepancy with the number density of He bubbles though both were in the same order of magnitude. The discrepancy could simply be due to the limited statistics collected across the 3 simulation boxes. Yamaoto had more bubbles to gather statistics from so more simulations may be needed. The He bubbles of this size were also difficult to image at this size and that difficulty may result in an undercount.

Other areas to consider was the idealized representation of the material system in the KMC model. The NFAs have a high amount of defects and dislocations within the grain that were not represented in the simulation box and other solutes like W and Cr were not included as well. Kurtz finds that the preferred nucleation sites of the He bubbles in a non-NFA ferritic steel at 673K and 773K were at the dislocations that were still plentiful in NFAs alongside the nano-oxides[64]. This could be the source of discrepancies in between results given the absence of dislocation in the simulation box.

The He/Vac ratio of the He bubbles investigated in the KMC results were reasonable with the expectations from literature. The He bubbles at 773K provided the most well defined bubbles for analysis. Once the bubbles reach a certain size, the He/Vac ratio consolidated within a particular bounds of 1.3-1.8 He/Vac. In investigations about the stability of the He bubbles, Morishita [56] found the most stable bubbles energetically have a 1.8 Ha/Vac ratio and Fu's [174]

investigation found a He/Vac ratio of 1.3 were the most stable. So the observed He/Vac ratios seen in the KMC were agreeable. The smallest bubbles with less than 10 vacancies have the greatest variability in He/Vac ratio from the oversized influence from their interfaces due to their large relative surface area/volume ratio.

6.5.3 Segregation

The lack of segregation of the solute elements can be attributed to a number of factors. In the beginning of the simulation, the vast majority of solute atoms were incorporated into the oxides owing to the low solubility of all in bcc Fe at the processing temperature. That the irradiation occurs at lower temperatures means that the solutes were even less favorable to be in solution.

The presence of He bubbles in the system does not appear to ultimately affect segregation of the oxide constituent atoms. Most point defects had no interactions with the bubbles before they were annihilated at the grain boundary. The primary cause of separation of the Y and Ti atoms from the oxides was through the ballistic dissolution mechanism. A free solute atom <1nm from the surface of the oxide would likely remain in the neighborhood as the oxides also act as defect sinks. All of the mechanisms that apply to the grain boundary would also apply to the oxide surfaces. Since the inverse Kirkendall effect would keep the Y solutes close to the oxide. This is evidenced by analyzing the composition change in the oxides where there was relatively little decline in the Y component of the oxide in comparison to the Ti content.

6.5.4 Microstructure Evolution

The large oxides of the 14YWT did not dissolve under neutron irradiation for either the He or non-He cases but did experience a slight decline in overall size as expected. There was no

radiation induced precipitation of oxides in the bulk. Like with the segregation of solutes, the He bubbles do not appear to have a substantial effect of the stability of the oxides. The point defects continue to migrate through the system relatively unimpeded by the bubbles. It gives more credence to the theory of ballistic dissolution being the cause of oxide shrinkage rather than the increases population of point defects from irradiation. It was possible that further irradiation to higher damage rates would a more drastic impact of the bubbles.

6.5.5 Next Steps

The next steps for the KMC would be to study the effect of irradiation dose rate on the characteristics of the bubbles if the temperature is held constant. A similar investigation of the effects of the rate of He insertion would also be valuable. The model could also continue to be modified to allow for a larger box size to investigate any effect that might have on the outcome of the He+neutron irradiation particularly with the 873K case.

6.6 Conclusion

A KMC model was created for the purposes of investigating the formation of He bubbles under neutron irradiation typical in an NFA, the primary goal to asses to effectiveness of the nano-oxides in preventing He from reaching the grain boundary. He bubbles formed in this model nucleated and grew on the Y-Ti-O oxides at smaller sizes and a higher number density than when there are no oxides in the system. This outcome is linked to improved resistance to radiation-induced embrittlement. The preferred nucleation site was at the <111> interfaces which in line with expectations from experiments. The KMC model also replicates findings the bubble size and number density under irradiation treatments in prior studies, showing the bubble size increases

with increasing temperature. A limited investigation suggested that dose rate has little effect on the resulting He bubble distribution.

Chapter 7: Conclusions and Future Plans

7.1 Summary

This project expanded on the use of computer models to study radiation damage in nuclear materials. A mean-field rate-theory model was used to study segregation behavior under irradiation in the Fe-Ti-Y-O system, though without the influence of nano-oxide precipitates considered. A 5 element KMC model, more advanced than the binary or ternary KMC models seen before, was developed to simulate the precipitation of Y-Ti-O nano-oxides and study their durability under irradiation, suppression effect on segregation, and interaction with He atoms. The mechanism of He bubble nucleation and growth could be more clearly understood through these simulations. The KMC model was able to replicate the behavior of the nano-oxides in experiments for both precipitation heat treatments and irradiation. Likewise, the He bubble behavior also followed experimental data.

A unique new steady-state detection algorithm was developed comprised of three statistical tests: the f-test, t-test, and the 'projection test' developed in this manuscript. It was confirmed the SSD could detect steady-state in many types of data trends that pose issues for steady-state detection and was not fooled by data that could potentially give a false positive. This SSD algorithm was trialed in this project for the timely validation of the parameterization of the Fe-Y-O and Fe-Ti-Y-O systems by ending several long-term simulations once steady-state was detected.

Additionally, a test, the ppSSD, was made that analyzes a small window of data and determines the minimum number of data points needed to achieve a particular level of probability the projection test is correct. This information can be useful in the automated scheduling of

numerous long-term computing threads, allowing the computer to abort simulations that would take too long and thus save computational expense.

In the investigation, precipitation of nano-oxides in Fe-Y-O and Fe-Ti-Y-O systems was simulated by the KMC model at three different temperatures (1023K, 1123K, and 1223K). Nano-oxides formed in the simulation box replicated literature values for average oxide size, number density, and oxide composition. In line with literature, the addition of Ti resulted in the production of finer oxides. The simulations also showed the expected temperature dependence with higher temperatures precipitating fewer but larger oxides. The presence of a defect sink did not result in significant changes in the oxide characteristics apart from an absence of oxide nucleation in the area around the grain boundary.

The coarsening behavior of the nano-oxides, specifically very low rate of coarsening at reactor temperatures and the departure from the expected $1/3^{rd}$ power law was investigated. Findings from this investigation found the ability of the nano-oxides to trap vacancies at the interfaces caused the deviation by hampering the vacancy movement, so dislocations are not the only mechanism the coarsening resistance can be attributed to. Additionally, there is a low thermodynamic incentive for the oxides to coarsen, contributing to the slow coarsening rate.

To investigate the stability of the oxides under irradiation, the KMC model subjected two compositions of NFAs (12YWT and 14YWT) to neutron irradiation. Instead of performing reviews of dozens of separate irradiation experiments from different groups on slightly different materials to extract trends in oxide behavior, the temperature and dose rate trends on oxide size and number density were observed through the 12YWT simulations. The oxides were generally stable against dissolution with a clear trend of only the smallest less stable oxides dissolving and joining other precipitates. Interestingly, there was a greater decline in size at lower dose rates than

at higher dose rates, attributed to the higher defect populations at high dose rates bringing solutes back to the oxides at a faster rate. No significant enrichment of solutes was observed at the grain boundary due the oxides acting as alternative sites for the free solutes to migrate. Suggesting that oxides population would play a role in reducing RIS.

The He simulation results were also successful. The He bubbles were observed to nucleate at the <111> oxide interfaces at smaller sizes and higher number density than an oxide-less pure Fe system. according to expectations. Close agreement with the size and number density of the He bubbles with the KMC model results at 773K as were found in an experiment. The characteristics of the stable He bubbles also matched thermodynamic predictions, exhibiting a He/Vac ratio ranging from 1.3-1.8. The He bubbles were also found not to have any impact on overall oxide stability owing to the limited interaction the bubbles had with point defects.

7.2 Future Potential

Possible avenues of study from here would be using the KMC model for more long-term simulations of irradiation so we can see the influence of temperature and dose rate on long-term behavior of the oxides past 8 dpa. There is also the study of when the He bubble becomes a void. The He simulations did not observe this phenomenon but it is possible with a longer term simulation or a simulation with a more intense He/dpa rate. Along with the SSD algorithm, the KMC can be bundled into a larger artificial intelligence software to accelerate the development of nuclear materials by making predictions about which materials would be best to use.

Appendix

A.1: Derivation for Chapter 3 Equation 8

Start with:

$$\mu - \Delta Y_{pass} \leq \hat{y} \leq \mu + \Delta Y_{pass} \quad \text{(A.1.1)}$$

Substitute the projected point $\hat{y}$ with its formula, $\hat{y} = b_1(X^* - \bar{X}) + \mu$,

$$\mu - \Delta Y_{pass} \leq b_1(X^* - \bar{X}) + \mu \leq \mu + \Delta Y_{pass} \quad \text{(A.1.2)}$$

Rearrange with algebra:

$$|b_1|(X^* - \bar{X}) \leq \Delta Y_{pass} \quad \text{(A.1.3)}$$

A.2: Derivation for Chapter 3 Equation 9:

Start with:

$$|b_1|(X^* - \bar{X}) = \Delta Y_{pass}$$

(A.2.1)

Substitute $|b_1|$ with the slope threshold:$|b_1| = Z_P S_{b1}$

$$(Z_P S_{b1}) \times (X^* - \bar{X}) = \Delta Y_{pass}$$

(A.2.2)

Substitute $(X^* - \bar{X})$ with a function of the data window lengths: $(X^* - \bar{X}) = \zeta \Delta x_w$

$$(Z_P S_{b1}) \times \zeta \Delta x_w + \bar{y} = \bar{y} + \Delta Y_{pass} \quad \text{(A.2.3)}$$

Rearrange with algebra:

$$\zeta = \frac{\Delta Y_{pass}}{(Z_P S_{b1})} * \left(\frac{1}{\Delta x_w}\right) \quad \text{(A.2.4)}$$

Substitute $|b_1|$ and S_{b1} with their empirical relation $S_{b1} = \varepsilon\varphi$:

$$\zeta = \frac{\Delta Y_{pass}}{(Z_P * \varepsilon * \varphi)} * \left(\frac{1}{\Delta x_w}\right) \quad \text{(A.2.5)}$$

$$\zeta = \frac{\Delta Y_{pass}}{(Z_P * \varepsilon)\varphi} * \left(\frac{1}{\Delta x_w}\right) \quad \text{(A.2.6)}$$

Substitute for φ using $\varphi = \frac{s_y}{\Delta x_w \sqrt{N_f}}$:

$$\zeta = \frac{(\Delta Y_{pass}/s_y)\Delta x_w \sqrt{N_f}}{(Z_P * \varepsilon)} * \left(\frac{1}{\Delta x_w}\right) \quad \text{(A.2.7)}$$

Rearrange with algebra to get the window size N_f:

$$N_f = \zeta^2 \left(\frac{Z_p \varepsilon}{(\Delta Y_{pass}/s_y)} \right)^2 \quad \text{(A.2.8)}$$

Substitute for ζ using $\zeta = \frac{(X^* - \bar{X})}{\Delta x_w}$:

$$N_f = \left(\frac{(X^* - \bar{X})}{\Delta x_w} \right)^2 \left(\frac{(Z_p \varepsilon}{(\Delta Y_{pass}/s_y)} \right)^2 \quad \text{(A.2.9)}$$

Substitute for Δx_w using $\Delta x_w \sim \langle \Delta x_i \rangle N_f$:

$$N_f \sim \left(\frac{(X^* - \bar{X})}{\langle \Delta x_i \rangle N_f} \right)^2 \left(\frac{Z_p \varepsilon}{(\Delta Y_{pass}/s_y)} \right)^2$$

(A.2.10)

Rearrange:

$$N_f \sim \left(\frac{(X^* - \bar{X})}{\langle \Delta x_i \rangle} \right)^{2/3} \left(\frac{Z_p \varepsilon}{(\Delta Y_{pass}/s_y)} \right)^{2/3} \quad \text{(A.2.11)}$$

References

[1] G. R. Odette, M. J. Alinger, and B. D. Wirth, "Recent developments in irradiation-resistant steels," *Annual Review of Materials Research,* vol. 38, pp. 471-503, 2008.

[2] K. Nordlund, "Historical review of computer simulation of radiation effects in materials," *Journal of Nuclear Materials,* vol. 520, pp. 273-295, 2019/07/01/ 2019.

[3] C. Nellis and C. Hin, "Radiation induced segregation in quaternary Fe-Ti-Y-O alloys," *Journal of Alloys and Compounds,* vol. 701, pp. 82-93, 2017/04/15/ 2017.

[4] C. Nellis, T. Danielson, A. Savara, and C. Hin, "The F-t-Pj-RG method: An adjacent-rolling-windows based steady-state detection technique for application to kinetic Monte Carlo simulations," *Computer Physics Communications,* vol. 232, pp. 124-138, 2018/11/01/ 2018.

[5] C. Nellis, C. Hin, and A. Savara, "The -relation and a simple method to predict how many data points are needed for relevant steady-state detection," *AIChE Journal,* vol. 64, no. 9, pp. 3354-3359, 2018.

[6] S. J. Zinkle and G. S. Was, "Materials challenges in nuclear energy," *Acta Materialia,* vol. 61, no. 3, pp. 735-758, 2013/02/01/ 2013.

[7] OECD, *Status Report on Structural Materials for Advanced Nuclear Systems*. 2014.

[8] E. Zarkadoula *et al.*, "The nature of high-energy radiation damage in iron," *Journal of Physics: Condensed Matter,* vol. 25, no. 12, p. 125402, 2013/02/28 2013.

[9] D. J. Bacon, A. Calder, and F. Gao, "Defect production due to displacement cascades in metals as revealed by computer," *Journal of Nuclear Materials,* vol. 251, pp. 1-12, 11/01 1997.

[10] X. Zhang *et al.*, "Radiation damage in nanostructured materials," *Progress in Materials Science,* vol. 96, pp. 217-321, 2018/07/01/ 2018.

[11] A. Souidi, M. Hou, C. S. Becquart, L. Malerba, C. Domain, and R. E. Stoller, "On the correlation between primary damage and long-term nanostructural evolution in iron under irradiation," *Journal of Nuclear Materials,* vol. 419, no. 1, pp. 122-133, 2011/12/01/ 2011.

[12] G. S. Was, *Fundamentals of radiation materials science: metals and alloys* (no. Book, Whole). New York;Berlin;: Springer, 2007.

[13] K. G. Field, L. M. Barnard, C. M. Parish, J. T. Busby, D. Morgan, and T. R. Allen, "Dependence on grain boundary structure of radiation induced segregation in a 9 wt.% Cr model ferritic/martensitic steel," *Journal of Nuclear Materials,* vol. 435, no. 1-3, pp. 172-180, 2013.

[14] Y. Dai, G. R. Odette, and T. Yamamoto, "1.06 - The Effects of Helium in Irradiated Structural Alloys," in *Comprehensive Nuclear Materials*, R. J. M. Konings, Ed. Oxford: Elsevier, 2012, pp. 141-193.

[15] T. Yamamoto *et al.*, "The transport and fate of helium in nanostructured ferritic alloys at fusion relevant He/dpa ratios and dpa rates," *Journal of Nuclear Materials,* vol. 367-370, pp. 399-410, 2007/08/01/ 2007.

[16] R. E. Stoller, "The influence of helium on microstructural evolution: Implications for DT fusion reactors," *Journal of Nuclear Materials,* vol. 174, no. 2, pp. 289-310, 1990/11/02/ 1990.

[17] N. H. Packan and K. Farrell, "Simulation of first wall damage: Effects of the method of gas implantation*1," *Journal of Nuclear Materials,* vol. 85-86, pp. 677-681, 1979.

[18] M. J. Alinger, G. R. Odette, and D. T. Hoelzer, "On the role of alloy composition and processing parameters in nanocluster formation and dispersion strengthening in nanostuctured ferritic alloys," *Acta Materialia,* vol. 57, no. 2, pp. 392-406, 2009/01/01/ 2009.

[19] M. K. Miller, K. F. Russell, and D. T. Hoelzer, "Characterization of precipitates in MA/ODS ferritic alloys," *Journal of Nuclear Materials,* vol. 351, no. 1, pp. 261-268, 2006/06/01/ 2006.

[20] M. J. Alinger, *On the formation and stability of nanometer scale precipitates in ferritic alloys during processing and high temperature service*. University of California, Santa Barbara, 2004.
[21] Z. Li, Z. Lu, R. Xie, C. Lu, Y. Shi, and C. Liu, "Effects of Y2O3, La2O3 and CeO2 additions on microstructure and mechanical properties of 14Cr-ODS ferrite alloys produced by spark plasma sintering," *Fusion Engineering and Design,* vol. 121, pp. 159-166, 2017/10/01/ 2017.
[22] F. Siska *et al.*, "Strengthening mechanisms of different oxide particles in 9Cr ODS steel at high temperatures," *Materials Science and Engineering: A,* vol. 732, pp. 112-119, 2018/08/08/ 2018.
[23] W. Li *et al.*, "The effect of Zr, Ti addition on the particle size and microstructure evolution of yttria nanoparticle in ODS steel," *Powder Technology,* Article vol. 319, pp. 172-182, 2017.
[24] H. Kishimoto, M. J. Alinger, G. R. Odette, and T. Yamamoto, "TEM examination of microstructural evolution during processing of 14CrYWTi nanostructured ferritic alloys," *Journal of Nuclear Materials,* vol. 329-333, pp. 369-371, 2004/08/01/ 2004.
[25] G. R. Odette, "On the status and prospects for nanostructured ferritic alloys for nuclear fission and fusion application with emphasis on the underlying science," *Scripta Materialia,* vol. 143, pp. 142-148, 2018/01/15/ 2018.
[26] D. S. Gelles, "Swelling in several commercial alloys irradiated to very high neutron fluence," *Journal of Nuclear Materials,* vol. 122, no. 1, pp. 207-213, 1984/05/02/ 1984.
[27] C. Cabet, F. Dalle, E. Gaganidze, J. Henry, and H. Tanigawa, "Ferritic-martensitic steels for fission and fusion applications," *Journal of Nuclear Materials,* vol. 523, pp. 510-537, 2019/09/01/ 2019.
[28] S. M. Bruemmer, E. P. Simonen, P. M. Scott, P. L. Andresen, G. S. Was, and J. L. Nelson, "Radiation-induced material changes and susceptibility to intergranular failure of light-water-reactor core internals," *Journal of Nuclear Materials,* vol. 274, no. 3, pp. 299-314, 1999/09/01/ 1999.
[29] B. N. Singh, "On the influence of grain boundaries on void growth," *The Philosophical Magazine: A Journal of Theoretical Experimental and Applied Physics,* vol. 28, no. 6, pp. 1409-1413, 1973/12/01 1973.
[30] O. El-Atwani *et al.*, "The role of grain size in He bubble formation: Implications for swelling resistance," *Journal of Nuclear Materials,* vol. 484, pp. 236-244, 2017/02/01/ 2017.
[31] A. Hirata, T. Fujita, Y. R. Wen, J. H. Schneibel, C. T. Liu, and M. W. Chen, "Atomic structure of nanoclusters in oxide-dispersion-strengthened steels," *Nature Materials,* vol. 10, no. 12, pp. 922-926, 2011/12/01 2011.
[32] M. K. Miller, C. M. Parish, and Q. Li, "Advanced oxide dispersion strengthened and nanostructured ferritic alloys," *Materials Science & Technology,* Article vol. 29, no. 10, pp. 1174-1178, 2013.
[33] J. Hetherly, E. Martinez, Z. F. Di, M. Nastasi, and A. Caro, "Helium bubble precipitation at dislocation networks," *Scripta Materialia,* vol. 66, no. 1, pp. 17-20, 2012/01/01/ 2012.
[34] M. J. Alinger, G. R. Odette, and D. T. Hoelzer, "The development and stability of Y–Ti–O nanoclusters in mechanically alloyed Fe–Cr based ferritic alloys," *Journal of Nuclear Materials,* vol. 329-333, pp. 382-386, 2004/08/01/ 2004.
[35] D. Pazos, M. Suárez, A. Fernández, P. Fernández, I. Iturriza, and N. Ordás, "Microstructural comparison of Oxide Dispersion Strengthened Fe-14Cr steels produced by HIP and SPS," *Fusion Engineering and Design,* vol. 146, pp. 2328-2333, 2019/09/01/ 2019.
[36] A. J. London *et al.*, "Effect of Ti and Cr on dispersion, structure and composition of oxide nano-particles in model ODS alloys," *Acta Materialia,* vol. 97, pp. 223-233, 2015/09/15/ 2015.
[37] C. Lu, Z. Lu, R. Xie, Z. Li, C. Liu, and L. Wang, "Effect of Y/Ti atomic ratio on microstructure of oxide dispersion strengthened alloys," *Materials Characterization,* vol. 134, pp. 35-40, 2017/12/01/ 2017.

[38] D. T. Hoelzer, J. Bentley, M. A. Sokolov, M. K. Miller, G. R. Odette, and M. J. Alinger, "Influence of particle dispersions on the high-temperature strength of ferritic alloys," *Journal of Nuclear Materials,* vol. 367-370, pp. 166-172, 2007/08/01/ 2007.

[39] Y. Ijiri, N. Oono, S. Ukai, S. Ohtsuka, T. Kaito, and Y. Matsukawa, "Oxide particle–dislocation interaction in 9Cr-ODS steel," *Nuclear Materials and Energy,* vol. 9, pp. 378-382, 2016/12/01/ 2016.

[40] C. P. Massey *et al.*, "Stability of a model Fe-14Cr nanostructured ferritic alloy after long-term thermal creep," *Scripta Materialia,* vol. 170, pp. 134-139, 2019/09/01/ 2019.

[41] N. Sakaguchi, M. Endo, S. Watanabe, H. Kinoshita, S. Yamashita, and H. Kokawa, "Radiation-induced segregation and corrosion behavior on Σ3 coincidence site lattice and random grain boundaries in proton-irradiated type-316L austenitic stainless steel," *Journal of Nuclear Materials,* vol. 434, no. 1, pp. 65-71, 2013/03/01/ 2013.

[42] N. Cunningham, Y. Wu, D. Klingensmith, and G. R. Odette, "On the remarkable thermal stability of nanostructured ferritic alloys," *Materials Science and Engineering: A,* vol. 613, pp. 296-305, 2014/09/08/ 2014.

[43] M. Ratti, D. Leuvrey, M. H. Mathon, and Y. de Carlan, "Influence of titanium on nano-cluster (Y, Ti, O) stability in ODS ferritic materials," *Journal of Nuclear Materials,* vol. 386-388, pp. 540-543, 2009/04/30/ 2009.

[44] S.-Y. Zhong *et al.*, "The Effect of Y/Ti Ratio on Oxide Precipitate Evolution in ODS Fe-14 Wt Pct Cr Alloys," *Metallurgical and Materials Transactions A,* vol. 46, no. 3, pp. 1413-1418, 2015/03/01 2015.

[45] L. Barnard, N. Cunningham, G. R. Odette, I. Szlufarska, and D. Morgan, "Thermodynamic and kinetic modeling of oxide precipitation in nanostructured ferritic alloys," *Acta Materialia,* vol. 91, pp. 340-354, 2015/06/01/ 2015.

[46] M. K. Miller and D. T. Hoelzer, "Effect of neutron irradiation on nanoclusters in MA957 ferritic alloys," *Journal of Nuclear Materials,* vol. 418, no. 1, pp. 307-310, 2011/11/01/ 2011.

[47] I. M. Lifshitz and V. V. Slyozov, "The kinetics of precipitation from supersaturated solid solutions," *Journal of Physics and Chemistry of Solids,* vol. 19, no. 1, pp. 35-50, 1961/04/01/ 1961.

[48] X. Liu, Y. Miao, Y. Wu, S. A. Maloy, and J. F. Stubbins, "Stability of nanoclusters in an oxide dispersion strengthened alloy under neutron irradiation," *Scripta Materialia,* vol. 138, pp. 57-61, 2017/09/01/ 2017.

[49] X. Liu *et al.*, "Radiation resistance of oxide dispersion strengthened alloys: Perspectives from in situ observations and rate theory calculations," *Scripta Materialia,* vol. 148, pp. 33-36, 2018/04/15/ 2018.

[50] E. Martínez, O. Senninger, A. Caro, F. Soisson, M. Nastar, and B. P. Uberuaga, "Role of Sink Density in Nonequilibrium Chemical Redistribution in Alloys," *Physical Review Letters,* vol. 120, no. 10, p. 106101, 03/08/ 2018.

[51] O. El-Atwani, J. E. Nathaniel, A. C. Leff, K. Hattar, and M. L. Taheri, "Direct Observation of Sink-Dependent Defect Evolution in Nanocrystalline Iron under Irradiation," *Scientific Reports,* vol. 7, no. 1, p. 1836, 2017/05/12 2017.

[52] G. S. Was *et al.*, "Emulation of reactor irradiation damage using ion beams," *Scripta Materialia,* vol. 88, pp. 33-36, 2014/10/01/ 2014.

[53] J. P. Wharry, M. J. Swenson, and K. H. Yano, "A review of the irradiation evolution of dispersed oxide nanoparticles in the b.c.c. Fe-Cr system: Current understanding and future directions," *Journal of Nuclear Materials,* vol. 486, pp. 11-20, 2017/04/01/ 2017.

[54] H. Trinkaus and B. N. Singh, "Helium accumulation in metals during irradiation – where do we stand?," *Journal of Nuclear Materials,* vol. 323, no. 2, pp. 229-242, 2003/12/01/ 2003.

[55] X. Gai, R. Smith, and S. D. Kenny, "Inert gas bubbles in bcc Fe," *Journal of Nuclear Materials,* vol. 470, pp. 84-89, 2016/03/01/ 2016.
[56] K. Morishita, R. Sugano, B. D. Wirth, and T. Diaz de la Rubia, "Thermal stability of helium–vacancy clusters in iron," *Nuclear Instruments and Methods in Physics Research Section B: Beam Interactions with Materials and Atoms,* vol. 202, pp. 76-81, 2003/04/01/ 2003.
[57] T. Seletskaia, Y. N. Osetsky, R. E. Stoller, and G. M. Stocks, "Calculation of helium defect clustering properties in iron using a multi-scale approach," *Journal of Nuclear Materials,* vol. 351, no. 1, pp. 109-118, 2006/06/01/ 2006.
[58] L. Zhang, Y. Zhang, and G.-H. Lu, "Structure and stability of He and He–vacancy clusters at a Σ5(310)/[001] grain boundary in bcc Fe from first-principles," *Journal of Physics: Condensed Matter,* vol. 25, no. 9, p. 095001, 2013/01/11 2013.
[59] E. Martínez, D. Schwen, and A. Caro, "Helium segregation to screw and edge dislocations in α-iron and their yield strength," *Acta Materialia,* vol. 84, pp. 208-214, 2015/02/01/ 2015.
[60] L. Yang, Y. Jiang, Y. Wu, G. R. Odette, Z. Zhou, and Z. Lu, "The ferrite/oxide interface and helium management in nano-structured ferritic alloys from the first principles," *Acta Materialia,* vol. 103, pp. 474-482, 2016/01/15/ 2016.
[61] T. Danielson, E. Tea, and C. Hin, "First-principles investigation of helium in Y2O3," *Journal of Physics D: Applied Physics,* vol. 49, no. 6, p. 065301, 2015/12/24 2015.
[62] T. Danielson and C. Hin, "Structural and electronic effects of helium interstitials in Y2Ti2O7: A first-principles study," *Journal of Nuclear Materials,* vol. 452, no. 1, pp. 189-196, 2014/09/01/ 2014.
[63] G. R. Odette, P. Miao, D. J. Edwards, T. Yamamoto, R. J. Kurtz, and H. Tanigawa, "Helium transport, fate and management in nanostructured ferritic alloys: In situ helium implanter studies," *Journal of Nuclear Materials,* vol. 417, no. 1, pp. 1001-1004, 2011/10/01/ 2011.
[64] R. J. Kurtz, G. R. Odette, T. Yamamoto, D. S. Gelles, P. Miao, and B. M. Oliver, "The transport and fate of helium in martensitic steels at fusion relevant He/dpa ratios and dpa rates," *Journal of Nuclear Materials,* vol. 367-370, pp. 417-422, 2007/08/01/ 2007.
[65] P. D. Edmondson, C. M. Parish, Y. Zhang, A. Hallén, and M. K. Miller, "Helium bubble distributions in a nanostructured ferritic alloy," *Journal of Nuclear Materials,* vol. 434, no. 1, pp. 210-216, 2013/03/01/ 2013.
[66] P. D. Edmondson, C. M. Parish, Q. Li, and M. K. Miller, "Thermal stability of nanoscale helium bubbles in a 14YWT nanostructured ferritic alloy," *Journal of Nuclear Materials,* vol. 445, no. 1, pp. 84-90, 2014/02/01/ 2014.
[67] J. Ribis, E. Bordas, P. Trocellier, and Y. Serruys, "Comparison of the neutron and ion irradiation response of nano-oxides in oxide dispersion strengthened materials," *Journal of materials research,* vol. 30, no. 14, pp. 1-12, 20/2015.
[68] T. Yamamoto, Y. Wu, G. Robert Odette, K. Yabuuchi, S. Kondo, and A. Kimura, "A dual ion irradiation study of helium–dpa interactions on cavity evolution in tempered martensitic steels and nanostructured ferritic alloys," *Journal of Nuclear Materials,* vol. 449, no. 1, pp. 190-199, 2014/06/01/ 2014.
[69] M. J. Swenson and J. P. Wharry, "The comparison of microstructure and nanocluster evolution in proton and neutron irradiated Fe–9%Cr ODS steel to 3 dpa at 500 °C," *Journal of Nuclear Materials,* vol. 467, pp. 97-112, 2015/12/01/ 2015.
[70] C. Domain, C. Becquart, and A. de Backer, *Atomistic Modeling of Radiation Damage in Metallic Alloys*. 2018.
[71] A. Dunn, R. Dingreville, E. Martínez, and L. Capolungo, "Synchronous parallel spatially resolved stochastic cluster dynamics," *Computational Materials Science,* vol. 120, pp. 43-52, 2016/07/01/ 2016.

[72] S. Rokkam, A. El-Azab, P. Millett, and D. Wolf, "Phase field modeling of void nucleation and growth in irradiated metals," *Modelling and Simulation in Materials Science and Engineering,* vol. 17, no. 6, p. 064002, 2009/08/24 2009.
[73] R. A. Johnson and N. Q. Lam, "Solute segregation in metals under irradiation," *Physical Review B,* vol. 13, no. 10, pp. 4364-4375, 05/15/ 1976.
[74] T. R. Allen and G. S. Was, "Modeling radiation-induced segregation in austenitic Fe–Cr–Ni alloys," *Acta Materialia,* vol. 46, no. 10, pp. 3679-3691, 6/12/ 1998.
[75] J. P. Wharry and G. S. Was, "A systematic study of radiation-induced segregation in ferritic–martensitic alloys," *Journal of Nuclear Materials,* vol. 442, no. 1–3, pp. 7-16, 11// 2013.
[76] J. P. Wharry and G. S. Was, "The mechanism of radiation-induced segregation in ferritic–martensitic alloys," *Acta Materialia,* vol. 65, pp. 42-55, 2/15/ 2014.
[77] K. Y. Khromov, V. G. Vaks, and I. A. Zhuravlev, "Studies of concentration and temperature dependences of precipitation kinetics in iron-copper alloys using kinetic Monte Carlo and stochastic statistical simulations," *Journal of Experimental and Theoretical Physics,* vol. 116, no. 2, pp. 236-251, 2013/02/01 2013.
[78] J. A. Aguiar *et al.*, "Nanoscale morphologies at alloyed and irradiated metal-oxide bilayers," *Journal of Materials Science,* vol. 50, no. 7, pp. 2726-2734, 2015/04/01 2015.
[79] D. Gendt, "Kinetics of niobium carbide precipitation in ferrite," France2001, Available: http://inis.iaea.org/search/search.aspx?orig_q=RN:34067994.
[80] C. Hin, B. D. Wirth, and J. B. Neaton, "Formation of Y2O3 nanoclusters in nanostructured ferritic alloys during isothermal and anisothermal heat treatment: A kinetic Monte Carlo study," *Physical Review B,* vol. 80, no. 13, Oct 2009, Art. no. 134118.
[81] C. Hin and B. D. Wirth, "Formation of oxide nanoclusters in nanostructured ferritic alloys during anisothermal heat treatment: A kinetic Monte Carlo study," *Materials Science and Engineering: A,* vol. 528, no. 4, pp. 2056-2061, 2011/02/25/ 2011.
[82] C. Hin, Y. Bréchet, P. Maugis, and F. Soisson, "Kinetics of heterogeneous dislocation precipitation of NbC in alpha-iron," *Acta Materialia,* vol. 56, no. 19, pp. 5535-5543, 2008/11/01/ 2008.
[83] C. Hin, Y. Bréchet, P. Maugis, and F. Soisson, "Kinetics of heterogeneous grain boundary precipitation of NbC in α-iron: A Monte Carlo study," *Acta Materialia,* vol. 56, no. 19, pp. 5653-5667, 2008/11/01/ 2008.
[84] F. Soisson, "Kinetic Monte Carlo simulations of radiation induced segregation and precipitation," (in English), *Journal of Nuclear Materials,* Article vol. 349, no. 3, pp. 235-250, Mar 2006.
[85] G. S. Was *et al.*, "Assessment of radiation-induced segregation mechanisms in austenitic and ferritic–martensitic alloys," *Journal of Nuclear Materials,* vol. 411, no. 1, pp. 41-50, 2011/04/01/ 2011.
[86] C. S. Becquart and C. Domain, "Introducing chemistry in atomistic kinetic Monte Carlo simulations of Fe alloys under irradiation," *physica status solidi (b),* vol. 247, no. 1, pp. 9-22, 2010/01/01 2010.
[87] E. Vincent, C. S. Becquart, and C. Domain, "Microstructural evolution under high flux irradiation of dilute Fe–CuNiMnSi alloys studied by an atomic kinetic Monte Carlo model accounting for both vacancies and self interstitials," *Journal of Nuclear Materials,* vol. 382, no. 2, pp. 154-159, 2008/12/01/ 2008.
[88] B. D. Wirth and E. M. Bringa, "A Kinetic Monte Carlo Model for Helium Diffusion and Clustering in Fusion Environments," *Physica Scripta,* p. 80, 2004.
[89] C. S. Deo *et al.*, "Helium bubble nucleation in bcc iron studied by kinetic Monte Carlo simulations," *Journal of Nuclear Materials,* vol. 361, no. 2, pp. 141-148, 2007/04/15/ 2007.

[90] X. Guo, X. Zhang, J. Xue, and W. Li, "KMC simulation of helium bubble formation in alpha-Fe," *Nuclear Instruments and Methods in Physics Research Section B: Beam Interactions with Materials and Atoms,* vol. 307, pp. 77-80, 2013/07/15/ 2013.
[91] L. Barnard, J. D. Tucker, S. Choudhury, T. R. Allen, and D. Morgan, "Modeling radiation induced segregation in Ni–Cr model alloys from first principles," *Journal of Nuclear Materials,* vol. 425, no. 1, pp. 8-15, 2012/06/01/ 2012.
[92] J. Ribis and Y. de Carlan, "Interfacial strained structure and orientation relationships of the nanosized oxide particles deduced from elasticity-driven morphology in oxide dispersion strengthened materials," *Acta Materialia,* vol. 60, no. 1, pp. 238-252, 2012/01/01/ 2012.
[93] Y. Jiang, J. R. Smith, and G. R. Odette, "Formation of Y-Ti-O nanoclusters in nanostructured ferritic alloys: A first-principles study," *Physical Review B,* vol. 79, no. 6, p. 064103, 02/06/ 2009.
[94] B. B. Nielsen and A. v. Veen, "The lattice response to embedding of helium impurities in BCC metals," *Journal of Physics F: Metal Physics,* vol. 15, no. 12, pp. 2409-2420, 1985/12 1985.
[95] K. Nordlund, J. Wallenius, and L. Malerba, "Molecular dynamics simulations of threshold displacement energies in Fe," *Nuclear Instruments and Methods in Physics Research Section B: Beam Interactions with Materials and Atoms,* vol. 246, no. 2, pp. 322-332, 2006/05/01/ 2006.
[96] G. H. Kinchin and R. S. Pease, "The Displacement of Atoms in Solids by Radiation," *Reports on Progress in Physics,* vol. 18, no. 1, pp. 1-51, 1955/01/01 1955.
[97] M. J. Norgett, M. T. Robinson, and I. M. Torrens, "A proposed method of calculating displacement dose rates," *Nuclear Engineering and Design,* vol. 33, no. 1, pp. 50-54, 1975/08/01/ 1975.
[98] A. Seeger, "Atomic defects in metals and semiconductors," in *Festkörperprobleme 16: Plenary Lectures of the Divisions "Semiconductor Physics" "Metal Physics" "Low Temperature Physics" "Thermodynamics and Statistical Physics" of the German Physical Society Freudenstadt, April 5–9, 1976*, J. Treusch, Ed. Berlin, Heidelberg: Springer Berlin Heidelberg, 1976, pp. 149-178.
[99] M. Mock and K. Albe, "Diffusion of yttrium in bcc-iron studied by kinetic Monte Carlo simulations," *Journal of Nuclear Materials,* vol. 494, pp. 157-164, 2017/10/01/ 2017.
[100] S. L. Shang *et al.*, "Vacancy mechanism of oxygen diffusivity in bcc Fe: A first-principles study," *Corrosion Science,* vol. 83, pp. 94-102, 2014/06/01/ 2014.
[101] L. Ventelon, B. Wirth, and C. Domain, "Helium–self-interstitial atom interaction in α-iron," *Journal of Nuclear Materials,* vol. 351, no. 1, pp. 119-132, 2006/06/01/ 2006.
[102] P. Klugkist and C. Herzig, "Tracer diffusion of titanium in α-iron," *physica status solidi (a),* vol. 148, no. 2, pp. 413-421, 1995.
[103] R. Barlow and P. J. Grundy, "The determination of the diffusion constants of oxygen in nickel and α-iron by an internal oxidation method," *Journal of Materials Science,* journal article vol. 4, no. 9, pp. 797-801.
[104] E. Vincent, C. S. Becquart, and C. Domain, "Ab initio calculations of self-interstitial interaction and migration with solute atoms in bcc Fe," *Journal of Nuclear Materials,* vol. 359, no. 3, pp. 227-237, 12/15/ 2006.
[105] B. W. Zhang, G. Liu, and K. Han, "The Fe-Y (iron-yttrium) system," *Journal of Phase Equilibria,* vol. 13, no. 3, pp. 304-308, 1992/06/01 1992.
[106] J. L. Murray, "The Fe−Ti (Iron-Titanium) system," *Bulletin of Alloy Phase Diagrams,* vol. 2, no. 3, pp. 320-334, 1981/12/01 1981.
[107] P. J. Spencer and O. Kubaschewski, "A thermodynamic assessment of the iron-oxygen system," *Calphad,* vol. 2, no. 2, pp. 147-167, 1978/01/01/ 1978.
[108] F. Kano, K. Fukuya, S. Hamada, and Y. Miwa, "Effect of carbon and nitrogen on grain boundary segregation in irradiated stainless steels," *Journal of Nuclear Materials,* vol. 258-263, pp. 1713-1717, 1998/10/01/ 1998.

[109] S. Hofmann and J. Erlewein, "A model of the kinetics and equilibria of surface segregation in the monolayer regime," *Surface Science,* vol. 77, no. 3, pp. 591-602, 1978/11/01 1978.
[110] P. Lejcek, L. Zheng, S. Hofmann, and M. Sob, "Applied Thermodynamics: Grain Boundary Segregation," *Entropy,* vol. 16, no. 3, pp. 1462-1483, 2014.
[111] K. Ishida, "Effect of grain size on grain boundary segregation," *Journal of Alloys and Compounds,* vol. 235, no. 2, pp. 244-249, 3/15/ 1996.
[112] D. M. M. Guttmann, "Grain Boundary Segregation in Multicomponent Systems," in *Interfacial Segregation*, J. M. B. W.C. Johnson, Ed.: American Society for Metals, 1977.
[113] P. Lejček, S. Hofmann, and J. Janovec, "Prediction of enthalpy and entropy of solute segregation at individual grain boundaries of α-iron and ferrite steels," *Materials Science and Engineering: A,* vol. 462, no. 1–2, pp. 76-85, 7/25/ 2007.
[114] P. Lejček, M. Šob, V. Paidar, and V. Vitek, "Why calculated energies of grain boundary segregation are unreliable when segregant solubility is low," *Scripta Materialia,* vol. 68, no. 8, pp. 547-550, 2013/04/01/ 2013.
[115] C. W. He, M. F. Barthe, P. Desgardin, S. Akhmadaliev, M. Behar, and F. Jomard, "Positron studies of interaction between yttrium atoms and vacancies in bcc iron with relevance for ODS nanoparticles formation," *Journal of Nuclear Materials,* vol. 455, no. 1–3, pp. 398-401, 12// 2014.
[116] S. Takaki, J. Fuss, H. Kuglers, U. Dedek, and H. Schultz, "The resistivity recovery of high purity and carbon doped iron following low temperature electron irradiation," *Radiation Effects,* vol. 79, no. 1-4, pp. 87-122, 1983/01/01 1983.
[117] J. Li, "AtomEye: an efficient atomistic configuration viewer," *Modelling and Simulation in Materials Science and Engineering,* vol. 11, no. 2, pp. 173-177, 2003/01/30 2003.
[118] T. Stan, Y. Wu, J. Ciston, T. Yamamoto, and G. R. Odette, "Characterization of polyhedral nano-oxides and helium bubbles in an annealed nanostructured ferritic alloy," *Acta Materialia,* vol. 183, pp. 484-492, 2020/01/15/ 2020.
[119] J. Ribis and F. Leprêtre, "Interface roughening in irradiated oxide dispersion strengthened steels," *Applied Physics Letters,* vol. 111, no. 26, p. 261602, 2017/12/25 2017.
[120] E. Clouet and M. Nastar, "Monte Carlo Study of the Precipitation Kinetics of Al3Zr in Al-Zr," in *Complex Inorganic Solids: Structural, Stability, and Magnetic Properties of Alloys*, P. E. A. Turchi, A. Gonis, K. Rajan, and A. Meike, Eds. Boston, MA: Springer US, 2005, pp. 215-239.
[121] X. Boulnat, M. Perez, D. Fabrègue, S. Cazottes, and Y. de Carlan, "Characterization and modeling of oxides precipitation in ferritic steels during fast non-isothermal consolidation," *Acta Materialia,* vol. 107, pp. 390-403, 2016/04/01/ 2016.
[122] R. M. Bethea and R. R. Rhinehart, *Applied Engineering Statistics*. Taylor & Francis, 1991.
[123] S. Cao and R. R. Rhinehart, *J. Proc. Cont. ,* vol. 5, no. 6, pp. 363-374, 1995.
[124] J. D. Kelly and J. D. Hedengren, "A steady-state detection (SSD) algorithm to detect non-stationary drifts in processes," *Journal of Process Control,* vol. 23, no. 3, pp. 326-331, 3// 2013.
[125] P. R. Brown and R. R. Rhinehart. (2000) Automated steady-state identification in multivariable systems. *Hydrocarbon Processing* [Article]. 79. Available: http://link.galegroup.com.ezproxy.lib.vt.edu/apps/doc/A66497207/AONE?u=viva_vpi&sid=AONE&xid=e7e3e820
[126] S. Asmussen, P. Glynn, and H. Thorisson, "Stationarity detection in the initial transient problem," *ACM Transactions on Modeling and Computer Simulation (TOMACS),* vol. 2, no. 2, pp. 130-157, 1992.
[127] L. W. Schruben, "Detecting Initialization Bias in Simulation Output," *Operations Research,* vol. 30, no. 3, pp. 569-590, 1982.

[128] M. L. Darby, M. Nikolaou, J. Jones, and D. Nicholson, "RTO: An overview and assessment of current practice," *Journal of Process Control,* vol. 21, no. 6, pp. 874-884, 7// 2011.
[129] C. Celis, É. Xavier, T. Teixeira, and G. R. Pinto, "Steady State Detection in Industrial Gas Turbines for Condition Monitoring and Diagnostics Applications," in *ASME Turbo Expo 2014: Turbine Technical Conference and Exposition*, 2014, pp. V006T06A001-V006T06A001: American Society of Mechanical Engineers.
[130] R. R. Rhinehart, "Automated steady and transient state identification in noisy processes," in *2013 American Control Conference*, 2013, pp. 4477-4493.
[131] J. Wu, S. Zhou, and X. Li, "Acoustic Emission Monitoring for Ultrasonic Cavitation Based Dispersion Process," *Journal of Manufacturing Science and Engineering,* vol. 135, no. 3, pp. 031015-031015, 2013.
[132] D. L. Simon and J. S. Litt, "A Data Filter for Identifying Steady-State Operating Points in Engine Flight Data for Condition Monitoring Applications," *Journal of Engineering for Gas Turbines and Power,* vol. 133, no. 7, p. 71603, 2011.
[133] S. Narasimhan, C. S. Kao, and R. S. H. Mah, "Detecting changes of steady states using the mathematical theory of evidence," *AIChE Journal,* vol. 33, no. 11, pp. 1930-1932, 1987.
[134] T. Jiang, B. Chen, X. He, and P. Stuart, "Application of steady-state detection method based on wavelet transform," *Computers & Chemical Engineering,* vol. 27, no. 4, pp. 569-578, 4/15/ 2003.
[135] S. Cao and R. R. Rhinehart, "An efficient method for on-line identification of steady state," *Journal of Process Control,* vol. 5, no. 6, pp. 363-374, 1995/12/01 1995.
[136] R. R. Rhinehart, "Convergence criterion in optimization of stochastic processes," *Computers & Chemical Engineering,* vol. 68, pp. 1-6, 9/4/ 2014.
[137] S. Cao and R. R. Rhinehart, "Critical values for a steady-state identifier," *Journal of Process Control,* vol. 7, no. 2, pp. 149-152, 1997/01/01 1997.
[138] N. A. Shrowti, K. P. Vilankar, and R. R. Rhinehart, "Type-II critical values for a steady-state identifier," *Journal of Process Control,* vol. 20, no. 7, pp. 885-890, 8// 2010.
[139] G. W. Snedecor and W. G. Cochran, *Statistical methods*, 8th ed. ed. Ames :: Iowa State University Press, 1989.
[140] D. S. Moore and G. P. McCabe, *Introduction to the practice of statistics*, 5th ed. ed. New York :: W.H. Freeman and Co., 2006.
[141] M. Núñez, T. Robie, and D. G. Vlachos, "Acceleration and sensitivity analysis of lattice kinetic Monte Carlo simulations using parallel processing and rate constant rescaling," *The Journal of Chemical Physics,* vol. 147, no. 16, p. 164103, 2017/10/28 2017.
[142] A. Haddadi and K. Hashtrudi-Zaad, "Real-Time Identification of Hunt–Crossley Dynamic Models of Contact Environments," *IEEE Transactions on Robotics,* vol. 28, no. 3, pp. 555-566, 2012.
[143] S. Leye, R. Ewald, and A. M. Uhrmacher, "Composing problem solvers for simulation experimentation: a case study on steady state estimation," *PloS one,* vol. 9, no. 4, p. e91948, 2014.
[144] K. Pawlikowski, "Steady-state simulation of queueing processes: survey of problems and solutions," *ACM Computing Surveys (CSUR),* vol. 22, no. 2, pp. 123-170, 1990.
[145] M. Kim, S. H. Yoon, P. A. Domanski, and W. Vance Payne, "Design of a steady-state detector for fault detection and diagnosis of a residential air conditioner," *International Journal of Refrigeration,* vol. 31, no. 5, pp. 790-799, 8// 2008.
[146] A. P. J. Jansen and I. ebrary, *An introduction to kinetic Monte Carlo simulations of surface reactions* (no. Book, Whole). Heidelberg;Berlin;: Springer, 2012.
[147] T. Danielson, J. E. Sutton, C. Hin, and A. Savara, "SQERTSS: Dynamic rank based throttling of transition probabilities in kinetic Monte Carlo simulations," *Computer Physics Communications,* vol. 219, no. Supplement C, pp. 149-163, 2017/10/01/ 2017.

[148] C. Zener, "Theory of Growth of Spherical Precipitates from Solid Solution," *Journal of Applied Physics,* vol. 20, no. 10, pp. 950-953, 1949/10/01 1949.
[149] R. Forschungszentrum, J. Gmbh, G. Kampmann, and P. Voorhees, "5 Homogeneous Second-Phase Precipitation," 01/28 2005.
[150] A. J. Ardell, "On the coarsening of grain boundary precipitates," *Acta Metallurgica,* vol. 20, no. 4, pp. 601-609, 1972/04/01/ 1972.
[151] A. Baldan, "Review Progress in Ostwald ripening theories and their applications to nickel-base superalloys Part I: Ostwald ripening theories," *Journal of Materials Science,* vol. 37, no. 11, pp. 2171-2202, 2002/06/01 2002.
[152] Z. Liang, C. Chang, C. Abromeit, J. Banhart, and J. Hrisch, "The kinetics of clustering in Al–Mg–Si alloys studied by Monte Carlo simulation," *International Journal of Materials Research (formerly Zeitschrift fuer Metallkunde),* vol. 103, p. 980, 08/01 2012.
[153] E. A. Marquis, "Core/shell structures of oxygen-rich nanofeatures in oxide-dispersion strengthened Fe–Cr alloys," *Applied Physics Letters,* vol. 93, no. 18, p. 181904, 2008/11/03 2008.
[154] M. K. Miller, D. T. Hoelzer, E. A. Kenik, and K. F. Russell, "Stability of ferritic MA/ODS alloys at high temperatures," *Intermetallics,* vol. 13, no. 3, pp. 387-392, 2005/03/01/ 2005.
[155] L. Barnard, "First Principles-Based Thermokinetic Modeling of Steels and Ni Alloys for Nuclear Applications," Ph.D., University of Wisconsin, Madison, 2013.
[156] J. Ribis, M. L. Lescoat, S. Y. Zhong, M. H. Mathon, and Y. de Carlan, "Influence of the low interfacial density energy on the coarsening resistivity of the nano-oxide particles in Ti-added ODS material," *Journal of Nuclear Materials,* vol. 442, no. 1, Supplement 1, pp. S101-S105, 2013/11/01/ 2013.
[157] D. A. Huse, "Corrections to late-stage behavior in spinodal decomposition: Lifshitz-Slyozov scaling and Monte Carlo simulations," *Physical Review B,* vol. 34, no. 11, pp. 7845-7850, 12/01/ 1986.
[158] F. Soisson and C.-C. Fu, "Cu-precipitation kinetics in $\ensuremath{\alpha}\text{\ensuremath{-}}\mathrm{Fe}$ from atomistic simulations: Vacancy-trapping effects and Cu-cluster mobility," *Physical Review B,* vol. 76, no. 21, p. 214102, 12/06/ 2007.
[159] N. Castin, M. I. Pascuet, and L. Malerba, "Modeling the first stages of Cu precipitation in α-Fe using a hybrid atomistic kinetic Monte Carlo approach," *The Journal of Chemical Physics,* vol. 135, no. 6, p. 064502, 2011/08/14 2011.
[160] G. Prévot, "Ostwald ripening of three-dimensional clusters on a surface studied with an ultrafast kinetic Monte Carlo algorithm," *Physical Review B,* vol. 84, no. 4, p. 045434, 07/18/ 2011.
[161] T. Chen *et al.*, "Temperature dependent dispersoid stability in ion-irradiated ferritic-martensitic dual-phase oxide-dispersion-strengthened alloy: Coherent interfaces vs. incoherent interfaces," *Acta Materialia,* vol. 116, pp. 29-42, 2016/09/01/ 2016.
[162] D. Madland and A. Ignatyuk, "Fission neutron spectra of uranium-235," Tech. Rep. NEA/WPEC-9, OECD-NEA2003.
[163] Y. G. Li, Y. Yang, M. P. Short, Z. J. Ding, Z. Zeng, and J. Li, "IM3D: A parallel Monte Carlo code for efficient simulations of primary radiation displacements and damage in 3D geometry," *Scientific Reports,* vol. 5, no. 1, p. 18130, 2015/12/11 2015.
[164] E. Aydogan *et al.*, "Response of 14YWT alloys under neutron irradiation: A complementary study on microstructure and mechanical properties," *Acta Materialia,* vol. 167, pp. 181-196, 2019/04/01/ 2019.
[165] R. S. Nelson, J. A. Hudson, and D. J. Mazey, "The stability of precipitates in an irradiation environment," *Journal of Nuclear Materials,* vol. 44, no. 3, pp. 318-330, 1972/09/01/ 1972.
[166] J. Ribis, E. Bordas, P. Trocellier, Y. Serruys, Y. de Carlan, and A. Legris, "Radiation-sustained nanocluster metastability in oxide dispersion strengthened materials," *Nuclear Instruments and*

Methods in Physics Research Section B: Beam Interactions with Materials and Atoms, vol. 365, pp. 22-25, 2015/12/15/ 2015.
[167] J. Wang *et al.*, "Atom probe tomography characterization of high-dose ion irradiated MA957," *Journal of Nuclear Materials,* vol. 545, p. 152528, 2021/03/01/ 2021.
[168] T. R. Allen *et al.*, "Radiation response of a 9 chromium oxide dispersion strengthened steel to heavy ion irradiation," *Journal of Nuclear Materials,* vol. 375, no. 1, pp. 26-37, 2008.
[169] T. Schuler, D. R. Trinkle, P. Bellon, and R. Averback, "Design principles for radiation-resistant solid solutions," *Physical Review B,* vol. 95, no. 17, p. 174102, 05/10/ 2017.
[170] C. Lu, Z. Lu, R. Xie, C. Liu, and L. Wang, "Microstructure of a 14Cr-ODS ferritic steel before and after helium ion implantation," *Journal of Nuclear Materials,* vol. 455, no. 1, pp. 366-370, 2014/12/01/ 2014.
[171] C. J. Ortiz, M. J. Caturla, C. C. Fu, and F. Willaime, "He diffusion in irradiated $\ensuremath{\alpha}\text{\ensuremath{-}}\mathrm{Fe}$: An ab-initio-based rate theory model," *Physical Review B,* vol. 75, no. 10, p. 100102, 03/26/ 2007.
[172] L. Li, J. Shi, L. Peng, W. Jiang, and G. Qian, "Formation and migration of helium pair in bcc Fe from first principle calculations," *Computational Materials Science,* vol. 170, p. 109192, 2019/12/01/ 2019.
[173] M. Vallinayagam, M. Posselt, and J. Faßbender, "Interaction of O–Y and O–Y–Ti clusters embedded in bcc Fe with He, vacancies and self-interstitial atoms," *Journal of Physics: Condensed Matter,* vol. 31, no. 48, p. 485702, 2019/08/30 2019.
[174] C.-C. Fu and F. Willaime, "Ab initio study of helium in $\ensuremath{\alpha}\text{\ensuremath{-}}\mathrm{Fe}$: Dissolution, migration, and clustering with vacancies," *Physical Review B,* vol. 72, no. 6, p. 064117, 08/24/ 2005.
[175] T. Suzudo, H. Kaburaki, and M. Yamaguchi, "Modeling of the grain boundary segregation of helium in α-Fe," *Journal of Nuclear Materials,* vol. 417, no. 1, pp. 1102-1105, 2011/10/01/ 2011.
[176] Y. Zhang, W.-Q. Feng, Y.-L. Liu, G.-H. Lu, and T. Wang, "First-principles study of helium effect in a ferromagnetic iron grain boundary: Energetics, site preference and segregation," *Nuclear Instruments and Methods in Physics Research Section B: Beam Interactions with Materials and Atoms,* vol. 267, no. 18, pp. 3200-3203, 2009/09/15/ 2009.
[177] D. Stewart, Y. Osetskiy, and R. Stoller, "Atomistic studies of formation and diffusion of helium clusters and bubbles in BCC iron," *Journal of Nuclear Materials,* vol. 417, no. 1, pp. 1110-1114, 2011/10/01/ 2011.